REPORT DOCUMENTATION PAGE

Form Approved
OMB No. 0704-0188

1. AGENCY USE ONLY (Leave blank)	2. REPORT DATE	3. REPORT TYPE AND DATES COVERED
	June 27, 1996	07/01/93 - 06/30/96 FINAL

4. TITLE AND SUBTITLE
Micro-Structure in Particulate Media - A Lattice Type Approach and Its Validation

5. FUNDING NUMBERS
F49620-93-1-0435

6. AUTHOR(S)
Muniram Budhu, George Frantziskonis, and S. Ramakrishnan

AFOSR-TR-96
0343

7. PERFORMING ORGANIZATION NAME(S) AND ADDRESS(ES)
Department of Civil Engineering and Engineering Mechanics
College of Engineering and Mines
The University of Arizona
Tucson, AZ 85721

9. SPONSORING/MONITORING AGENCY NAME(S) AND ADDRESS(ES)
AFOSR/NA
110 Duncan Avenue Suite B115
Bolling AFB, DC 20332-0001

NA

10. SPONSORING/MONITORING AGENCY REPORT NUMBER
93-1-0435

19960726 045

11. SUPPLEMENTARY NOTES

12a. DISTRIBUTION/AVAILABILITY STATEMENT
Approved for Public Release; distribution is unlimited

12b. DISTRIBUTION CODE

13. ABSTRACT (Maximum 200 words)

The objective of this research is to develop a lattice type model for describing the micro mechanical behavior of particulate media. In this model, each particle is replaced by a lattice and the interactions between each particle and its neighbors are described through contact nodes. An assembly of particles is then transformed into a two dimensional truss. Bars connecting the contact points of the particles represent the particles and constraints are prescribed at the nodes of the truss to describe sliding, bonding and rebonding. When a deformation mechanism develops, the truss becomes a pin jointed frame to derive the kinetics of the assembly.

The mechanics, formulation and numerical implementation of the lattice type model are presented. Numerical tests comprising two dimensional assemblies of disks, arranged as very loose and very dense packings, were subjected to simple shear deformation. The results show the distribution of the internal forces, the load and displacement paths, and the deformation mechanisms. Although the packings were homogenous and isotropic, the applied simple shear strains result in inhomogeneous deformation. Deformation takes place through chains or clusters of particles. Photoelastic experiments on disks gave results that are in accord with the lattice model predictions. The lattice model is conceptually simple but has some powerful features (for examples, initial imperfections, anisotropy, and particle crushing can be considered) that can provide significant insights into the micro mechanical behavior of particulate media.

14. SUBJECT TERMS
LATTICE TYPE MODEL
PARTICULATE MEDIA

15. NUMBER OF PAGES
Part I - 171
Part II - 75

16. PRICE CODE

17. SECURITY CLASSIFICATION OF REPORT	18. SECURITY CLASSIFICATION OF THIS PAGE	19. SECURITY CLASSIFICATION OF ABSTRACT	20. LIMITATION OF ABSTRACT
UNCLASSIFIED	UNCLASSIFIED	UNCLASSIFIED	UL

DISCLAIMER NOTICE

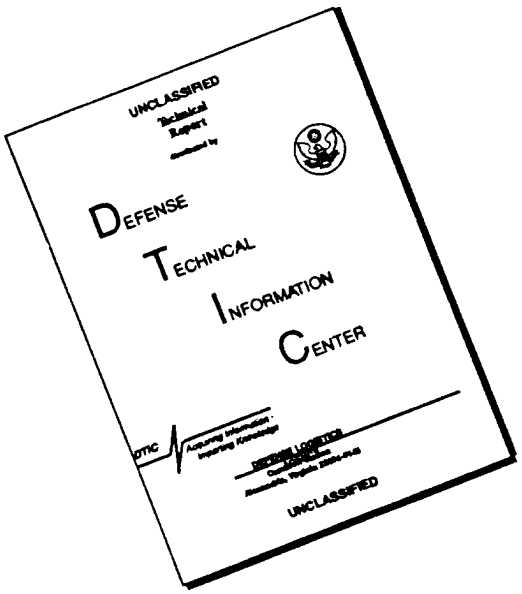

THIS DOCUMENT IS BEST QUALITY AVAILABLE. THE COPY FURNISHED TO DTIC CONTAINED A SIGNIFICANT NUMBER OF PAGES WHICH DO NOT REPRODUCE LEGIBLY.

A LATTICE TYPE MODEL FOR PARTICULATE MEDIA

PART I

Report to the

National Science Foundation
concerning NSF Grant No: MSM 9224488

and

Air Force Office of Scientific Research
concerning AFOSR Grant No: F49620-93-1-0435

by

S. Ramakrishnan
Muniram Budhu
George Frantziskonis

June, 1996

Department of Civil Engineering and Engineering Mechanics
University of Arizona
Tucson, AZ-85721

PREFACE

The research described in this report was funded by Grant No. MSM 9224488 from the National Science Foundation and by Grant No. F49620-93-1-0435 from the Air Force Office of Scientific Research. The report is divided into two parts. Part 1 contains the theoretical development, implementation and results of a lattice type model. Part II contains an experimental verification of the lattice type model through photoelastic experiments and image processing of photosensitive disks tested in a simple shear apparatus developed as part of this research. Each Part is self contained.

TABLE OF CONTENTS

page

LIST OF ILLUSTRATIONS

FIGURE PAGE

FIGURE PAGE

ABSTRACT

The objective of this research is to develop a lattice type model for describing the micro mechanical behavior of particulate media. In this model, each particle is replaced by a lattice and the interactions between each particle and its neighbors are described through contact nodes. An assembly of particles is then transformed into a two dimensional truss. Bars connecting the contact points of the particles represent the particles and constraints are prescribed at the nodes of the truss to describe sliding, bonding and rebonding. When a deformation mechanism develops, the truss becomes a pin jointed frame to derive the kinetics of the assembly.

The mechanics, formulation and numerical implementation of the lattice type model are depicted. Numerical tests comprising two dimensional assemblies of disks, arranged as very loose and very dense packings, were subjected to simple shear deformation. The results show the distribution of the internal forces, the load and displacement paths, and the deformation mechanisms. Although the packings were homogenous and isotropic, the applied simple shear strains result in inhomogeneous deformation. Deformation takes place through chains or clusters of particles. Photoelastic experiments on disks, presented in Part II of this report, gave results that are in agreement with the predictions from the lattice type model. The lattice type model is conceptually simple but has some powerful

features (for examples, initial imperfections, anisotropy, and particle crushing can be considered) that can provide significant insights into the micro mechanical behavior of particulate media.

CHAPTER 1

INTRODUCTION

1.1 Particulate materials

A particulate material may be defined as one composed of mutually contacting solid particles or structural units within the liquid and/or the gaseous phase and which exhibit dilatancy, contractancy and sensitivity to applied stresses. The description of a particle as "solid" or "grain" is relative. A 'solid particle' is that part of the skeleton which moves as a single unit during a

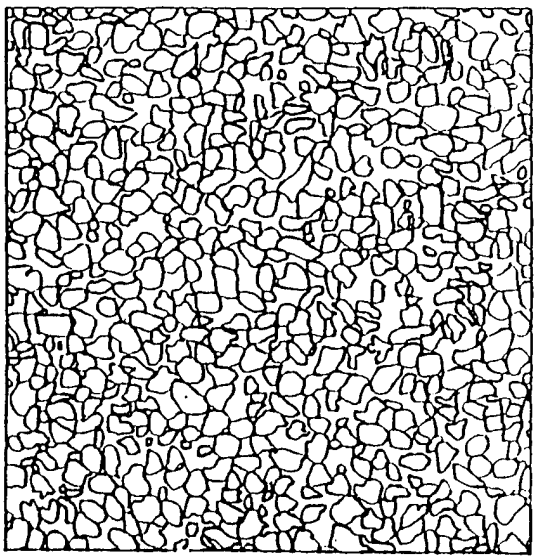

Fig. 1.1 Structure of a Particulate material

mechanical loading process. Thus a grain may be defined as an assemblage of elementary particles. The structure of a particulate material is schematically shown in Fig. 1.1.

The grains of a particulate material are typically in mutual contact. The existence of the mutual contact restricts the freedom or autonomy of motion of the individual grains and thus conditions the strength and the rigidity of a particulate material. The strength and rigidity depend on the number and strength of the contact bonds which are themselves a function of the size, shape, roughness, relative position and strength of the grains, and of the nature of interaction between the grains (Feda, 1982). The most significant feature of particulate materials is that their deformation is brought about by mutual sliding of the grains (intergranular deformation), in contrast to the deformation of the individual grains (intragranular deformation) typical of continuous media. Thus the limitations of the continuum theories for the behavior of particulate materials which do not account for the micro-structural effects have led to the development of models dependent upon particle level interactions.

1.2 Mechanics of Particulate Materials

In a structural approach to the mechanics of particulate materials, the grains are idealized to a set of elastic spheres in mutual contact. Most of the

research on the behavior of a set of elastic spheres is based on Hertz's solution (Johnson, 1985) for two deformable elastic bodies in contact. Hertz's theory of normal contacts was extended by Mindlin (1949) to include the effect of tangential forces at the contacts. The Hertz-Mindlin theory of contacts provides a foundation for research into the mechanical behavior of particulate media.

The uncertainties regarding interior stresses in samples of sand led to the development of models of granular media that are geometrically simpler than sand. These models consist of assemblies of disks (Fig. 1.2) or spheres and may be analytical, physical or numerical.

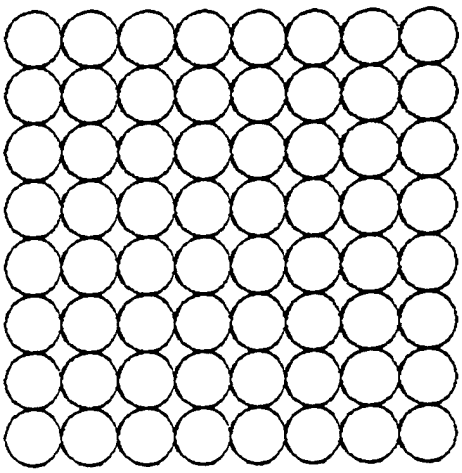

Fig. 1.2 Disk assembly model of Particulate medium

Experimental difficulties and limitations of the analytical approaches which

will be discussed in the next chapter have encouraged the development of numerical techniques. Cundall and Strack (1979a) developed a powerful numerical technique called the Discrete Element Method (DEM), wherein an assembly of rigid disks are linked by normal and tangential springs at contacts and the problem is treated as a dynamical one. Kishino (1988) modified this method for the analysis of statical behavior of granular materials and called it as Disk Model Analysis (DMA). Expressions for elastic constants (Bathurst and Rothensburg, 1988), constitutive relationships (Chang and Misra, 1989a,b) and structure of shear bands (Bardet and Proubet, 1991b and 1992) have been investigated for particulate materials using various concepts/techniques incorporating the effects of micro-structural properties.

1.3 Statement of the Problem

Recently, there has been a growing interest among physicists and engineers (Krajcinovic and Basista, 1991; Adley and Sadd, 1992; Dai and Frantziskonis, 1994; Frantziskonis et.al, 1994) to study the behavior of materials through a lattice-type network. The mechanical behavior of particulate materials, composed of granular and/or fibrous microstructures, is inherently involved with the transmission of loads along discrete paths within the material (Adley and Sadd, 1992). Based on the fact that granular materials transmit loads only through contacts, such

materials have been modelled with network theories (Trollope and Burman, 1980). It is this network like pattern of load distribution in a particulate material in the form of a lattice that has led to the proposed development of the lattice type model for particulate media in this research.

Oda (1972a,b,c) studied the effects of initial fabrics and their relations on the mechanical properties of granular materials. The fabric of a granular material is quantified by several measures such as the axial ratios of particles, orientation of contact normals and orientation of branch vectors (Konishi and Naruse, 1988). The lattice type model would very well incorporate the effects of fabric, as the lattice structure is evolved by linking the particle contacts. An attractive feature of the lattice type model would be the modelling of particles within their micro-structures as different from the modelling of contacts in the current numerical approach, DEM. Thus the lattice type model would be a conceptually simple model incorporating several features of particulate media such as particle shapes, particle interactions, particle kinetics and load path and is expected to reveal significant aspects of particulate material behavior.

1.4 Objective of this research

The objective of this research is to determine whether a lattice type simulation can lead to significant insights and understanding of the mechanical

behavior of particulate media and thus result in a better understanding of it's behavior.

1.5 Scope of this research

- Develop the mathematical concepts of a lattice type model for particulate media.
- Develop a computer program for the numerical implementation of the concepts formulating the lattice type model.
- Validate the potential of the lattice type model by conducting numerical tests on particulate packings and comparing the results with existing laboratory test results on granular materials, DEM and experiments on photoelastic disks.
- Explain the failure mechanisms in particulate media from numerical test results and investigate the effects of initial imperfections.
- Evaluate and interpret the physical quantities related to the macro-mechanical behavior of particulate media from the micro-structural properties.

1.6 Organization of text

The introduction and background presented in this chapter provides an overall view of the contents of this report. Chapter. 2 deals with the literature review of the research work carried out to understand the mechanical behavior of particulate media. This chapter begins with continuum theories, a description of Hertz-Mindlin contact theory, disk model analysis of particulate media, description of discrete element method (DEM), review of the numerical tests using DEM, concept of fabric in granular media, micro-structural continuum theories and a review of lattice modelling related to the mechanics of solids.

In Chapter. 3, the mathematical concepts related to the lattice type model and the numerical implementation of the concepts using a computer program are explained. Chapter. 4 deals with numerical tests on particulate packings and the discussion of the results. Chapter. 4 also includes a qualitative comparison of the numerical test results with laboratory test results on granular materials, evaluation of physical quantities related to macro-mechanical behavior of particulate media and an explanation of failure mechanisms in particulate media. The report is concluded in Chapter. 5, listing out the conclusions of this research and recommendations for future research.

CHAPTER 2

LITERATURE REVIEW

2.1 Continuum theories

Continuum theories constitute the earliest attempts in the modeling of the loading response of particulate/granular materials. In this macroscopic theory, constitutive relationships are derived from the analysis of experimentally determined stress-strain response of granular materials. The prediction of loading response requires (1) a theoretical model that exhibits the major features of the material response and (2) the quantitative determination of material parameters which characterize the model.

The most commonly used continuum theories can be broadly classified under two categories as the deformation theory and plasticity theory. Deformation theory implies the existence of a relatively simple relationship between the stress and strain tensors. The hyperbolic soil model of Duncan and Chang (1970) is an example of a model which uses deformation theory. The model is based on a generalization of Hooke's law for isotropic behavior and it cannot model anisotropic responses, shear dilatancy and postpeak strain softening. Limitations of the deformation theory led to the development of a number of plasticity-based models. The most widely used of these models is the

incremental theory of plasticity in which the total strain increment is expressed as the sum of the elastic and plastic strain increments.

A major limitation of the continuum theories when applied to granular materials is that no account is taken of the effects of micro-structural properties and particle level interactions. This led to the development of models based on micro-mechanical behavior of particles for which the basis is the contact theories of Hertz (1882) and Mindlin (1949).

2.2 Hertz-Mindlin theory of contacts

The relative movement of two deformable elastic bodies in contact resulting from normal force was studied by Hertz (1882). When two elastic bodies are pressed together with a normal force, 'N' (Fig. 2.1), a small circular surface is developed with a radius called contact radius. Hertz derived expressions for the contact radius (a), the normal displacement (δ_n) and the normal stiffness (K_n) as

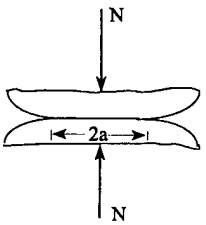

Fig. 2.1 Hertzian contact of two elastic bodies under a normal load 'N'

$$a = [\frac{3(1-\nu)RN}{8G}]^{1/3} \quad \textbf{(2.1)}$$

$$\delta_n = 2\,[\frac{3(1-\nu)N}{8GR^{1/2}}]^{2/3} \quad \textbf{(2.2)}$$

$$K_n = \frac{1-\nu}{2Ga} \quad \textbf{(2.3)}$$

where R is the radius of the sphere, ν is the Poisson's ratio and G is the shear modulus.

Mindlin (1949) included the effect of tangential forces at the contact and found that the tangential force at the contact induces a deformation in the form of a slip over a part of the contact surface. When the tangential force exceeds the frictional strength at the contact, sliding takes place. Based on Mindlin's (1949) results, the relative tangential displacement and the tangential contact stiffness are given by

$$\delta_s = \frac{3(2-\nu)\mu N}{8Ga}\,[1 - (1 - \frac{T}{\mu N})^{2/3}] \quad \textbf{(2.4)}$$

$$K_s = \frac{T}{\delta_s} \quad \textbf{(2.5)}$$

where μ is the coefficient of friction at the contact, T is the tangential force at the contact, (δ_s) is the tangential displacement at the contact and (K_s) is the tangential stiffness at the contact.

The expressions for normal stiffness and the tangential stiffness derived by Hertz and Mindlin provided the basis for research into the micro-mechanical behavior of particulate media.

2.3 Disk model analysis of particulate media

The mechanical behavior of particulate media, composed of a random packing of grains of various sizes, is studied by geometrically simpler models consisting of assemblies of disks or spheres. The outcome of such research has led to a better understanding of the behavior of particulate media and to the establishment of new concepts or models for direct application in practice. The solution technique for these models could be analytical, physical or numerical. The analytical approach is to evolve closed form solutions. The physical approach is to conduct laboratory experiments. The numerical approach is to conduct numerical tests through numerical computations based on certain mathematical concepts and implementing the concepts using computer programs.

An analytical model for cubic arrays of spheres of uniform size was proposed by Deresiewicz (1958) which predicted a non-linear and hysteretic

stress-strain behavior. Ultimate failure was also accommodated in the formulation. This analytic approach, however, was restricted to cubic/hexagonal arrays of spheres and the spheres were uniform in size.

Experiments on assemblies of optically sensitive disks has led to the direct measurement of contact forces and displacements of individual particles. Forces at contacts have been obtained from the birefringent-effect in polarized light and displacements were found by comparison of photographs made at various stages of the experiment. This method originates from the work of Dantu (1957) and Wakabayashi (1957) and was applied by De Josselin De Jong and Verruijt (1969), Drescher and De Josselin De Jong (1972) and Oda and Konishi (1974). Some limitations of the experimental techniques are: (1) the material of the disks should be optically sensitive (2) the disks do not adequately represent real particulate media.

With the advent of powerful computers, numerical techniques have become the most widely used approach for modeling assemblies of disks and spheres. In a numerical test, any data such as stress, strain, particle displacements and packing structure at various stages of the test can be stored numerically and can be visualized using graphics programs. The flexibility of numerical modeling extends to loading configurations, particle sizes, size distributions and physical properties of the particles.

Serrano and Rodriguez-Ortiz (1973) developed a numerical model for assemblies of disks and spheres. Hertzian-type contact compliances were used

for normal forces, the effects of tangential forces were considered according to the theories of Mindlin and Deresiewicz (1953), and shape changes were negligible. The numerical model was based on matricial relationships between contact forces, particle displacements and the boundary forces or displacements. A stiffness matrix was constructed that takes into account the geometrical arrangement of particles and the current stiffness at each contact. Inverting the matrix resulted in the computation of incremental displacements from the last known forces with an iteration procedure to deal with slip at contacts. Only one contact was allowed to slip at a time and it was necessary to reform the stiffness matrix when new contacts were established or contacts separated. A major limitation of the approach was the large computational time required in solving the equations even for a very small number (100) of particles. This led to the development of discrete element method (DEM), in which the particles were treated as discrete elements and the solution technique was at particle level through an iterative process.

2.4 Discrete Element Method

Cundall and Strack (1979a) developed a numerical technique called the distinct element method using a time marching scheme, based on the idea that time step can be chosen small enough that during a single time step, disturbances cannot propagate from any disk further than it's immediate neighbors. This

method has been successfully applied to the study of granular media and later researchers refer to this method as discrete element method (DEM). The method is based on the Hertz-Mindlin contact theories and Newton's second law of motion. The elastic behavior of a disk is replaced by the action of springs attached virtually at the contact points in the normal and tangential directions, and the disk itself is displaced and rotated rigidly (Fig. 2.2). Disks can overlap each other and only at that time a contact force is produced between them. The boundary can be either strain-controlled or stress-controlled, and the interaction between a boundary element and a disk is specified in a similar way as the interaction between disks. The DEM was implemented using a computer program called BALL and was used to perform numerical tests on two-dimensional assemblies of disks under a variety of boundary conditions.

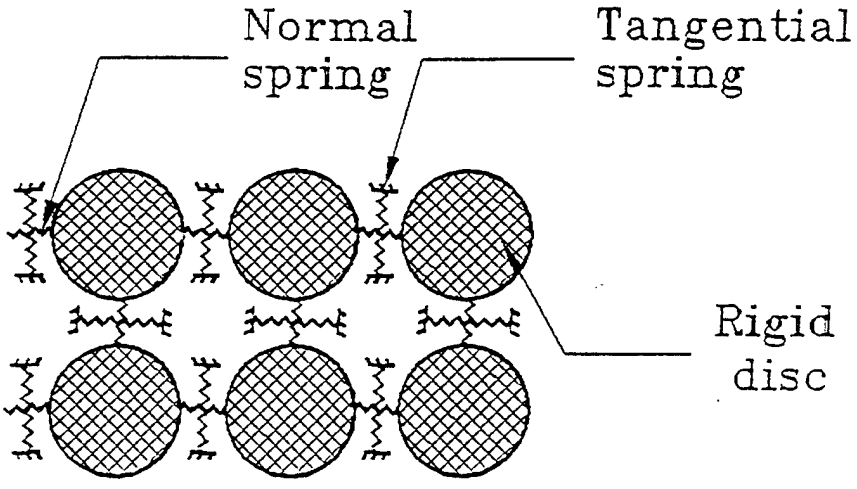

Fig. 2.2 Modeling of disks in the Discrete Element Method

The BALL program uses an explicit time-marching scheme to track the motion of individual particles with the motion of each being governed by conservation of momentum. The sequence of calculations in the BALL program is shown in Fig. 2.3. The principles involved in the calculations can be explained with respect to two particles x and y in contact at point C (Fig. 2.3). Two unit vectors e_i and t_i are defined as pointing from the center of disk x to the center of disk y and rotated 90^0 clockwise respectively. The relative velocities X_i, of the particle contacts are expressed as the components of the linear and angular velocities of the contacting particles. The normal and shear components of these velocities may then be calculated as the projections of X_i in the appropriate directions of e_i and t_i respectively. The velocities are assumed constant over a time step/increment Δt. Thus, the incremental displacements are obtained by time integration. The normal and shear stiffnesses k_n and k_s are then used to obtain the incremental normal and shear components of the contact forces. These are then added to the previous values to obtain total normal and shear forces with the constraint that the shear force is limited to a fraction of the normal force $(\tan\Phi_u)$ plus a constant cohesion. This sequence of calculations is performed for each contact prior to the application of the motion equations for any particle. Since all forces are known at every contact point translational and rotational accelerations are calculated through a difference approximation to Newton's second law.

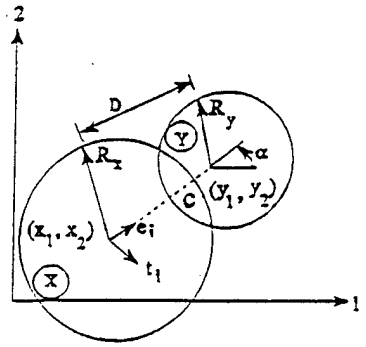

$e_i = (y_i - x_i) / D = (\cos\alpha,\ \sin\alpha)$

$t_i = (\sin\alpha,\ -\cos\alpha)$

Particle Center	Translational Velocity	Rotation Rate
(x_1, x_2)	$\dot{x}_i$	$\dot{\theta}_x$
(y_1, y_2)	$\dot{y}_i$	$\dot{\theta}_y$

FORCE-DISPLACEMENT LAW

For all contacts

1. Relative Velocities: $\dot{X}_i = (\dot{x}_i - \dot{y}_i) - (\dot{\theta}_x R_x + \dot{\theta}_y R_y)\, t_i$

   $\dot{n} = \dot{X}_i e_i, \qquad \dot{s} = \dot{X}_i t_i$

2. Relative Displalcements: $\Delta n = \dot{n}\,\Delta t, \qquad \Delta s = \dot{s}\,\Delta t$
3. Contact Force Increments: $\Delta F_n = k_n \Delta n, \qquad \Delta F_s = k_s \Delta s$
4. Total Forces: $F_n = F_n^{n-1} + \Delta F_n, \qquad F_s = F_s^{n-1} + \Delta F_s$
5. Check for Slip: $F_s = \min(F_s,\ F_n \tan\phi_\mu + c)$

For all particles

6. Calculate Moment: $M_x = \Sigma F_x R_x, \quad M_y = \Sigma F_y R_y$

EQUATIONS OF MOTION

1. Assume Force & Moment Constant over Δt: $(t^{n-1/2}$ to $t^{n+1/2})$
2. Acceleration: $\ddot{x}_i^n = \Sigma F_i / m, \qquad \ddot{\theta}^n = \Sigma M / I$
3. Velocity: $\dot{x}_i^{n+1/2} = \dot{x}_i^{n-1/2} + (\ddot{x}_i^n)\Delta t, \quad \dot{\theta}^{n+1/2} = \dot{\theta}^{n-1/2} + (\ddot{\theta}^n)\Delta t$
4. Assume Velocities constant over Δt: $(t^n$ to $t^{n+1})$
5. Displacements: $x_i^{n+1} = x_i^n + (\dot{x}^{n+1/2})\Delta t$
6. Rotation: $\theta^{n+1} = \theta^n + (\dot{\theta}^{n+1/2})\Delta t$

INCREMENT TIME

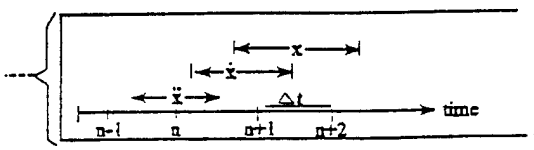

Fig. 2.3 Calculation sequence in DEM (Strack and Cundall, 1978)

Time t^0 refers to time step t = 0, time t^n refers to time t = n Δt and time $t^{n+1/2}$ refers to time t = n Δt + Δt/2. The moments and forces are assumed to be constant from time $t^{n-1/2}$ to $t^{n+1/2}$ so that the velocities centered at time $t^{n+1/2}$ are obtained by integrating the accelerations over Δt and incrementing the previous values. A second integration yields the new position and rotation centered at t^{n+1}. The time step is taken to be small enough so that the particles are unaffected by motions more than one diameter away. The new total velocities will then be used to calculate the accelerations at time t^{n+1} after the force-displacement relations have again been applied to the contacts. As interparticle overlaps change, contacts are deleted and new ones are added and consequently the changes in fabric occurring in granular media are captured. Cundall and Strack (1979b) modified the BALL program for the modeling of particles in three dimensions giving it a new name called TRUBAL. The computer program BALL and the numerical tests conducted using it are elaborately described in Strack and Cundall (1978) and Cundall and Strack (1979b). Several aspects of particulate material behavior have been investigated using BALL, TRUBAL and later modifications of the original program and concepts by many researchers, which are briefly reviewed in the next section.

2.5 Review of Numerical Experiments

Cundall and Strack (1979a) performed numerical biaxial tests on two-

dimensional assemblies of disks using the DEM and validated the potential of the technique by qualitatively comparing the contact force vector plots (Fig. 2.4) with the results of experiments on photoelastic disks by De Josselin De Jong and Verruijt (1969). Cundall and Strack (1979c) performed numerical simple shear test on a two-dimensional assembly of cylinders similar to that performed experimentally by Oda and Konishi (1974). Even though the packing arrangement in the numerical test was different from the experiment, the total number of particles and the size distribution of the particles (ratio of number of particles of different sizes) used in the numerical test were same as in the experiment. The good agreement of the plots

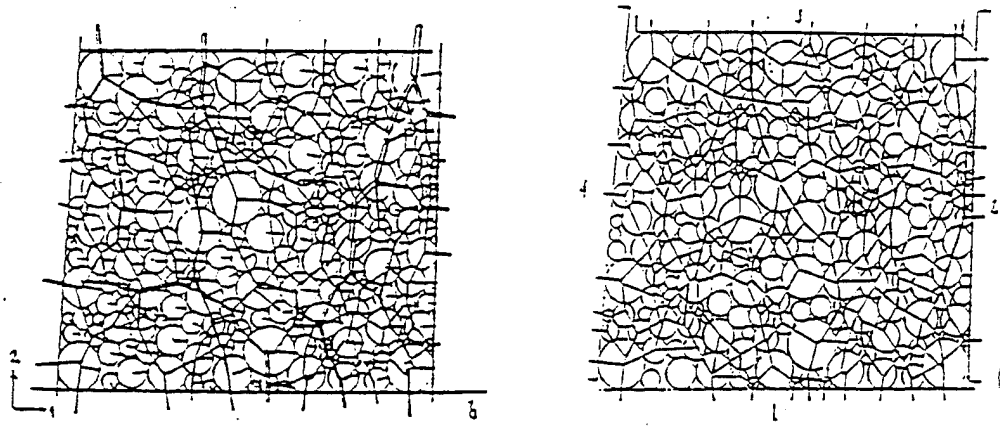

(a) Ball program (b) Photoelastic experiment

Fig. 2.4 Vector plot of contact forces from Ball program and De Josselin De Jong (1969)

of the total shear force and volumetric strain versus shear strain between the numerical test and the experiment led to the validation of DEM quantitatively.

Thus the method was established as a powerful tool for developing constitutive laws for idealized granular materials.

The mechanisms observed in the deformation and failure of granular media was explained by Cundall et. al (1982). The observed mechanisms showed that in granular media, forces are never transmitted across a sample in a uniform way, but are concentrated in 'chains' of particles. Between the chains, particles may carry little or no load. Sliding contacts are almost never observed between particles comprising the major force chains. The total number of contacts in a sample is found to decrease when the sample is loaded deviatorically. The contact deletions occur mainly for contacts with contact normals in the direction of minor principal strain. The microscopic observations in the numerical tests showed that a granular assembly consisted of two phases; Phase A, made up of stiff columns which behaves like a pin-jointed structure that dissipates no energy and imposes local deformation patterns on Phase B particles. Phase B acts like a truly plastic material that dissipates energy at many contacts and serves as a restraint on Phase A.

Based on the observations from the numerical tests, Cundall and Strack (1983) introduced a measure called constraint ratio (CR) expressed in terms of the number of particles, number of contacts and number of sliding contacts. The constraint ratio was used to interpret the structural stability of granular materials. If CR > 1, the system was found to be over constrained or statically indeterminate and the assembly was found to have a positive resistance to deformation. If CR

< 1, there were more degrees of freedom than constraints and deformation was found to take place for zero or negative increment in loading. If CR = 1, the granular assembly was found to have reached a condition of limiting stress and at this stage the assembly was found to develop a "mechanism" and deformation proceeds in a particular mode with no increase in stress.

Cundall (1988) presented results from several numerical experiments on dense sphere assemblies in three dimensions using TRUBAL and established good comparison with the results of physical experiments described by Ishibashi and Chen (1988). The nature of localization in frictional materials was investigated by Cundall (1989) using two methods; (1) a continuum calculation with a strain-hardening constitutive model and (2) using the discrete element method. It was shown that continuum calculations done with random spatial distributions of physical properties can give rise to localization in the strain-hardening regime. It was found that localized shear band decreases in thickness as shearing proceeds. The shear band was characterized by dilatation, reduction in the parallel stress component and average particle spins that deviated significantly from the rotation of the bulk material. Cundall et.al (1989) performed compression/extension shear tests by applying strain rates to a three dimensional granular assembly and evaluated incremental elastic moduli during loading and unloading using the discrete element method. This was done with an emphasis on the variation of elastic wave speeds as the sample is loaded and unloaded. The elastic moduli were evaluated in three orthogonal directions at

various stages of loading and unloading. It was suggested that the elastic moduli which is a P-wave measurement could be used as a sensitive measure of strain-induced anisotropy. The histograms of normal component of contact forces showed that force distributions were heavily biased towards the low values and it was established that theories that assume symmetrical distributions of contact forces about the mean were erroneous.

Kishino (1987) developed a numerical method called Disk Model Analysis (DMA) for the statical behavior of granular materials. Unlike the DEM which treats the problem as a dynamical one, the DMA uses a contact stiffness matrix for the equilibrium of the disks and hence is more suitable for the static deformation of granular materials. The DMA considers a fixing vector defined as a vector which consists of the force and moment required for fixing a disk at it's center and is calculated in terms of the contact forces applied at it's contact points and the body force at the center of gravity. The contact stiffness matrix is defined as a set of additional fixing vectors required to give unit movements of a disk while other disks were being fixed. To attain the equilibrium state of the disk assembly, each disk is displaced and rotated iteratively according to the contact stiffness matrix defined from the locations of neighboring disks. The DMA was used to perform biaxial tests on disk assemblies. The constitutive properties were evaluated and changes in fabric was evolved. However, a comparison of the results between the DEM and DMA was not presented.

Thornton and Sun (1993) performed numerical axisymmetric compression

tests on dense and loose systems of three dimensional polydisperse systems of spheres using the DEM. The objective of the study was to evaluate the effects of initial density and coefficient of interparticle friction on the evolution of various micromechanical parameters. It was observed that both the maximum and ultimate angles of internal shearing resistance increased when the interparticle friction is increased. It was noted that the rate of dilation is significantly affected by the magnitude of the interparticle friction (μ). The larger the value of μ, the higher is the rate of dilation, particularly for the loose granular assemblies. The results of numerical simulations were compared with the laboratory axisymmetric compression tests on well-rounded glass ballotini, sub-rounded Welland river sand and angular crushed glass performed by Parikh (1967). The mobilized angle of shearing resistance ($\sin \Phi_{max}$) for a dense assembly of glass ballotini with a μ= 0.3 was obtained as 0.48 and was comparable to the $\sin \Phi_{max}$ obtained from numerical simulation as 0.45. Numerical test results for dense assembly with a μ= 0.6 gave a $\sin \Phi_{max} = 0.51$. Results reported by Parikh (1967) on Welland river sand was in the range of $0.56 < \sin \Phi_{max} < 0.68$ and that reported by Bishop (1973) on Ham river sand was in the range of $0.54 < \sin\Phi_{max} < 0.68$. The numerical simulation predicts a much lower value for $\sin \Phi_{max}$ as compared with laboratory test results and it was established that such a high difference was due to the angularity of the particles in the laboratory test. Thus it was concluded that if the numerical simulations were to represent sand, it is necessary to model non-spherical particles and that merely increasing the coefficient of interparticle

friction was not sufficient.

Rothensburg and Bathurst (1992) presented results of numerical biaxial tests of dense 2D assemblies of elliptical particles. The objective of the tests was to study the effects of varying the aspect ratio (A_r = larger dimension/shorter dimension of ellipse) of the elliptical particles and it was shown that the shear strength was a function of particle shape. The interparticle friction was maintained constant at a value of $\mu = 0.5$ for all the test simulations. For $1.0 < A_r < 1.353$, the mobilized angle of internal shear resistance for the assembly increased with aspect ratio in the range of 26.5^0 to 42^0. This work also demonstrated the importance of modeling non-spherical particles in the computer simulations of granular media.

Bardet and Proubet (1991a) developed a numerical technique based on adaptative dynamic relaxation (ADR) for the mechanics of granular materials. This method was pursued as it was more computationally efficient than the DEM and it enhanced the rate of convergence and accuracy. A granular assembly was idealized as disks linked by normal and tangential springs at contacts (Fig. 2.2) and the Hertz-Mindlin contact theory was assumed for the force-displacement law. The equilibrium of the disks was accomplished through the ADR technique as different from the Newton's second law in DEM. Only the numerical tests carried out with the ADR technique is reviewed here and the reader may refer to Bardet and Proubet (1991a) for a detailed review of the principles and procedures involved in the ADR technique.

Bardet and Proubet (1991b) investigated the structure of persistent shear bands in granular materials by numerically simulating an idealized two-dimensional assembly of particles. Numerical biaxial test was performed on an assembly of 2000 disks with two rigid boundaries in the major principal stress direction and two flexible boundaries in the minor principal stress direction. The numerical test was intended to simulate the rubber membranes of the triaxial tests in contrast to periodic boundaries used in the numerical test of Cundall (1989). The residual friction angle (Φ_r) for the granular assembly was obtained as 14^0 with particles of interparticle friction angle of 26.5^0. The displacement fields at various stages of axial strains indicated the formation of two shear bands with an inclination of 52^0 and 38^0 with horizontal. With the progress of deformation, only the shear band inclined at 52^0 persisted. This was consistent with the Mohr-Coulomb theory which predicts the failure plane at an angle of $45+\Phi_r/2 = 45+14/2 = 52^0$. The displacement, volumetric strain, void ratio, rotations of particles, rotations of their neighborhoods and contact orientations were also examined inside the shear band. The conclusions of the shear band analysis were that shear band width reduces with axial strain and the contacts are oriented in the direction of the shear band. The number of these contacts per particle is minimal and that the rotation of particles, the gradient of their rotation and the rotations of their neighborhoods are concentrated inside the shear bands.

Computer simulations using DEM and other methods have been very powerful techniques to understand the mechanics of granular materials. The

numerical simulations which incorporate the microstructural effects have helped in understanding the stress-strain response, volume change behavior, development of failure mechanisms, evaluation of physical quantities related to the macro-mechanical behavior, stress and strain induced anisotropy, formation and persistence of shear bands and the behavior of granular assemblies in various stress paths. A limitation of the computer simulations on disk/sphere assemblies is that they do not incorporate irregularly shaped particles and particle fracture and thus a only limited capability exists to highlight and visualize specific microstructural events which may control the macroscopic response.

2.6 Concept of Fabric in Granular Media

Fabric of granular material means spatial arrangement of solid particles and associated voids (Oda, 1972a) or, in short, the packing structure. Oda (1972a, 1972b, 1972c) performed a series of triaxial tests on granular materials of various packing structures and presented the concept of fabric in his paper "Significance of fabric in granular mechanics" (Oda, 1978). Oda explained the fabric by two concepts; (a) orientation (b) packing. The orientation of the particles was defined by a term called axial ratio (Fig. 2.5a) while the packing was based on the branch vector and contact normal (Fig. 2.5b).

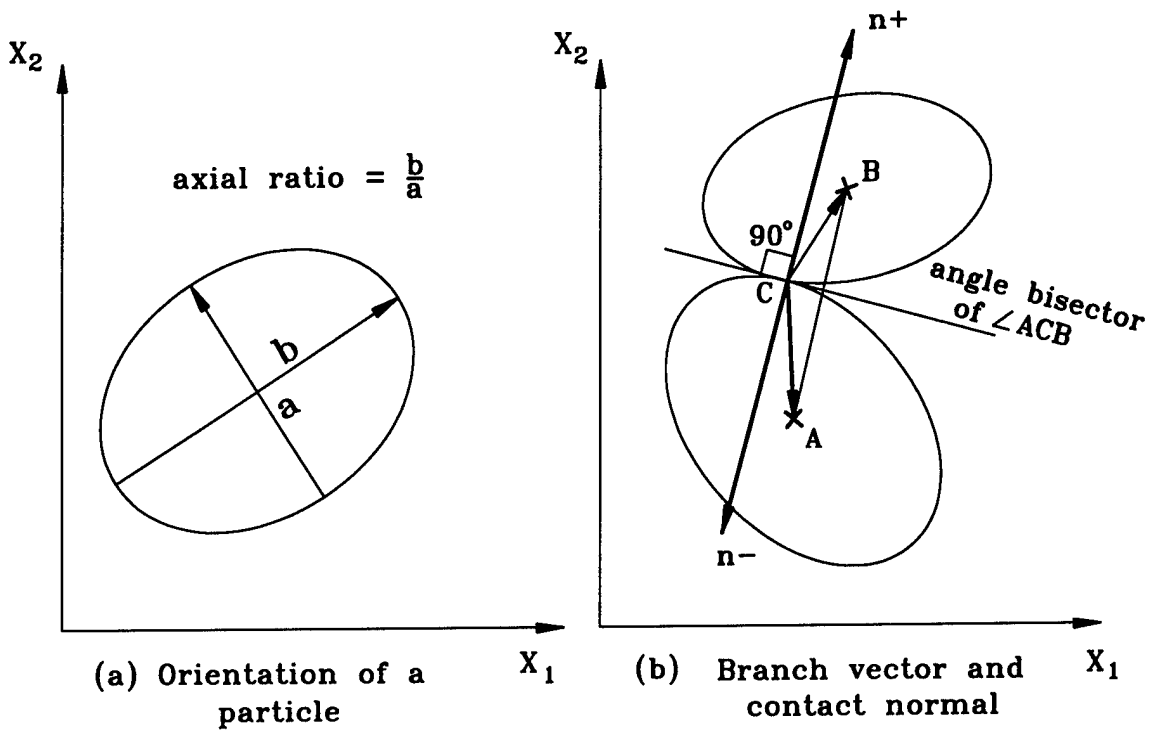

Fig. 2.5 Fabric measures of particles

Branch vector is the vector from the centroid of particles to the contact point. Contact normal is the direction of the normal to the contact surface when two particles are pressed by a contact force and the direction of this is obtained by drawing a normal to the angle bisector of the branch vectors AC and BC (Fig. 2.5b). Quantifying orientation, branch vectors and contact normals of the particles in a granular material in terms of averages, standard deviation and probability density functions are elaborately dealt in Oda (1978). One of the methods to analyze the changes in fabric of a granular material is to construct a plot of the

distribution of contact normals in various directions in the four quadrants of an XY coordinate system (Fig. 2.6). The shift in the direction of the distribution of contact normals indicates the shift in the direction of the principal stress in a granular material as shown in Fig. 2.6.

(a) Vertical load (b) Simple shear

Fig. 2.6 Frequency distribution of contact normals in simple shear test (Oda and Konishi, 1974)

The effect of initial fabric on mobilized strength, dilatancy rate and secant deformation modulus were presented by Oda (1972a) on the results of triaxial tests. Based on the experimental results, Oda (1972b and 1972c) derived expressions for the mobilized stress ratio and dilatancy rate in terms of the fabric measures. In order to represent the distribution of contact normals as a continuous function, Oda et.al. (1982) introduced a fabric tensor which is a function of the number of contacts and the XY components of the branch vectors

and the contact normals.

Thornton and Barnes (1986) performed biaxial constant mean stress test and a constant volume test on a dense assembly of 1000 disks using the DEM. The objective of these tests was to study the induced structural anisotropy during the deformation of granular assemblies. The anisotropy of a granular assembly is defined by the distribution of contact normals in the four quadrants of an XY coordinate system (eg. Fig. 2.6). If the distribution was random and could be approximated by a uniform distribution, then the structure was in effect isotropic. Anisotropy was indicated by a non-uniform distribution. It was shown that even though the two tests were subjected to different strain histories, the degree of induced structural anisotropy evolved in an identical manner. Also a Fourier series expression was derived for a probability density function to express the observed discrete distributions of contact normals (eg. Fig. 2.6) as a continuous distribution. Nemat-Nasser and Mehrabadi (1983 and 1984) derived constitutive relationships based on fabric measures. As an alternative to the fabric measures in terms of the contact normals, Konishi and Naruse (1988) derived an expression for a term called void tensor in terms of the size, shape and orientation of local voids.

An effort to verify the fabric-stress relations through experiments was carried out by Subhash et.al (1991). Simple shear tests were conducted on a two-dimensional assembly of oval cross-sectional rods. The components of the fabric tensor were measured over one cycle of shearing. The orientations of the principal

axes of all commonly used fabric tensors were observed to change sharply with the reversal of the shearing direction.

Unlike the continuum models, the fabric based relationships incorporated the microstructural quantities. Thus it is an analytical approach accounting for the microstructural effects through statistical parameters. Relationships have been evolved for the various physical quantities related to the macro-mechanical behavior of particulate media in terms of the initial fabric measures. These relationships require the data consisting of particle geometry, number of contacts and particles and contact orientations during various stages of deformation of a particulate medium. These are to be obtained through experimental photographs. The various fabric based relationships do not account for the micromotions of the individual particles and thus is limited in it's capability to predict the changes in packing structure under a deformation. This led to the development of microstructural continuum theories which incorporate not only the various fabric measures but also the microstructural deformations and the micromotions of the individual particles.

2.7 Microstructural Continuum theory

Microstructural continuum theory (Bathurst and Rothensburg, 1988; Chang and Misra, 1989a,b) is an analytical approach and is implemented using computer codes through incremental loading. In this theory, the micromotions of the

particles are expressed as linear or higher order functions of the coordinates of the centroid of particles and the macroscopic strain simulated according to the type of deformation (biaxial, simple shear, etc.). The theory incorporates the terms related to the microstructural properties and also the terms related to packing structure such as contact normal, branch vector etc. The microstructural continuum theory was pursued as the computational time required was less than that taken by the computer simulation methods such as DEM and DMA. Both the microstructural continuum theory and the DEM idealize a granular assembly as an assembly of rigid disks/spheres linked by normal and tangential springs at contacts (Fig. 2.2). The difference between the two approaches is in the transmission of boundary disturbances to the internal particles. In the DEM, the boundary displacements/forces are transferred to the neighboring particles one by one and the particles are brought to equilibrium through an iterative process. In the micro-structural continuum method, the particle displacements within a particulate assembly are assumed to be a polynomial function of the macroscopic strain applied at the boundary and the particle coordinates. Thus, the macroscopic strains are related to particle displacements which in turn are related to the displacements of the contacts. The contact displacements are obtained from the components of the relative displacements of the particles, as the particles are assumed to be rigid. The contact displacements are related to the contact forces through the Hertz-Mindlin contact theory which in turn are related to the macroscopic stress through Hill's (1963) averaging principle described in Chapter.

4. Thus, a constitutive relationship is established between the macroscopic stress and macroscopic strain as a function of the microstructural properties and packing structure. The packing structure is also updated at the end of an incremental deformation according to the particle locations and the loss and gain of contacts.

Bathurst and Rothensburg (1988) derived explicit expressions for elastic constants in terms of microstructure and verified the expressions with the results from numerical tests. In their study, the micromotions of particles were incorporated. However, the contacts were assumed to be indestructible and thus the evolution of packing structure with deformation was not considered.

Chang and Misra (1989a) evolved stress-strain relationships for regular cubical and hexagonal packings of disks based on microstructural continuum theory and obtained good comparison with laboratory biaxial tests at very low strains of $\epsilon_y = 0.00015$. Chang and Misra (1989b) developed a constitutive relationship assuming a linear displacement field for the particles. In this model, the evolution of packing structure for a random assembly of particles during a deformation was also included. The results from the model had good agreement with the numerical tests conducted using the numerical model of Serrano and Rodriguez-Ortiz (1973) at low strain levels of $\epsilon_y = 0.0005$ in biaxial tests on assemblies of rods. Constitutive relationships incorporating second order polynomial functions for particle displacements and particle rotations can be found in Chang and Liao (1990), Chang (1990) Chang and Misra (1990) and Misra

(1990).

An experimental effort to provide data to relate the macroscopic strain to the micromotions of the particles was carried out by Gill (1993) on granular materials under uniaxial strain. The conclusion was that the displacement fields are not directly proportional to applied macroscopic strain as predicted by local theories. Strain in the immediate vicinity of the loading cap was found to be greater than the applied macroscopic strain with other regions of the specimen generally experiencing strain levels less than the applied macroscopic strain. Gill (1993) observed that displacements within a heighborhood of grains are non-uniform and obeys an exponential distribution and proposed a theory based on the diffusion equation. However no theoretical relationships were derived for the micromotions of particles based on the diffusion theory. The experimental study established the fact that displacement fields are not directly proportional to the macroscopic strain, a fundamental assumption in the microstructural continuum theories.

2.8 Lattice model

A lattice approach coupled with a statistical analysis has been used by physicists to study the failure of brittle materials (Krajcinovic and Silva, 1982; Hermann and Roux, 1990). Historically, first application of lattices to structural problems is credited to Hrenikoff (1941). In the lattice approach in which a

material is simulated by a system of bars/links, was undertaken from the fact that a lattice represents a physically justified and computationally efficient approximation of a continuum. Great advantages of the lattices was that the analyses of dilution processes (sequential removal of links) and the determination of the influence of the disorder (introduced by a random spatial distribution of the link parameters) are computationally not very demanding (Hermann and Roux, 1990). The important features of lattices are: (a) ability to consider more complex states of stresses and strains and (b) efficiency in providing estimates of the influence of stress concentrations and spatial correlations of defects on the macro-response of the system.

Krajcinovic and Silva (1982) used a parallel bar model to study the failure of a perfectly brittle material subjected to tension. In this approach, the material was replaced by a system of parallel bars of identical stiffnesses connected to hinges at one end and to a very rigid member at the other end. All bars were assumed to be perfectly elastic and an initial disorder was introduced by assuming the rupture strengths of the individual links to follow a probability distribution function. The elongation of the system was then expressed as a function of the applied force and a parameter called "damage", where damage was defined as a ratio between the number of ruptured bars and the total number of bars. The extent of damage in turn was a function of the rupture strength distribution and the applied force. This model was useful in predicting the behavior of certain classes of brittle ceramics reinforced with continuous fibers

and long cortical bones. A limitation of this model was that it ignored the stress fluctuations and defect interaction and this led to the development of models consisting of triangular lattices (Hansen et. al 1989). Thus, the emphasis of physicists in using lattices was for the study of disorder in materials through statistical methods (Krajcinovic and Basista, 1991).

The interests of engineers have been to evolve continuum like models for materials with lattice-like microstructure or to use lattices for the analysis of continuum. The relationship between a continuum and a gridwork of discrete elements was first examined in some early work by Hrennikoff (1941) and later by Newmark (1949) which involved analyzing a continuum by replacing it with an equivalent elastic gridwork. The reverse possibility of replacing a large repetitive gridwork with an equivalent continuum was studied by Kollar et. al (1985), Dow et.al (1985) and Noor and Russell (1986). These studies presented methods to simplify certain calculations for large space trusses and space frames. Recently Dai and Frantziskonis (1994) used the lattice approach to model a brittle material through the data obtained from ultrasonic scanning. The data was used to assign failure stress and stiffness for each bar in the discretized members of the lattice. The lattice model predicted crack patterns similar to that were observed in experiments. Also, Frantziskonis et.al (1994) used a lattice approach to study the fiber matrix interface in composite materials.

A lattice approach called discrete stiffness model (DSM) was developed by Trollope and Burman (1980) to study the mechanics of granular media. The

model was originally developed for the movement of blocks of rocks and was later extended for granular media. The lattice arrangement was formed by linking the particle centroids as nodes with bars having a joint element between the nodes and at the contact point. The details of the lattice model and joint element are elaborately dealt in Burman (1974) and are not reviewed here as this would involve extensive discussion for a proper understanding of the approach.

The discrete stiffness model was applied on granular wedges to assess the stress distribution and stability of the slopes under gravity load. The study was chosen on granular wedges as they have direct relevance to practical structures such as earth and rock-fill dams, road and rail embankments, etc. The normal stress distribution on the bottom boundary from the model had good agreement with experimental observation. The DSM was used to study the variation of normal and shear stresses at the base of granular wedges and the displacement patterns due to vertical settlements of the wedges simulated by downward displacements. The main conclusion of the study was that the displacement patterns do not reflect the internal stress distribution. The study suggested that interpretation of displacement monitoring of earth and rock structure requires careful evaluation. In the DSM, the contacts were considered to be indestructible and thus evolution of the packing structure was not considered and the study was confined to granular wedges under gravity load.

Following an approach similar to DSM, Boardman (1990) and Sadd et. al

(1992) studied the wave propagation in granular media. The lattice was formed by linking particle centroids and elements were modeled as 1-D dynamic bar element with lumped mass at the end nodal points (Fig. 2.7a). The element possessed both normal and tangential stiffness and damping coefficients whose numerical values were obtained from dynamic photoelastic experiments. A modified bar element incorporating the contact characteristics was used (Fig. 2.7). In this method, there was no joint element as in DSM. The degree of freedom at a node consisted of the normal and tangential displacements and a rotation (rotation of particles). The stiffness matrix was constituted from the normal stiffness (K_n), tangential stiffness (K_s) and the radii of the particles (Figs. 2.7b and 2.7c).

The finite element model was applied on 1D and 2D assemblies of disks made of Homalite-100 subjected to a dynamic load on a disk at the top of the assemblies. The resulting wave speed and the magnitude and orientation of the contact forces obtained from the lattice model had good agreement (10-20% accurate) with the results from photoelastic experiments. However, the application of the lattice model was limited to small deformations and thus loss and gain of contacts due to fabric changes were not considered.

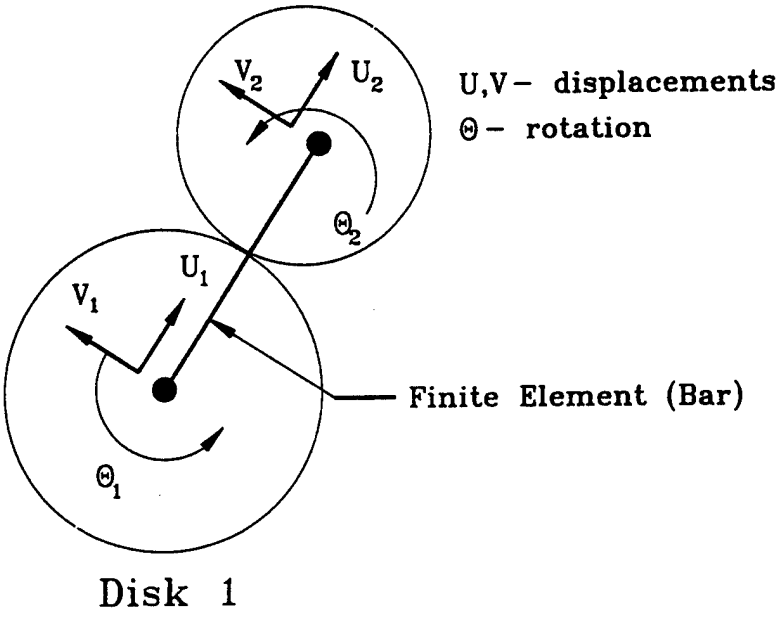

(a) Basic element of the elastic network

K_n – normal stiffness
K_t – tangential stiffness
r_1, r_2 – radii of particles

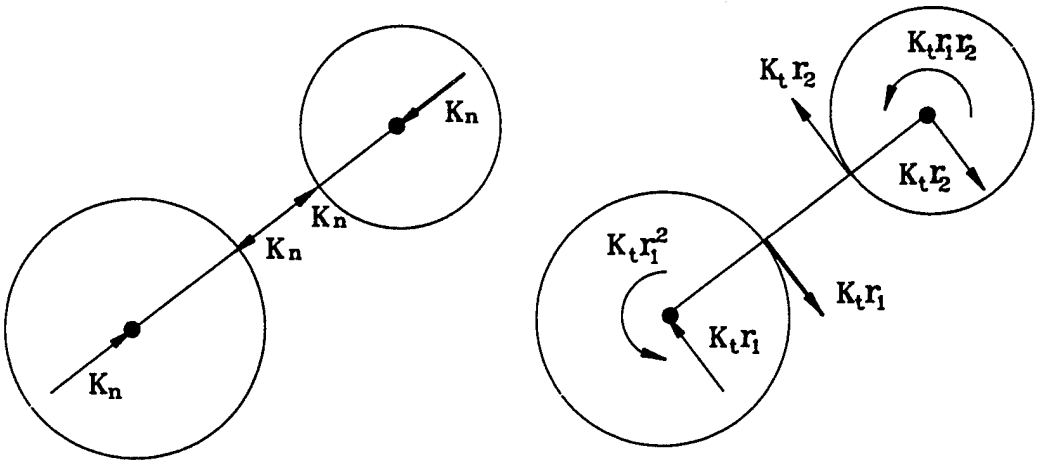

(b) Disk equilibrium for normal forces

(c) Disk equilibrium for tangential forces

Fig. 2.7 Elastic network modeling of granular media (Sadd et.al, 1992)

In particulate materials, loads are transmitted along discrete paths within the material through particle contacts. The dispersion of loads within the material can be envisioned to be through a network formed by linking the particle contacts. It is this network pattern of load distribution within a particulate material that gave rise to the idea of lattice type simulation of particulate materials presented in this research. The lattice simulation is carried out by linking the particle contacts as different from the lattice approaches of Trollope and Burman (1980) and Sadd et. al (1992) in which the lattice was formed by linking the particle centroids. Thus the lattice type model in this research attempts to model a particle itself as a lattice within the microstructure of the particle.

CHAPTER 3

FORMULATION OF THE LATTICE TYPE MODEL FOR PARTICULATE MEDIA

3.1 Model Formulation

3.1.1 General

In the lattice type simulation of a two-dimensional assembly of particles, the assembly is transformed into a network of bars representing the load path within the particles (Fig. 3.1). Nodes are introduced at particle contacts and are

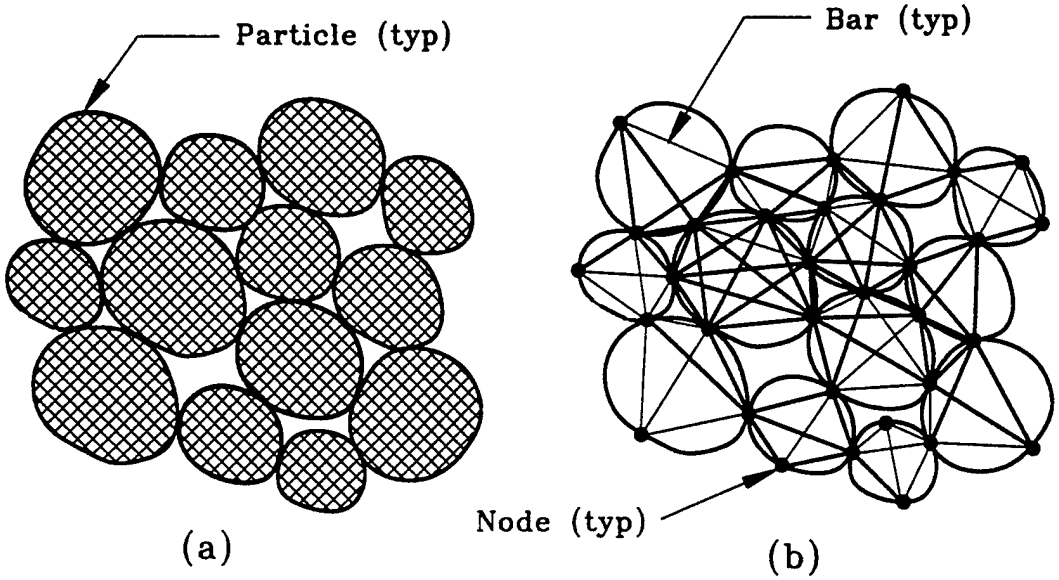

Fig. 3.1 (a) Particle arrangement (b) Lattice type simulation

linked by bars. A contact node on a particle is linked to every other contact node on that particle with bars resulting in a truss. If the number of contacts around a particle is less than four, then bondless nodes are introduced around the particle, so as to have a minimum of four nodes forming the lattice for the particle. This is necessary because, during the deformation process, the trajectory of the centroid of a particle is traced from the displacements of the centroid of the polygon formed by linking the contacts around that particle. Particles of irregular shape can be approximated to disks of circular/elliptical cross-sections or mapped using the theory of morphology (Luerkens, 1991). However, this is not pursued at this stage of the research.

The elastic modulus of the bars within a particle is assumed to be equal to the elastic modulus of the particle. The lengths of the bars depend on the geometry of the particles and the location of the contact points. Since the bar areas are dependent on the bar forces which are not known initially, the initial cross-sectional areas of all the bars in the lattice are proportioned to the initially applied boundary load (P) on a boundary particle.

Consider the circular disk under a diametrically opposite load in Fig. 3.2. The initial cross-sectional area (A) of the bars in the lattice is set equal to the area of a bar of length equal to the average diameter of the particles (L) and subjected to a load P that will give the displacement (δ) in the above elastic disk. 'A' is

given by A = (PL)/(Eδ); where E is the elastic modulus of the particle and δ is the relative vertical displacement of A relative to C in the disk shown in Fig. 3.2. With these parameters (lengths, areas and elastic moduli), the truss is analyzed for a given load

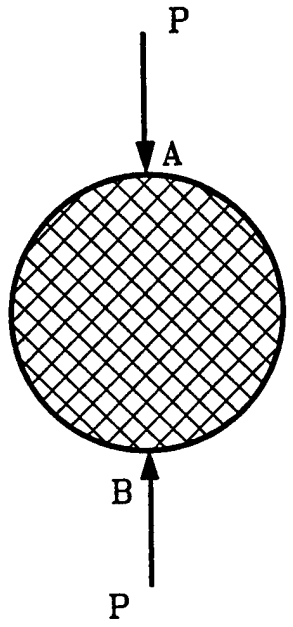

Fig. 3.2 Disk under a Vertical Load

under appropriate boundary conditions using the "standard" governing equation (3.1) in structural mechanics:

$$[K]\ \{D\} = \{R\} \tag{3.1}$$

where [K] is the global stiffness matrix of the truss, {D} is the displacement vector comprised of the displacements of the nodes of the truss in the X and Y coordinate directions and {R} is the global load vector comprised of the loads

acting at the nodes of the truss in X and Y directions. [K] is a square matrix of size "2Nx2N" where 'N' is the total number of nodes in the truss structure and {D} and {R} are column vectors of size "2Nx1". The above equation is solved for the unknown displacement vector.

3.1.2 Formulation of Global Stiffness matrix

The lattice type model (LTM) is a global technique which simulates the entire assembly of particles in a particulate medium as a truss structure. Therefore, the first step in the computational process is to evaluate the global stiffness matrix [K]. The global structure stiffness matrix [K] is generated by taking the sum of element stiffness matrices of the truss (bar) elements using

$$[K] = \sum_{n=1}^{nel} [k] \tag{3.2}$$

where [k] is the element stiffness matrix and "nel" is the total number of elements in the truss structure. The element stiffness matrix [k] for a truss element is a function of the elastic modulus, length and area of cross-section of the bar element and also the sines and cosines of the angle made by the orientation of the bar with the positive direction of X-axis (Fig. 3.3a).

Consider a bar element of length 'L' and cross-sectional area 'A' shown in

Fig. 3.3a with a back node 'i' and fore node 'j' and which makes an angle β with the positive direction of X-axis. Let the elastic modulus of the material of the bar be 'E'. The input data for the analysis are the X and Y coordinates of the nodes of the bar 'i' and 'j'. The matrix [k] is generated by computing the length and the sines and cosines of β from Equations (3.3) and (3.4) respectively.

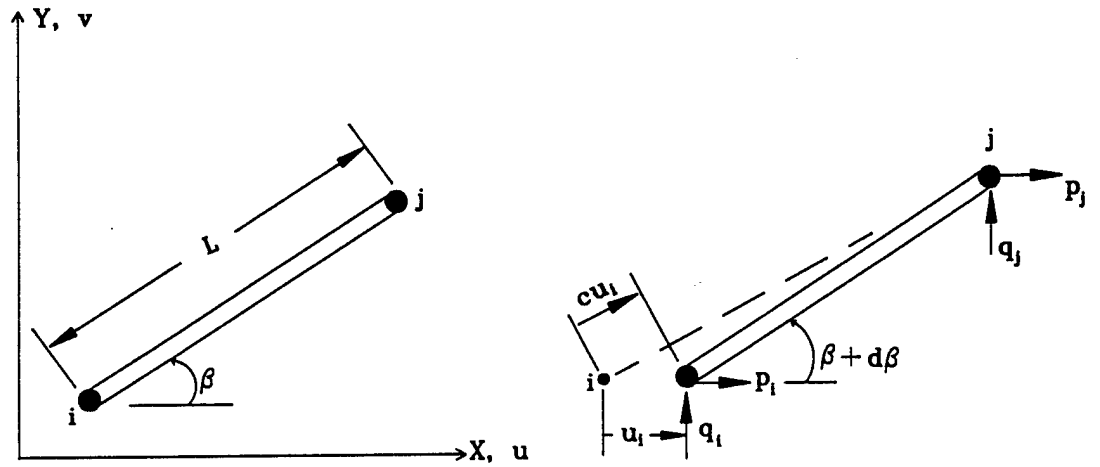

(a) arbitrarily oriented in the xy plane

(b) after imposed displacement $u_i \neq 0$, $v_i = u_j = v_j = 0$

Fig. 3.3 Truss element

$$L = [(x_j - x_i)^2 + (y_j - y_i)^2]^{1/2} \tag{3.3}$$

$$s = \sin\beta = \frac{(y_j - y_i)}{L}, \quad c = \cos\beta = \frac{(x_j - x_i)}{L} \tag{3.4}$$

The degrees of freedom in a truss are the X and Y displacements of the nodes. The displacements along the degrees of freedom for the bar in Fig. 3.3 are denoted by u_i, v_i at node 'i' and u_j, v_j at node 'j'. The elements of the matrix [k] are generated by assembling the column vectors (matrices) obtained by imposing a displacement in the direction of each degree of freedom (d.o.f) while other degrees of freedon are set at zero. The first of these four cases is shown in Fig. 3.3b in which a displacement is imposed at node 'i' in the X-direction. This displacement induces an axial shortening equal to cu_i of the bar element which in turn produces an axial compressive force 'F' given by

$$F = (AE/L)\,cu_i \tag{3.5}$$

The x and y components of F at nodes 'i' and 'j' are given by $p_i = -p_j = Fc$ and $q_i = -q_j = Fs$. These force components p_i, p_j, q_i, q_j are grouped as a column vector and is called the load vector for the bar element. When the expression for 'F' in Equation (3.5) is substituted in the expressions for p_i, p_j, q_i, q_j, there is a common factor $(AE/L)\,u_i$. Taking this common factor out of the expressions for p_i, p_j, q_i, q_j, the load vector is expressed in a matricial form as

$$\frac{AE}{L}\begin{Bmatrix} c^2 \\ cs \\ -c^2 \\ -cs \end{Bmatrix} u_i = \begin{Bmatrix} p_i \\ q_i \\ p_j \\ q_j \end{Bmatrix} \tag{3.6}$$

In a similar manner, displacements can be imposed along the other degrees of freedom as v_i, u_j and v_j and equations similar to Equation (3.6) can be obtained for each of these degrees of freedom. Superimposing the four equations for the four degrees of freedom, Equation (3.7) is obtained, which represents the element level equation for a bar subjected to imposed displacements of u_i, v_i at node 'i' and u_j, v_j at node 'j'.

$$\frac{AE}{L}\begin{Bmatrix} c^2 & cs & -c^2 & -cs \\ cs & s^2 & -cs & -s^2 \\ -c^2 & -cs & c^2 & cs \\ -cs & -s^2 & cs & s^2 \end{Bmatrix}\begin{Bmatrix} u_i \\ v_i \\ u_j \\ v_j \end{Bmatrix} = \begin{Bmatrix} p_i \\ q_i \\ p_j \\ q_j \end{Bmatrix} \tag{3.7}$$

The term AE/L multiplied by the square matrix in Equation (3.7) is referred to as the element stiffness matrix [k]. Representing the vector comprised of the displacement componets as the displacement vector {d} and the load vector at element level as {r}, Equation (3.7) is rewritten as Equation (3.8) which is called the equilibrium equation of the element.

$$[k]\ \{d\} = \{r\} \tag{3.8}$$

Summation of the element stiffness matrices [k] results in the global stiffness matrix [K] given by Equation (3.2).

3.1.3 Formulation of Global load vector

There are three types of loads imposed on a truss structure and each of these is incorporated in the global load vector {R} by different computational procedures. The three types of loads are

(1) Through prescribed nodal loads

(2) Through prescribed nodal displacements

(3) Through prescribed internal initial axial forces in the bars.

In the previous section, it was shown through Equation (3.7) that if the displacements are prescribed, then the resulting forces at the ends of the bar to keep it in equilibrium can be determined. Contrary to this, if the loads are prescribed, then the displacements can be determined. Unlike the case of a single bar element, in a global truss structure, the displacement or a load at a node will have global influence. The computational procedures used to include the effects of the above loading types are explained here. The elements in the load vector {R} corresponding to node 'j' are denoted as $R(2j-1)$ and $R(2j)$, which represents the loads in the X and Y directions respectively. The elements of the load vector {R} are initially set to zero and then assembled to include the effects of various types of loads.

Let P_1 and P_2 be the prescribed nodal loads in a truss at a node 'j' in the X and Y directions. Then the effects of these are included in the load vector {R}

by adding the loads to the components of the load vector algebraically as $R\ (2j-1) = R\ (2j-1) + P_1$ and $R\ (2j) = R\ (2j) + P_2$.

The second loading condition of prescribed nodal displacements is incorporated in the load vector by first modifying the load vector and then the stiffness matrix. The reader may refer to Cook (1981) for details additional to the ones presented here. Consider a stipulated displacement δ at a node 'k' in a truss in the X-direction, whose d.o.f number is denoted as n = (2k - 1). The effect of this is included in the load vector by modifying the load vector {R} through Equation (3.9) for every element R(i) of the load vector, with 'i' ranging from 1 to 2N, where N is the total number of nodes in the truss.

$$R(i) = R(i) - K(i,n)\ \delta \tag{3.9}$$

After modifying the load vector for all the prescribed nodal displacements, the load vector is again modified by setting the elements of the load vector equal to the prescribed displacements only for d.o.f where displacements are prescribed. Therefore, for the above example, the load vector is modified as R(n) = δ. After the above two procedures, the stiffness matrix is modified by setting K(n,n) = 1 and all the other elements of the row 'n' and column 'n' of [K] equal to zero.

The effect of initial internal forces in the bars of a truss are incorporated in the load vector {R} by adding the components of the forces at the two ends of the bars to the components of {R} corresponding to the nodes. An internal force 'F' in a bar shown in Fig. 3.3 exerts a force of $p_i = -p_j = Fc$ and $q_i = -q_j = Fs$

which is expressed in a matricial form as Equation (3.10).

$$\begin{Bmatrix} p_i \\ q_i \\ p_j \\ q_j \end{Bmatrix} = \begin{Bmatrix} -Fc \\ -Fs \\ Fc \\ Fs \end{Bmatrix} \tag{3.10}$$

Then, the elements of the load vector {R} is modified as follows.

$$\begin{Bmatrix} R(2i-1) \\ R(2i) \\ R(2j-1) \\ R(2j) \end{Bmatrix} = \begin{Bmatrix} R(2i-1) \\ R(2i) \\ R(2j-1) \\ R(2j) \end{Bmatrix} + \begin{Bmatrix} p_i \\ q_i \\ p_j \\ q_j \end{Bmatrix} \tag{3.11}$$

3.1.4 Computation of Axial forces

After evolving the global stiffness matrix and the global load vector, the next step is the solution of Equation (3.1) which results in the displacement vector {D}. The solution is carried out using the Gaussian elimination method. From the displacement of the nodes, the components of the load acting at the two ends of an element are computed using Equation (3.7). From these components, the axial force in a bar 'k' is computed as $F_k = \frac{p_i}{c}$.

3.1.5 Normal force, Shear force and Shear force ratio

When two particles are pressed together with a contact force, a contact surface develops and the contact normal is defined as the direction normal to the contact surface (Fig. 2.5b). For two particles of circular cross-sections, the contact normal is the direction linking the centroids of the two particles in contact (Fig. 3.4).

The normal force and shear force at a contact node are computed by taking the algebraic sum of the components of the axial forces in the bars in the direction of the contact normal and tangential to the contact normal (Fig. 3.4) and are given by

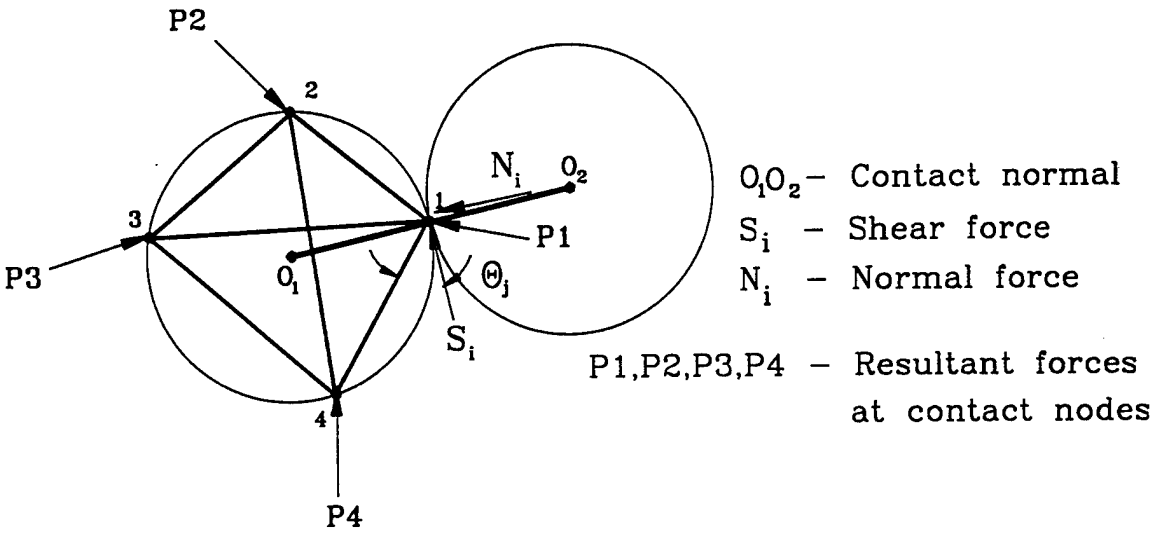

Fig. 3.4 Particle under contact forces

$$N_i = \sum_{j=1}^{n-1} F_j \sin\theta_j \tag{3.12}$$

$$S_i = \sum_{j=1}^{n-1} F_j \cos\theta_j \tag{3.13}$$

where N_i = normal force at the contact node 'i'; S_i = shear force at the contact node 'i'; F_j = axial force in bar 'j'; θ_j = angle made by bar 'j' with the shear force direction at the contact node 'i'; n = number of contacts around a particle. Shear force ratio at a contact node 'I' denoted by r_i is the ratio of the absolute value of the shear force divided by the normal force and is given by

$$r_i = \frac{S_i}{N_i} \tag{3.14}$$

Since the contact area for the computation of the contact shear stress and contact normal stress are the same, the shear stress ratio defined as the shear stress divided by the normal stress is equal to the shear force ratio. Therefore, the shear force ratios will also be referred to as shear stress ratios.

3.1.6 Cross-sectional areas of bars

The cross-sectional areas of the bars are updated at the end of each load

increment based on the new contact forces around the particles. The area of a bar is found by computing the displacements of an elastic disk under contact forces and then determining the bar area that will give an equivalent displacement in the direction of the bar. In this research, only particles with circular cross-sections are considered and thus only the method to compute the displacements in a circular disk is explained here. However, the method can be extended to particles of elliptical or other shaped cross-sections.

The state of stress in the two dimensional element of a continuum is shown in Fig. 3.5. The stresses σ_x, σ_y and τ_{xy} are the normal stress in the X-direction, normal stress in the Y-direction and shear stress. From theory of elasticity,

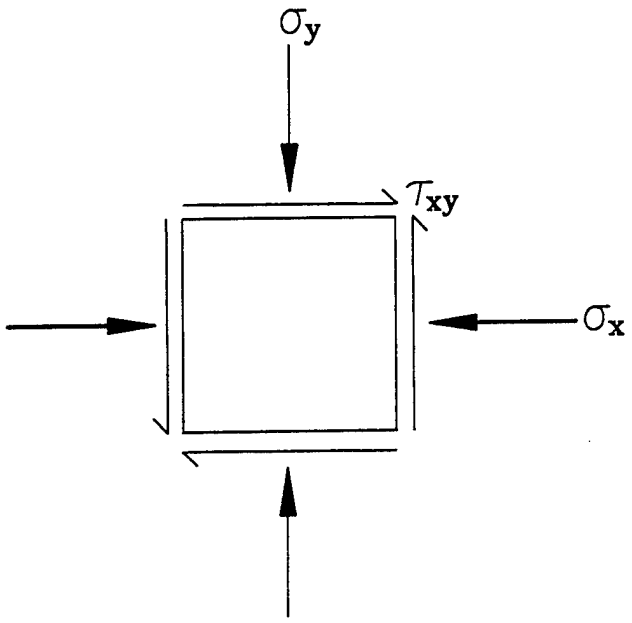

Fig. 3.5 State of stress in the two dimensional element of a continuum

Michell (1900) derived expressions for the stresses σ_x, σ_y and τ_{xy} in an infinite half space of continuum acted upon by a point load. From these expressions, Michell (1902) derived expressions for σ_x, σ_y and τ_{xy} at a point in a circular disk acted upon by an equal and opposite load acting along a chord of the disk. The displacements of the points of a circular disk acted upon by a set of contact forces is derived from the above expressions for stresses. The circular disk problem and the derivation of the stresses are also given in Timoshenko and Goodier (1970) and in Frocht (1948).

The X and Y components of the displacements of the contact points of the disk shown in Fig. 3.4 are determined by superimposing the displacements produced by each contact force (Fig. 3.6). Consider only the contact force P1 acting on the disk (Fig. 3.6b) at node 1. Then, the resultant of P2, P3 and P4 denoted as P5 and equal to P1 in magnitude will be acting at node 5 along the line of action of P1 and opposite to the direction of P1. The displacements produced by P1 and P5 will be symmetrical about the line AB, a diameter of the circle normal to the line of action of P1. Then, it can be seen that the displacements produced by the load P1 on the circular disk is only in the semi-circular portion of the disk towards the right of AB. Therefore, the influence of P1 is only at nodes 1 and 4. The displacements due to load P1 are equal to δ_{11} at node 1 and δ_{41} at node 4. The displacements δ_{11} and δ_{41} are obtained from the expressions for displacements in a circular disk acted upon by an equal and

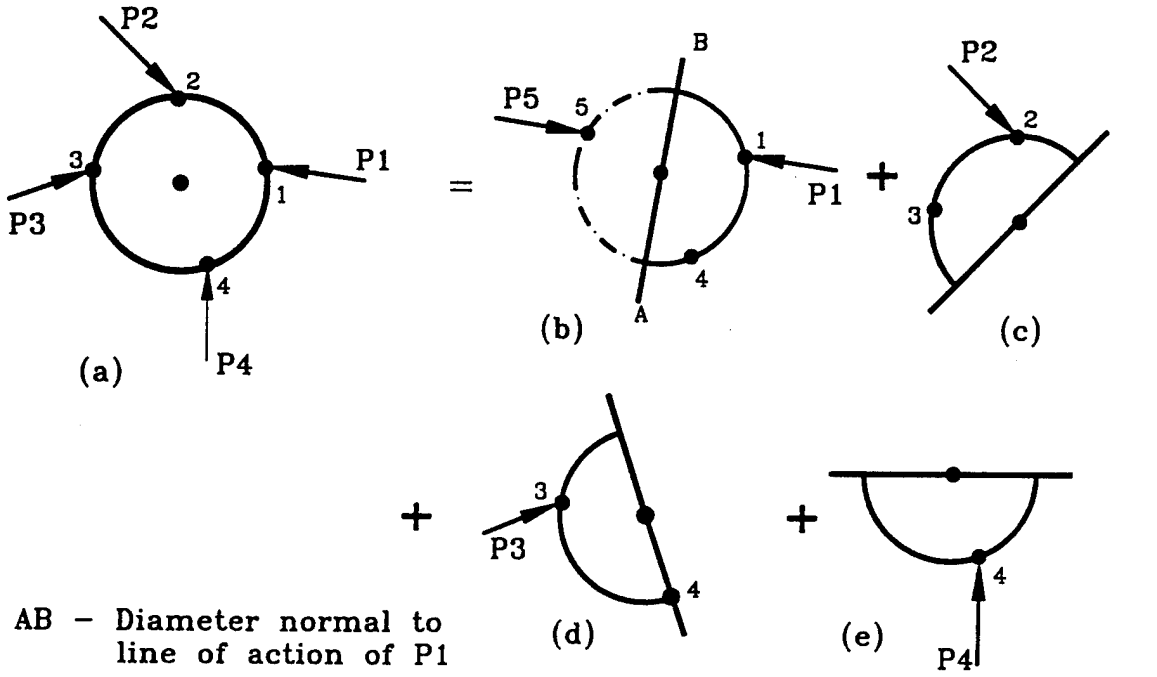

Fig. 3.6 Superposition of Displacements

opposite load acting along a chord of the circle similar to the disk in Fig. 3.6b. The expressions for the displacements are derived in Appendix - 1.

Following the above approach, the displacements caused by the loads P2, P3 and P4 acting at nodes 2, 3 and 4 at their points of application and at other nodes are also determined. Finally, the resultant displacements Δ_1, Δ_2, Δ_3 and Δ_4 at nodes 1, 2, 3 and 4 are determined using the rule of superimposition as

$$\Delta_1 = \delta_{11} \tag{3.15}$$

$$\Delta_2 = \delta_{22} \tag{3.16}$$

$$\Delta_3 = \delta_{33} + \delta_{32} \tag{3.17}$$

$$\Delta_4 = \delta_{44} + \delta_{41} + \frac{\delta_{43}}{2} \tag{3.18}$$

The displacements of the contacts are resolved in the direction of each bar and the relative displacements in the direction of each bar are computed. The bar areas are then updated using

$$A_j = \frac{F_j L_j}{E_j \delta_j} \tag{3.19}$$

where A_j = cross-sectional area of bar 'j'; F_j = axial force in the bar; L_j = length of the bar; E_j = Elastic modulus of the bar and δ_j = relative displacement of the nodes of bar 'j' in the direction of bar 'j'.

As an example of a lattice type simulation, consider a circular disk (Fig. 3.7) under a diametrically opposite load and restrained by lateral supports. The vertical displacement at A can be found using the expressions for displacements in Appendix - 1. Let δ_{DA} be the horizontal displacement at D due to the vertical load, if there were no lateral supports. If a horizontal load 'R' acts at B and D in opposite direction which will produce a horizontal displacement (δ_{DD}) equal to δ_{DA}, then 'R' will be the lateral reaction in the disk restrained by lateral supports.

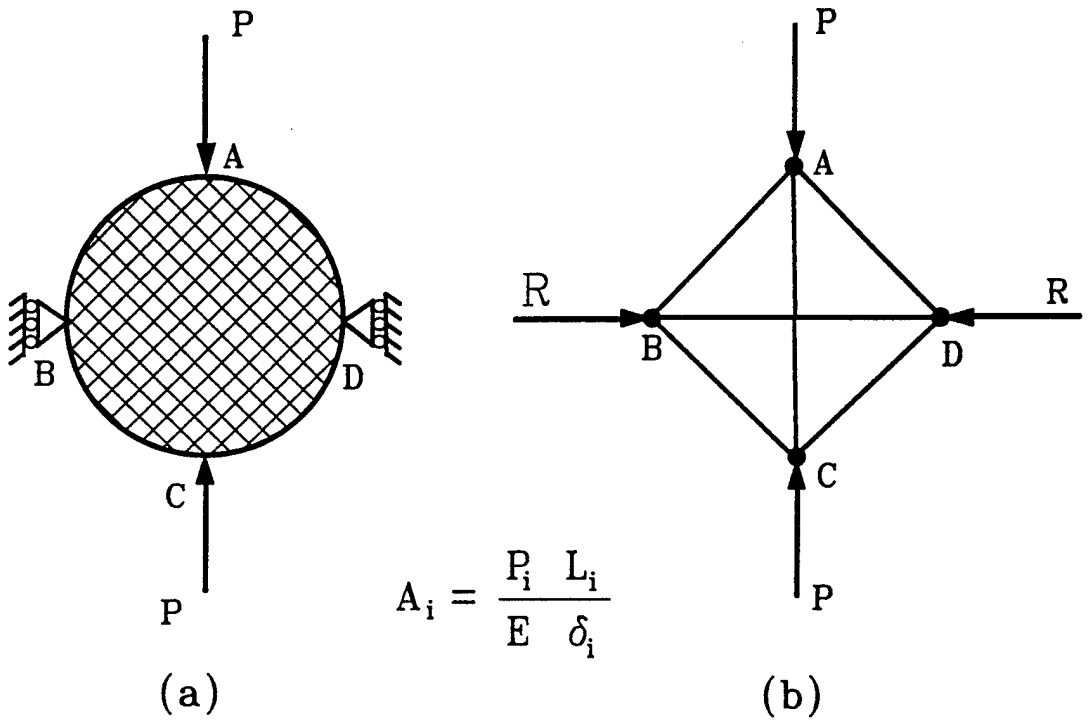

$$A_i = \frac{P_i \; L_i}{E \; \delta_i}$$

Fig. 3.7 (a) Disk under vertical load (b) Equivalent lattice

The expression for δ_{DD} is given in Appendix - 1, which will be a function of the lateral support reaction 'R'. By setting δ_{DD} equal to δ_{DA}, 'R' can be found. By considering the force equilibrium equations at A and D, the bar forces can be evaluated. Resolving the displacement of A in the direction of bars AC and AD, the deformations of these bars can be evaluated. Then the equivalent bar areas can be computed from Equation (3.19).

If a bar is in tension, the axial force in that bar is set to zero and the unbalanced forces are redistributed through an initial stress analysis. The area of the bar is then reduced to a low value equal to 10^{-8} times the maximum of the

cross-sectional area of all the bars within the lattice forming the particulate assembly. The acronym "AWBAR" is used to denote this reduced area.

Since the cross-sectional areas of all the bars are set equal to the same value for the initial load analysis, equivalent bar areas which will simulate the exact contact force distribution within a particulate assembly under the initial load are accomplished through an iterative process. The bar areas are updated after the analysis under the initial load. Again the initial load analysis is carried out with the updated bar areas and again the bar areas are updated. The process is repeated until the maximum bar area within the lattice converges to an accuracy of six decimal places with respect to the bar area in previous iteration step. At this stage, additional load is applied on the particulate assembly.

3.1.7 Redistribution of Additional shear forces

If the shear stress ratio at a contact node exceeds the coefficient of friction of the material (μ), the additional shear force is redistributed to the other contacts by applying an equal and opposite shear force at the contact as shown in Fig. 3.8 and given by Equation (3.20).

$$\Delta S_i = (r_i - \mu)\, N_i \tag{3.20}$$

where ΔS_i is the additional shear force at the contact node 'i', r_i is the shear stress ratio and N_i is the normal force.

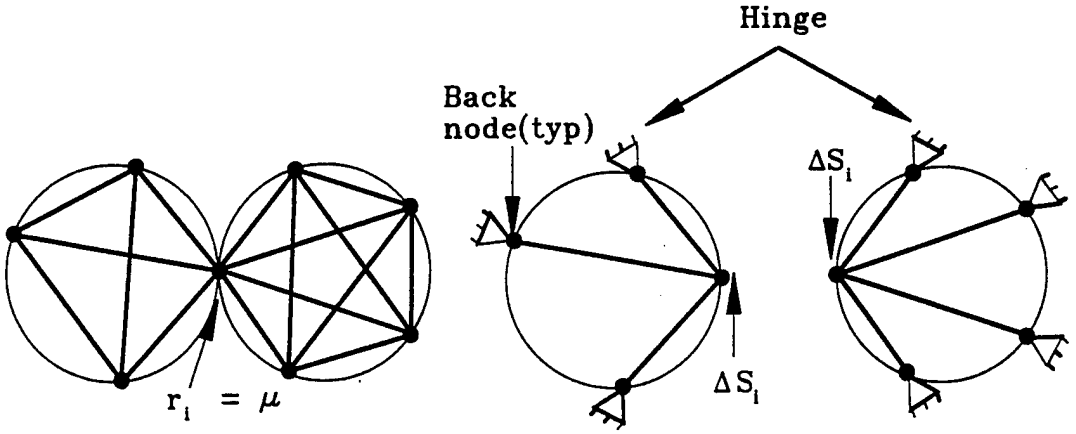

Fig. 3.8 Redistribution of additional shear forces

Every bar has two nodes referred to as fore node and back node. When an additional shear force is redistributed at a contact node, then the contact node is designated as fore node and the other node as the back node for all the bars linked to the contact node. The additional shear force is applied at the contact node and resolved into the bars as axial forces relative to the stiffnesses of the bars and assuming the back nodes of the bars as hinged (Fig. 3.8). These axial forces are applied as initial axial loads in the bars and an initial stress analysis is carried out. Thus, the shear stress ratios at the contacts which exceeded 'μ' are reduced. The additional shear forces are redistributed at all the nodes where the shear stress ratios exceed 'μ' in a single analysis. Also, when additional shear forces are redistributed at one contact node, it may increase the shear stress ratios at neighboring nodes which are above 'μ'. Due to the above two reasons, an iterative process is required to bring down the shear stress ratios at the contact

nodes which exceeded 'μ' to 'μ'.

3.1.8 Bonding and Debonding of Contacts

When the normal force at a contact becomes zero, the contact is split into two nodes (debonding). Constraints are imposed to check for possible re-bonding of contacts based on the particle geometry, location of the centroids of particles and the equations (relationship between X and Y coordinates) of the imaginary plates representing the boundaries of the particulate assemblies. An example of

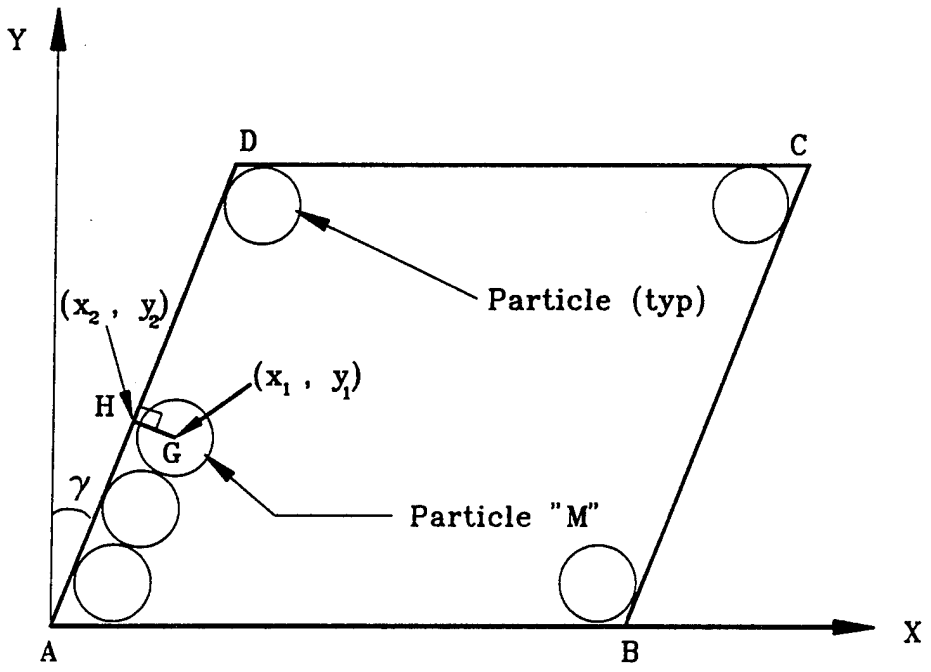

Fig. 3.9 Bonding and Debonding of Particles

the bonding and debonding can be shown with respect to the boundaries in a simple shear apparatus shown in Fig. 3.9.

Consider the particle 'M' of radius 'R' in the particulate assembly in Fig. 3.9 subjected to a shear strain 'γ'. In order to check whether the particle 'M' is in contact with the boundary AD, the following procedures are followed.

(1) Derive the equation of line AD

(2) Draw a perpendicular from the centroid of particle to line AD

(3) Determine the perpendicular distance GH as 'D'.

(4) If $D < (R + \Delta x)$ then the contact at H is re-bonded and if $D > (R + \Delta x)$ then the contact is de-bonded, where Δx is a tolerance equal to 0.0001 mm.

The centroid of the particle 'M' is located at (x_1 , y_1). The slope of the line AD is, $sp = \tan (90 - \tan^{-1}\gamma)$. Therefore the equation of AD is $y = sp\ x$. Since the product of the slopes of two perpendicular lines is equal to -1, the slope of GH is $-\frac{1}{sp}$ from which the equation of line GH can be written as $y = -\frac{1}{sp} x + ct$, where 'ct' is a constant. Since (x_1 , y_1) is a point in GH, $y_1 = -\frac{1}{sp} x_1 + ct$ from which the constant 'ct' can be obtained as $ct = \frac{1}{sp} x_1 + y_1$.

In order to determine the perpendicular distance 'D', the point of intersection 'H' at (x_2 , y_2) is to be determined. Since (x_2 , y_2) is a point on line

GH and also on line AD, the point (x_2 , y_2) can be substituted in the equations for lines AD and GH, derived above, and the two equations can be solved for x_2, y_2. This process gives $x_2 = \frac{(x_1 + sp\ y_1)}{(1 + sp^2)}$ and $y_2 = sp\ x_2$. The length of line GH denoted as 'D' is then determined as $D = \sqrt{(x_1 - x_2)^2 + (y_1 - y_2)^2}$. This value of 'D' is checked for the criterion in step (4). Similar procedures are followed for the right, top and bottom boundaries.

When nodes split, the bar areas of the bars linked to the split nodes are set equal to AWBAR. The nodes are renumbered before each analysis in order to obtain a minimum bandwidth for the stiffness matrix.

3.2 Kinetics of particles

3.2.1 Single particle approach

Particle kinetics means the sliding, rotation and rolling of particles with respect to the neighboring particles or boundaries. In the lattice type model, the micro slips occurring at contacts are neglected. When the lattice equivalent of the particulate assembly in Fig. 3.1 is subjected to a load, the joints are treated as rigid. Therefore, during the truss analysis, relative movement between two

particles due to the sliding of particles at a contact is not considered. A contact node is considered to have failed if the shear force ratio at that contact exceeds 'μ'. A particle having four contacts with only one failed contact cannot have significant relative movement relative to neighboring particles or boundaries. However, if a particle has 'n' nodes and if all the nodes except two nodes (n-2) have failed, then the particle can rotate and translate relative to the neighboring particles. Based on this assumption, a method was evolved to handle the kinetics of particles as described below.

The rotation and translation of particles are assumed to be caused by the additional shear forces (Equation 3.20) acting at the contacts. The displacements of the contact nodes due to these forces are found by carrying out an analysis of the lattice within the microstructure of the particles (Fig. 3.10) by considering only one particle at a time. The boundary conditions in this analysis for the bonded contacts are spring/elastic supports. The stiffnesses of these springs are: normal force divided by normal displacement and shear force divided by tangential displacement. The loads are the additional shear forces exceeding the coefficient of friction (μ) multiplied by the normal force. Tangential springs are not present at the nodes where additional shear forces are applied. The lattice within the microstructure of the particles are rotated and translated one by one, updating the coordinates of the contacts each time. At the end of this process, an initial stress analysis is carried out to bring the truss in Fig. 3.1 to equilibrium in the

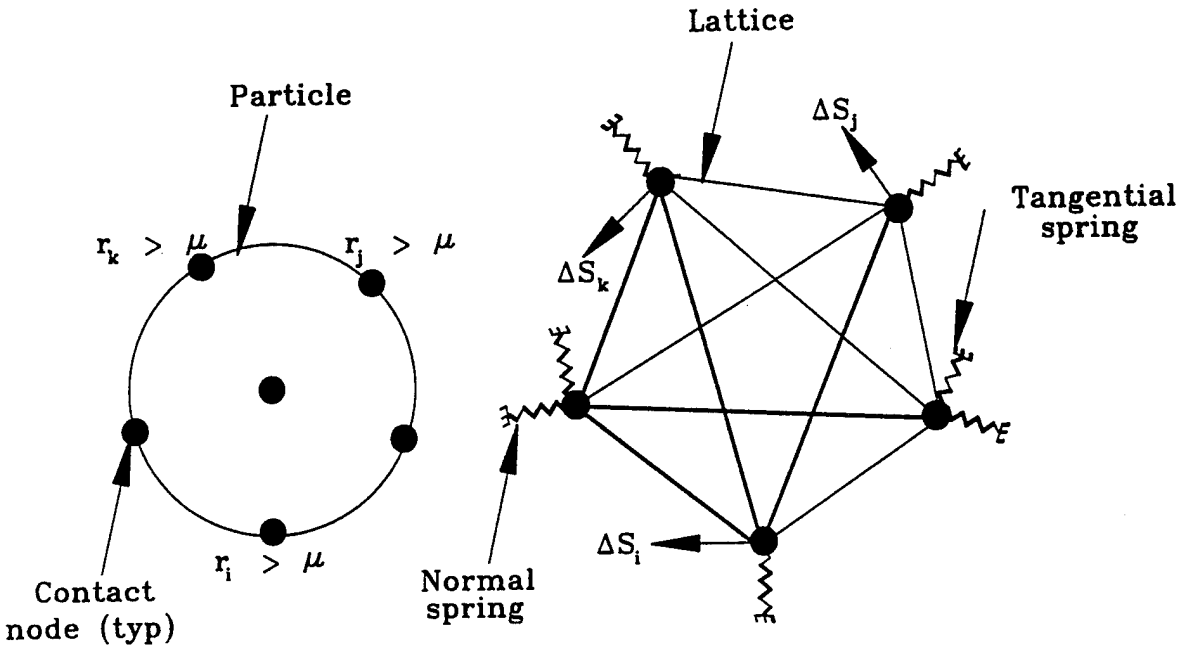

Fig. 3.10 Single particle approach to particle kinetics

updated coordinate position.

After implementing the above procedure, the approach was found to be computationally inefficient and also erroneous. The reasons for these are to be explained in relation to some numerical values related to a numerical test. Therefore, the simple shear test of a two dimensional assembly of disks representing quartz grains shown in Fig. 3.11a is chosen. The simple shear conditions simulated here are non-ideal conditions (Budhu, 1988) allowing free vertical movement of the top boundary. The simple shear strain is applied on the particle assembly by subjecting the lattice equivalent of the disk assembly to a

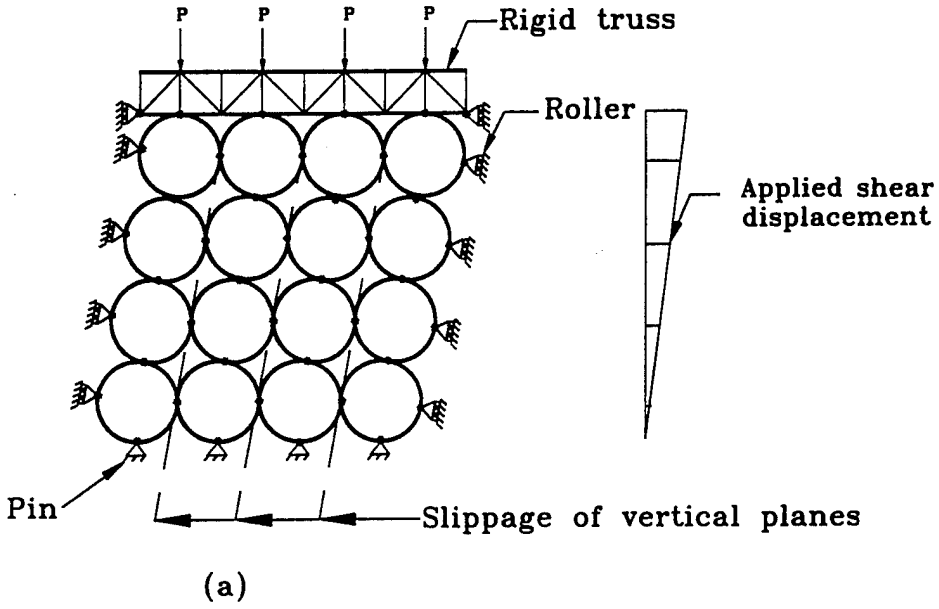

(a)

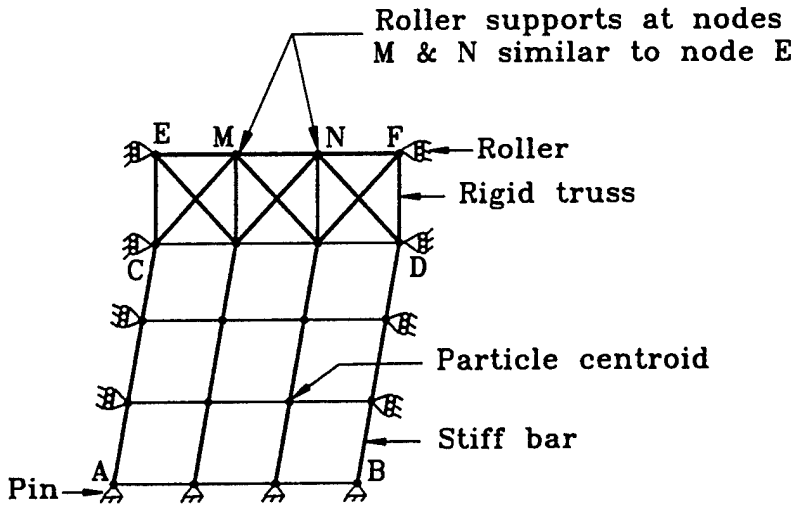

(b)

Fig. 3.11 (a) Development of mechanism in a loose packing subjected to simple shear strain (b) Mechanism framework

triangular variation of displacements as shown in Fig. 3.11a.

The particle assembly was subjected to incremental shear strains of 10^{-5}. This limiting value was chosen in order to keep the increase in the value of the shear stress ratios below 20% of the coefficient of friction at contacts. With incremental shear strains equal to 10^{-5}, the number of increments required to reach a shear strain of 0.20 is equal to $0.20/10^{-5} = 20{,}000$. This is computationally very inefficient and hence was found as one limitation of the single particle approach.

Laboratory experiments on the loose packing similar to that shown in Fig. 3.11a showed that when the packing is subjected to simple shear test conditions, the volume of the packing decreases (Dragoo, 1995). When the lattice equivalent of the particulate packing was subjected to an incremental shear strain, there was an increase in volume. When the vertical planes transformed into slippage planes, the single particle approach was applied to handle particle kinetics and this resulted in a decrease in volume. However, the net change in volume from the analysis for incremental shear strain and from the analysis for particle kinetics was an increase in volume which is not in accordance with the experiments.

As stated in Chapter. 1, predominant deformation in particulate media is caused by the sliding and rotation of particles with only a small contribution from particle deformations. The above mentioned shear strain of 10^{-5} is in the range of the strains due to deformation of particles. Therefore, an alternative method

was required to deal with the kinetics of particles. One such alternative technique developed is a global mechanism approach described in the next section.

3.2.2 Global mechanism approach

Numerical and experimental observations on granular assemblies (Cundall and Strack, 1983; Drescher and De Josselin De Jong, 1972) have shown that large forces are carried by chains of particles and the assembly deforms like a pin-jointed structure when a mechanism is reached and the deformation proceeds with no increase in stress. Thus, a mechanism in a granular assembly can be defined as a stage at which the assembly cannot carry an additional load and the assembly deforms under a constant applied load. It was observed that when a granular assembly is subjected to a deviatoric stress, particles lose contact in the minor principal stress direction and the number of contacts decreases. Based on the above observations in numerical tests using the DEM, Cundall and Strack (1983) defined a term called "constraint ratio" (CR) to check the development of mechanism in a granular assembly as

$$CR = \frac{C\,(2 - S)}{3N} \tag{3.21}$$

where, N = number of particles; C = number of contacts; S = fraction of sliding

contacts (number of sliding contacts divided by the number of contacts). The numerical tests of Cundall and Strack (1983) showed that when CR = 1, a mechanism had developed.

In the lattice type model, a particulate assembly is checked for the development of a mechanism after an incremental load is applied on the truss shown in Fig. 3.1. A mechanism is assumed to have been reached if any of the following two conditions are satisfied (1) The increment in load is zero due to the application of an incremental strain (such as biaxial or simple shear) on the truss shown in Fig. 3.1. (2) The shear stress ratio at (n-2) contacts around all the particles have reached 'μ', where 'n' is the number of contacts around a particle while the constraint ratio is less than 1.2. The first condition is the general condition for a random assembly of particles. However, for a regular assembly disks shown in Fig. 3.11a, the first condition is not fulfilled and then the second condition is to be checked for the development of a mechanism.

If a particulate assembly develops into a mechanism, further deformation is simulated through a "mechanism framework" (Fig. 3.11b). To formulate this structure, nodes are introduced at particle centroids and are linked with bars. Stiffness of bars linking particle centroids with non-sliding contacts are very large or "infinite" (10^8) relative to the stiffness of bars linking particle centroids with sliding contacts. The mechanism analogy is explained with respect to the simple shearing (non-ideal) of an assembly of disks representing quartz grains shown in

Fig. 3.11a. In this assembly, a mechanism develops when all the vertical planes fail and the column of disks rotates by rolling over the bottom of the assembly. This is simulated by the mechanism framework shown in Fig. 3.11b. Appropriate boundary conditions are simulated through rollers, hinges and rigid boundary trusses.

The incremental shear strain applied on the lattice equivalent of the particulate assembly in Fig. 3.11a is 0.00001, the reason for this limiting value was discussed earlier. However, since the mechanism approach is a method to simulate the predominant deformation due to sliding and rotation of particles, the incremental shear strain on the mechanism framework (Fig. 3.11b) is 0.001 which is 100 times 0.00001. At a rate of the above incremental shear strain, the number of increments required to reach a shear strain of 0.20 will be $0.20/0.001 = 200$. It was shown in the previous section that the number of increments required to reach a shear strain of 0.20 is 20,000 using the single particle approach. Therefore, it can be seen that the mechanism approach which takes only 200 increments is computationally very efficient.

With the centroids of the particles updated through the mechanism action, the lattice shown in Fig. 3.1 is reformed in the new position. In this new position, the axial forces in the bars prior to the mechanism are input as initial bar forces and an initial load analysis is carried out for equilibrium. The new shear stress ratios at the contacts are then computed and incremental load is applied. The

criterion for mechanism is again checked and the process is repeated.

3.3 Numerical implementation of the lattice type model

3.3.1 General

A computer program was written to implement the concepts of the lattice type model in section 3.2. Two different data set are prepared: truss data and particles data which is referred to as disks data here. Truss data consist of nodal coordinate data, connectivity data, boundary condition data, geometric property data, material property data and load data. Disks data consist of the coordinates of the centroids of disks, number of contacts around a disk, number of bars in a disk, node numbers of the contact nodes, member numbers linked to the contact nodes, back nodes of the bars linked to the contact nodes, disk numbers linked to the contact nodes and the node and disk numbers linked to the boundaries. The authors has prepared computer programs to generate the data for regular arrays of circular disks arranged as very loose and very dense packings (Fig. 3.12). The basic data required to prepare the above data are the radii of the particles and the X-Y coordinates of the centroid of the particles.

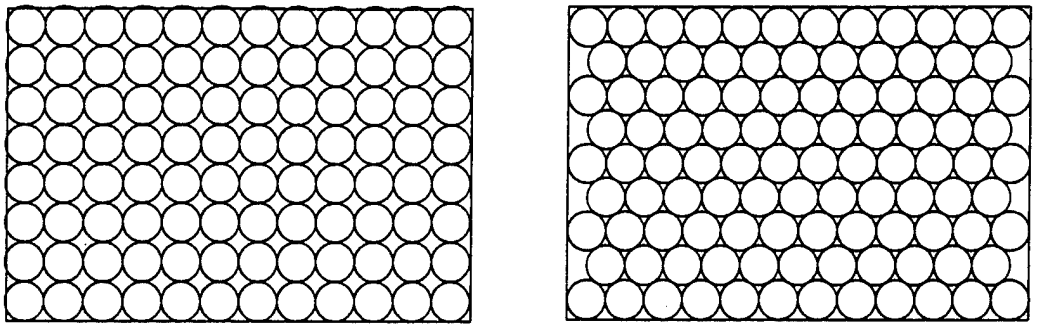

(a) Loose packing (96 disks) (b) Dense packing (104 disks)

Fig. 3.12 Loose and Dense packings

With the above data, an assembly of particles transformed into a truss is analyzed for a given load and prescribed loading condition (biaxial, simple shear etc.) along the procedures listed in the flow chart shown in Fig. 3.13.

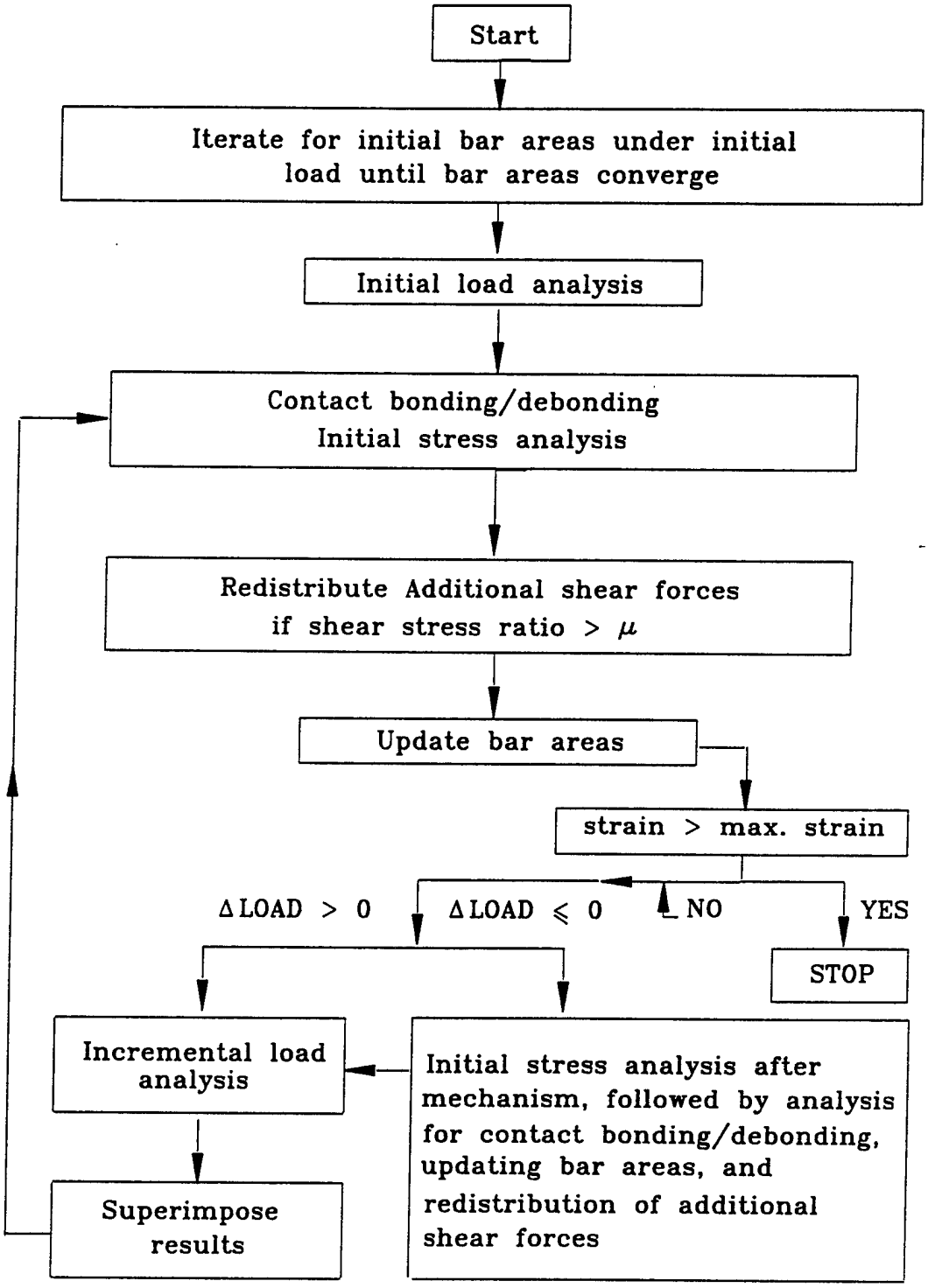

Fig. 3.13 Flow chart of procedures in the Lattice Type Model

3.3.2 Techniques in numerical simulation - A brief outline

Several numerical problems were dealt with during the course of this research and these are listed here as general computational information to benefit future researchers in lattice modeling.

The boundaries for simulating non-ideal simple shearing of an assembly of disks shown in Fig. 3.11a is simulated through a top rigid truss supported by two horizontal rollers at the two bottom ends of the rigid truss to allow the free vertical movement of the top boundary. The elastic modulus of each bar of this truss is set equal to the elastic modulus of the particles. The cross-sectional areas of the bars of this truss are set equal to 10^{+6} times the maximum of all the cross-sectional areas of the bars simulating the particulate assembly. In the lattice type model (LTM), the axial forces are redistributed for equilibrium after updating the coordinates of the nodes of the truss. At this stage, the axial forces in the rigid truss are not redistributed as these will have considerable influence on the particulate assembly due to it's large stiffness. By setting the two ends of the rigid truss on rollers, it was found that the top truss does not remain horizontal and deflects as shown in Fig. 3.14 when a shear strain is applied. Originally, it was brought to horizontal position by applying a vertical displacement for the two ends of the truss (Fig. 3.14). Thus, a truss analysis was to be carried out to bring the top truss to a horizontal position after every analysis for incremental

load, redistribution of additional shear forces etc.

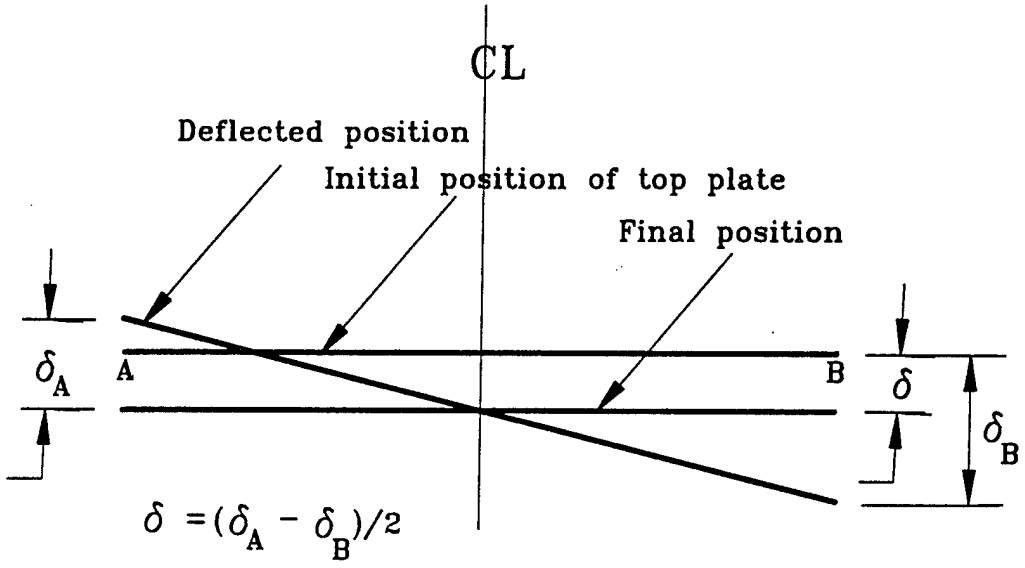

Fig. 3.14 Deflection of top plate in simple shear test

This was a time consuming process and thus the boundary conditions were changed to fix every node of the top rigid truss in the horizontal direction. With these boundary conditions, it was found that the vertical displacements of the top truss nodes were accurate to six decimal places and thus the top truss did not deflect.

Frictionless boundaries simulated by rollers as shown in Fig. 3.11a has boundary effects and thus the planes adjacent to the vertical boundaries never fail. Therefore, the behavior of a particulate assembly will not be very accurate in regions with at least one to two particle diameters away from the vertical boundaries. This leads to particles not separating (contact forces becoming zero)

even after the distance between the particles exceeds the sum of the radii of the particles in the new position after updating the coordinates through the mechanism framework. To rectify this problem, the contacts are split and the axial forces are redistributed when the distance between two particles exceeds the sum of their radii plus a tolerance of 2% of the sum of radii.

When the axial forces in the bars become tensile forces, a very low cross-sectional area is set for those bars (AWBAR = 10^{-8} times the maximum of all the cross-sectional areas in the particulate assembly). When these weak bars get linked to the top rigid truss at the boundary, there is a difference in stiffness between these bars and the bars of the rigid truss with an order of magnitude of 10^{14}. This would be the maximum order of difference that can be obtained with computations accurate to a double precision. However even with a bar area of AWBAR for the weak bars, axial forces upto a maximum of 10^{-4} times the maximum of the axial forces in the bars continues to develop in the weak bars. Therefore, these bar forces are set to zero and an initial stress analysis is carried out for equilibrium.

As particles lose contact, stress-free zones are developed, where particles remain in contact with neighboring particles or boundary with just one or two contacts. If a particle has at least two contacts linked to the global truss shown in Fig. 3.1, it is sufficient to keep the stiffness matrix non-singular. However, even if only two contacts of a particle are in contact with neighboring particles,

there are situations of the stiffness matrix becoming singular. One such situation is shown in Fig. 3.15. From this figure it can be seen that three particles can group together and

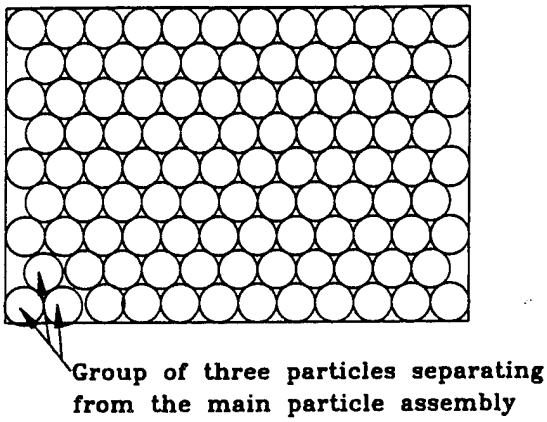

Fig. 3.15 Particles separating from the main particulate assembly

can get separated from the global truss or the stressed part of the particulate assembly resulting in the singularity of the [K] matrix. Therefore, a condition is stipulated that at least three nodes of a particle should be in contact with neighboring particles, and the areas of the bars linked to these nodes are set equal to AWBAR.

Because of the above mentioned constraints and boundary effects, the

accuracy of computations decreases and the errors get accumulated as a particulate assembly undergoes deformation. Therefore, contact forces do not reduce to exactly zero, but only to a very low value. Hence, a critical value is set for the contact force in order to split a node. The critical value of contact force at which a contact is split is increased as the material undergoes deformation. The critical value is increased as constraint ratio approaches one. The variation in the critical value is due to the decrease in the accuracy of computations during a deformation. The initial value is set as 0.10% of the maximum contact force and is increased to 2.0% of the maximum contact force when constraint ratio equals one.

It was stated that a mechanism is identified when the increment in load is equal to zero. However, the numerical tests reveal that it does not always become zero but gives a low positive value. This is assumed to be due to the presense of the existence of weak bars at forced contacts and boundary effects explained earlier. Hence a mechanism is identified if the increment in load is less than a minimum value. This value is equal 0.50% of the applied load (axial load in a biaxial test and shear force in a simple shear test) from zero strain to the incremental strain in the initial tangent of the stress-strain curve for the material.

In the mechanism framework shown in Fig. 3.11b, it was stated that weak bars are introduced by linking particle centroids if the particles have a sliding contact. A contact is a stick and slip contact if the distance between two particles

is less than the sum of the radii of the particles plus Δx (0.01 mm = 0.2% of the sum of radii). Particles with such stick and slip contacts are linked by weak bars in the mechanism framework.

When an initial stress analysis is carried out after updating the coordinates or updating the cross-sectional areas of the bars, the truss in Fig. 3.1 is analyzed for unbalanced forces coming at the nodes. It has been found that even if a very small unbalanced force (say 0.0001N) acts at a node where there are only two strong bars (bar area > 100.00 x AWBAR), it causes enormous displacement and alters the results drastically. Therefore a condition is set that if there are only two active bars (bar area > 100.00 x AWBAR) linked to a node, these bar areas should be greater than 10^4 times AWBAR and also that the minimum of the angles made by the bar with X-axis and Y-axis should be greater than 10 degrees. Otherwise, the unbalanced loads at these nodes are set to zero and it has been found that this leads to an accuracy loss in the range of ± 2%.

3.4 Lattice modeling with centroid of particles

The authors began the work by simulating the lattice by linking the particle contacts with the particle centroids as the nodes (Fig. 3.16). Even though the results were in general agreement with the behavior of granular media, it was found that the method was not sufficiently general and can lead to sensuous

errors. Therefore, the modeling approach was changed to a lattice formed by linking only the particle contacts, the results of which will be the subject matter of this research. Considerable work was done using the modeling approach shown

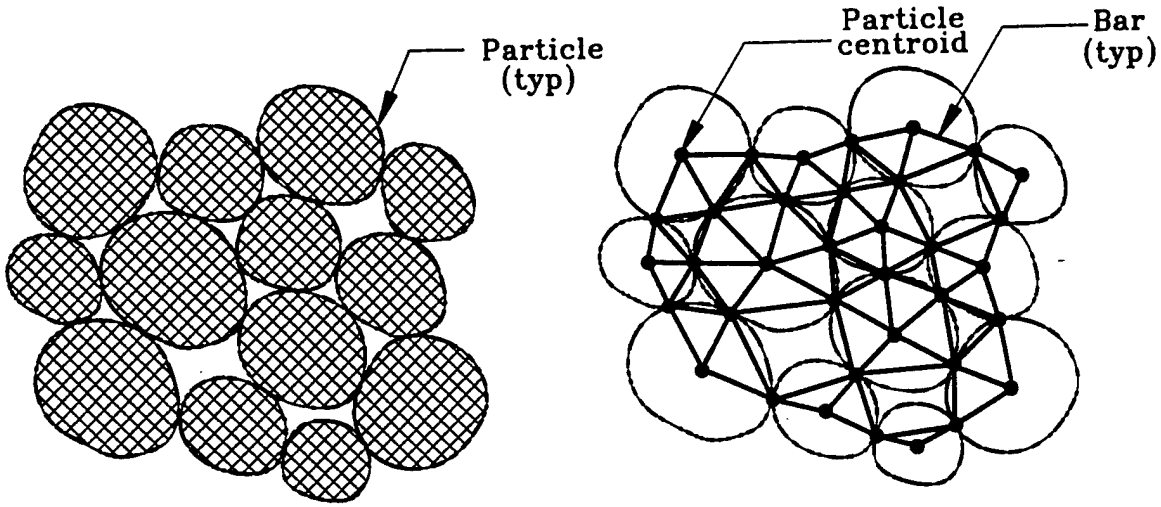

Fig. 3.16 Lattice type simulation with particle centroids

in Fig. 3.16. The results and methods adopted in this approach and it's shortcomings are presented in Budhu et.al (1994) and Ramakrishnan (1996).

3.5 Differences in approach between Lattice Type Model and Discrete Element Models

A distinct feature of the lattice type model is that the particle itself is replaced by a lattice and thus the (elastic) behavior of the particle is retained within the microstructure of the particle. In the current numerical models for particulate media (DEM and DMA), the elastic behavior of the particles are replaced by virtual springs at contacts, the disks are translated and rotated rigidly. The lateral forces developed due to the Poisson effect of the particles are not neglected in the lattice type model.

In the DEM and DMA, the stiffnesses of the springs are a function of elastic modulii and radii of the disks in contact. If two particles of different radii are in contact, then the contact stiffnesses of the springs are evaluated using an average radius. However, in the lattice type model the stiffnesses of the bars of the lattice are a function of the radius of the particle forming the lattice and there is no averaging procedure. In the available literature on DEM, there is no information as how to compute the contact stiffnesses if two particles of different elastic modulii are in contact. In the lattice type model the elastic modulus of the bars of the lattice being equal to the elastic modulus of the particles, the stiffness of the lattice is proportioned to the stiffness of the particles. Also in the lattice type model, as the contacts are modeled as joints in a lattice, the interaction at

contacts will automatically get related to the relative stiffnesses of the disks in contact. Thus, the lattice type model has significant potential to study the effects of weak particles (particles with low elastic modulus) randomly placed within a particulate medium, on it's macro-mechanical behavior.

A notable feature of the lattice type model is that the relative sliding, rotation and rolling of particles are all handled in one step through a global approach using the mechanism truss. Also, the development of a mechanism is automatically highlighted by the global stiffness matrix (due to the reformation of the bar areas) through the increment in load becoming zero.

Although the potential of the lattice type model to carry out study the behavior of particulate media with arbitrary particle shapes is not yet carried out, it can be stated that the method has capabilities for this. The lattice formation of a random packing can be carried out by taking an image of the particle assembly. The bar areas are to be evolved by taking the nearest ellipse fitting the particle shape. Also, the model has capabilities to study the effect of particle fracture. Application of the lattice type model for random packings with random particle shapes and for study of particle fracture shall be a scope for future research.

CHAPTER 4

APPLICATION OF LATTICE TYPE MODEL TO A TWO DIMENSIONAL ARRAY OF DISKS

4.1 General

In this chapter, the lattice type model is applied to two dimensional assemblies of circular disks. The disks of diameter 2.54 mm are arranged into a loosest packing of 96 particles and a densest packing of 104 particles (Fig. 3.12). The material of the spheres is considered to be quartz. The packings are subjected to an initial vertical load followed by a simple shear strain loading (Fig. 4.1).

4.2 Material properties

The properties of the material quartz considered herein are (Mantell, 1958)

Elastic modulus (E)	= 50.0 GPa.
Poisson's ratio (υ)	= 0.20
Shear modulus (G)	= 20.8 GPa
Friction coefficient (μ)	= 0.50

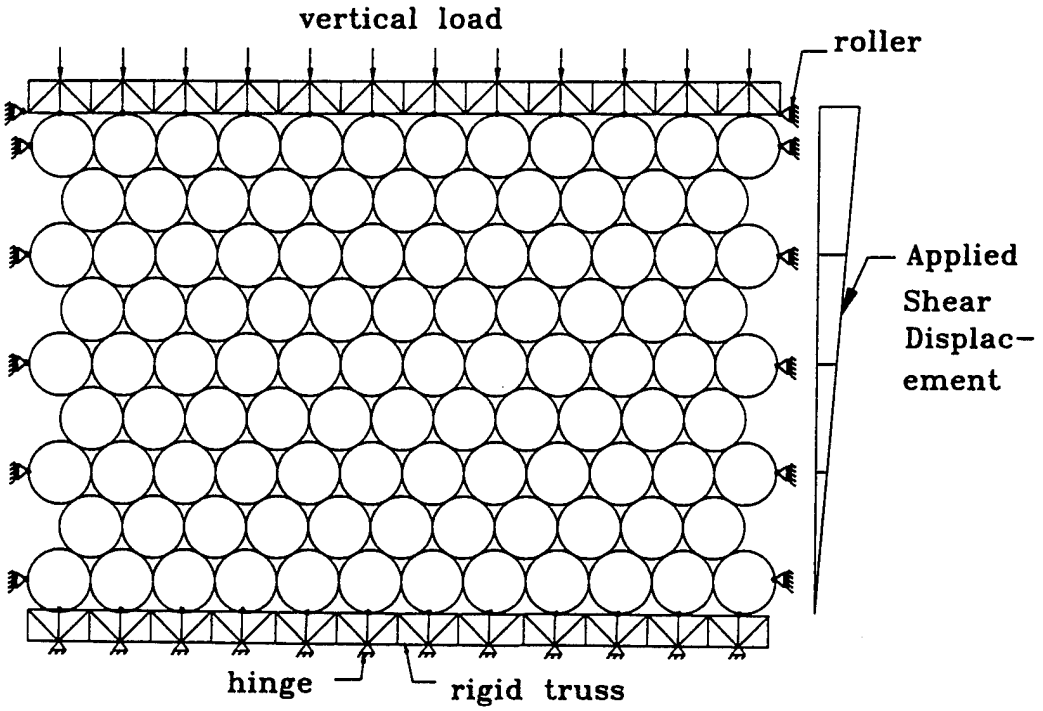

Fig. 4.1 Simulation of simple shear

4.3 Geometric properties

The geometric properties required for the analysis of a truss are the cross-sectional areas and lengths of the bars. The lengths of bars are determined from the X and Y coordinates of the contact nodes. The initial cross-sectional areas of the bars are obtained by procedures described in Chapter. 3.

4.4 Boundary conditions

For both the loose and dense packings the following boundary conditions are assumed. (1) The bottom boundary is fixed and can mobilize friction and thus the bottom nodes are taken to be on hinges. (2) The vertical boundaries are frictionless and are simulated by rollers. (3) The top boundary is simulated by a very rigid truss to represent a load platen. The nodes of the rigid truss are restrained in the X-direction and are free in the Y-direction. Thus, the top truss is allowed to move up or down, simulating the so-called non-ideal simple shear conditions (Budhu, 1988), i.e., allowing a volume change of the material.

4.5 Loading condition and Lattice/truss analysis

The loading is comprised of a vertical load followed by the superposition of a simple shear displacement (forward shear) as shown in Fig. 4.1. The total applied vertical load is 268.00 N. The vertical load is applied as nodal loads of 22.16 N at the top level nodes of the rigid truss (Fig. 4.1). The simple shear straining is simulated by applying a triangular variation of displacements for the nodes attached to the vertical boundaries as shown in Fig. 4.1.

The particulate packings, simulated as a lattice/truss as shown in Fig. 3.1b, are analyzed for the loading condition along the steps given in the flow chart

shown in Chapter. 3 (Fig. 3.13). The results of the analysis of the loose and dense packings are presented separately in Sections 4.7 and 4.8. The results are presented in relation to the state of stress in simple shear and an average stress tensor which are briefly presented in the next section.

4.6 State of stress in simple shear and average stresses

The ideal system of stresses on an element, rectangular in cross-section subjected to simple shear strain is shown in Fig. 4.2. In this figure, the following notations are used for the stresses. σ_{xx} - Normal stress on vertical planes, σ_{yy} - Normal stress on horizontal planes, τ_{xy} - Shear stress on vertical planes, τ_{yx} - Shear stress on horizontal planes, σ_{22} - Lateral stress. In general, it is difficult to reproduce these stresses in the laboratory tests, in particular the complementary shear stresses τ_{yx} and τ_{xy}. Consequently, the distributions of stresses and strains near the vertical boundaries of laboratory samples are non-uniform. However, the state of stress in the central zone of particulate packings (Examples: Figs. 4.3a and 4.3b) are expected to be uniform. The state of stress in an infinitesimally small element at the center of the central core can be assumed to represent the state of stress in the central core. The components of this stress tensor in the central core can be evaluated from the magnitude and location of the discrete contact forces acting at the boundaries of the central core.

The concept of evaluating an average stress tensor to determine the average constitutive behavior of a certain region of a material was addressed by Hill (1963). The procedure is to convert a discrete set of contact forces to an

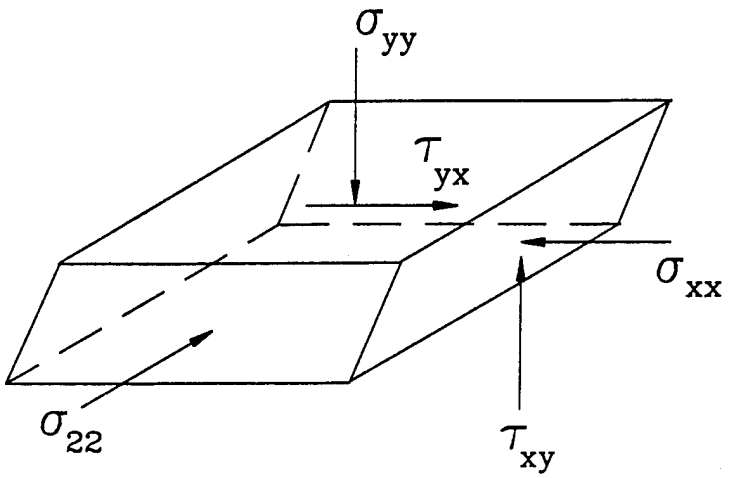

Fig. 4.2 Stress for Ideal simple shear

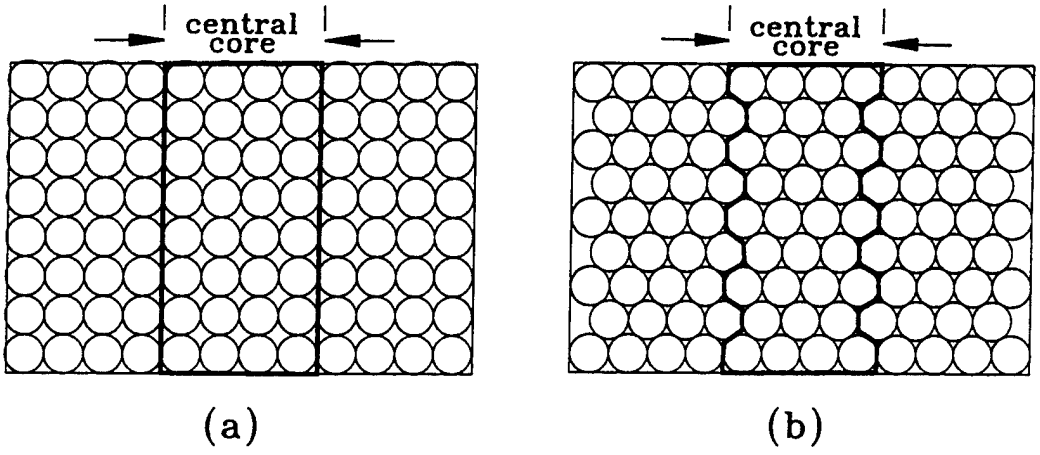

Fig. 4.3 Central core in (a) Loose packing (b) Dense packing

equivalent state of stress in a continuum. Based on Hill's averaging principle, the average stresses in a two-dimensional element σ_{xx}, σ_{yy}, τ_{xy} and τ_{yx} at the center of the particulate packing shown in Fig. 4.1 can be computed. Hill's concept was also applied by Drescher and De Josselin de Jong (1972) for the evaluation of average stresses in assemblies of disks using the contact forces determined from photoelastic experiments. The average stress tensor $\bar{\sigma}_{ij}$ at the center of a volume of material shown in Fig. 4.4 with a Cartesian coordinate system 1, 2 is defined as:

$$\bar{\sigma}_{ij} = \frac{1}{V} \int_V \sigma_{ij} \, dV \tag{4.1}$$

where σ_{ij} is the actual stress state at each point of the body and V is its volume. The average stress tensor is defined for an infinitesimally small element at the center of the control volume and it can be transformed into an expression containing the forces acting at the boundary of the control volume as follows.

$$\sigma_{ij} = \delta_{ik} \, \sigma_{jk} = x_{i,k} \, \sigma_{kj} \tag{4.2}$$

where δ_{ik} is the Kronecker delta, x_i are the coordinate directions (i = 1, 2, 3 for x, y, z directions) and the comma indicates partial differentiation with respect to the coordinates. Substituting Equation. (4.2) into Equation (4.1), we get

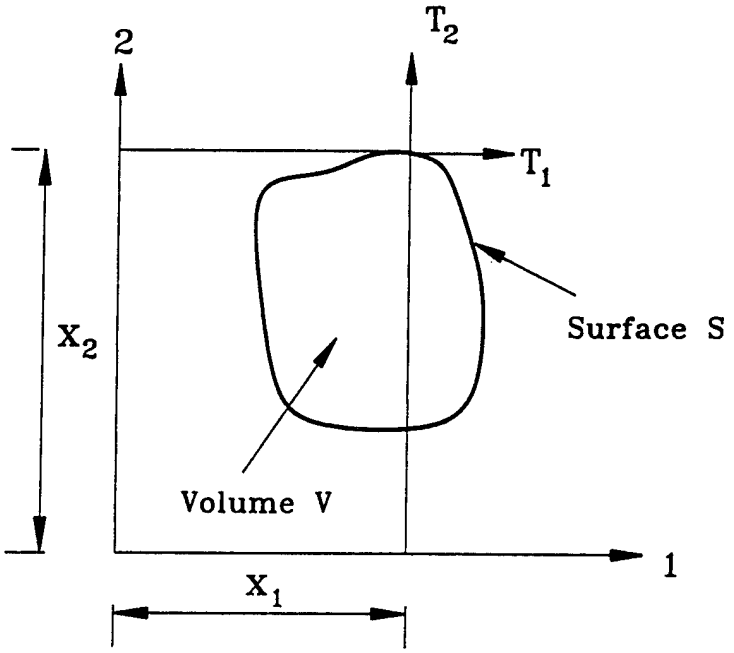

Fig. 4.4 General distribution of forces T_1 and T_2 around surface S of volume V

$$\bar{\sigma}_{ij} = \frac{1}{V} \int_V x_{i,k}\, \sigma_{kj}\, dV \tag{4.3}$$

The stress state σ_{kj} satisfies the equilibrium equations

$$\sigma_{kj,\,j} = 0 \tag{4.4}$$

Using this condition, Equation. (4.3) can be expressed as

$$\bar{\sigma}_{ij} = \frac{1}{V} \int_V (x_i\, \sigma_{kj})_{,\,k}\, dV \tag{4.5}$$

Using Gauss's divergence theorem, Equation. (4.5) can be written as

$$\bar{\sigma}_{ij} = \frac{1}{V} \int_S x_i \, \sigma_{kj} \, n_k \, dS = \frac{1}{V} \int_S p_j \, x_i \, dS \qquad (4.6)$$

where n_i are the vector of direction cosines of the outward normal at coordinates x_i on the surface and p_j are the vector of stress components. Thus, it can be seen from Equation. (4.6) that the average stress tensor can be obtained by integrating the products $p_j \, x_i$ over the boundary of the volume V. For a set of discrete forces T_j over the surface (Fig. 4.4), Equation. (4.6) becomes

$$\bar{\sigma}_{ij} = \frac{1}{V} \sum_{m=1}^{n} T_j^m \, x_i^m \qquad (4.7)$$

The average stresses at the center of the assembly of particles shown in Fig. 4.1 are found using Equation. (4.7) from the normal and shear forces at the contacts between the particles and the boundaries. In the absence of body couples in a two dimensional element, $\tau_{xy} = \tau_{yx}$. The shear stress ratios on the vertical and horizontal planes are defined as τ_{xy} / σ_{xx} and τ_{yx} / σ_{yy} respectively.

From the components of the average stress tensor, the principal stresses σ_{11} and σ_{33} and the angle ψ made by the major principal stress plane with the positive direction of X-axis (Fig. 4.5) are determined from

$$\sigma_{11} = \frac{\sigma_{xx} + \sigma_{yy}}{2} + \sqrt{\left(\frac{\sigma_{xx} - \sigma_{yy}}{2}\right)^2 + \tau_{xy}^2} \qquad (4.8)$$

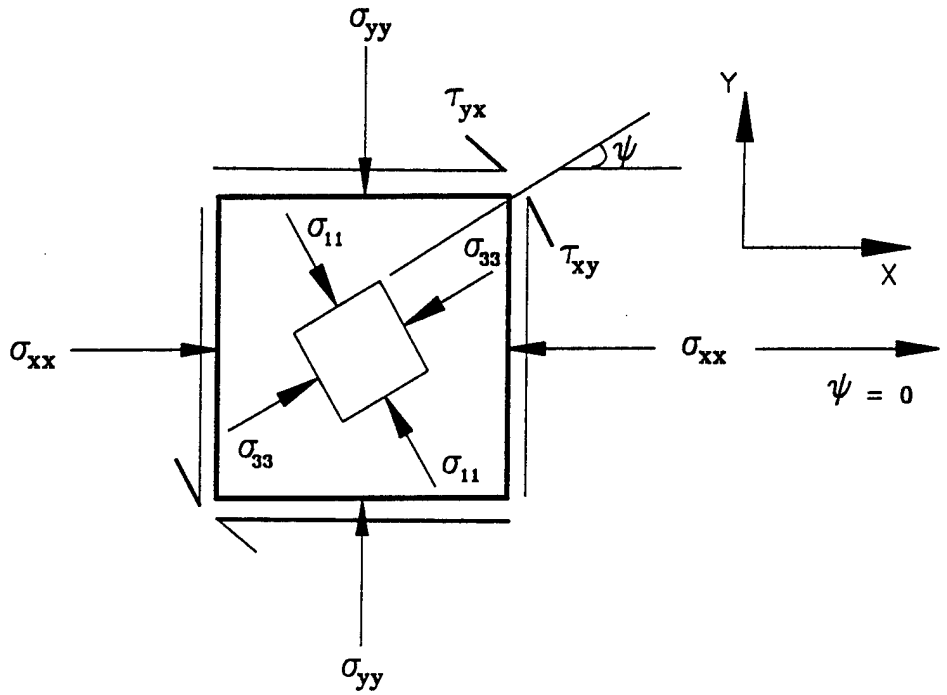

Fig. 4.5 Principal stresses in a two dimensional element

$$\sigma_{33} = \frac{\sigma_{xx} + \sigma_{yy}}{2} - \sqrt{\left(\frac{\sigma_{xx} - \sigma_{yy}}{2}\right)^2 + \tau_{xy}^2} \tag{4.9}$$

and

$$\tan 2\psi = -\frac{2\tau_{xy}}{\sigma_{xx} - \sigma_{yy}} \tag{4.10}$$

4.7 Loose packing, results and discussions

4.7.1 Shear stress ratios and contact forces

The shear stress ratios at the contact nodes for the loose packing are shown in Figs. 4.6a and 4.6b at small shear strains (γ) of 0.001%, 0.002% and in Figs 4.6c and 4.6d at large shear strains of 30% and 40%. The above shear strains are chosen in order to show the large variation in the magnitudes of the shear stress ratios during the shearing process. Relative sliding of particles occurs at a contact when the shear stress ratio at that contact exceeds the coefficient of friction. When there is a continuous line/curve of sliding contacts, a slippage/sliding plane develops. A comparison of Fig. 4.6a and Fig. 4.6b shows that slippage is initiated on vertical planes and the deformation pattern quickly resembles the tilting and frictional sliding of a column of particles. This deformation pattern or mechanism is then simulated by the "mechanism framework" explained in Chapter. 3. For examples, the mechanism frameworks at shear strains of 0.002% and 30% are shown in Figs. 4.7a and 4.7b. The deformation is one of a framed pin jointed structure subjected to lateral loads.

The change in the magnitude of normal forces at contacts are shown in Figs. 4.8a, 4.8b and 4.8c. The change in normal forces on the horizontal contact planes is only marginal while there is a substantial increase in the normal forces

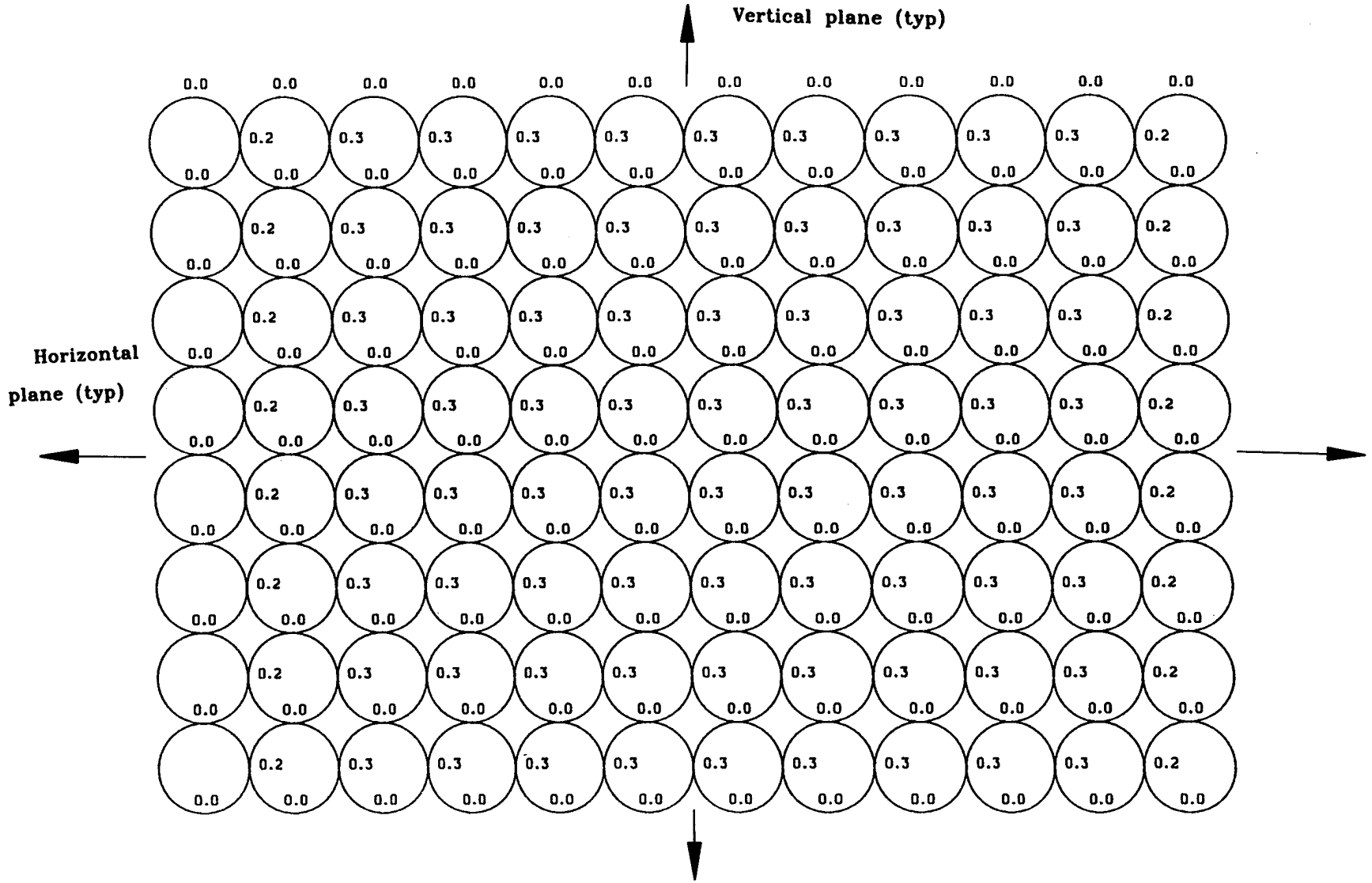

Fig. 4.6a Shear stress ratios at contacts for loose packing at γ = 0.001 %

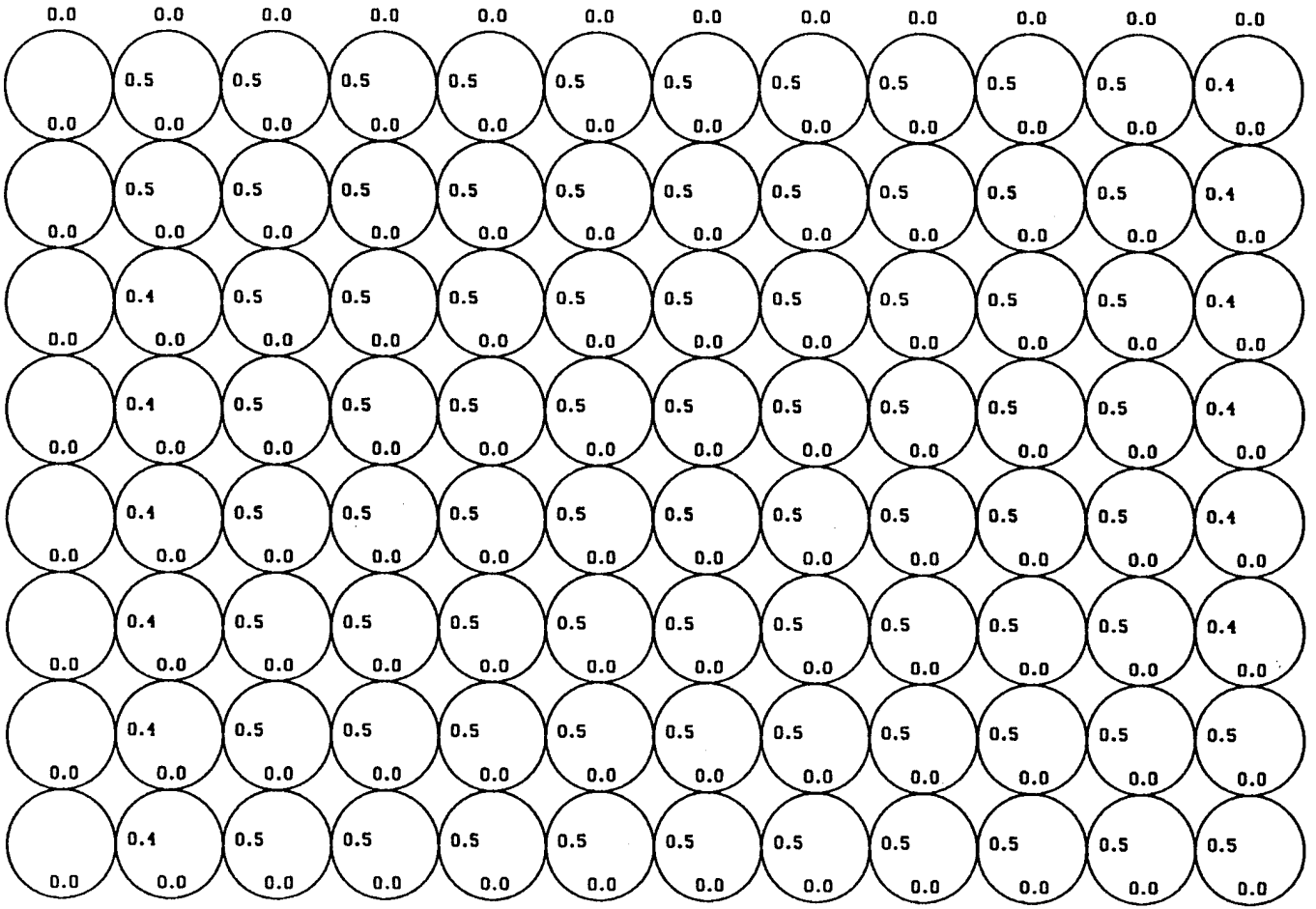

Fig. 4.6b Shear stress ratios at contacts for loose packing at γ = 0.002 %

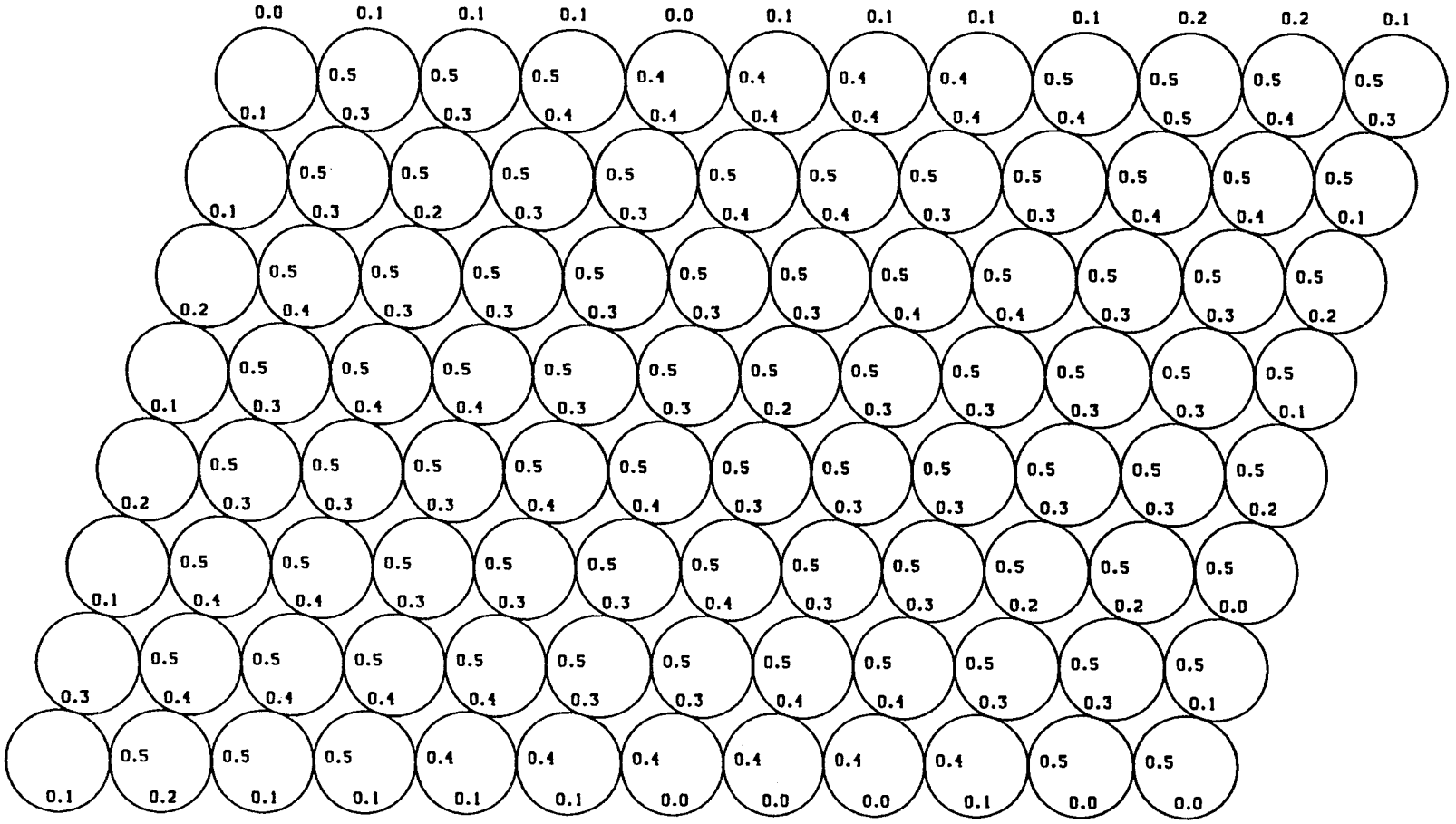

Fig. 4.6c Shear stress ratios at contacts for loose packing at γ = 30 %

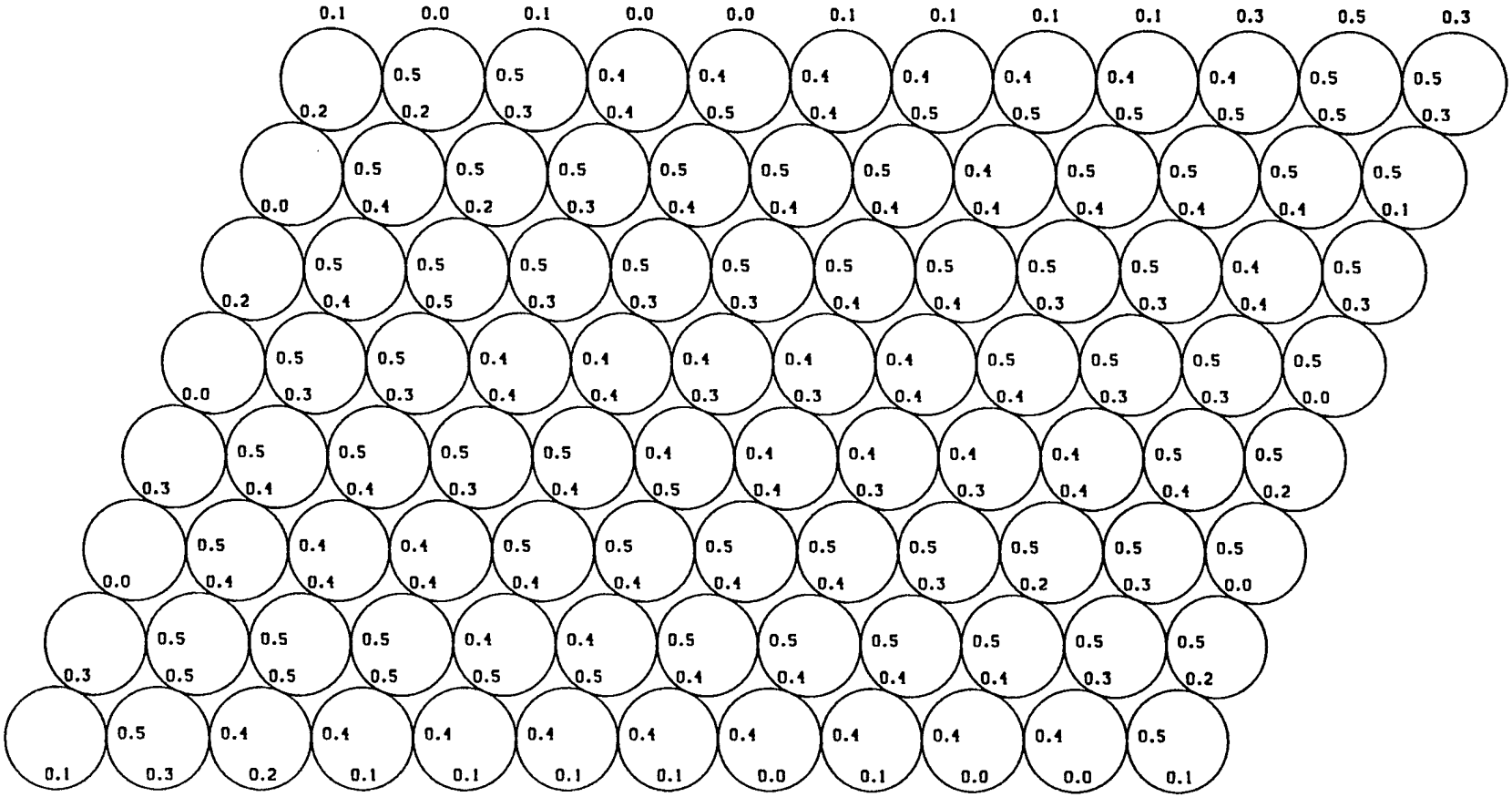

Fig. 4.6d Shear stress ratios at contacts for loose packing at γ = 40 %

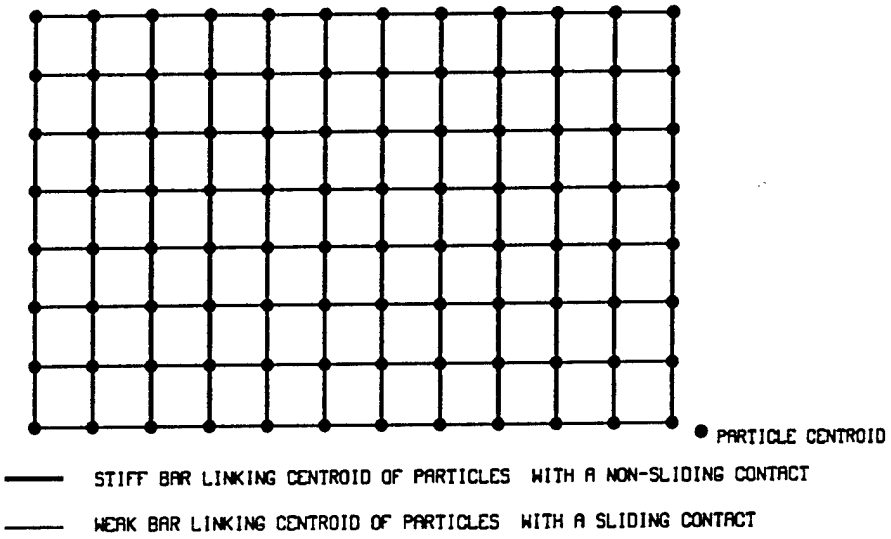

(a)

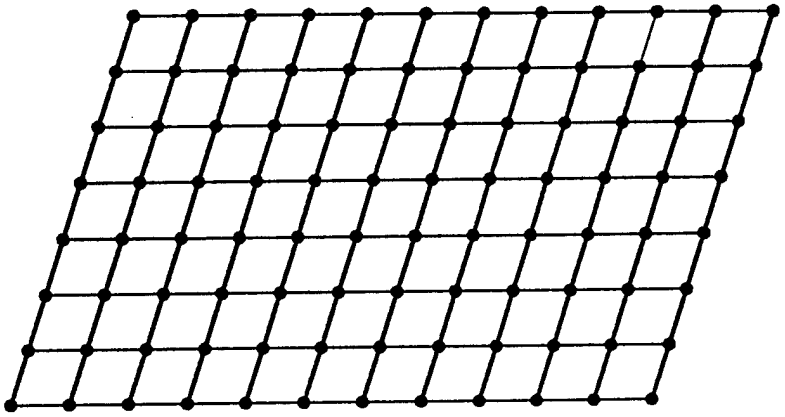

(b)

Fig. 4.7a,b Mechanism frameworks for loose packing at
(a) $\gamma = 0.002\%$ (b) $\gamma = 30\%$

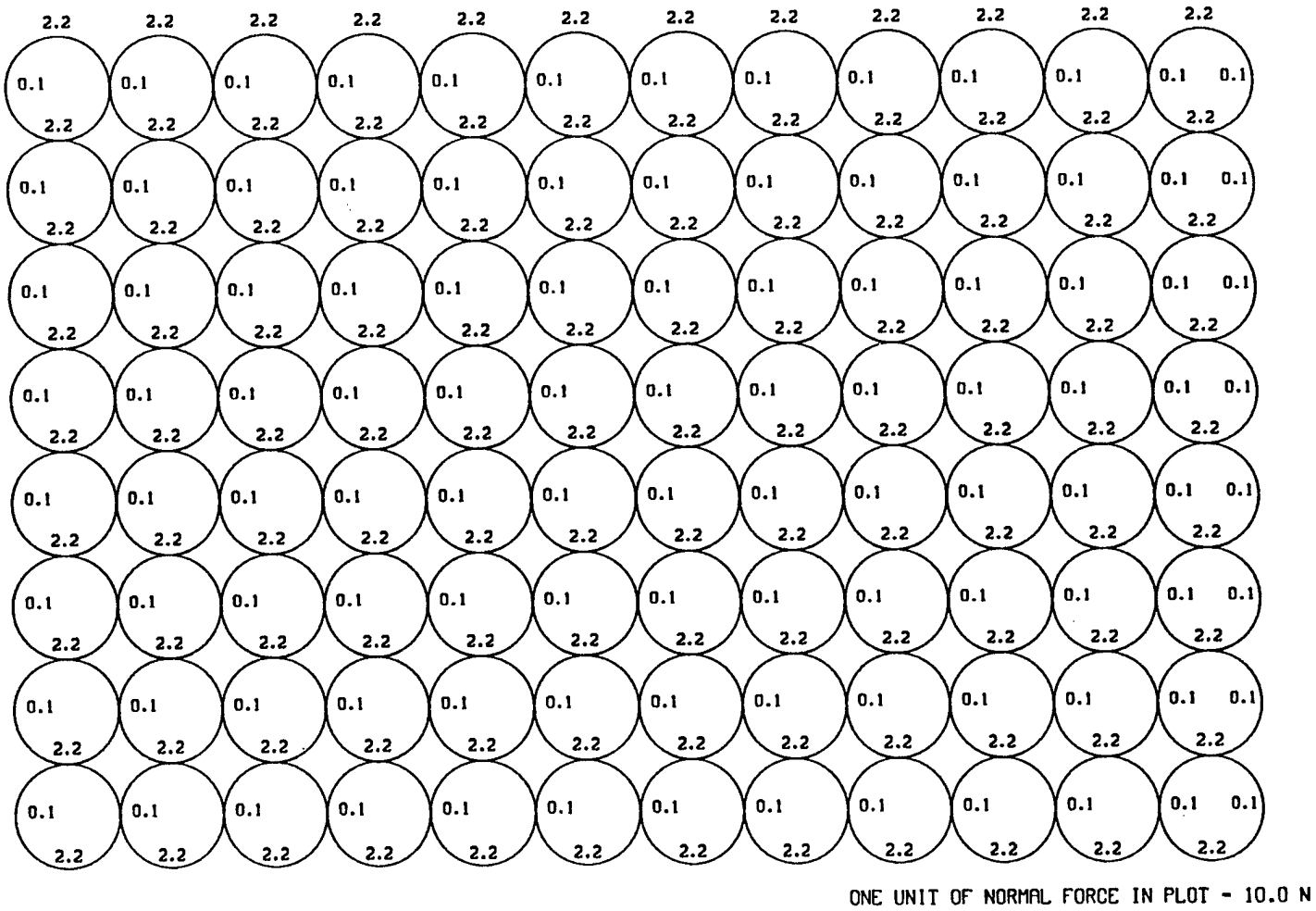

Fig. 4.8a Normal forces at contacts for loose packing at Vertical load

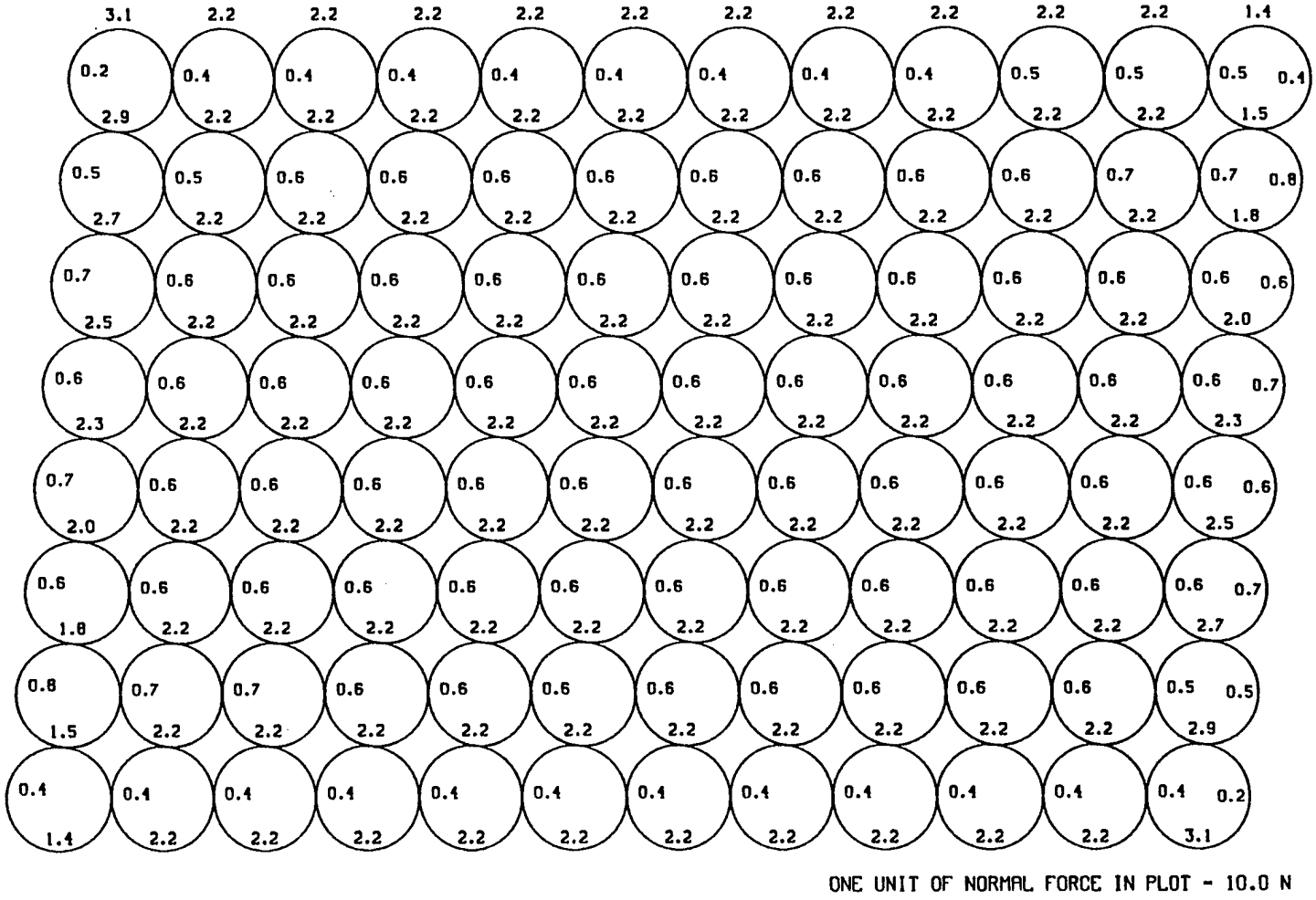

Fig. 4.8b Normal forces at contacts for loose packing at γ = 10 %

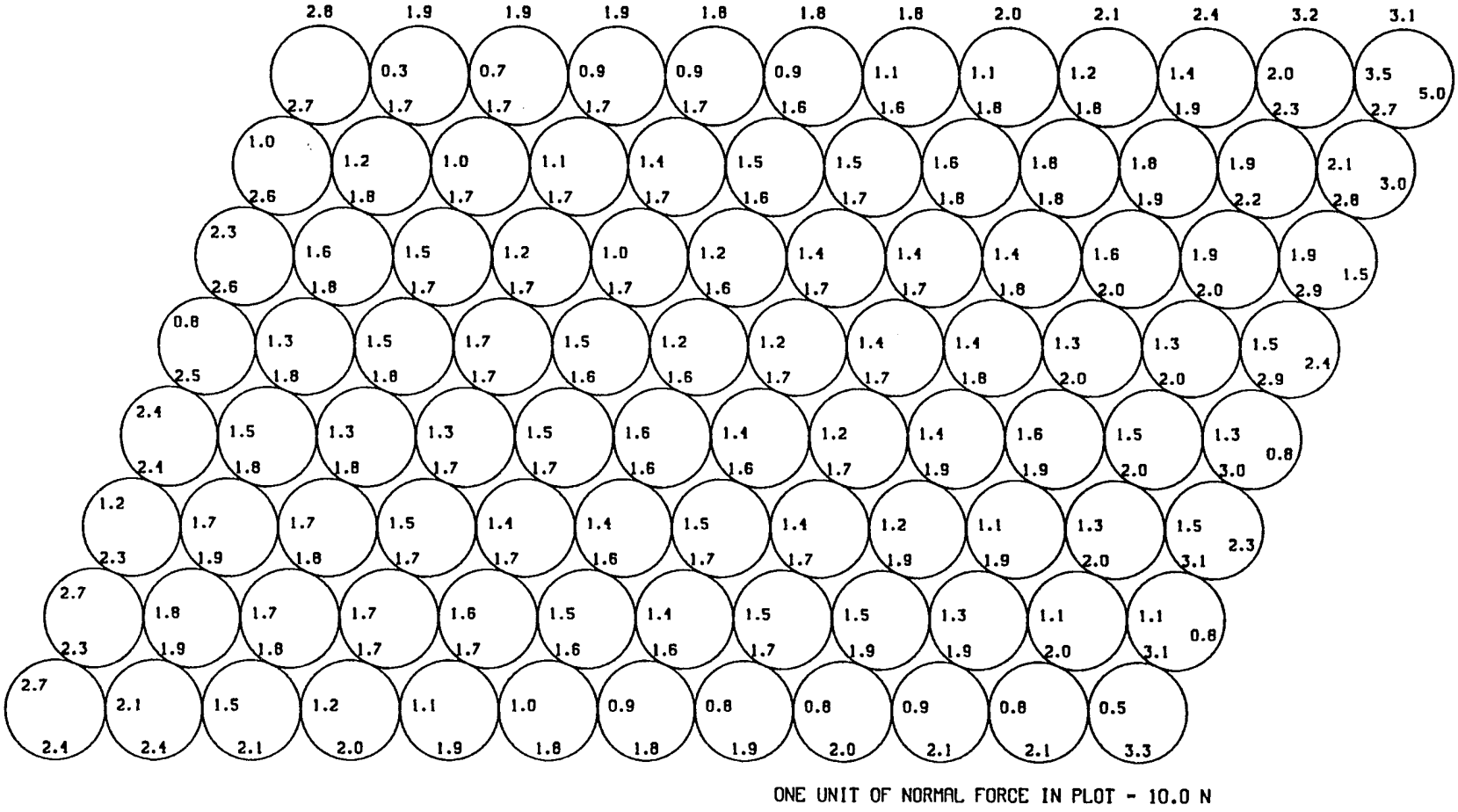

Fig. 4.8c Normal forces at contacts for loose packing at γ = 40 %

on the vertical contact planes. Since the contacts on vertical planes continue to slide and the normal forces increase, the shear forces at these contacts increase considerably. For equilibrium of the particles, the shear forces at the contacts on horizontal planes should also increase. This can be seen from the substantial increase in shear stress ratios at the contacts on horizontal planes (Fig. 4.6c) at a large shear strain of 30%, while there is only a marginal decrease in the normal forces. As the material tends to move towards the closest packing configuration, the shear stress ratios at contacts on vertical planes continue to be sliding ones until a shear strain of about 30% while there is a considerable increase in the shear stress ratios on horizontal planes due to the increased shear forces at contacts on these planes. At a shear strain of 40% (Fig. 4.6d), the shear stress ratios at contacts on vertical planes decrease and they now become non-sliding contacts. At this shear strain, it can be seen that continuity of sliding contacts prevails neither along horizontal planes nor along vertical planes.

4.7.2 Contact forces and fabric changes

The variation of the magnitude and orientation of contact forces are shown using vector plot of contact forces within the particulate assemblies (Fig. 4.9a). The thickness of lines in these diagrams indicates the magnitude of the contact

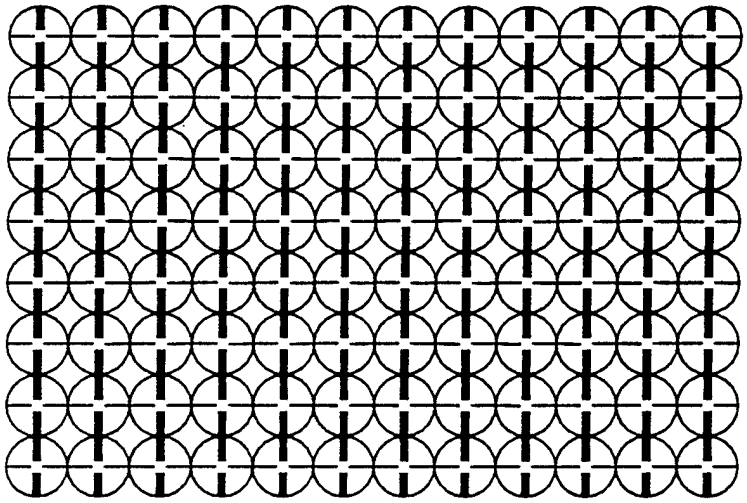

MAXIMUM CONTACT FORCE - 22.386 N

(a)

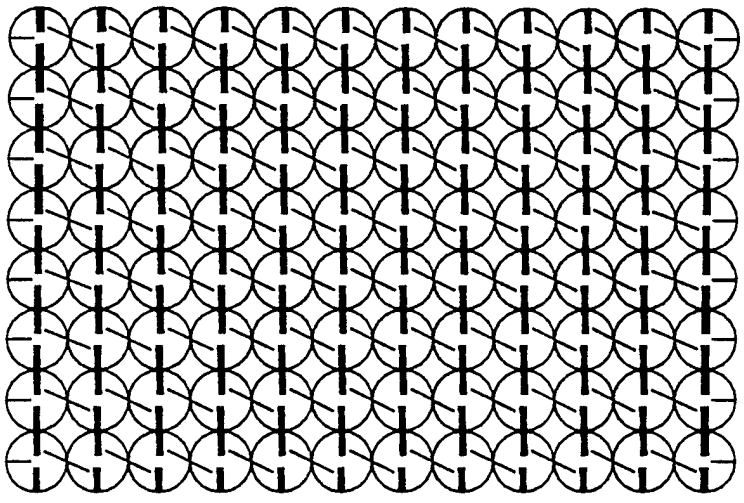

MAXIMUM CONTACT FORCE - 24.639 N

(b)

Fig. 4.9a,b Vector plot of contact forces for loose packing under (a) Vertical load (b) γ = 0.002 %

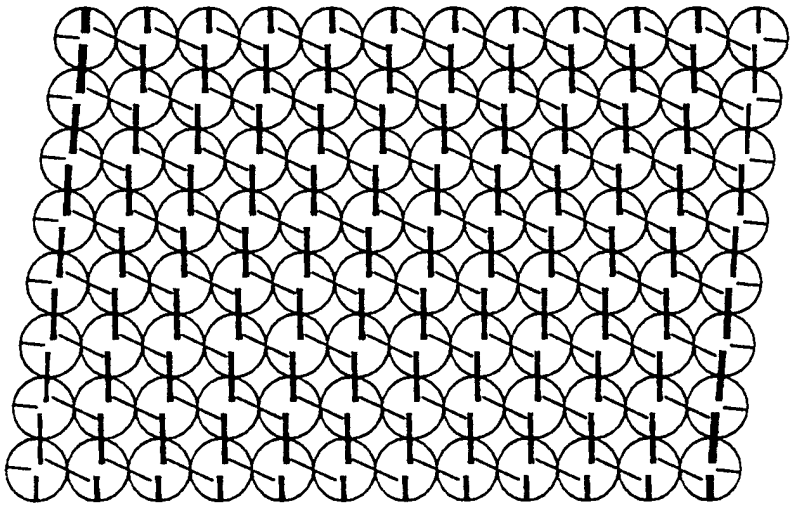

MAXIMUM CONTACT FORCE - 30.904 N

(c)

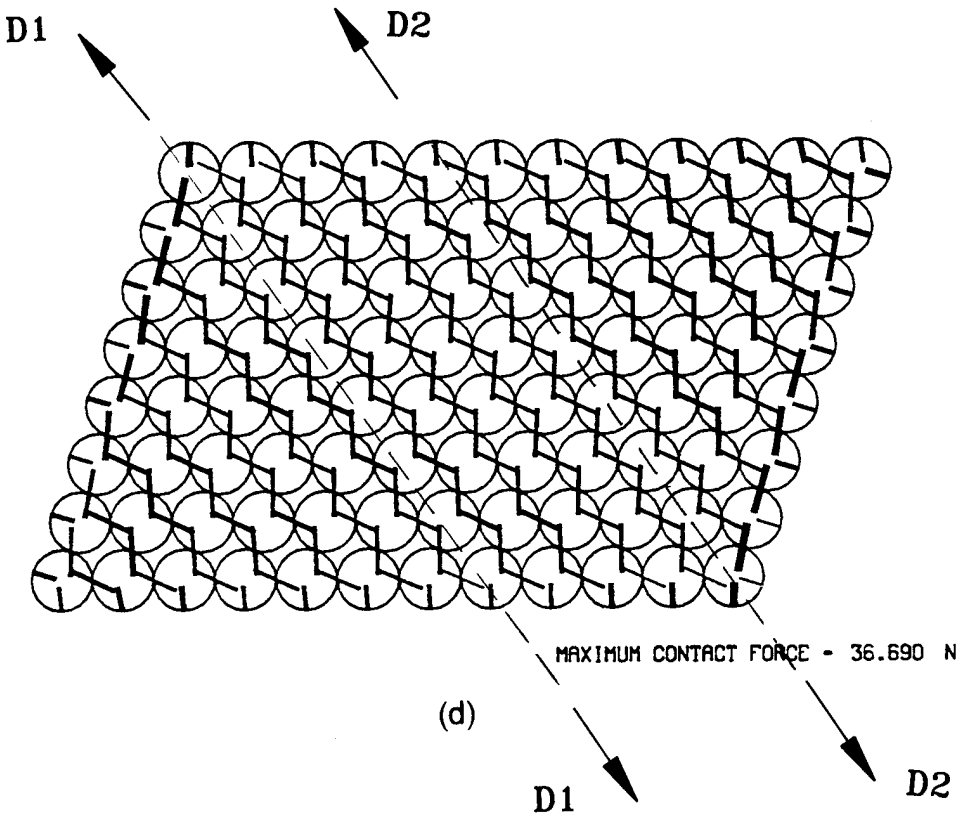

Fig. 4.9c,d Vector plot of contact forces for loose packing at (c) γ = 10% (d) γ = 30 %

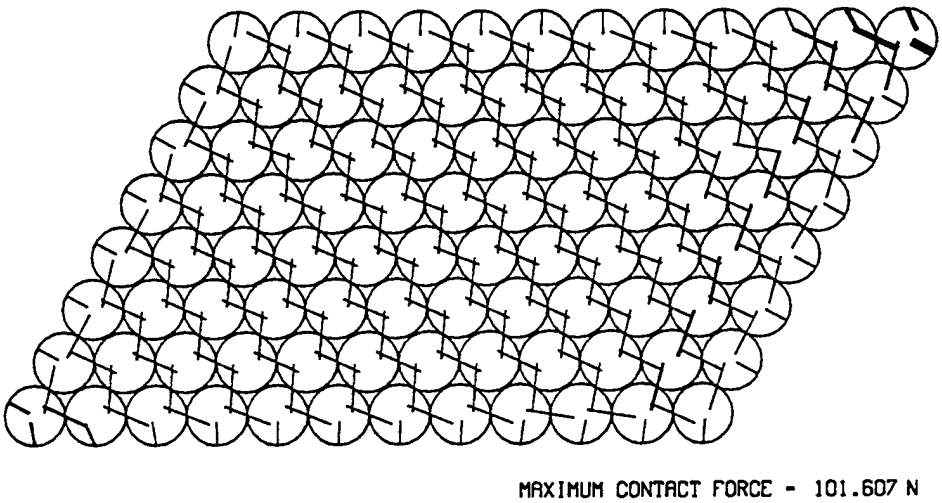

Fig. 4.9e Vector plot of contact forces for loose packing at γ = 50%

forces relative to the maximum contact force in the particulate assembly. These diagrams show the flow of contact forces and load paths as well as the changes in fabric or packing structure.

The vector plot of contact forces are shown in Fig. 4.9a under vertical load and in Figs. 4.9b, 4.9c, 4.9d and 4.9e at shear strains of 0.002%, 10%, 30% and 50% respectively. Obliquity of contact force is defined as the angle made by the orientation of the contact force with the contact normal at the contact. The contact normal for two particles of circular cross-section is the direction linking the centroid of the particles. The obliquity of contact forces on vertical planes under vertical load which were initially horizontal (Fig. 4.9a) is inclined at an angle of 26.5^0 $(\tan^{-1}0.5)$ at a shear strain of 0.002% (Fig. 4.9b). At a shear strain of 10% (Fig. 4.9c), the magnitude and orientation of contact forces in the middle ten columns of particles are uniform and non-uniformity can be seen only along the column of particles adjacent to the vertical boundaries. However, at a larger shear strain of 30% (Fig. 4.9d), contact forces of larger magnitude can be seen in the triangular zones to the right of line D2-D2 and to the left of line D1-D1. This non-uniformity is likely to be caused by the interaction between the right boundary and top boundary and between the left boundary and bottom boundary through the triangular zones shown in Fig. 4.9d.

The material tended to reach the closest packing configuration at a shear strain of 50% (Fig. 4.9e). At this shear strain, it can be seen that new contacts

have been established along columns of particles parallel to line D1-D1. The shearing could not be carried out further, as the scope of the computer code in this research does not incorporate the formation of new contact nodes and elements to develop a revised lattice.

From the vector plot of contact forces, it can be seen that over 60% of the assembly in the middle is under uniform loads. At the ends, the loads are significantly higher or lower (depending on the direction of shear) than the loads in the middle 60% of the assembly. This is expected since the vertical sides of the particulate assembly are assumed to be frictionless so that no complementary shear stress is developed there. The contact force distributions from the LTM results are similar to boundary stress distributions in non-ideal simple shear using elastic analysis of a continuum discussed by Roscoe (1953).

At higher shear strains, the contact force flow pattern resembles a staircase/steplike pattern. The contact forces on vertical planes increase and become almost equal to the contact forces on the horizontal planes as the material tends to reach the closest packing at 50%. This indicates that as the material tends to become a dense packing, the stress conditions reach a hydrostatic state.

4.8 Dense packing, results and discussions

4.8.1 General

For ease of following the deformation mechanism in the dense assembly of disks, certain symbols are used for the orientation of rows and columns of particles and these are shown in Fig. 4.10. Two lines AA and BB along the center line of diagonal particles are selected with line AA representing the short diagonal (compression) and line BB representing the long diagonal (tension) during simple shear. The horizontal row of particles are labelled as shown in Fig. 4.10.

4.8.2 Shear stress ratios, contact forces and fabric changes

The shear stress ratios at the contact nodes are shown in Fig. 4.11a under vertical load and in Figs. 4.11b, 4.11c, 4.11d and 4.11e at shear strains of 0.01%, 0.03%, 0.04% and 10% respectively. The normal component of the contact forces at contact nodes are shown in Fig. 4.12a under the vertical load and in Figs. 4.12b, 4.12c, 4.12d and 4.12e at shear strains of 0.01%, 0.03%, 0.04% and 10%. The dense packing arrangement in Fig. 4.1 is the densest packing that is physically possible in an assembly of disks of uniform size. Therefore, the material

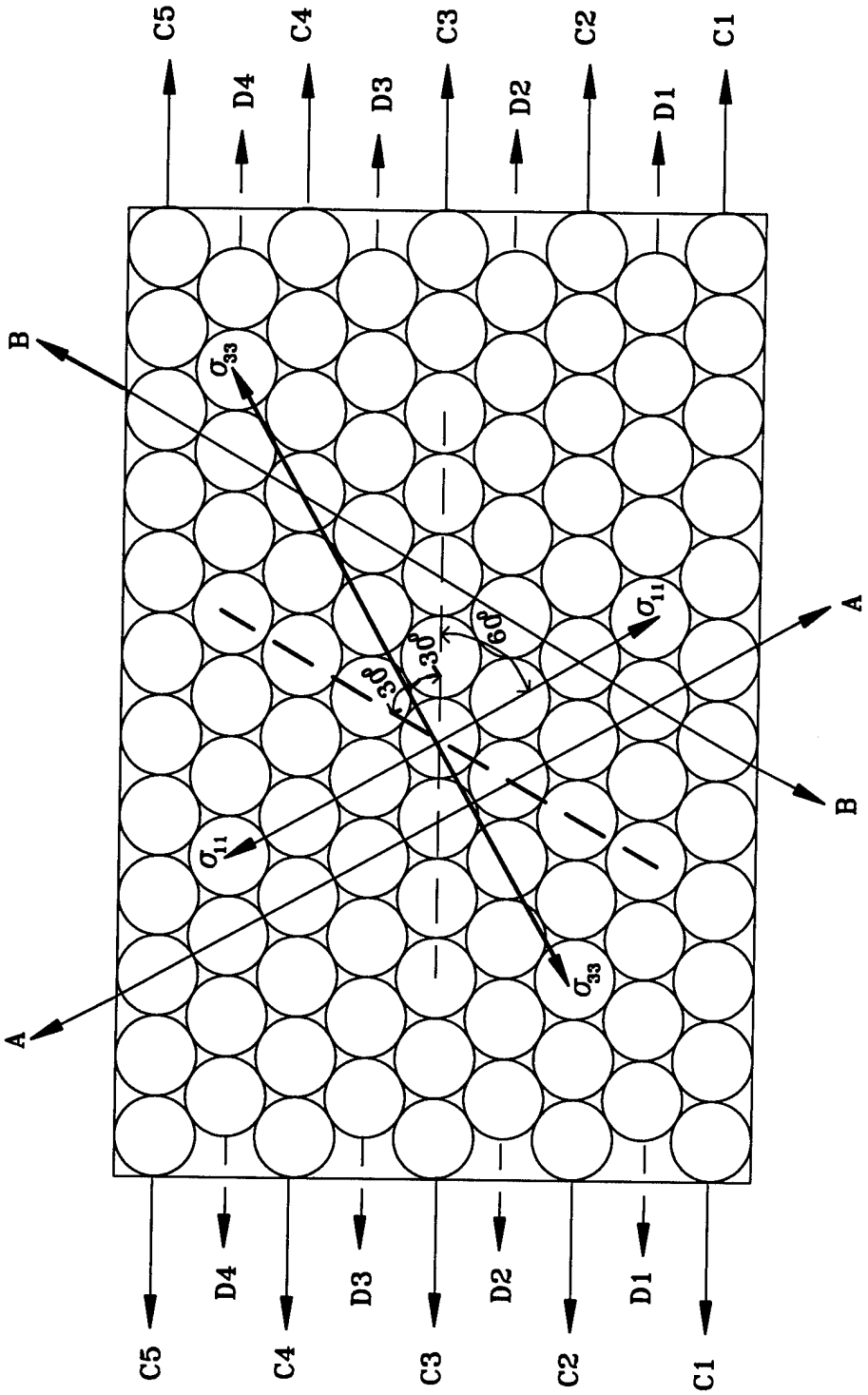

Fig. 4.10 Orientation of particles in the dense packing

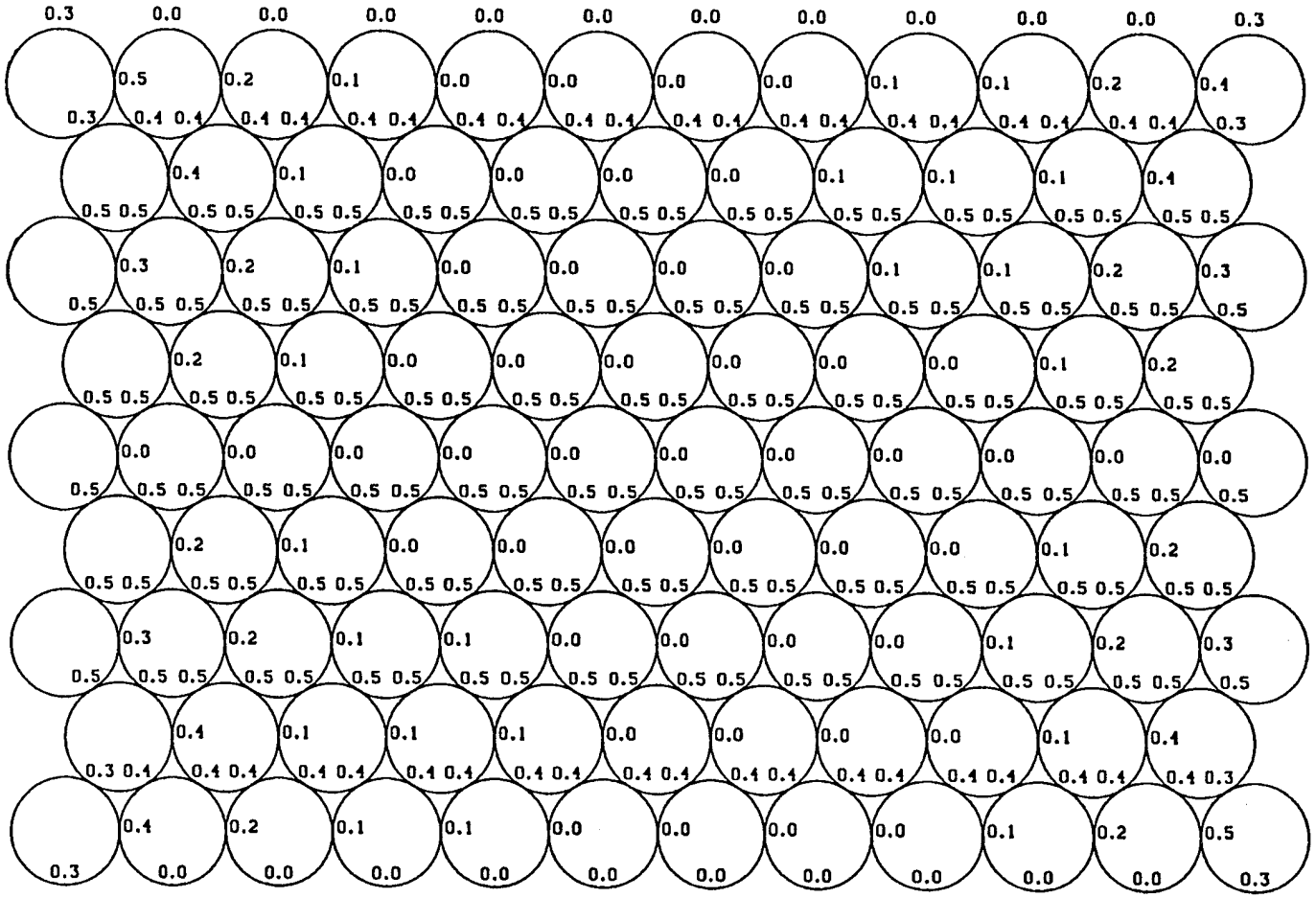

Fig. 4.11a Shear stress ratios at contacts for dense packing under vertical load

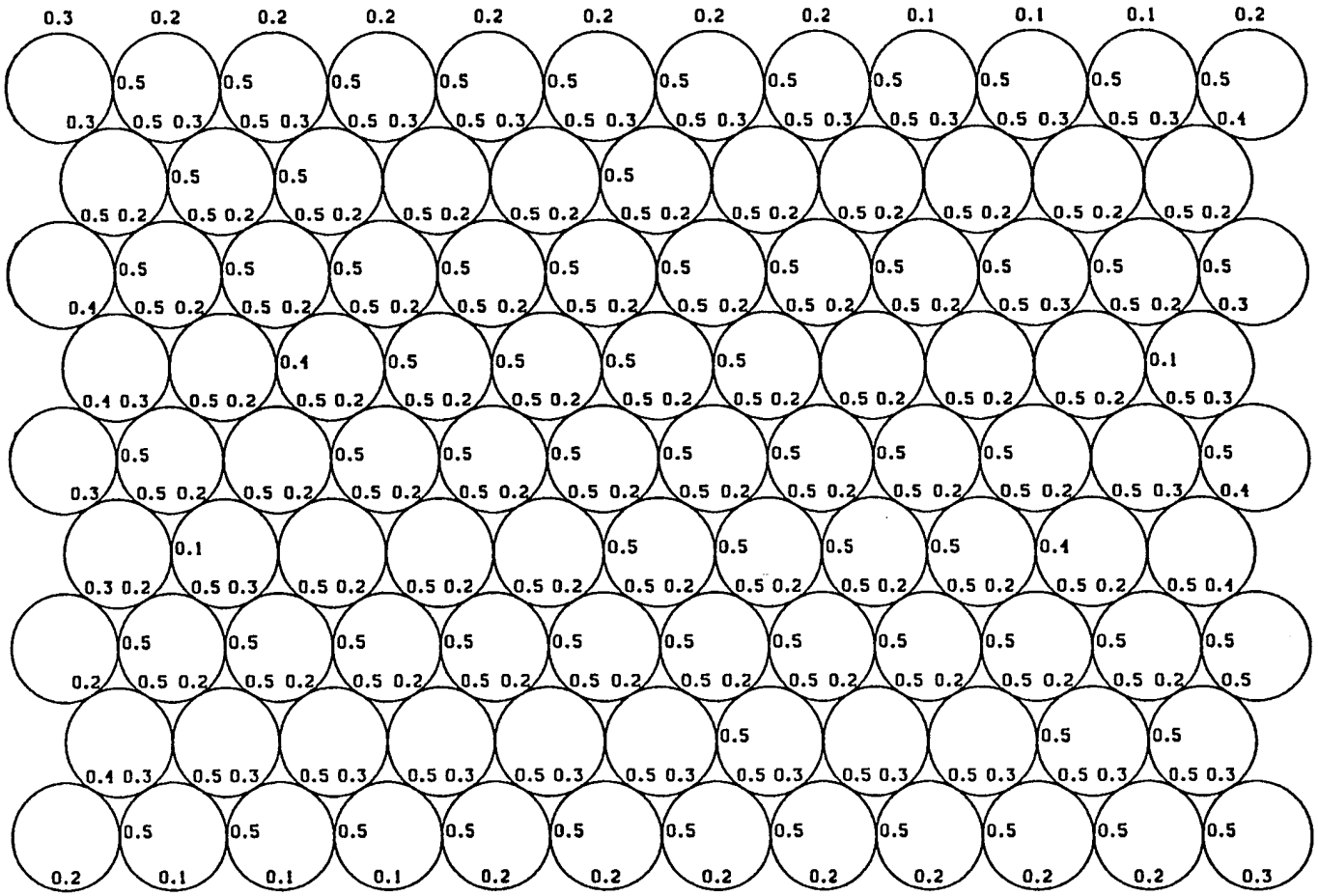

Fig. 4.11b Shear stress ratios at contacts for dense packing at γ = 0.01 %

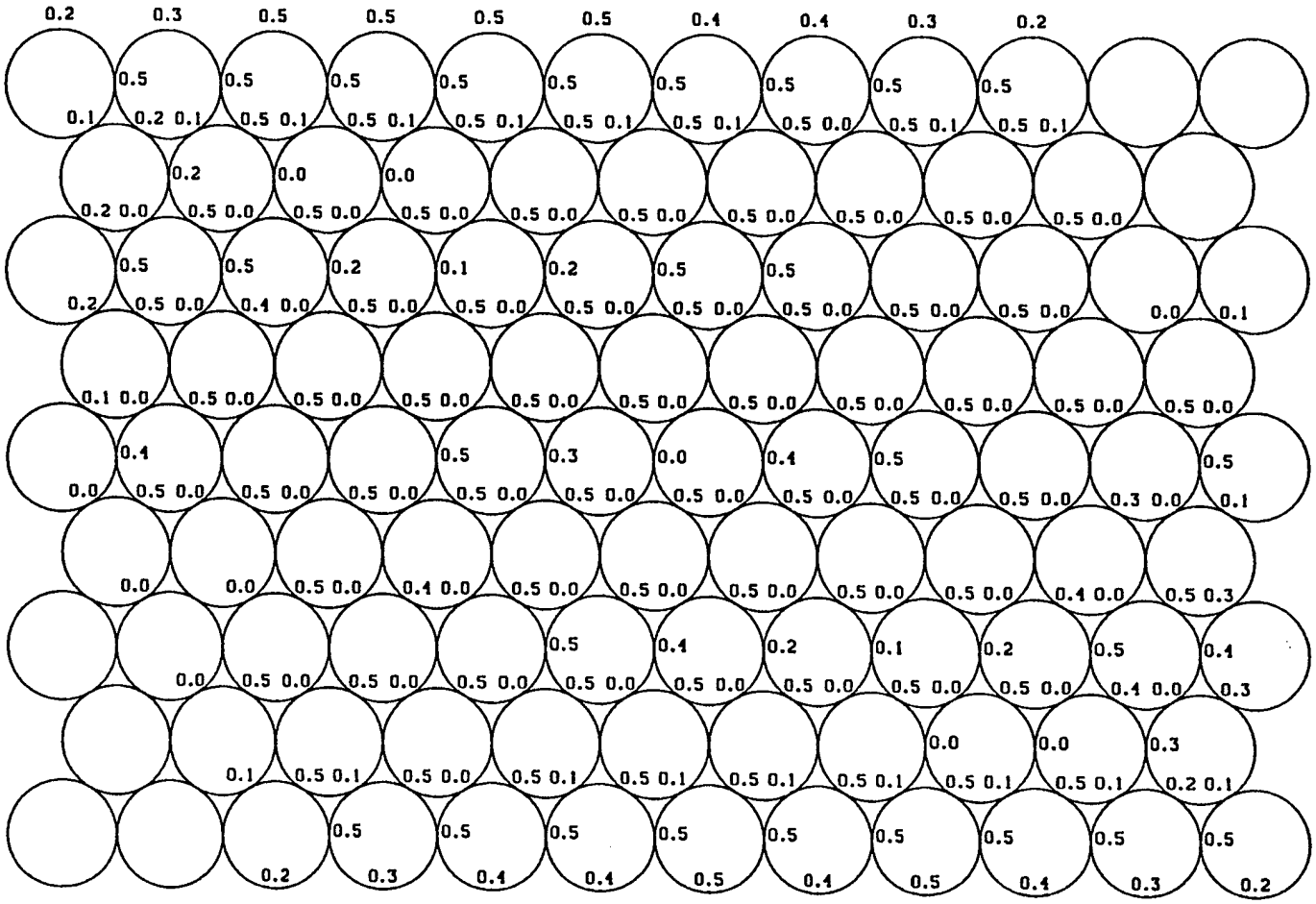

Fig. 4.11c Shear stress ratios at contacts for dense packing at γ = 0.03 %

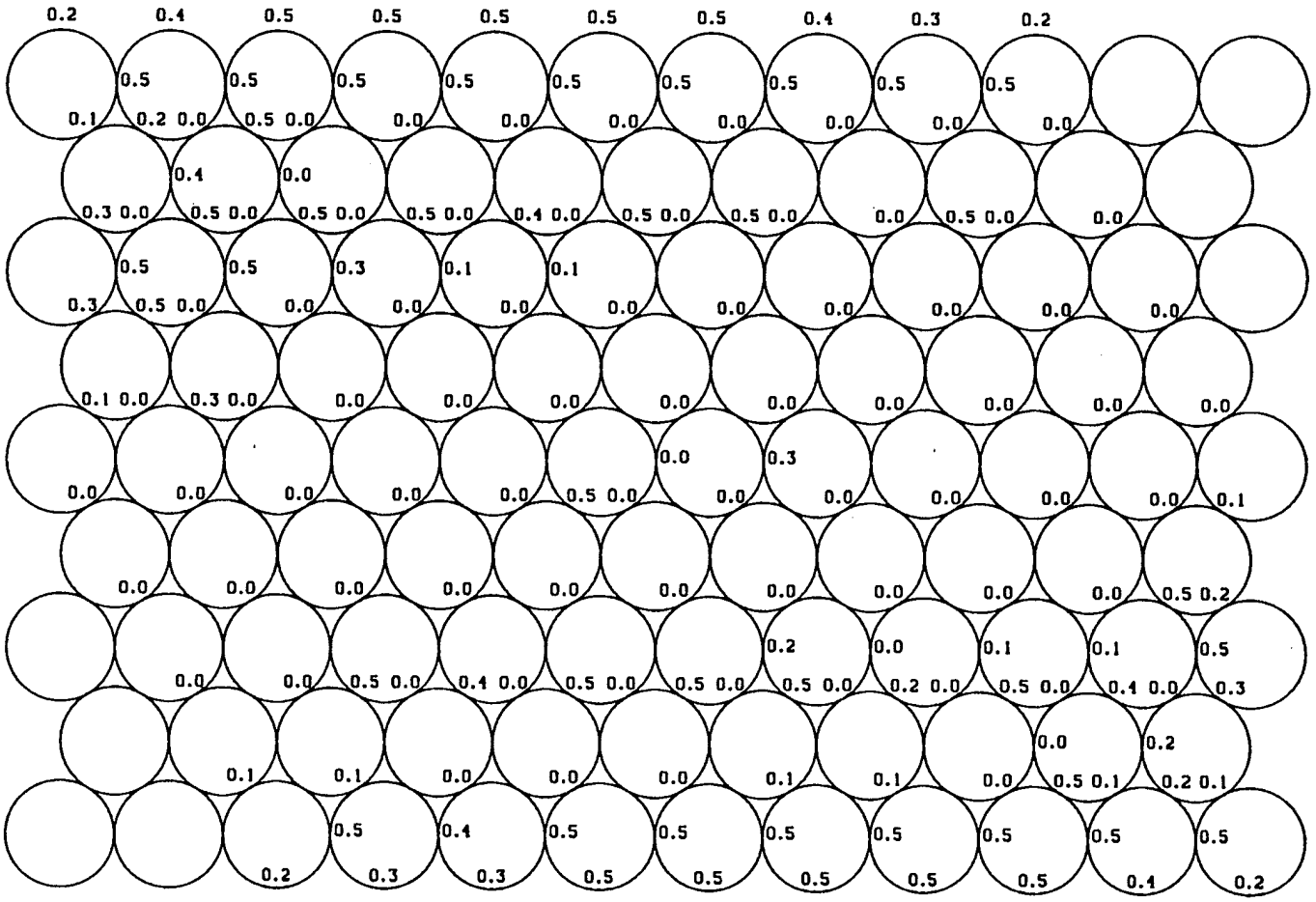

Fig. 4.11d Shear stress ratios at contacts for dense packing at γ = 0.04 %

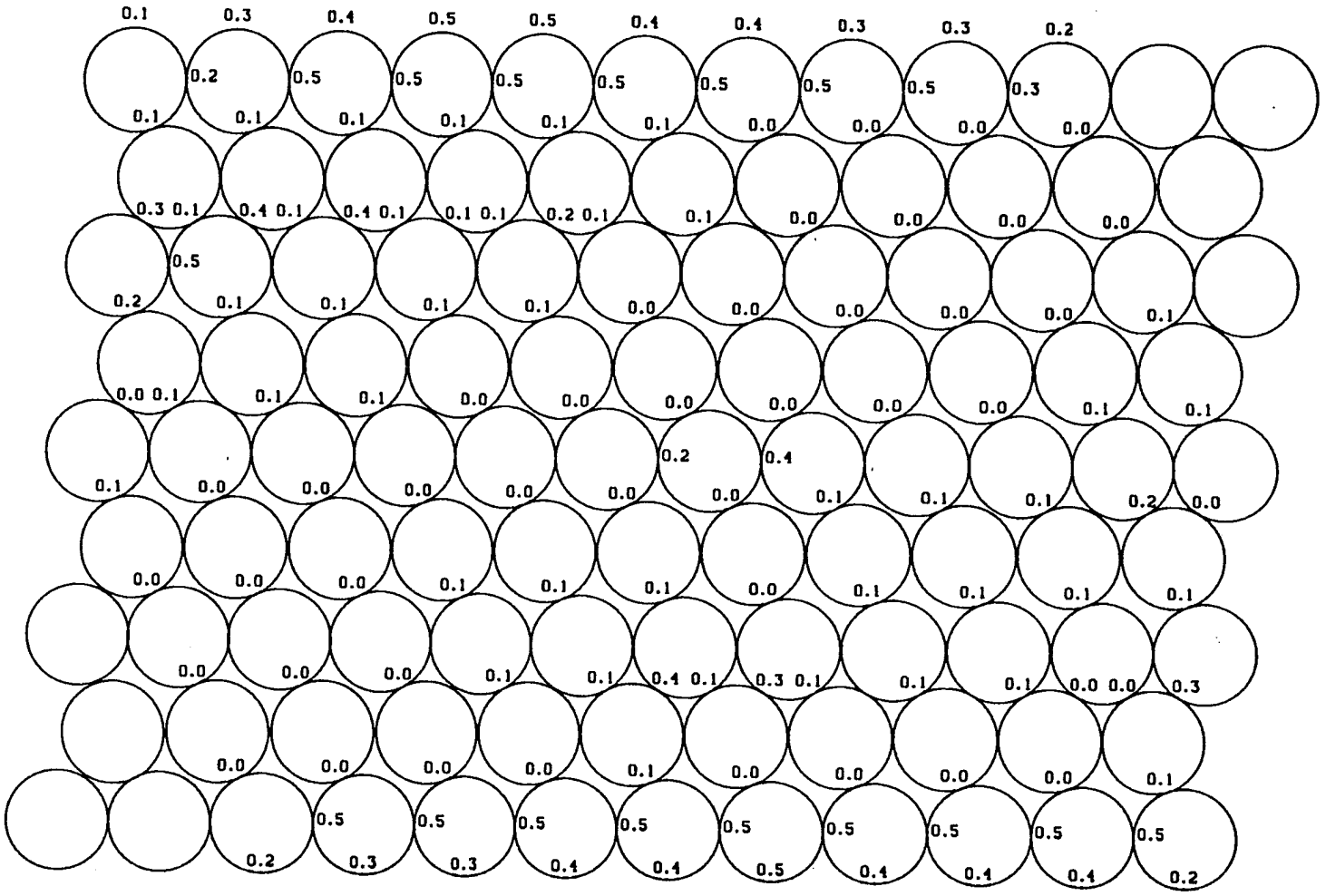

Fig. 4.11e Shear stress ratios at contacts for dense packing at γ = 10 %

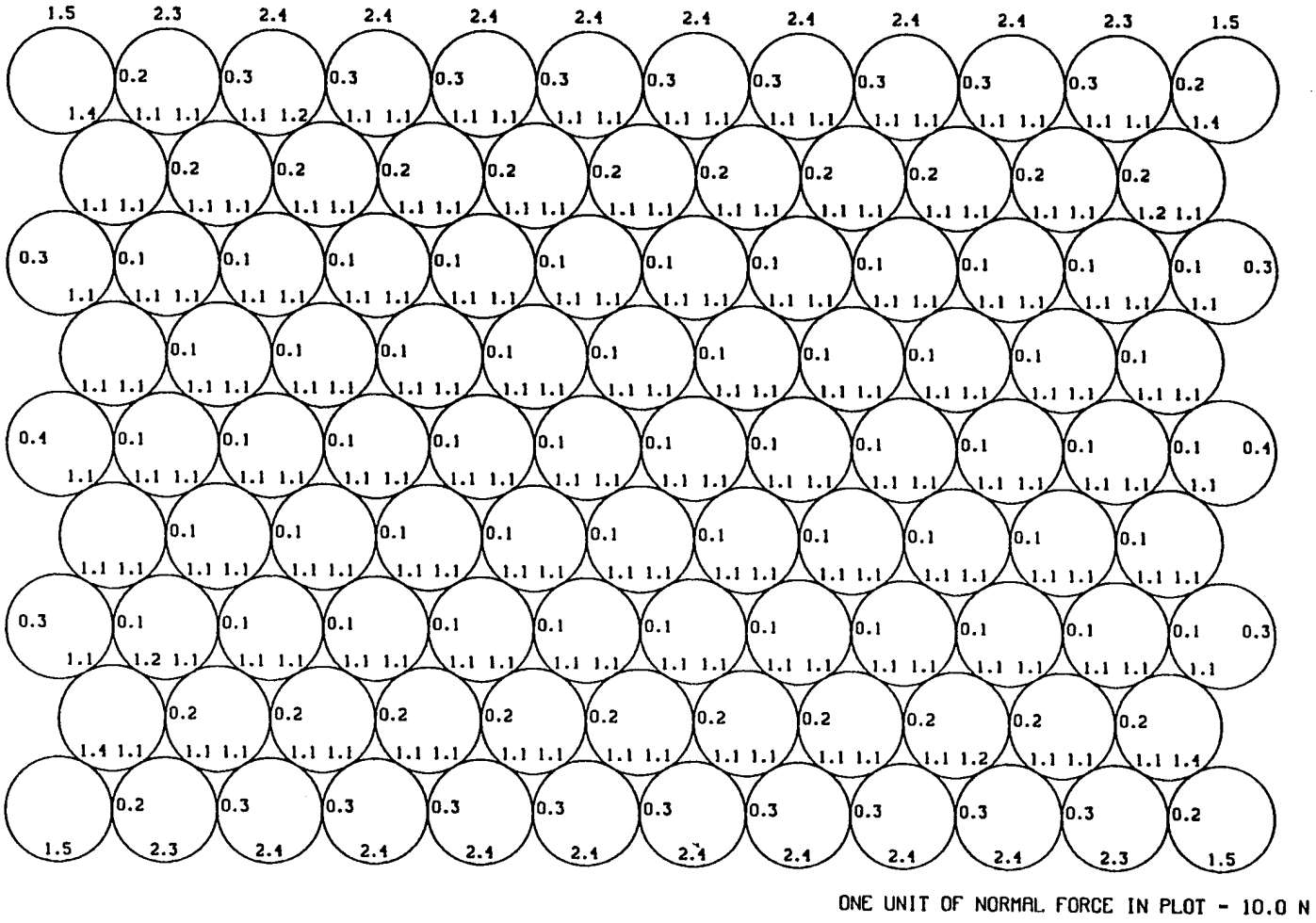

Fig. 4.12a Normal forces at contacts for dense packing under vertical load

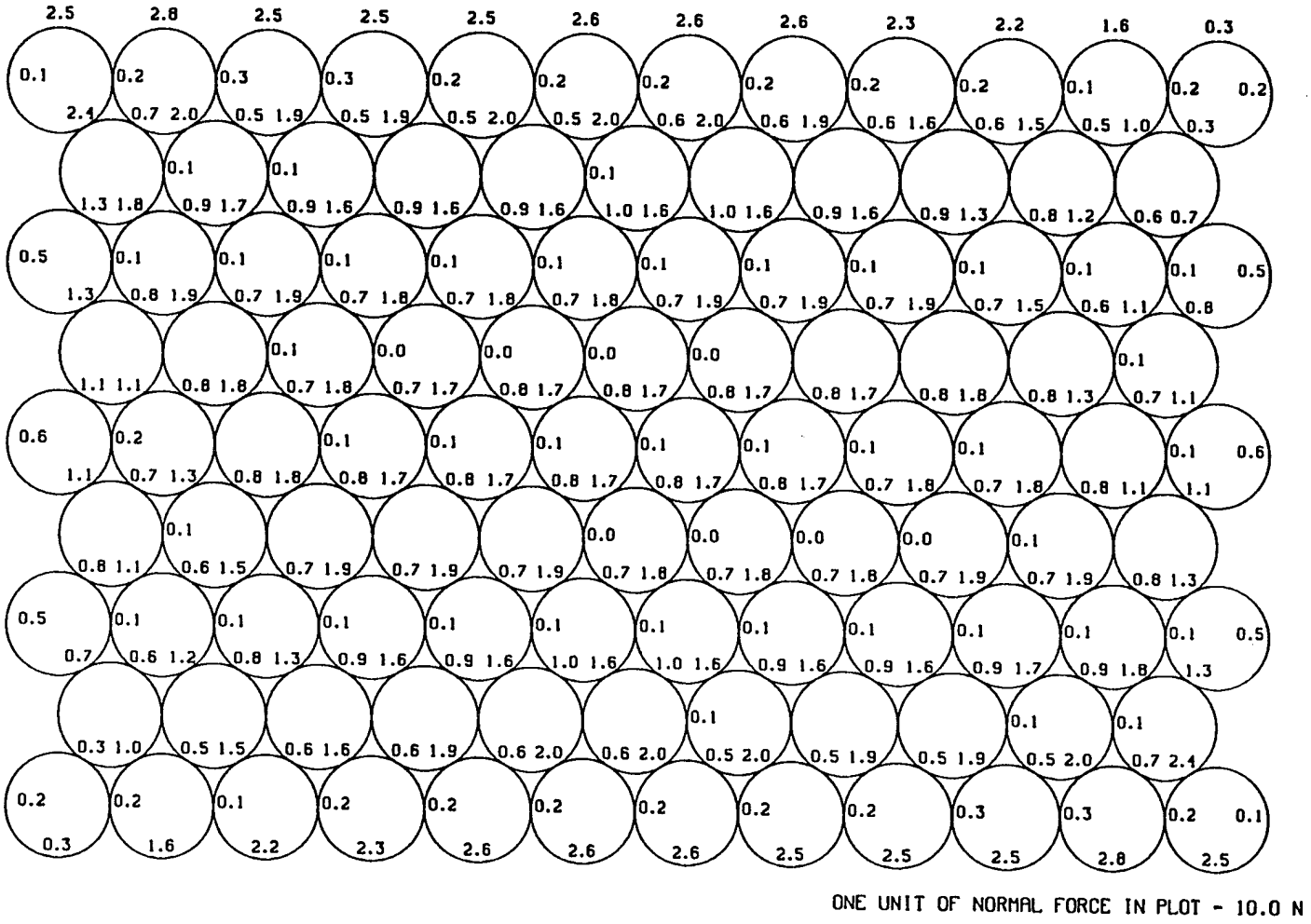

Fig. 4.12b Normal forces at contacts for dense packing at $\gamma = 0.01\%$

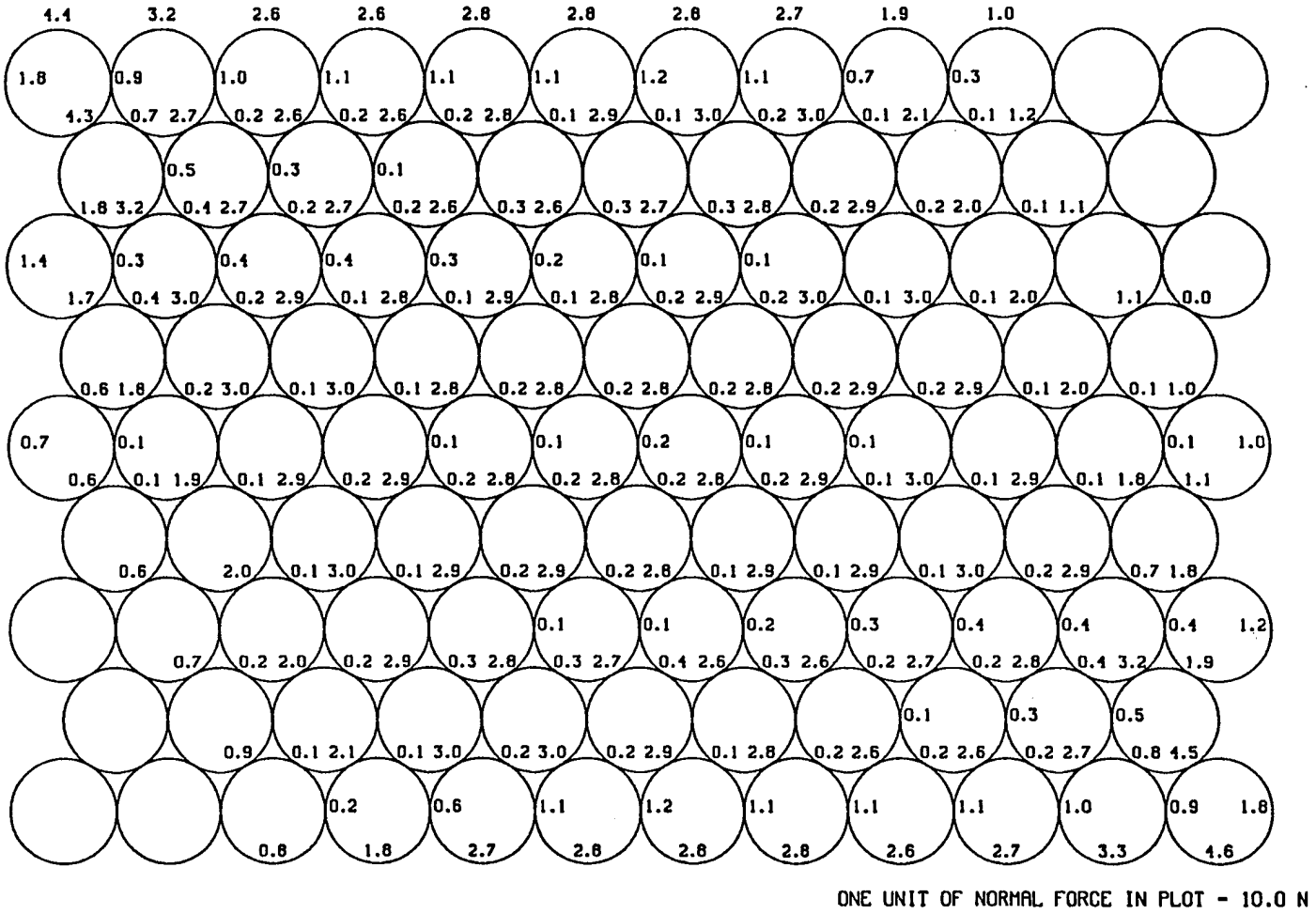

Fig. 4.12c Normal forces at contacts for dense packing at γ = 0.03 %

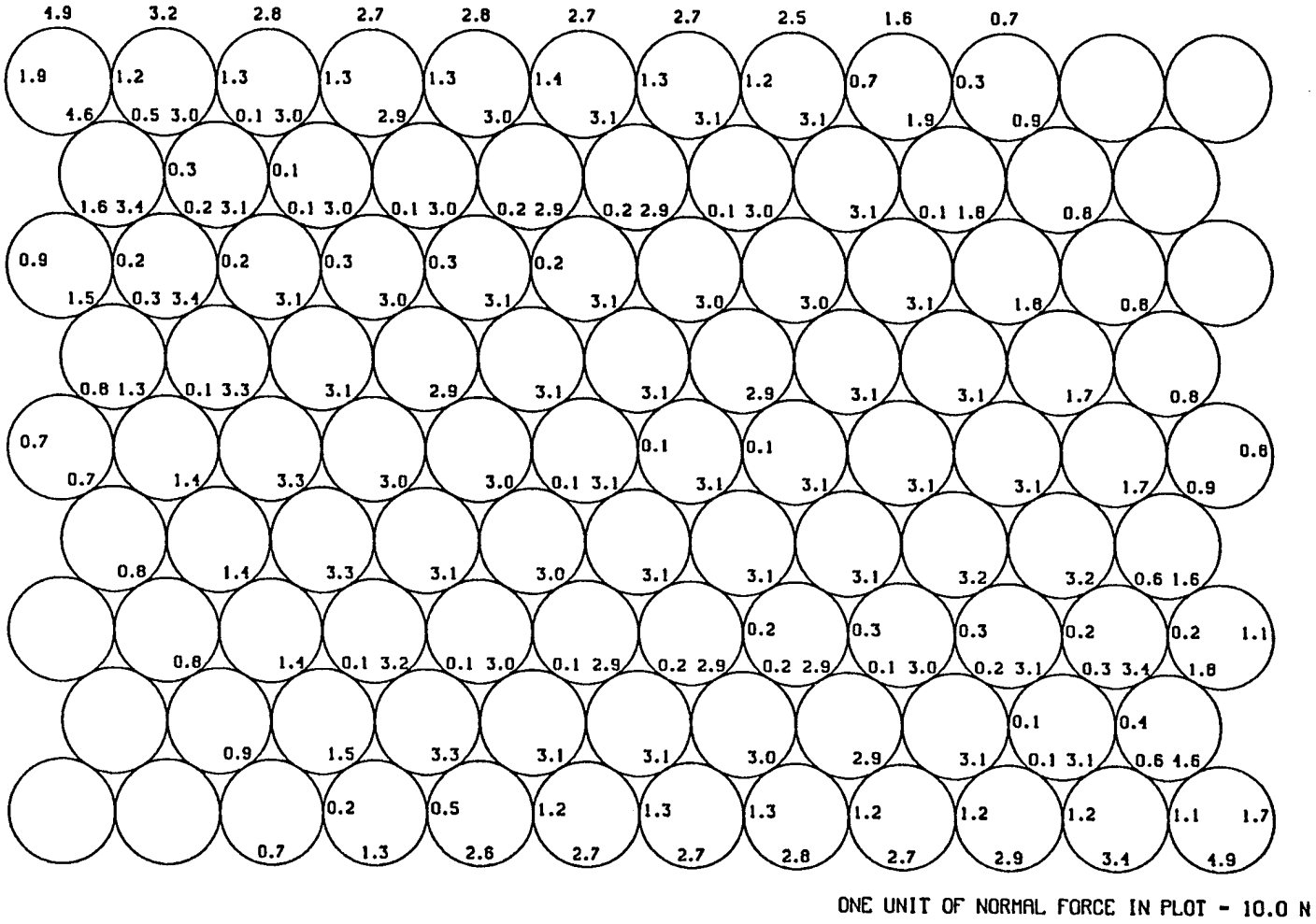

Fig. 4.12d Normal forces at contacts for dense packing at $\gamma = 0.04$ %

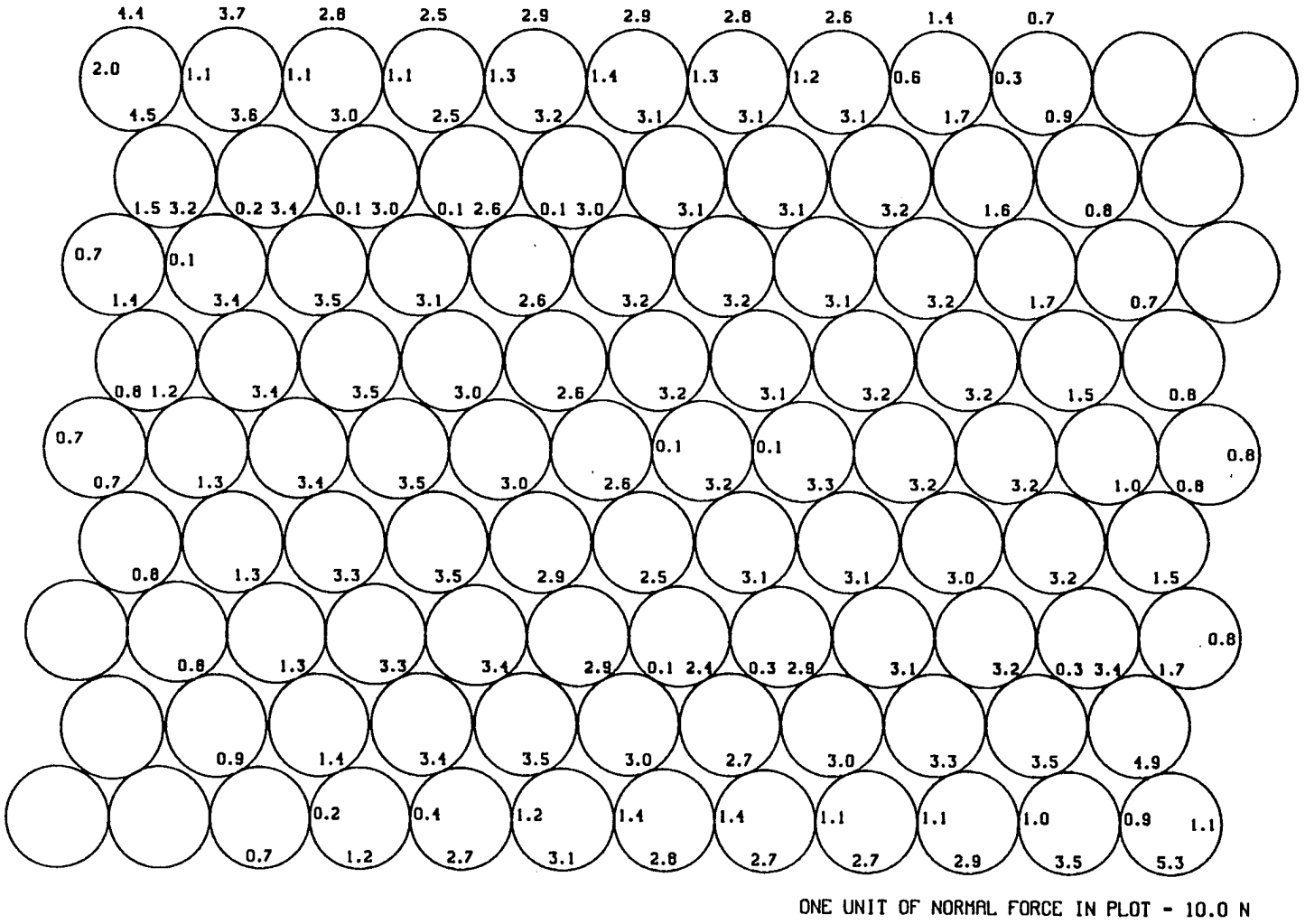

Fig. 4.12e Normal forces at contacts for dense packing at γ = 10 %

subjected to a simple shear strain has to dilate in order to undergo a deformation. The shear stress ratios under vertical load in Fig. 4.11a shows that (n-2) contacts are sliding in most of the particles where 'n' is the number of contacts around a particle. However, there is no mechanism at this stage as the material can carry deviatoric stress as will be seen in the stress-strain behavior later. Also, the constraint ratio computed under such condition is 1.7 which is far greater than one, a condition for the presense of a mechanism. An examination of Figs. 4.11a, 4.11b and 4.11c shows the progress of shear stress ratios leading to sliding contacts at the contacts on vertical planes. A comparison of Figs. 4.12a and 4.12b shows that the first step is the loss of contacts aligned along the lines D1-D1, D2-D2, D3-D3 and D4-D4. It can also be seen that the normal forces along the line of contacts parallel to line AA increase from 11.0 N to an average value of 18.0 N, while the normal forces along the line of contacts parallel to line BB decreases from 11.0 N to an average value of 8.0 N. In summary, Figs. 4.12a, 4.12b and 4.12c shows the increase or decrease of normal forces leading to stronger contacts or bondless nodes.

Through the above mentioned transformations, the assembly develops into a mechanism at a shear strain of 0.04%. Further deformations are simulated through the mechanism frameworks shown in Figs. 4.13a, 4.13b, 4.13c and 4.13d at various shear strains.

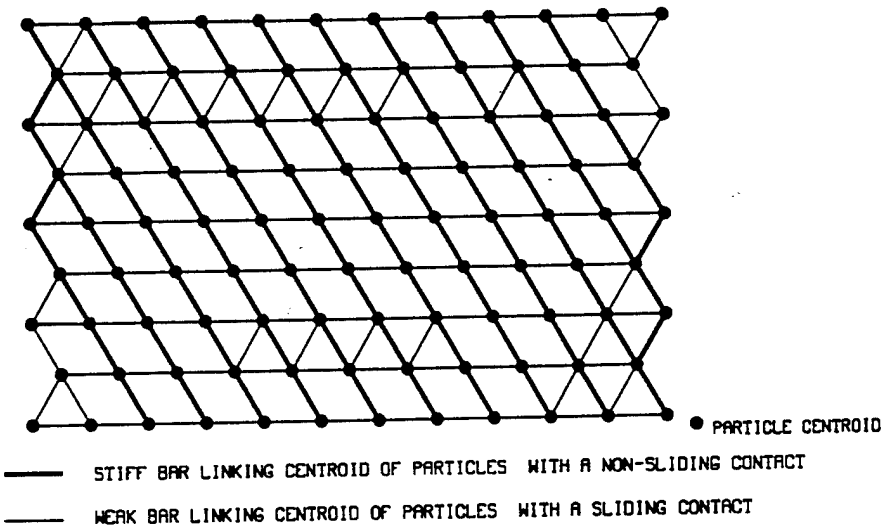

(a)

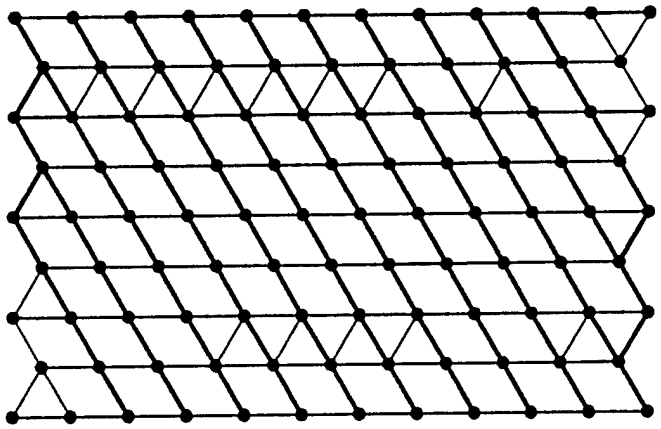

(b)

Fig. 4.13a,b Mechanism frameworks for dense packing at (a) γ = 0.04 % (b) γ = 1 %

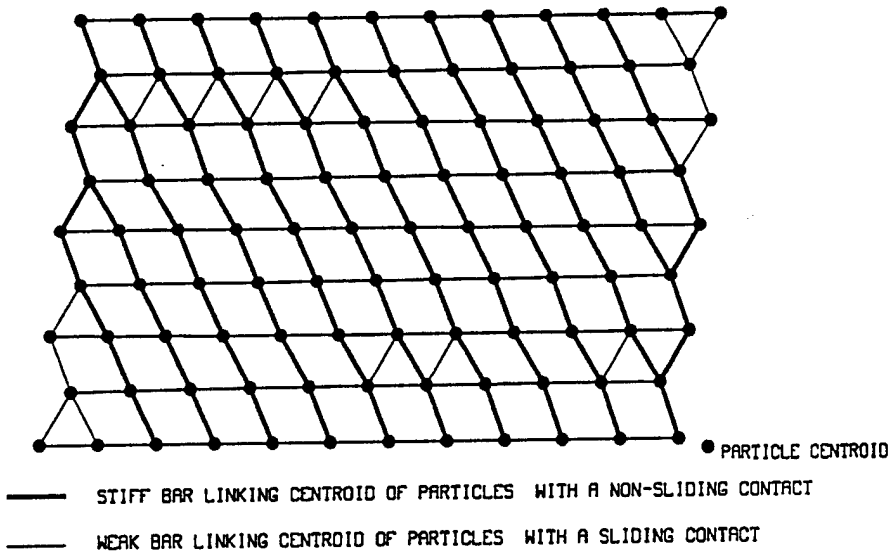

(c)

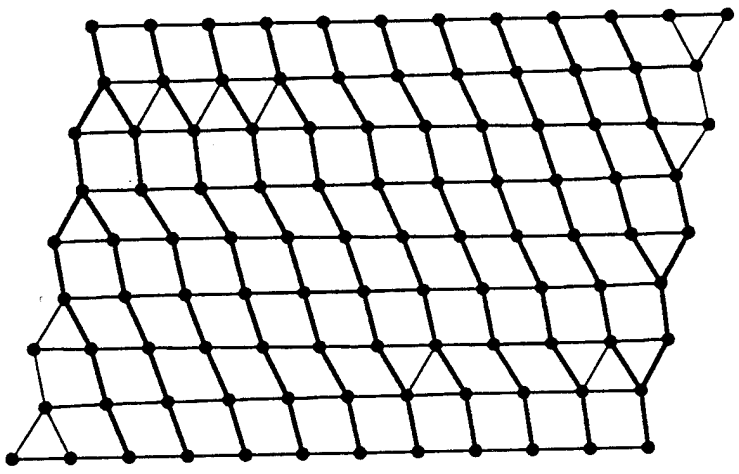

(d)

Fig. 4.13c,d Mechanism frameworks for dense packing at
(c) γ = 10 % (d) γ = 20 %

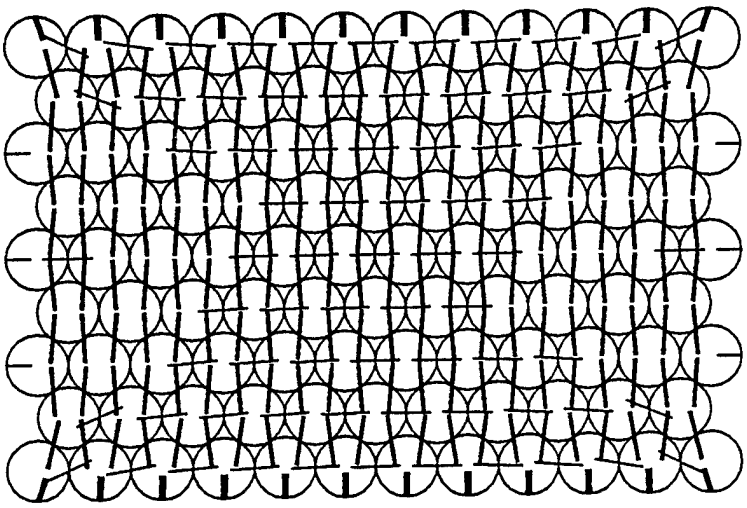

MAXIMUM CONTACT FORCE - 24.038 N

(a)

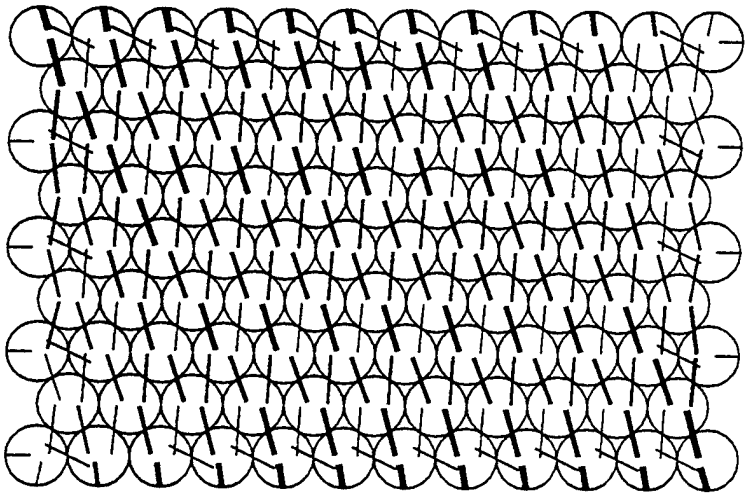

MAXIMUM CONTACT FORCE - 28.069 N

(b)

Fig. 4.14a,b Vector plot of contact forces for dense packing under (a) vertical load (b) γ = 0.01 %

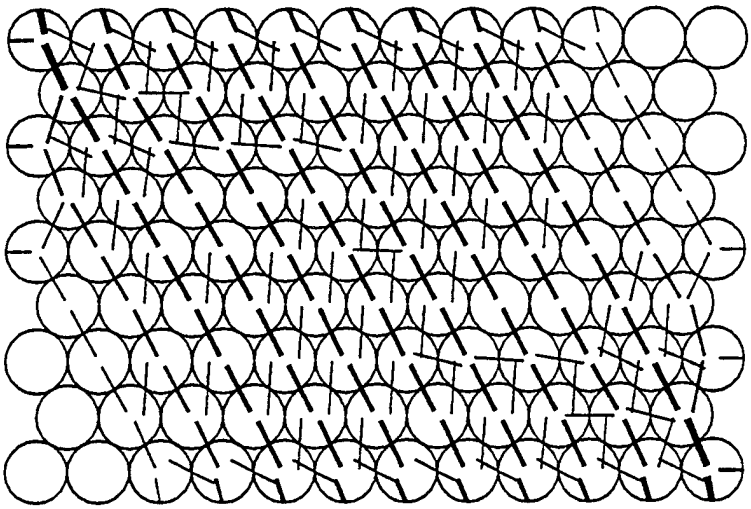

MAXIMUM CONTACT FORCE - 47.179 N

(c)

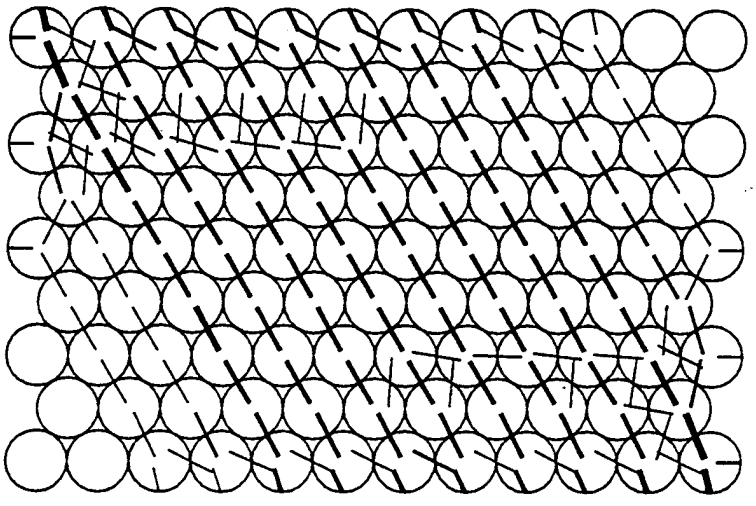

MAXIMUM CONTACT FORCE - 50.248 N

(d)

Fig. 4.14c,d Vector plot of contact forces for dense packing under (c) γ = 0.03% (d) γ = 0.04 %

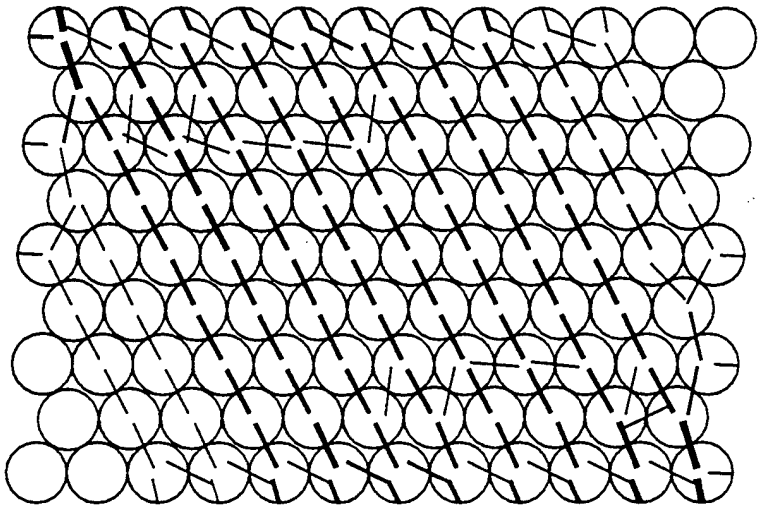

MAXIMUM CONTACT FORCE - 52.865 N

(e)

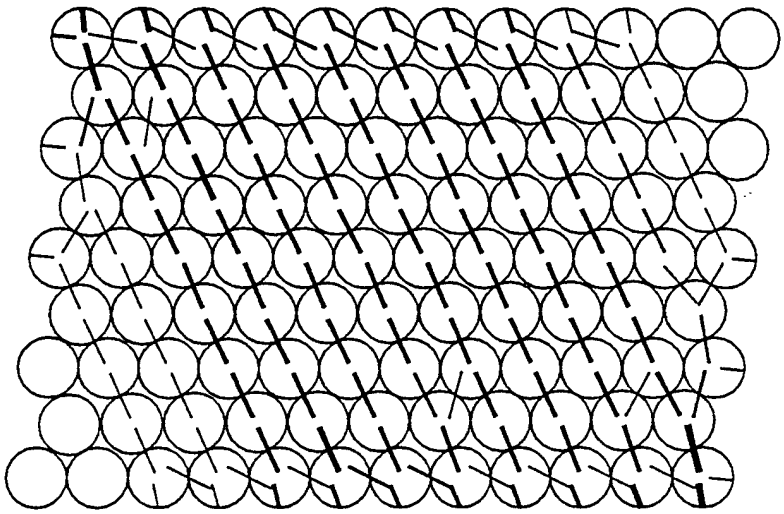

MAXIMUM CONTACT FORCE - 53.608 N

(f)

Fig. 4.14e,f Vector plot of contact forces for dense packing under (e) γ = 5 % (f) γ = 10 %

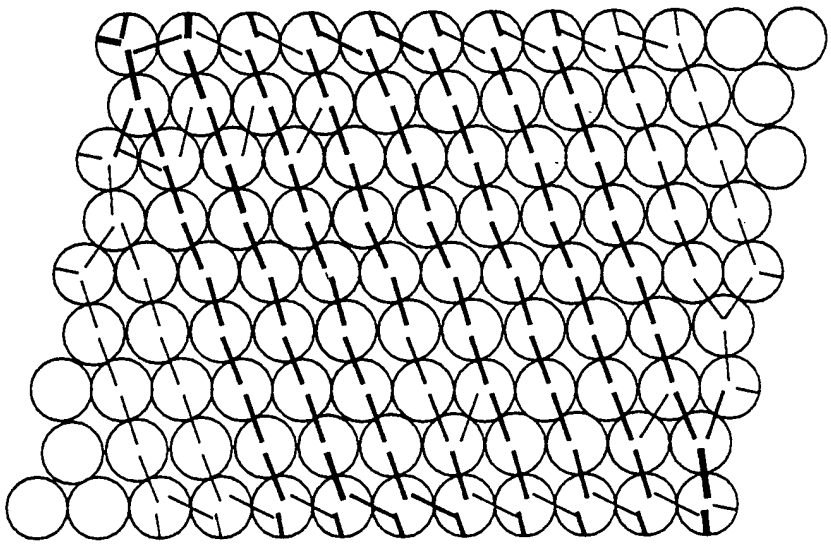

MAXIMUM CONTACT FORCE - 53.249 N

(g)

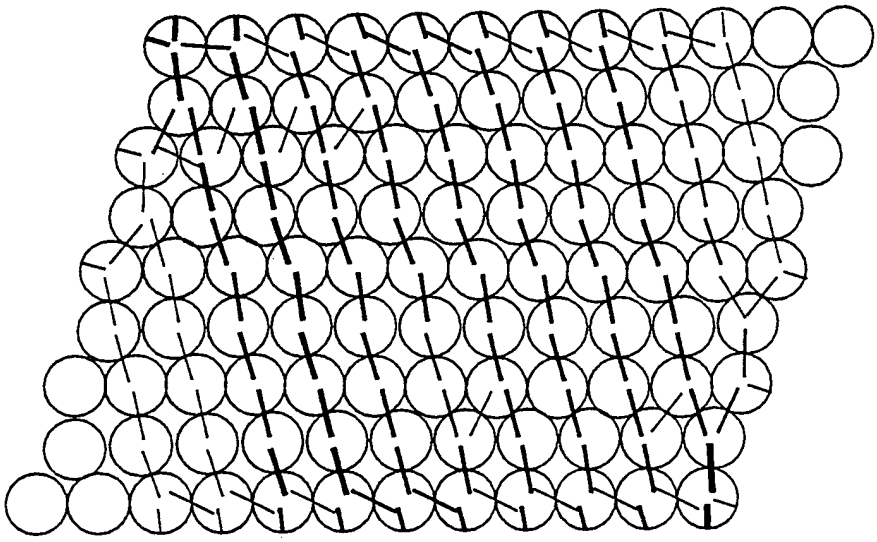

MAXIMUM CONTACT FORCE - 51.832 N

(h)

Fig. 4.14g,h Vector plot of contact forces for dense packing under (g) γ = 20 % (h) γ = 30 %

The load path or contact force flow over a range of shear strains is shown in Fig. 4.14a through Fig. 4.14h. Fig. 4.14a shows that larger loads flow predominantly in the vertical direction under the initial vertical load. Under the application of a shear strain of 0.01%, the path of the larger loads immediately tilts towards line AA (Fig. 4.14b) and at a shear strain of 0.04% the load path within the middle region of the central core is confined to paths along line AA (Fig. 4.14d). The magnitude and orientation of the contact forces at a large shear strain of 30% in Fig. 4.14h shows that certain particles are not in equilibrium. This is due to the accumulation of errors due to numerical approximations discussed in Chapter. 3 and also due to the mechanism framework not giving the correct position of the particles at very large shear strains.

An analysis of the variation of shear stress ratios between the initial vertical load (Fig. 4.11a) and a shear strain of 0.01% (Fig. 4.11b) shows that the line of contacts parallel to line AA changes from sliding to non-sliding contacts, which could be attributed to the increase in normal force at these contacts. However, the line of contacts parallel to line BB continues to be sliding contacts and this is caused by the decrease in normal forces at these contacts. The line of contacts along C1-C1, C2-C2 etc., which were originally non-sliding contacts, changes to sliding contacts. This is due to the mobilization of shear forces along these contacts as it can be seen from Figs. 4.12a and 4.12b that there is no significant change in the normal forces. The tranformations in contact forces and the fabric

changes from the initial vertical load to a shear strain of 0.04% can be summarized as follows:

- Stress-free zones develop at top right and bottom left corners of the particle assembly (Fig. 4.12d)
- Normal forces along the line of contacts parallel to line AA have doubled from the initial values (Fig. 4.12d).
- Line of contacts parallel to line BB become bondless nodes.
- Contacts along C1-C1, C5-C5 and at the interface between the rows of particles along C4-C4 and D4-D4 and along C2-C2 and D1-D1 remain as sliding contacts.
- Considerable reduction in the number of bonded contacts when shear strain reaches 0.04% (Fig. 4.12d).

A comparison of Fig. 4.11a with Fig. 4.11b shows the development of void spaces between particles along the column of particles parallel to line BB. However, the contacts along lines C2-C2, C3-C3, C4-C4 and D1-D1, D2-D2, D3-D3, D4-D4 remain as "stick and slip" contacts. The development of sliding and bondless contacts shows that the failure mechanism is brought about by the rotation of particles in a column-like arrangement along with sliding interfaces with their neighboring columns.

4.8.3 Distribution of normal and shear forces at boundaries

The variation of normal forces and shear forces at the bottom and top boundaries are shown in Figs. 4.15a and 4.15b respectively. The distribution of normal forces along the left and right boundaries is shown in Fig. 4.16 at various shear strains. The following observations are made from these graphs:

- The normal forces at the bottom boundary, decreases near the left boundary and becomes zero at high shear strains, then gradually increases to the middle region, then remains constant in the middle third region and then increases in the remaining one third region towards the right boundary. The variation at the top boundary follows a similar pattern from right to left.
- The normal forces on the left boundary follow a variation close to a linear path with zero at the bottom and increasing to a maximum value at the top. The variation on the right boundary follows a similar pattern from top to bottom.
- The shear forces at the bottom boundary is zero at the left end, increases gradually to the middle region and tend to remain constant.

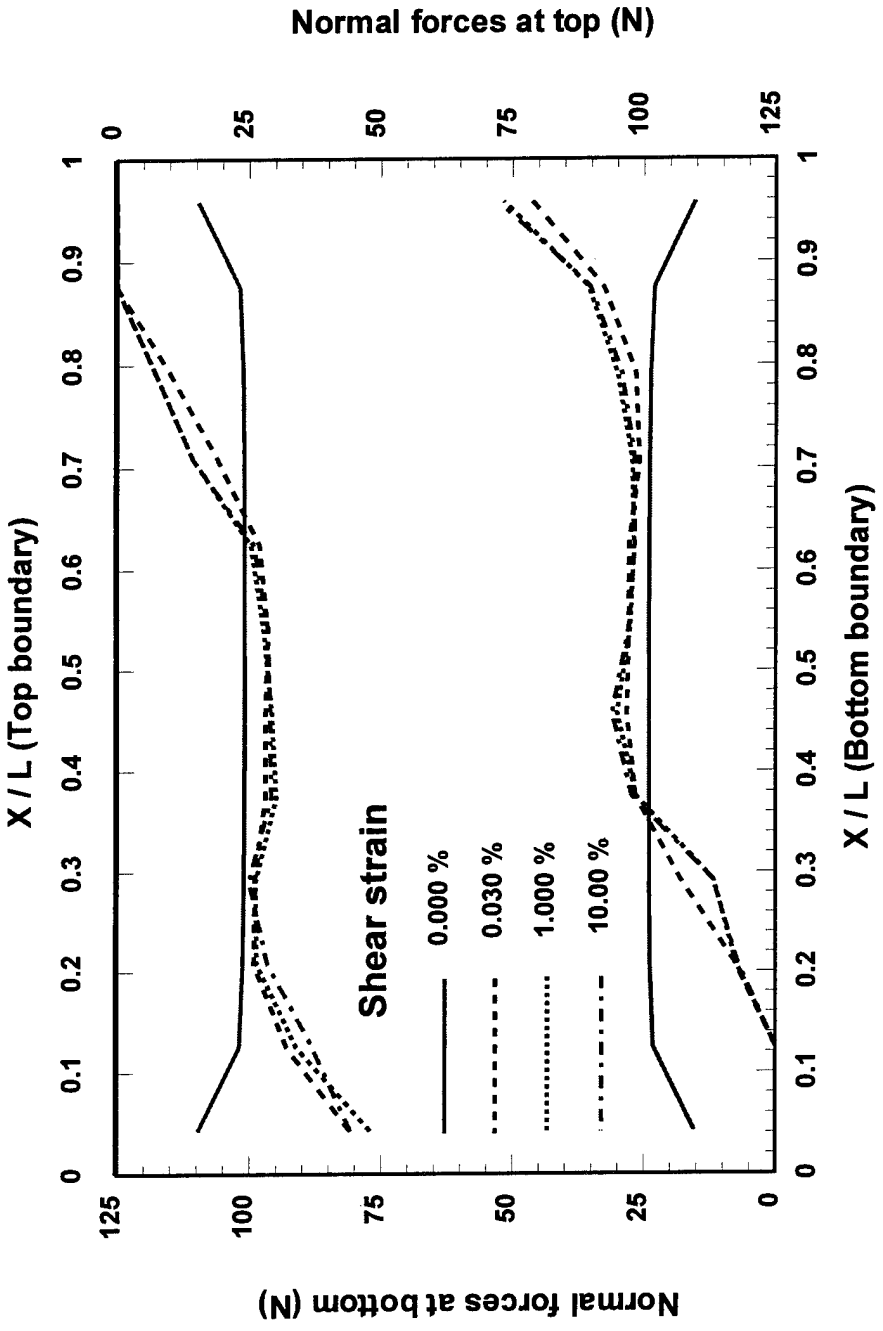

Fig. 4.15a Distribution of normal forces on the top and bottom boundaries for the dense packing

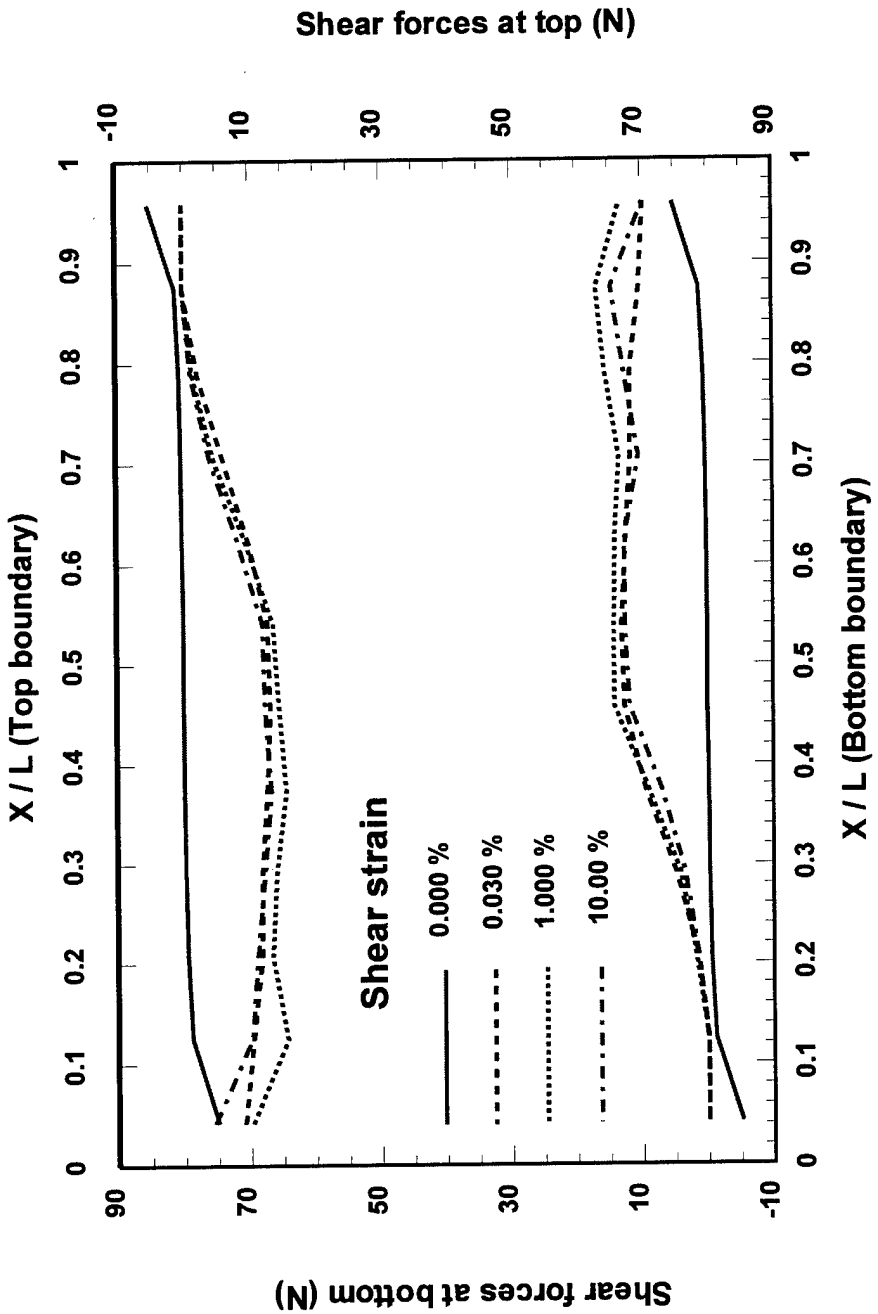

Fig. 4.15b Distribution of shear forces on the top and bottom boundaries for the dense packing

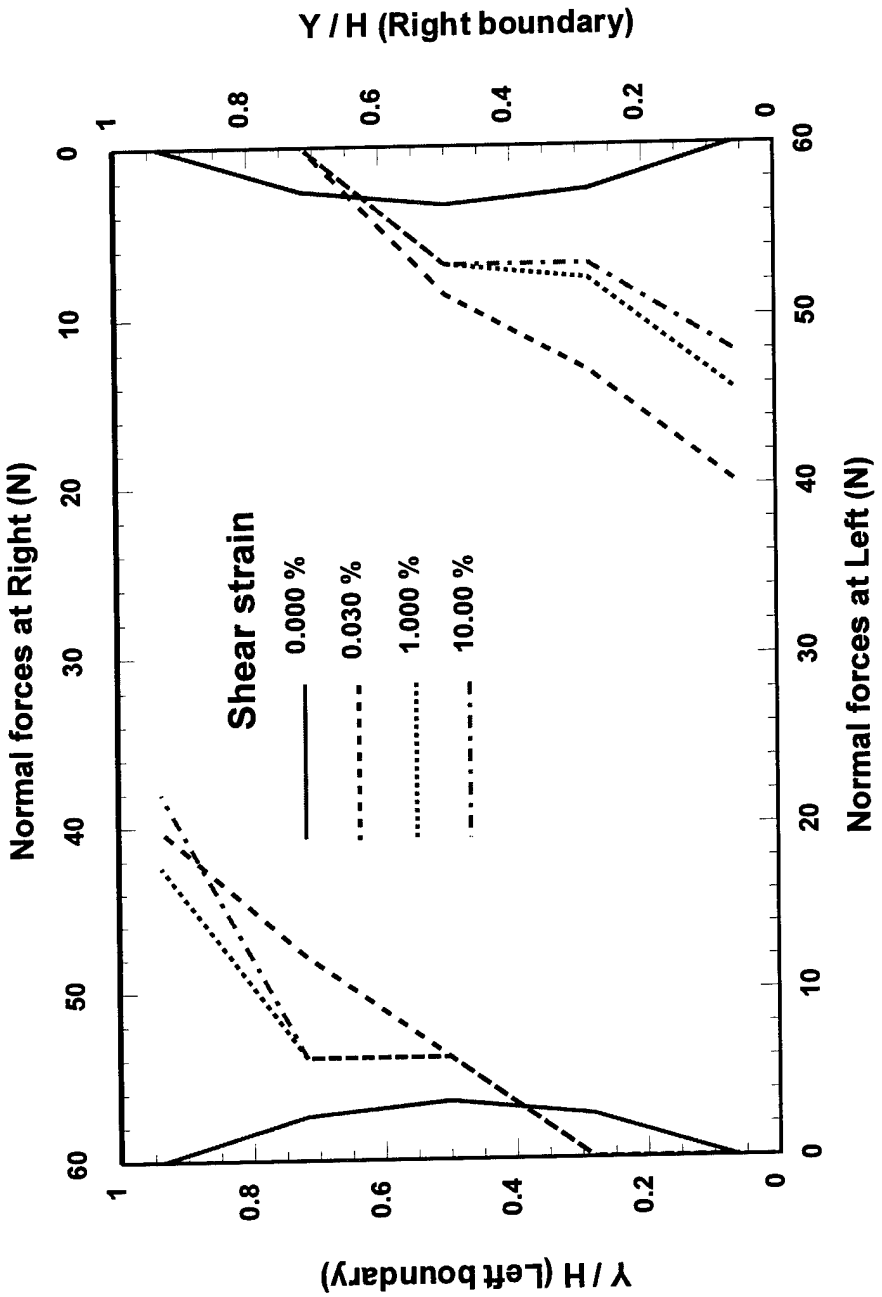

Fig. 4.16 Distribution of normal forces on the vertical boundaries for the dense packing

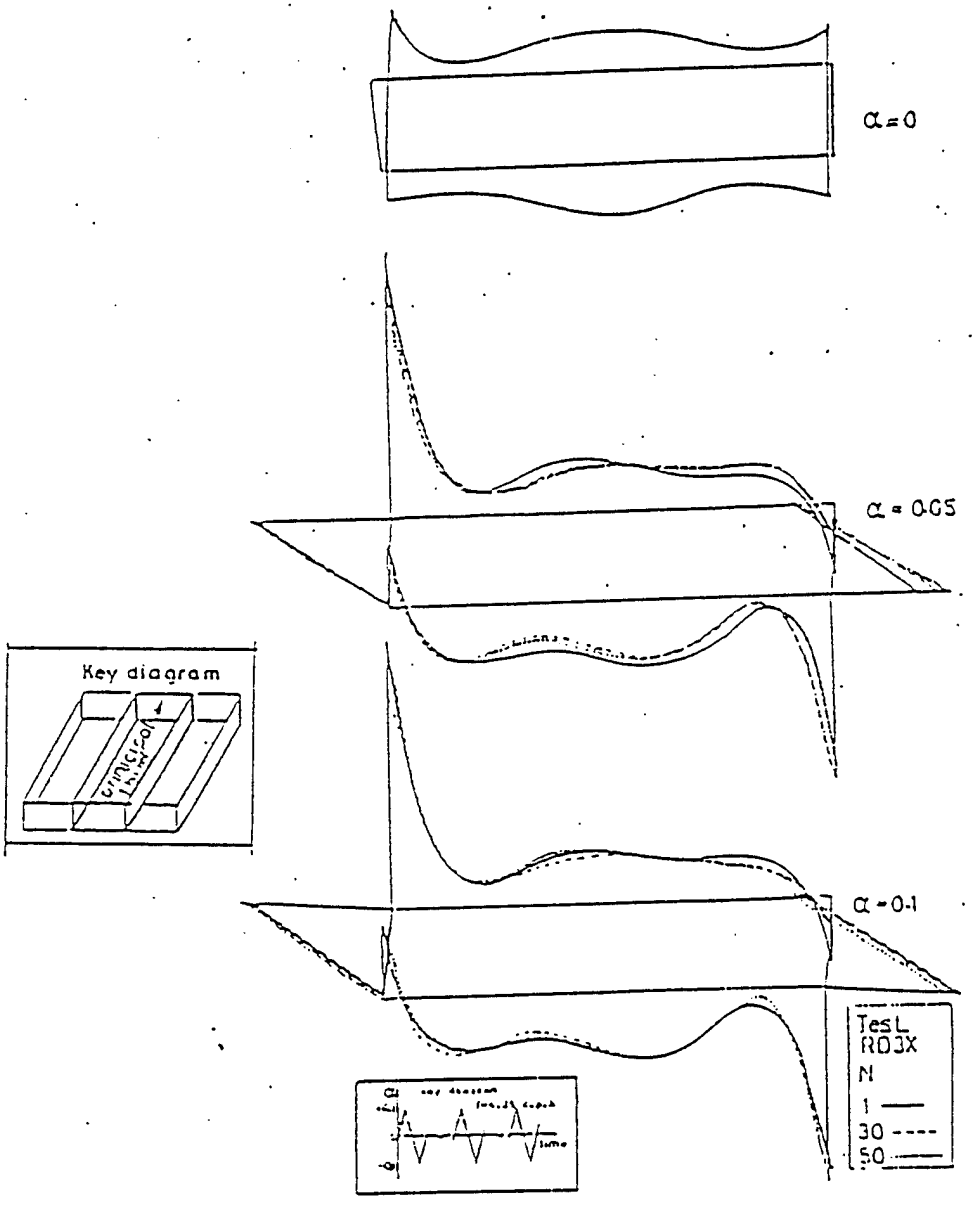

Fig. 4.17 Development of normal stresses during cyclic simple shear tests (Budhu, 1979)

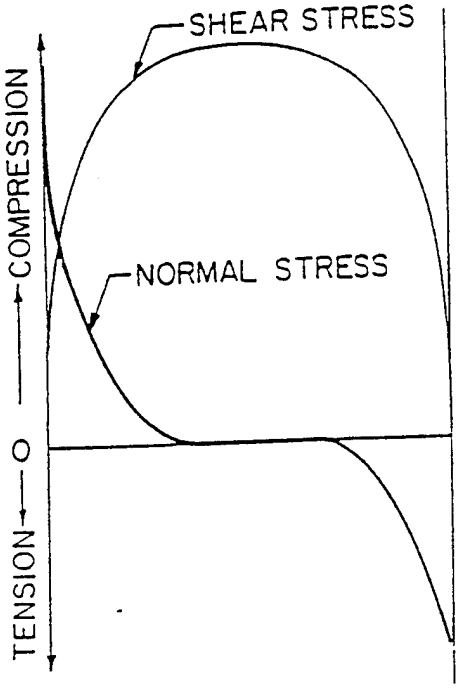

Fig. 4.18 Distribution of stresses in simple shear from elastic analysis (Roscoe, 1953)

The above observations are qualitatively in agreement with the distribution of normal stresses existing at boundaries in simple shear tests on sands (Budhu, 1979) shown in Fig. 4.17.

The normal and shear force distributions at the bottom boundary in Figs. 4.15a and 4.15b indicate that even though non-uniform states of stress prevail at the boundaries, conditions in the middle of the particulate assembly are uniform. Roscoe (1953) analyzed an elastic material deforming in the Cambridge simple shear apparatus using Airy's stress function. He showed that even though the stresses and strains on the boundaries of the sample as a whole may not be uniform, conditions in the middle third of the sample perpendicular to the direction of shear can be expected to be uniform. Thus the observations from the lattice type model are in agreement with results of Roscoe's analysis shown in Fig. 4.18.

4.8.4 Fabric changes, displacement fields and volume change behavior

From the deformation patterns shown in Figs. 4.14a through 4.14h, some relationships can be evolved between the fabric changes, displacement fields and volume change behavior. The displacement fields are shown in Figs. 4.19a, 4.19b and 4.19c at shear strains of 0.01%, 5% and 20% respectively. The variation of volumetric strain defined as the change in volume over the initial volume is

(a)

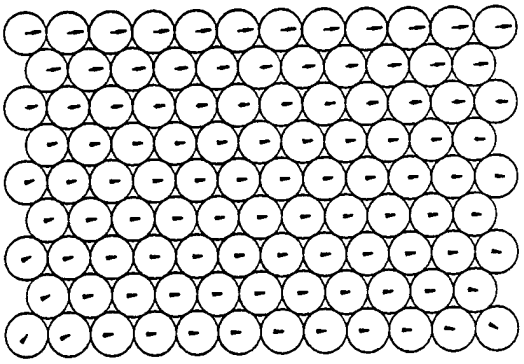

(b)

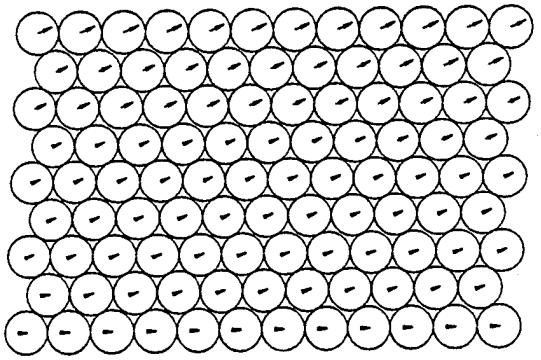

(c)

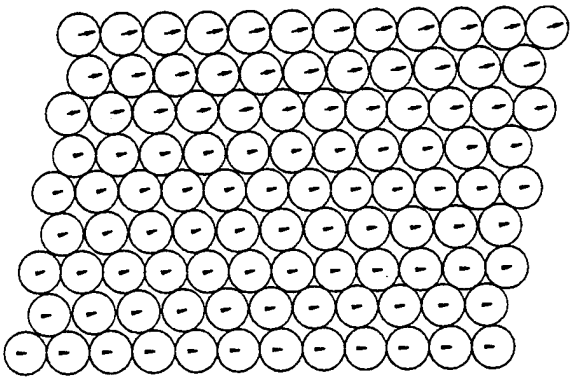

Fig. 4.19a,b,c Displacement fields for dense packing at
(a) $\gamma = 0.01\%$ (b) $\gamma = 5\%$ (c) $\gamma = 20\%$

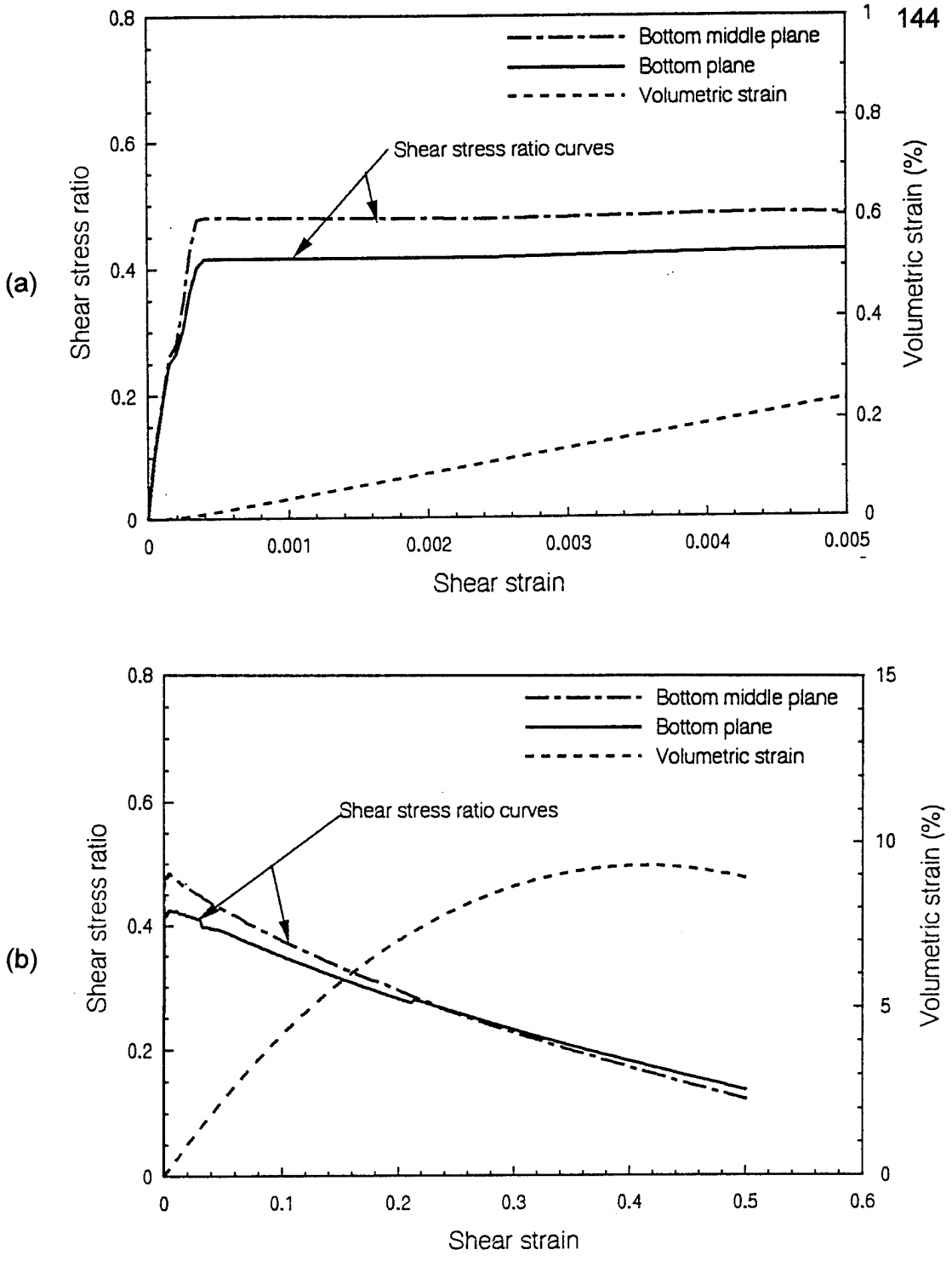

Fig. 4.20 Variation of shear stress ratio at bottom and volumetric strain for dense packing

(a)

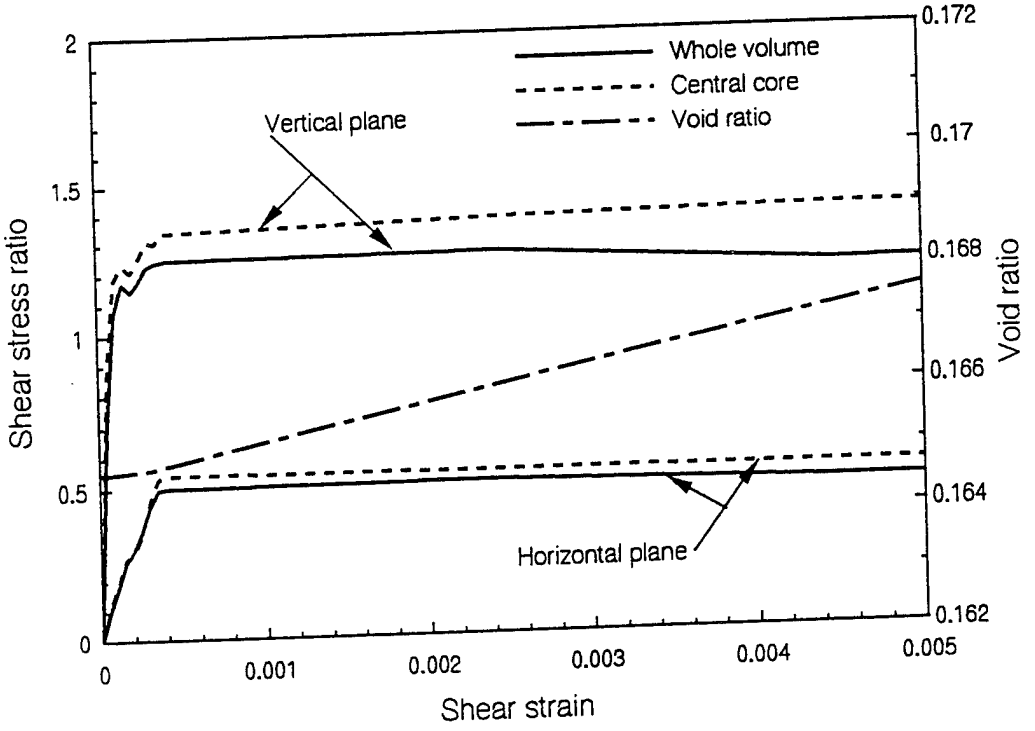

(b)

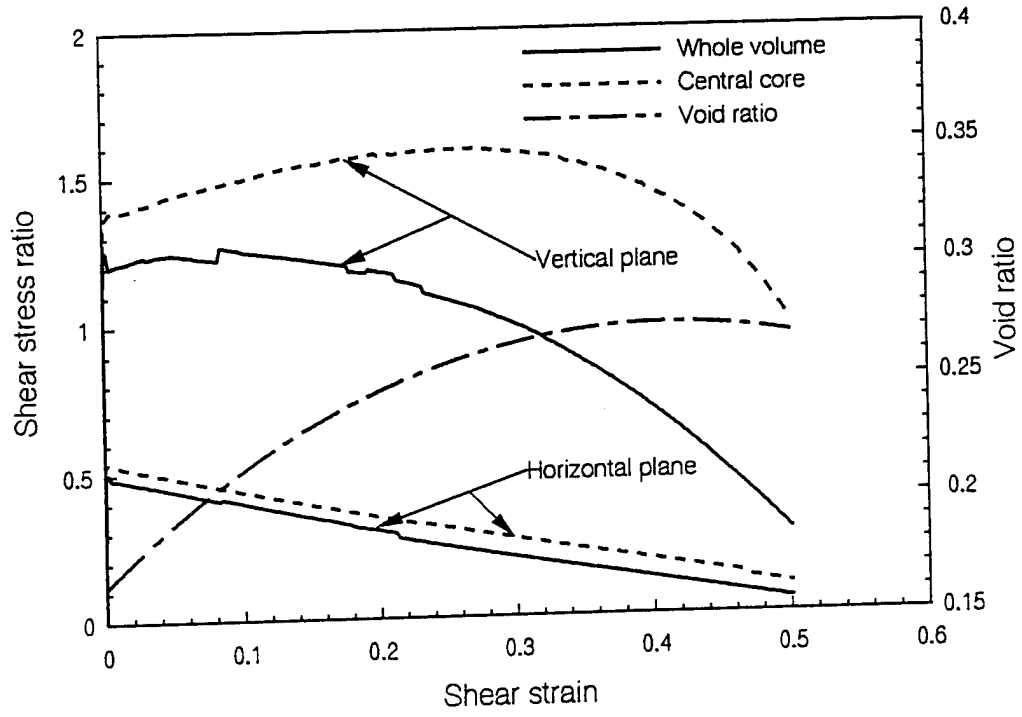

Fig. 4.21 Variation of shear stress ratios on vertical planes and horizontal planes and void ratio for dense packing

shown in Fig. 4.20a over a shear strain less than 0.5% and in Fig. 4.20b at large shear strains. The variation of void ratio is shown in Figs. 4.21a and 4.21b.

The volumetric strain and the void ratio curves show that the material dilates as expected for dense granular materials and the overall behavior from the two curves can be summarized as follows:

- $\gamma \leq 10\%$ - Linear.
- $10\% > \gamma \leq 30\%$ - Convex curves with a decreasing slope.
- $30\% > \gamma \leq 50\%$ - Volumetric strain and void ratio tends to remain constant.
- The void ratio of the dense packing changes from an initial value of 0.165 to a final value of 0.275 at shear strain 50%.
- The final void ratio of 0.275 is almost equal to 0.276, the initial void ratio of the loose packing which implies that the dense packing has transformed into a loose packing.

The major observations from the displacement fields (Figs. 4.19a,b,c) are that the displacements are predominantly:

- in the X-direction at a very low shear strain of 0.01%.
- in the Y-direction at an intermediate shear strain of 5%.
- in X-direction at a very large shear strain of 20%.

The fact that there is a steep rise in the volumetric strain until a shear strain of 10% is explained by the above variation of the displacement fields from a shear strain of 0.01% to 5%. The reason for the decrease in slope of the

volumetric strain curve is explained by the tranformation in the displacement fields from a shear strain of 5% to 20%. Thus, at large shear strains, the displacement fields have a larger component in the X-direction and at very large shear strains, the Y-component of the displacement fields become zero and thus the material ceases to dilate.

The displacement fields which influence the volumetric strain are in turn influenced by the fabric changes shown in Figs. 4.14a through 4.14h. The fabric changes are caused by the mechanism frameworks shown in Figs. 4.13a through 4.13d. A comparison of Figs. 4.13a,b,c shows that the chain of particles with strong bonds represented by the strong bars rotate about the base of the packing resulting in a large component of displacement in the Y-direction when the mechanism framework is subjected to a deformation. However, it is to be noticed that at a large shear strain of 20% (Fig. 4.13d) the above process has not continued and the strong chains can be seen to collapse. This collapse mechanism is explained with respect to Fig. 4.13d.

The collapse is caused by the preference of certain group of particles, to stay in contact or in "stick and slip contact", in certain regions. A general statement was made earlier that the fabric changes take place in such a way that void spaces are developed between particles along line BB. However, this is not true for certain region. Consider the row of particles D1-D1 and C2-C2 in the right half of the particle assembly and the row of particles D4-D4 and C4-C4 in

the left half of the particle assembly (Fig. 4.14g). Here a void space is not developed between the particles aligned along line BB. Now, comparing the mechanism frameworks in Figs. 4.13c and 4.13d, it is clear that the above row of particles have only translated in the X-direction. However, it is to be noticed that particles along the row D2-D2 have rotated with respect to the particles along row C2-C2 (Fig. 4.13d). Similar rotations can be seen in the top left regions also. Comparing the initial position of the particles and their positions at shear strain 30%, the rotations of the particles are as high as 30^0. Therefore, the conclusion of the above discussion is that it is this collapse mechanism that results in the retardation of the volumetric strain at high shear strains.

4.8.5 Shear stress ratio-shear strain behavior

The shear stress ratio-shear strain relationship for the dense packing at a shear strain less than 0.5% is shown in Fig.4.20a. Two curves are shown for the shear stress ratio-shear strain relationship. One is the ratio of the arithmetic average of the shear forces and normal forces over the entire bottom boundary while the other is for the middle one third of the bottom boundary. The reason for this choice is that the shear and normal forces are not distributed uniformly at the top and bottom boundaries and a uniform distribution prevails only in the middle third of the boundary (Figs. 4.15b and 4.15b). Thus, the average forces

normally measured by load transducers in laboratory tests at the bottom boundary are likely to be different from the average forces at the middle of the bottom boundary. This is confirmed in Figs. 4.20a where the middle gives a higher shear stress ratio (about 10%-15%) than the entire bottom boundary. In Fig. 4.20a, a "kink" can be seen in the curves at a shear strain of 0.02% which is caused by a large number of contacts becoming bondless.

The shear stress ratio-shear strain relationship at large strains is shown in Fig. 4.20b. Using continuum analogy, the general response can be summarized as follows:

- $\gamma \leq 0.02\%$ - Linear elastic.
- $0.02\% > \gamma \leq 0.04\%$ - A quasi-linear curve.
- $0.04\% > \gamma \leq 0.50\%$ - Perfectly plastic.
- $\gamma > 0.50\%$ - Strain softening.

The volumetric strain curve in Fig. 4.20b shows that in the range of shear strain from 30% to 50%, the volumetric strain tends to remain constant. This shows that the material shows a tendency to reach a sort of "critical state" at 30% shear strain. If the material has reached "critical state" at the shear strain of 30%, the stress-strain curve is expected to become horizontal. Even though this behavior is not seen, the stress-strain curves show a tendency to flatten.

Hill's averaging principle was used to transform the discrete set of contact forces on the boundaries to an equivalent state of stress at the center of the

packing (Fig. 4.3b). For the purpose of comparative study, the average stresses are computed from the contact forces at the boundary of the, central core and the whole volume of the packing, and both the results are discussed. The shear stress ratios were found for the vertical planes (τ_{xy} / σ_{xx}) and for the horizontal planes (τ_{yx} / σ_{yy}). Two levels of shear strains are selected to illustrate the response at small shear strains, $\gamma < 0.5\%$ (Fig. 4.21a) and large shear strains, $\gamma > 0.5\%$ (Fig. 4.21b). The interpretation of the results can be summarized as follows.

(1) The shear stress ratio on the vertical planes increases much more rapidly and to significantly higher levels than on the horizontal planes. For the central core, the ratio of the shear stress ratio on the vertical planes to the horizontal planes is about "3" at the shear strain $\gamma = 0.04\%$, when a mechanism is reached for the first time.

(2) The central core of the assembly gives shear stress ratio on the vertical planes about 10% greater than the whole assembly at a shear strain of 0.04% and the difference increases at higher shear strains. This is reasonable because it was shown that the middle third of the particle assembly is uniformly stressed (Fig. 4.15b and 4.15b). The difference for the horizontal planes is also about 10%, but this difference continues until 50% shear strain. The above behaviors are perhaps due to the freedom of movement for particles in the vertical direction as compared with zero strains in the horizontal direction.

(3) The shear stress ratio on vertical planes increases and reaches a peak value

of 1.35 at a shear strain of 0.04%, which is higher than the coefficient of friction of the material. Beyond this shear strain, the ratio keeps increasing marginally (for central core) until a shear strain of 30%, when the material ceases to increase in volume. However in the range of shear strains 0.5% to 30%, the shear stress ratio on vertical planes for the whole volume marginally decreases. The behavior for the central core and whole volume are contrary to each other and this could be attributed to the fact that there is more mobility of the particles in the central core than at the boundaries. Beyond a shear strain of 30%, the shear stress ratio on vertical planes for the central core as well as the whole volume decreases sharply.

(4) The shear stress ratio on horizontal planes reaches a peak value of 0.50 and decreases at larger strains.

The observations described above are a result of the continuously changing situation concerning the stresses (Figs. 4.22a,b). While a constant vertical load is applied, the normal stresses and shear stress increases and reaches a peak value at a shear strain of 0.04%, when a mechanism is developed (Fig. 4.22a). At large shear strains, the normal stress on horizontal planes (σ_{yy}) increases marginally while the normal stress on vertical planes (σ_{xx}) and the shear stress decreases. The increase or decrease in the values of the stresses in the central core at the shear strain of 0.04% relative to the initial vertical load conditions is as follows. The normal stress σ_{yy} increases by 11% whereas σ_{xx} and τ_{xy} decreases by 65%

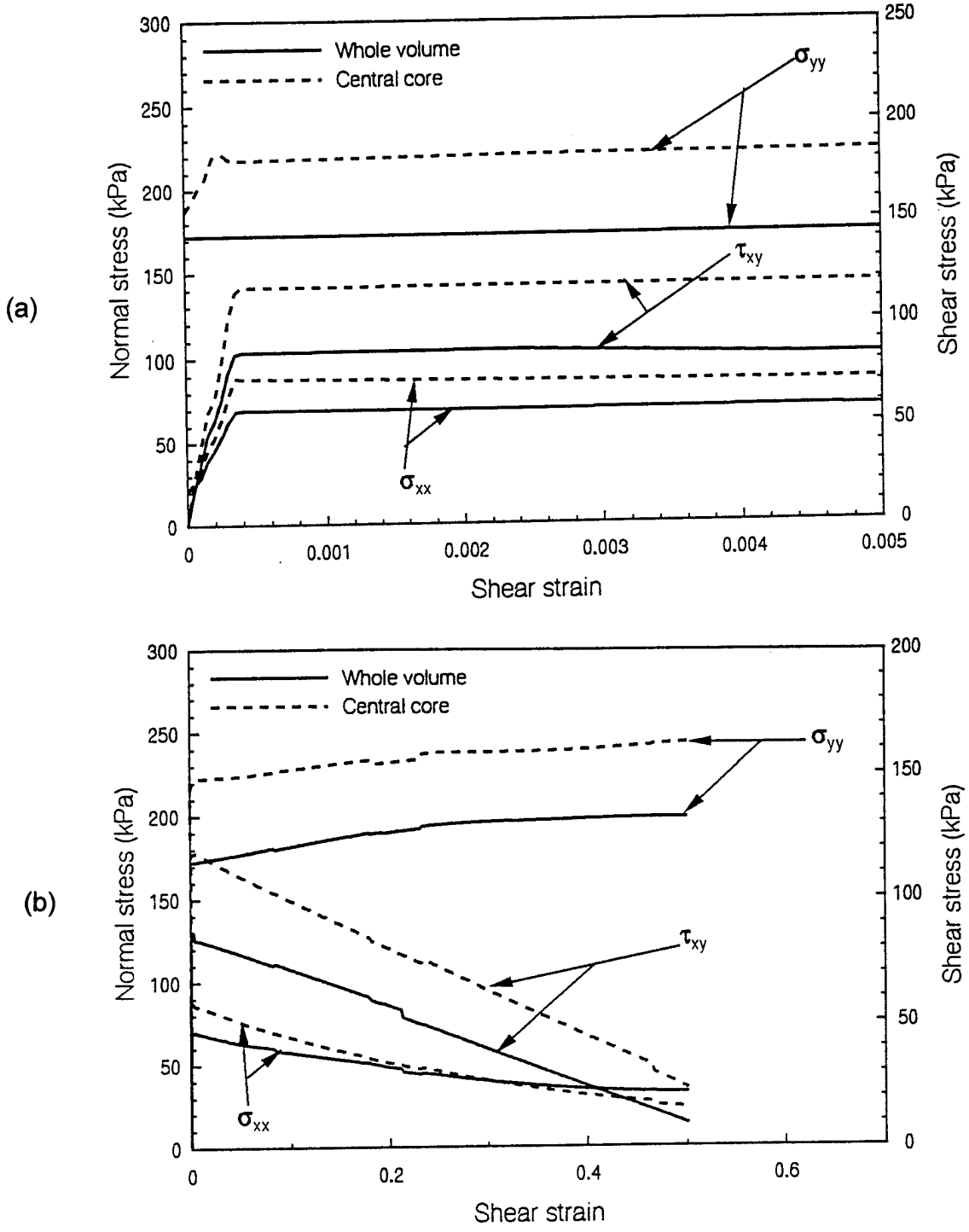

Fig. 4.22 Variation of normal and shear stresses for the dense packing

and 71% respectively. The contribution to σ_{xx} in the Hill's averaging principle comes from the lateral loads on the vertical boundaries. When the shear strain is increased, the component of the lateral load in the direction of X-axis decreases and therefore σ_{xx} decreases. Shear stress, τ_{xy}, decreases due to the decrease in the shear force as it can be seen from the softening of the shear stress ratio curve for the bottom boundary in Fig. 4.20b.

The stresses computed for the central core are higher than that for the whole volume. The values are compared at the shear strain of 0.04% relative to the initial condition; τ_{xy} is above by 40%, σ_{xx} is above by 28% and σ_{yy} is above by 29%. It is to be noticed that the maximum difference is in the shear stress while the differences in the normal stresses are almost the same. The difference could be attributed to the non-uniformity in the contact force flow paths at the top left corner zone and the bottom right corner zone (Figs. 4.14c,d,e) as compared to the central core where the load paths are oriented diagonally and uniformly.

In a granular material, failure is initiated when there is a continuous plane of slippage/sliding within the material. This stage is reached when the shear stress ratio at contacts on a plane exceeds the coefficient of friction of the material. Thus, in a granular material, failure is initiated in a zone of maximum shear stress ratio. By referring to the stress strain behavior of the dense packing in Fig. 4.21a, it can be seen that the slope of the shear stress ratio curve for vertical planes is

very steep compared to the curve for horizontal planes. Thus, the vertical planes reach the failure state at a much faster rate than the failure on horizontal planes.

De Josselin De Jong (1971) proposed that failure in simple shear could occur either by sliding on horizontal planes or sliding on vertical planes along with rotation. But, the sample will choose the latter mode with least resistance, if both modes of failure are equally possible for the prevailing boundary conditions. The results from the LTM concord with De Josselin De Jong's hypothesis.

The initial shear modulus for the dense packing can be evaluated from Fig. 4.20a in which the elastic limit appears to have reached at a shear strain of 0.0002. The shear modulus is evaluated as 287 Mpa. Assuming a Poisson's ratio of 0.20, the initial tangent elastic modulus is evaluated as 120 MPa. This value concords with the range of the typical initial elastic modulus for dense sands (100-200 MPa) given by Bowles (1988).

4.8.6 Failure mechanisms

During the shearing process, the load paths transform in such a way that contact forces are concentrated in stiff chains of particles (Figs. 4.14a through 4.14h). The shear stress ratios at contacts along these chains are far less than 'μ' and thus these contacts never slide. Sliding contacts can be seen only in relatively

unloaded directions or between the stiff chains of particles. From the Hill's averaging principle, the angle made by the major principal stress plane 'ψ' is computed as 30^0, at a shear strain of 0.04%, when a mechanism is reached. Based on this angle the directions of the major and minor principal stresses are shown in Fig. 4.10. It was earlier explained that the non-sliding contacts forming stiff chains of particles are along the line of contacts parallel to line AA (Figs. 4.14d-h) and that the line of contacts along horizontal rows of contacts along C2-C2, D2-D2 etc. and the line of contacts parallel to line BB become bondless. In Fig. 4.10, it is shown that the direction of minor principal stress makes an angle of 30^0 with the above mentioned line of contacts where debonding takes place. Therefore, it can be concluded that as a material deforms, the material chooses a mode of failure in such a way that non-sliding contacts with strong bonds are developed in the major principal stress direction and the material chooses the minor principal stress direction as the preferential direction for losing bonded contacts. The contacts between the major and minor principal stress directions remain as sliding contacts or as "stick and slip" contacts.

Cundall and Strack (1982 and 1983) performed numerical tests on assemblies of particles using DEM. The above mentioned observations from the lattice type model were observed by them in the results from DEM. Oda and Konishi (1974) performed simple shear tests on an assembly of photoelastic disks. The frequency distributions of the contact normals are given in Fig. 4 of their

paper. The photoelastic experiments also revealed that as the sample deforms in simple shear, the percentage of contacts in the major principal stress direction increases and the percentage of contacts in the minor principal stress direction decreases. Thus the observations from numerical tests using DEM and the photoelastic experiments concord with the observations in the lattice type model.

CHAPTER 5

CONCLUSIONS AND RECOMMENDATIONS

5.1 Conclusions

In this research, a lattice type model that can describe the micro mechanical behavior of particulate media has been formulated and numerical tests have been conducted on dense and loose assemblies of disks. The particulate media is transformed into a lattice comprising bars linking the contacts of the particles and a truss analysis is then conducted with appropriate joint constraints to determine the response of the particulate media under loads. The important features of the model are:

- A conceptually simple model that uses established methods of analysis.
- The particulate media itself is simulated by bars of representative stiffness unlike other existing methods, such as the Discrete Element Method, where the particles are replaced by springs at the contacts. This is especially important, if one wishes to consider phenomena such as particle (or grain) crushing and initial particle imperfections.

The results from the numerical tests on the ideal assemblies of disks in the loosest and densest packing established the robustness and potential of the lattice

type model to provide insights into the micro mechanical response of particulate media. Among the characteristics exhibited by the assemblies of disks are:

- Deformation occurs through groups or clusters of particles that slide, rotate, subdivide and regroup. This is consistent with observations from tests on real granular materials and images captured by photoelastic tests.
- Even for an ideal assembly of disks, the non-ideal simple shear strain deformation introduced non-uniformities in stresses that result in cluster formations.
- Certain established patterns of behavior in particular media such as compression in loose material and dilation in dense material are predicted by the lattice type model.
- Using Hill's averaging stress principle, the discrete set of contact forces was transformed into average stresses over a selected region of the dense assembly of disks to determine constitutive relationships. The results of the lattice type model were consistent with constitutive relationships observed in real particulate assemblies.

5.1 Recommendations

The lattice type model is still in its infancy and needs further development to assess whether it can be a viable, main stream model. The immediate needs

are:

1. Inclusion of additional contacts during deformation. This is necessary to simulate the formation of additional contacts when a particle moves into a new position and meets more neighbors than in its original position.

2. A comparative study with the Discrete Element Method.

3. A parametric study using random packing, random sizes, irregular shapes, bar stiffness, constraints for particle crushing, and initial particle imperfections.

4. Application of the model to real particulate systems such as sands. Here, an image of the intact sand can be taken and then digitized. The data can then be used to transform the sand structure into a lattice from which the analysis under the desired loading can be conducted.

5. A three-dimensional version of the model should be attempted since the analysis would be similar to a space truss.

6. The lattice type model can be extended to handle dynamic loading.

APPENDIX - 1

A - 1 : Displacements in an elastic disk

Fig. A1.1 shows an elastic disk acted upon by an equal and opposite load P along a chord of the circular cross-section of the disk.

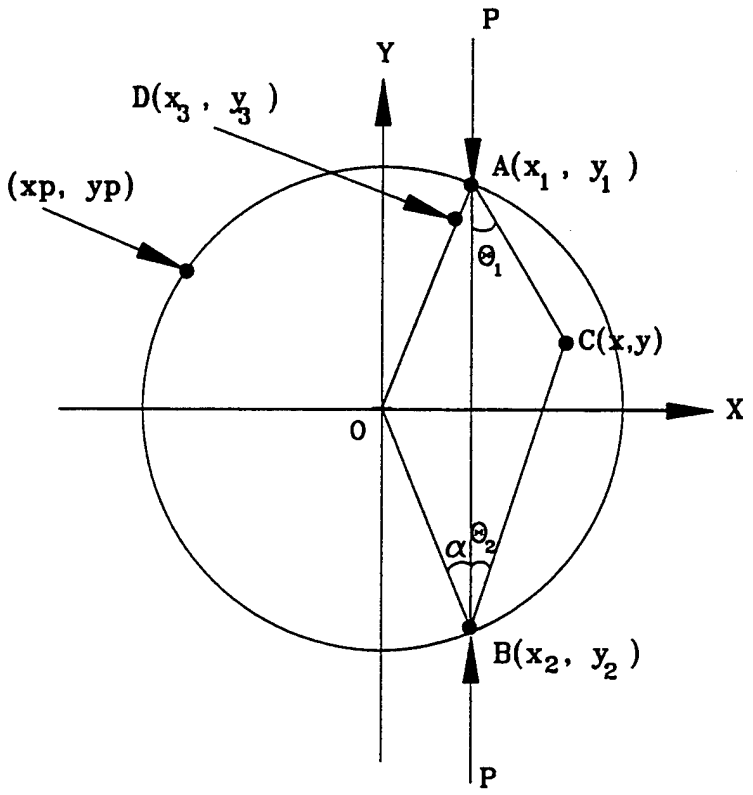

Fig. A1.1 Elastic disk under load along a chord

The expressions for stresses in this elastic disk are given in Frocht (1948). These expressions were derived from the original solutions of Michell (1900 and 1902) for stresses in an elastic half space. The normal stresses and shear stress σ_x, σ_y and τ_{xy} shown in Fig. 3.5 are given by Equations (A1.1), (A1.2) and (A1.3) respectively,

$$\sigma_x = \frac{-2P}{\pi t}\left[\frac{(y_1-y)(x-x_1)^2}{r_1^4} + \frac{(y_1+y)(x-x_1)^2}{r_2^4} - C\right] \tag{A1.1}$$

$$\sigma_y = \frac{-2P}{\pi t}\left[\frac{(y_1-y)^3}{r_1^4} + \frac{(y_1+y)^3}{r_2^4} - C\right] \tag{A1.2}$$

$$\tau_{xy} = \frac{2P}{\pi t}\left[\frac{(y_1-y)^2(x-x_1)}{r_1^4} - \frac{(y_1+y)^2(x-x_1)}{r_2^4}\right] \tag{A1.3}$$

where t is the thickness of the disk, d is the diameter of the disk, α is the angle between OA and AB, $C = \frac{\sin(\pi/2+\alpha)}{d}$, $r_1^2 = (x-x_1)^2 + (y_1-y)^2$ and $r_2^2 = (x-x_1)^2 + (y-y_2)^2 = (x-x_1)^2 + (y+y_1)^2$. From the above expressions for stresses, the displacement gradients can be obtained from the expressions

$$\frac{\partial u}{\partial x} = \epsilon_x = \frac{1}{E}(\sigma_x - \nu\,\sigma_y) \tag{A1.4}$$

$$\frac{\partial v}{\partial y} = \epsilon_y = \frac{1}{E}(\sigma_y - \nu\,\sigma_x) \tag{A1.5}$$

where u and v are the x and y components of the displacements, ϵ_x, ϵ_y are the engineering strains in the x and y directions and E and v are the elastic modulus and Poisson's ratio of the material of the disk.

The displacements u and v at a general point (xp, yp) are obtained by the integration of the displacement gradients between this point and a point where u and v displacements are zero. The displacement v is zero at all the points along x-axis. However, a point where the displacement u is zero cannot be determined in this disk problem as there is a rigid body motion. Therefore, only relative displacement of the point (xp, yp) with respect to the centroid of the disk can be determined. The equation of the line from origin (centroid) to the point (xp, yp) is obtained as y = mx, where m = yp/xp. The displacements u and v are given by

$$u = \int_0^{xp} \frac{\partial u}{\partial x} \Big|_{y = mx} dx \tag{A1.6}$$

$$v = \int_0^{yp} \frac{\partial v}{\partial y} \Big|_{x = \frac{1}{m} y} dy \tag{A1.7}$$

The displacement of point A, with respect to the centroid O is obtained by integrating the above expressions from (0, 0) to (x_1, y_1). However, this will lead to singularity and thus, theoretically, it is not possible to determine the displacement of A relative to the centroid O. Therefore, the displacement at A is

evaluated as a sum of the displacement of point D where the material yields along the line OA and the product of the displacement gradient at point D and the length of DA. It can be seen from Equations. (A1.1) and (A1.2) that the stresses are singular at point A. Therefore, a point D at (x_3, y_3), where the material yields, is obtained by setting the expression for the major principal stress at point D equal to the yield stress of the material. The major principal stress is given by

$$\sigma_1 = \frac{\sigma_x + \sigma_y}{2} + \sqrt{(\frac{\sigma_x - \sigma_y}{2})^2 + \tau_{xy}^2} \qquad \text{(A1.8)}$$

Since, σ_x, σ_y and τ_{xy} are functions of x and y, the stresses at point D are obtained by substituting (x_3, y_3) for (x, y) in the expressions for the stresses. Therefore, the expression for σ_1 which is set equal to the yield stress, will be a function of (x_3, y_3). Since (x_3, y_3) is a point along OA, substituting for $y_3 = m\, x_3$ (where m = slope of OA = y_1/x_1) will leave the expression for σ_1 in terms of x_3 and thus x_3 is evaluated. Then, y_3 is evaluated from $y_3 = m\, x_3$. Knowing (x_3, y_3), the expressions for evaluating the displacements at point A are given by

$$u_A = u_D + \frac{\partial u}{\partial x}\Big|_{(x_3, y_3)} (x_1 - x_3) \qquad \text{(A1.9)}$$

$$v_A = v_D + \frac{\partial v}{\partial y}\Big|_{(x_3, y_3)} (y_1 - y_3) \qquad \text{(A1.10)}$$

where u_A, v_A and u_D, v_D are the x and y components of the displacements at A and D respectively. u_D, v_D are evaluated from Equations. (A1.6) and (A1.7) respectively.

REFERENCES

Adley, M. D. and Sadd, M. H. (1992). "Continuum models for materials with lattice-like microstructure", in Computers & Structures Vol. 43, No. 1, pp. 13-18.

Bardet, J. P. And Proubet. J. (1991a). "An adaptative relaxation technique for the statics of granular materials", Computers and Structures, 39 (3/4): 221-229.

Bardet, J. P. and Proubet, J. (1991b). "A numerical investigation of the structure of persistent shear bands in granular media", Geotechnique, 41(4), pp. 599-613.

Bardet, J. P. and Proubet, J. (1992). "A shear band analysis in idealized granular materials", Journal of Engineering mechanics, ASCE, 118(2), pp. 397-415.

Bathurst, R. J. and Rothenburg, L. (1988). "Micro-mechanical aspects of isotropic granular assemblies with linear contact interactions", in J. Appl. Mech, Vol. 55, pp. 17-23.

Bishop, A.W. (1973). "Shear strength parameters for undisturbed and remoulded soil specimens", In Stress Strain Behavior of Soils, Edited by R.H.G. Parry, pp. 3-58.

Boardman, W.G. (1990). "Wave propagation in granular media simulated by elastic networks", Master's Thesis, Dept. Of Mechanical Engineering and Applied Mechanics, Univ. Of Rhode Island, U.S.A.

Bowles, J.E. (1988). Foundation analysis and design, Mc Graw Hill.

Burman, B.C. (1974). "Development of a numerical model for discontinua", Aust. Geomech.J.G4, No. 1, pp. 13-22.

Dragoo, B. (1995). "Two-dimensional photoelastic modelling of granular media using image processing", M. S. thesis, Department of Civil Engineering and Engineering mechanics, University of Arizona, Tucson, AZ.

Budhu, M. (1979). "Simple shear deformation of sands", Ph. D. thesis, Cambridge University, Cambridge, United Kingdom.

Budhu, M. (1988). "Failure state of a sand in simple shear", in Can. Geotech. J., 25, pp. 395-400.

Budhu, M., Ramakrishnan, S. and Frantziskonis, G. (1994). "Mechanics of particulate media - A lattice type approach", Proceedings; Workshop on Mechanics and Statistical Physics of Particulate Materials, Institute for Mechanics and Materials, University of California, San Diego, CA, June 8-10, 1994.

Chang, C.S. and Misra, A. (1989a). "Theoretical and experimental study of regular packings of granules", Journal of Engineering Mechanics, Vol. 115, No.4, pp. 704-720.

Chang, C. S. and Misra, A. (1989). "Computer simulation and modelling of mechanical properties of particulates", Computers and Geotechnics, 4, pp. 269-287.

Chang, C. S. and Liao, C. L. (1990). "Constitutive relation for a particulate medium with the effect of particle rotation", Int. J. Solids and Structures, Vol. 26, No. 4, pp. 437-453.

Chang, C. S. (1990). "Strain tensor and deformation for granular material", Journal of Engineering Mechanics, ASCE, Vol. 116, No. 4, 790-804.

Chang, C. S. and Misra, A. (1990). "Packing structure and mechanical properties of granulates", Journal of Engineering mechanics, ASCE, Vol. 116, No. 5, pp. 1077-1093.

Cundall, P. A. and Strack, O. D. L. (1979a). "A discrete numerical model for granular assemblies," Geotechnique, 29, pp. 47-65.

Cundall, P. A. and Strack, O. D. L. (1979b). "The distinct element method as a tool for research in granular media", Report to NSF concerning grant ENG 76-20711, Part 2, Dept. Civ. Min. Engrg. Univ. Minnesota.

Cundall, P. A. and Strack, O. D. L. (1979c). "The development of constitutive laws for soil using the distinct element method", Numerical Methods in Geomechanics, Aachen, ed. W. Wittke, pp. 289-298.

Cundall, P. A., Drescher, A., and Strack, O. D. L. (1982). "Numerical experiments on granular assemblies; Measurements and observations", Proceedings, IUTAM Conference on Deformation and Failure of Granular Materials, Delft, Edited by P. A. Vermeer and H. J. Luger, A. A. Balkema/ Rotterdam, pp. 355-370.

Cundall, P.A. and Strack, O.D.L. (1983). "Modelling of microscopic mechanisms in granular material", Mechanics of granular materials edited by J. T. Jenkins and

M. Satake, Elsevier, pp. 137-149.

Cundall, P. A. (1988). "Computer simulations of dense sphere assemblies", Micromechanics of granular materials, Ed. by M. Satake and J. T. Jenkins, Elsevier, Amsterdam, pp. 113-123.

Cundall, P.A. (1989). "Numerical experiments on localization in frictional materials", Ingenieur-Archiv, Vol. 59, No. 2, pp. 148-159.

Cundall, P. A., Jenkins, J. T. and Ishibashi, I. (1989). "Evolution of elastic moduli in a deforming granular assembly", Powders and Grains, Ed. by J. Biarez and R. Gourves, Balkema, pp. 319-322.

Dai, H. and Frantziskonis, G. (1994). "Heterogeneity, spatial correlations, size effects and dissipated energy in brittle materials", Mechanics of materials, Elsevier, pp. 103-118.

Dantu, P. (1957). "Contribution a l'etude mecanique et geometrique des milieux pulverulents", Proc. 4th Int. Conf. Soil Mech. Found. Engrg, London: 144-148.

De Josselin De Jong, G. and Verruijt, A. (1969). "Etude photo-elastique d'un epilement de disques", Cah. Grpe Fr. Etud. Rheol. 2 :73 - 86.

De Josselin De Jong, G. (1971). Stress-strain behavior of soils, In Proceedings, Roscoe Memorial Symposium, Edited by R.H.G. Parry, U.K. pp. 258-261.

Dow, J. O., Su, Z. W., Feng, C. C. and Bodley, C. (1985). "Equivalent continuum representation of structures composed of repeated elements", AIAA Journal, 23, pp. 1564-1569.

Deresiewicz, H. (1958). "Mechanics of granular material", Advd. appl. Mech. 5, pp. 233-306.

Drescher, A. and De Josselin De Jong, G. (1972). "Photoelastic verification of a mechanical model for the flow of a granular material", J. Mech. Phys. Solids, Vol. 20, pp. 337-351.

Duncan, J. M. and Chang, C. Y. (1970). "Nonlinear analysis of stress and strain in soils", J. Of Soil Mech. and Found. Div., ASCE, Vol. 96, No. SM5, pp. 1629-1653.

Feda, J. (1982). "Mechanics of particulate materials", Elsevier Pub Company.

Frantziskonis, G., Karpur, P., Matikas, T. E., Krishnamurthy, S. and Jero, P. D. (1994). "Fiber-matrix interface - information from experiments via simulation", Composite structures, Vol. 29, pp. 231-247.

Frocht, M. M. (1948). "Photoelasticity" Vol. 2, John Wiley & Sons, New York.

Gill, J. J. (1993). "The microstructural response of granular soil under uniaxial strain", Final report to AFOSR, Phillips Laboratory, Air Force Material Command, Kirtland AFB, NM.

Hansen, A., Roux, S., and Herrmann, H. J. (1989). J. Phys. France 50, 733.

Herrmann, H.J. and Roux, S. (1990). "Statistical models for the fracture of disordered media, North-Holland.

Hertz, H. (1882). "Uber die Behrungsfester Elastischer Korper", J. Reine Angew. Math, Vol. 92, No. 7, pp. 156-171.

Hill, R. (1963). "Elastic properties of reinforced solids: Some theoretical principles", Journal of mechanics and physics of solids, Vol. 11, No. 5, pp. 357-372.

Hrennikoff, A. (1941). "Solution of problems of elasticity by the framework method", Journal of Applied Mechanics, ASME, A-169-175.

Ishibashi, I. and Chen, Y.C. (1988). "Dynamic shear moduli and their relationship to fabric of granular materials", Micromechanics of granular materials, Ed. by M. Satake and J. T. Jenkins, Elsevier, Amsterdam, pp. 95-102.

Johnson, K.L. (1985). Contact mechanics, Cambridge University Press.

Kishino, Y. (1988). "Disc model analysis of granular media", Micromechanics of granular materials, Ed. by M. Satake and J. T. Jenkins, Elsevier, Amsterdam, pp. 143-152.

Kollar, L. and Hegedus, I. (1985). "Analysis and design of space frames by the continuum method", Elsevier.

Konishi, J. and Naruse, F. (1988). "A note on fabric in terms of voids", In Micromechanics of granular materials, Ed. by M. Satake and J. T. Jenkins, Elsevier, Amsterdam, pp. 39-46.

Konishi, J., Oda, M., and Nemat-Nasser, S. (1983), "Induced anisotropy in assemblies of oval cross-sectional rods in biaxial compression", Mechanics of granular materials edited by J. T. Jenkins and M. Satake, Elsevier, pp. 31-39.

Konishi, J. and Naruse, F. (1988). "A note on fabric in terms of voids", Micromechanics of granular materials, Ed. by M. Satake and J. T. Jenkins, Elsevier, Amsterdam, pp. 39-46.

Krajcinovic, D. and Silva, M.A. (1982). "Statistical aspects of the continuous damage theory", Int. J. Solids and Structures, Vol. 18, No. 7, pp. 551-562.

Krajcinovic, D. and Basista, M. (1991). "Rupture of central-force lattices revisited", in J. Phys. I , 1, pp. 241-245.

Luerkens, D. W. (1991). "Theory and application of morphological analysis", CRC press.

Mantell, C.L. (1958). Engineering materials handbook, McGraw Hill.

Mindlin, R.D. (1949). "Compliance of Elastic Bodies in Contact," J. Appl. Mech., Sept., 259-268.

Mindlin, R. D. and Deresiewicz, H. (1953). "Elastic spheres in contact under varying oblique forces", J. Appl. Mech., 20, 327-344.

Michell, J. H. (1900). Proc. London Math. Soc., Vol. 32, p. 44.

Michell, J. H. (1902). Proc. London Math. Soc., Vol. 34, p. 134.

Misra, A. (1990). "Constitutive relationships for granular solids with particle slidings and fabric changes", Ph. D dissertation, University of Massachusetts, Amherst, MA.

Nemat-Nasser, S. and Mehrabadi, M. (1983). "Stress and fabric in granular masses", in Mechanics of Granular materials edited by Jenkins, J.T and Satake, M., Elsevier, pp. 1-8.

Nemat-Nasser, S. and Mehrabadi, M. (1984). "Micromechanically based rate constitutive descriptions for granular materials", in Mechanics of Engineering Materials, Edited by C.S.Desai and R.H.Gallagher, John Wiley & Sons Ltd.

Newmark, N.M. (1949), "Numerical methods of analysis in bars, plates and elastic bodies," in 'Engineering' edited by L. E. Grinter, Macmillan.

Noor, A. K. and Russell, W. C. (1986). "Anisotropic continuum models for beamlike lattice trusses", Comp. Meth. Appl. Mech. Engrg., 57, pp. 257-277.

Oda, M. (1972a). "Initial fabrics and their relations to mechanical properties of granular material", Soil and Foundations, Journal of the JSSMFE, Vol. 12, No. 1, pp. 17-36.

Oda, M. (1972b). "The mechanism of fabric changes during compressional deformation of sand", Soils and Foundations, Journal of the JSSMFE, Vol. 12, No. 2, pp. 1-18.

Oda, M. (1972c). "Deformation mechanism of sand in triaxial compression tests", Soils and Foundations, Journal of the JSSMFE, Vol. 12, No. 4, pp. 46-63.

Oda, M. and Konishi, J., (1974), "Microscopic Deformation of Granular Material in Simple Shear," Soils and Foundations, 14: 25-38.

Oda, M., (1978), "Significance of fabric in granular mechanics", Proceedings, U.S.-Japan seminar on Continuum-Mechanical and Statistical Approaches in the Mechanics of Granular Materials, Ed. By S.C. Cowin and M. Satake, Gakujutsu Bunken Fukyu-kai, pp. 7-26.

Oda, M., Nemat-Nasser, S. and Mehrabadi, M.M. (1982), "A statistical study of fabric in a random assembly of spherical granules", Int. J. Anal. Methods in Geomech. 6, pp. 77-94.

Paikowsky, S.G. and DiRocco, K.J. (1993). "Image analysis of interparticle contact modeling", Digital Image Processing: Techniques and Applications in Civil Engineering: Proceedings of a Conference, Kona, Hawaii, Feb. 28 - Mar. 5.

Parikh, P. V. (1967). "The shearing behavior of sand under axisymmetric loading", Ph. D thesis, University of Manchester.

Ramakrishnan, S. (1996). "Mechanics of Particulate Media - A Lattice Type Approach", Ph.D dissertation, Department of Civil Engineering, University of Arizona, Tucson, U.S.A, In progress.

Roscoe, K. H., (1953), "An apparatus for the application of simple shear to soil

samples," Proceedings, 3rd Int Conference on Soil Mechanics and Foundation Engineering, Zurich, Vol. 1, pp. 186-191.

Rothensburg, L. and Bathurst, R. J. (1992). "Micromechanical features of granular assemblies with planar elliptical particles", Geotechnique, 42, 79-95.

Sadd, M. H., Qui, L., Boardman, W. G., Shukla, A. (1992). "Modelling wave propagation in granular media using elastic networks", Int. J. Rock Mech. Min. Sci. & Geomech. Abstr., Vol. 29, No. 2, pp. 161-170.

Serrano, A.A. and Rodriguez-Ortiz, J.M. (1973) "A contribution to the mechanics of heterogeneous granular media", Proceedings, Symposium on Plasticity and Soil Mechanics, Cambridge, U.K.

Strack, O. D. L. and Cundall, P. A., (1978). "The Distinct Element Method as a tool for Research in Granular Media," Report to NSF concerning grant ENG 76-20711, Part 1, Dept. Civ. Min. Engrg. Univ. Minnesota.

Shukla, A. and Damania, C. (1987). "Experimental investigation of wave velocity and dynamic contact stresses in an assembly of disks", Experimental mechanics, 30, 80-87.

Subhash, G., Nemat-Nasser, S., Mehrabadi, M. M., Shodja, H. M. (1991). "Experimental investigation of fabric-stress relations in granular materials", Mechanics of materials, Elsevier, pp. 87-106.

Thornton, C. and Barnes, D. J., (1986). "Computer Simulated Deformation of Compact Granular Assemblies," ACTA Mechanica, 64, 45-61.

Thornton, C. And Sun, G. (1993). "Axisymmetric compression of 3D polydisperse systems of spheres", Powders and Grains, Ed. by C. Thornton, Balkema, pp. 129-134.

Timoshenko, S.P. and Goodier, J.N. (1970). Theory of elasticity, McGraw Hill.

Trollope, D. H. and Burman, B. C., (1980), "Physical and Numerical Experiments with Granular Wedges.", Geotechnique, 30, 137-157.

Wakabayashi, T. (1957). "Photoelastic method for determination of stress in powdered mass", Proc. 7th Jap. Nat. Congr. Appl. Mech. pp. 153-192.

PART II

PHOTOELASTIC MODELING OF GRANULAR MEDIA USING IMAGE PROCESSING

by

Muniram Budhu

Brian Dragoo

S. Ramakrishnan

A report

to the

National Science Foundation

and

Air Force Office of Scientific Research

June, 1996

TABLE OF CONTENTS

CHAPTER **PAGE**

TABLE OF CONTENTS (cont.)

LIST OF FIGURES

FIGURE **PAGE**

FIGURE **PAGE**

ABSTRACT

A simple shear apparatus was designed and built to study force distribution within an assembly of photoelastic disks to compare with predictions from the lattice type model described in Part I. The principles and methods of photoelasticity were used to gain insights into how micro-level parameters affect the macro-level behavior of a particulate media. Photosensitive disks were arranged in the simple shear apparatus in dense and loose packings to simulate granular assemblies. Images of the displacements and deformation of the photosensitive disk assemblies were captured with a video camera, and an image processing software was modified to semi-automate the photoelastic analysis. Particle deformation mechanisms, volumetric strain relationships, and boundary stress patterns observed during simple shear testing were shown to be consistent with existing theories and experimental observations. Load redistribution under simple shear was observed to be extremely sensitive to frictional micro-variations on disk surfaces. The force distributions obtained from the photoelastic analyses were consistent with predictions of the lattice type model and lends credence to this model as a suitable approach to study the micromechanical behavior of particulate systems.

CHAPTER 1

1.0 Introduction

In Part I of this report, the theoretical basis for the lattice type model (LTM) has been described. Numerical experiments were conducted to establish the procedures of and predictions from the model. The applicability of LTM depends on whether its predictions are consistent with results from experiments or observed behavior of particulate media. A key feature of LTM is the prediction of the force distribution within a simulated particulate assembly. One way of establishing the goodness of the prediction is to determine the force distribution in an ideal system in a test setup and then compare the test results with the model prediction for the ideal system. A test method that offers promise is photoelastic experimental method and it was selected to evaluate the LTM.

1.1 Objective

The objective of this study is to observe and determine the force distribution and the behavior of packings of photoelastic disks in simple shear to compare with predictions from the lattice type model.

1.2 Scope

The following are included in the scope of this work:

- Design and construction of a simple shear box capable of (a) applying a constant vertical load to a two-dimensional assembly of disks, (b) deforming the assembly under simple shear, and (c) transmitting light for analysis by photoelasticity.

- Develop a method of contact force analysis using image processing.
- Perform simple shear experiments on both loose and dense assemblies of disks.
- Make observations for general comparison with current theories and observations on granular media under simple shear loading.
- Compare force distribution with predictions from the lattice-type model.

CHAPTER 2

LITERATURE REVIEW

2.0 Introduction

This chapter provides general information on prior research in areas of interest to the present work. Areas covered include photoelasticity, experimental investigations of microscopic mechanisms in the deformation of granular materials, photoelastic investigations of contact forces, elastic analyses of contact forces, and digital image processing and its applications in photoelastic analysis.

2.2 Photoelasticity

Stress analysis has proven valuable in the field of engineering. The ability to determine how stresses are distributed in a machine or structure under a given set of loads is crucial to its design. The most widely used method for stress analysis is the theory of elasticity - a mathematical theory that, while accurate, becomes increasingly involved as geometry and loading conditions become more complex. It is often difficult for engineers to find solutions to practical problems due to complex boundary conditions. Hence, experimental techniques are often called upon to aid in problem solving.

Photoelasticity is an experimental technique that takes advantage of the optical properties of a transparent material to quantify the distribution of stress within that material. Machine parts, tools, structures, and other load-

bearing objects can be analyzed for stress concentration and other failure-inducing phenomena when modeled and subjected to a photoelastic analysis. Photoelasticity, as a science, first appeared around the turn of the century, and by the 1930s it was developed into a feasible technique for stress analysis by Coker and Filon at the University of London (Frocht, 1941).

A model specimen cut from a transparent, photosensitive material reacts to stress by undergoing a change in index of light refraction that Maxwell, in 1853, observed to be proportional to the stresses induced on the specimen. This change can be quantified by subjecting the specimen to a field of polarized light in an apparatus known as a polariscope (see Chapter 3). The light that is passed through the specimen is extinguished in banded regions called fringes (Fig. 2.1) that are related to either the magnitude or direction of the principal stresses. If the polariscope is further modified (with the addition of optical plates), the light field can become circularly polarized. This technique allows the fringes related to the principal stress directions (isoclinics) to be eliminated, and the remaining stress magnitude-related fringes (isochromatics) can be used to calculate the magnitude of the principal stress difference ($\sigma_1 - \sigma_2$) at any point, which is equal to twice the maximum shear stress (τ_{max}) at that point.

The fringes develop as ordered bands as the stress in a specimen is increased, with fringe order (N) zero developing first, then fringe order 1, etc. The fringes are contours of equal principal stress difference, which is linearly related to the fringe order by a the stress-optic law,

$$\sigma_1 - \sigma_2 = \frac{Nf_\sigma}{h} \tag{2.1}$$

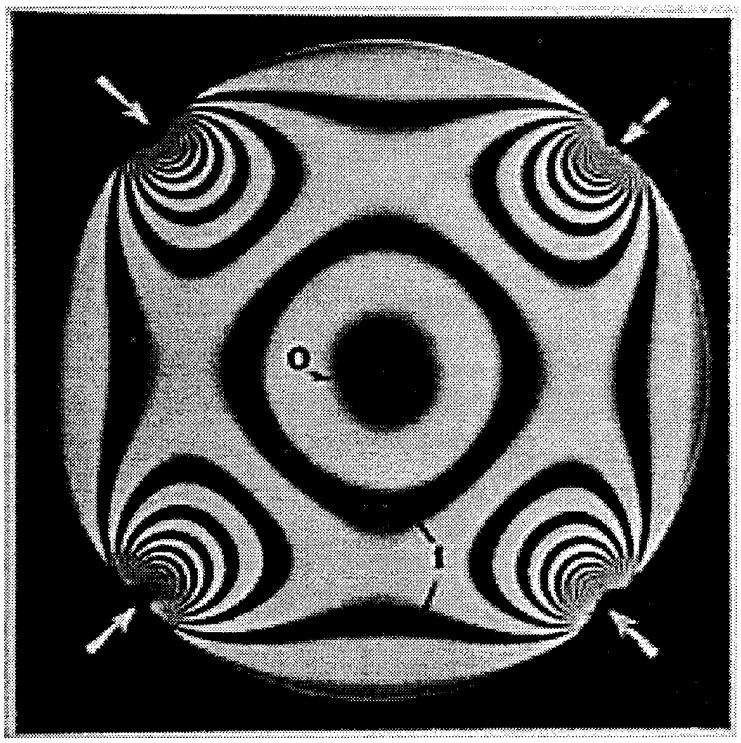

Figure 2.1 Photoelastic isochromatic fringes on a disk under four equal radial loads (from Frocht, 1941). Fringes are lines of constant principal stress difference and are ordered as integers, with fringe order zero the first to develop. Fringe order zero at the center reveals an isotropic point.

where f_σ is the fringe constant of the photosensitive material, and h is the thickness of the specimen (Dally, 1965). If f_σ is calibrated, and h is measured, the principal stress difference (and hence τ_{max}) can be read directly from a photoelastic image for any point in a specimen falling on an integered fringe, and can be interpolated for those falling between fringes. This technique revolutionized the field of stress analysis because it allowed machine parts or structures with shapes that were too complex to be readily handled by elasticity to be accurately analyzed for design purposes.

The finite element method (FEM) and other numerical techniques used in stress analysis for design have since replaced photoelasticity in many fields due to the ease with which boundary conditions can be changed in numerical models. In contrast, the study of different conditions by constructing and testing several photoelastic specimens is time consuming and requires a high degree of skill.

However, in the emerging field of non-continuum modeling, including the current study of the problem of stresses flowing in a granular assembly, photoelasticity can be used to determine the feasibility of proposed numerical methods.

2.2 Photoelastic Analyses of Contact Forces

De Josselin de Jong and Verruijt (1969) developed a technique to apply the principles of photoelasticity to the specific task of finding the magnitude and direction of a contact force between two disks (Fig. 2.2).

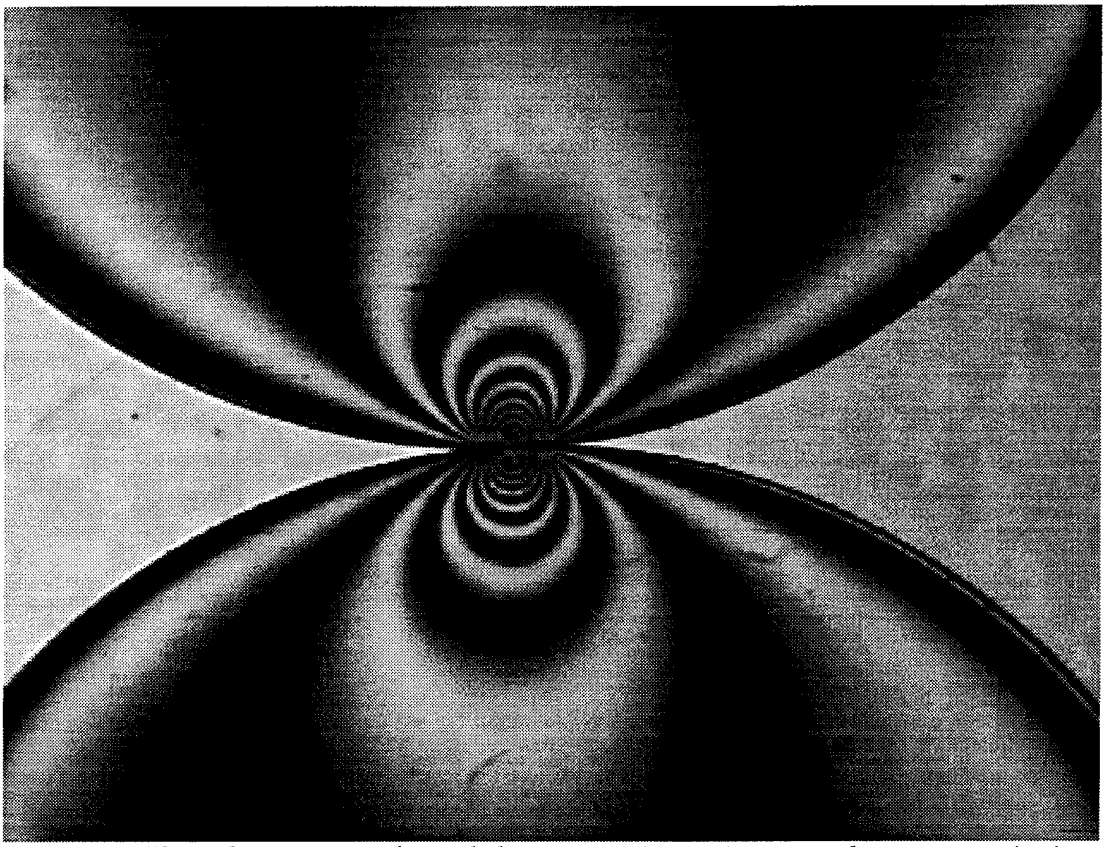

Figure 2.2. Photoelastic image of two disks representing an intergranular contact point in a particulate media.

In a contact stress problem on a linear elastic material, the geometry of the pattern of principal stress difference that develops (as represented by the photoelastic fringes) is known to be proportional to the concentrated force P such that:

$$\sigma_1 - \sigma_2 = P \cdot \mathrm{f}(x,y) \tag{2.2}$$

where f(x,y) is a function that expresses the shape of the isochromatic fringes.

Since the region of interest in the disk contact stress problem is close to the edge of the disk, de Josselin de Jong assumed that f(x,y) could be

approximated by a concentrated force acting on a semi-infinite plane as given by Frocht (1948):

$$f(x,y)=\frac{2}{\pi hd} \tag{2.3}$$

where d is the diameter of the circle that best approximates the fringe passing through both the contact point and the point (x,y), the center of the circle being on the line of action of the contact force.

By rearranging Eqns 2.1, 2.2, and 2.3, it can be shown that

$$\frac{P}{nd}=\text{constant} \tag{2.4}$$

for any contact force through a given material with a given thickness. This implies that if this constant were calibrated by measuring the diameter of a known fringe order produced by a known concentrated force on a semi-infinite plane, the value of the force through any contact could be determined by simply measuring the diameter of a known fringe order, and calculating the magnitude of P from the constant. And, as mentioned above, the force is known to act along a line connecting the contact point and the center of the circle which best approximates the measured fringe.

This method greatly simplifies the photoelastic analysis for this specific purpose. However, since the assumption that the disk is a semi-infinite plane only holds true near the contact area, care must be taken in the analysis so that this assumption is still valid. Care must also be exercised in using the

de Josselin de Jong and Verruijt method of contact force determination when measuring fringes very near the contact area.

Poritsky (1950) developed equations for stresses and deflections of two cylindrical bodies in contact under both normal and tangential distributed loads. These equations, which are expressed in terms of the Airy functions, can also be plotted as curves of constant principal stress difference for direct comparison with photoelastic fringes. By examining a plot of Poritsky's constant principal stress difference curves of a distributed contact force on a semi-infinite plane, it can be seen that fringe distortion is severe in the region near the contact. (Fig 2.3). Frocht showed from photoelastic studies that fringes in this region will be circles for a concentrated load.

Since de Josselin de Jong and Verruijt assume in their analysis that the contact load is concentrated rather than distributed, some discussion of how to measure fringes near the area of contact is necessary. Detailed discussion of a modified technique for contact force and magnitude determination based on the de Josselin de Jong and Verruijt analysis is presented in Chapter 4.

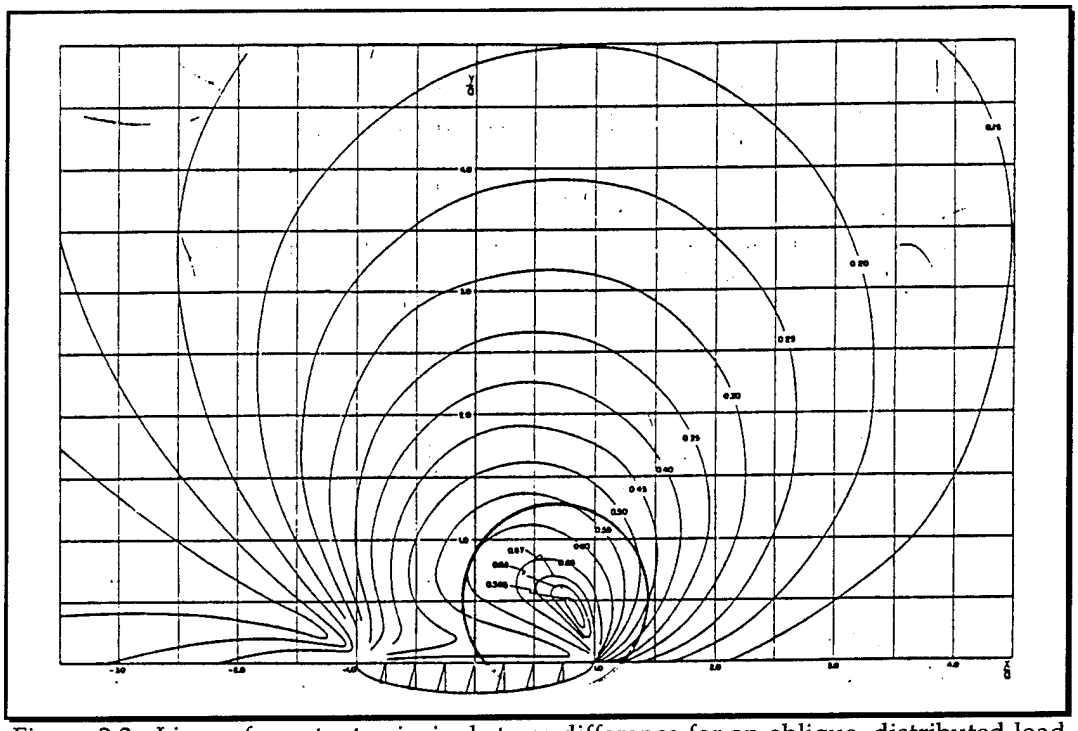

Figure 2.3. Lines of constant principal stress difference for an oblique, distributed load on a semi-infinite plane (from Poritsky, 1950). The circled region shows pronounced fringe deformation due to the distributed load.

2.3 Micro-mechanisms in the Deformation of Granular Media

2.3.1 Flow of a Granular Assembly

Drescher and de Josselin de Jong (1972) studied an assembly of photosensitive particles to gain insight into how a granular media flows under load. Their experimental setup allowed them to deform the assembly similar to a simple shear deformation (Fig 2.4).

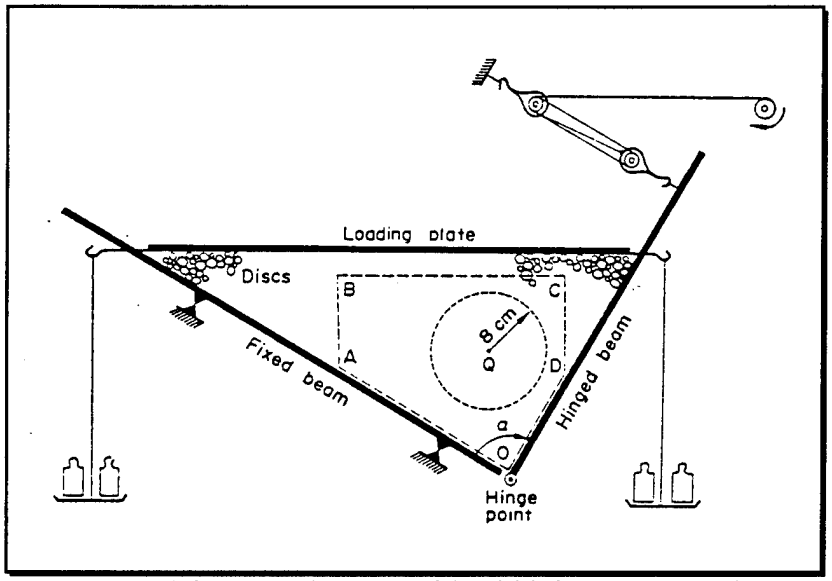

Figure 2.4. Schematic diagram of load/deformation mechanism used by Drescher and de Josselin de Jong (1972) for photoelastic investigation of stress flow through a granular assembly.

It is apparent from the photoelastic fringe patterns of Drescher and de Josselin de Jong's assembly (Fig 2.5) that forces are transmitted not uniformly throughout the assembly, but by chains of aligned contact forces. These chains then form relatively rigid blocks of particles that slide relative to one another. They concluded that since the probability of developing a chain in a specific location is small, that the distances between chains must be large; at least several disk diameters. The result of this is a discrete, rather than continuous force distribution, completely contrary to the continuum approach commonly taken for stress determination in soil mechanics problems.

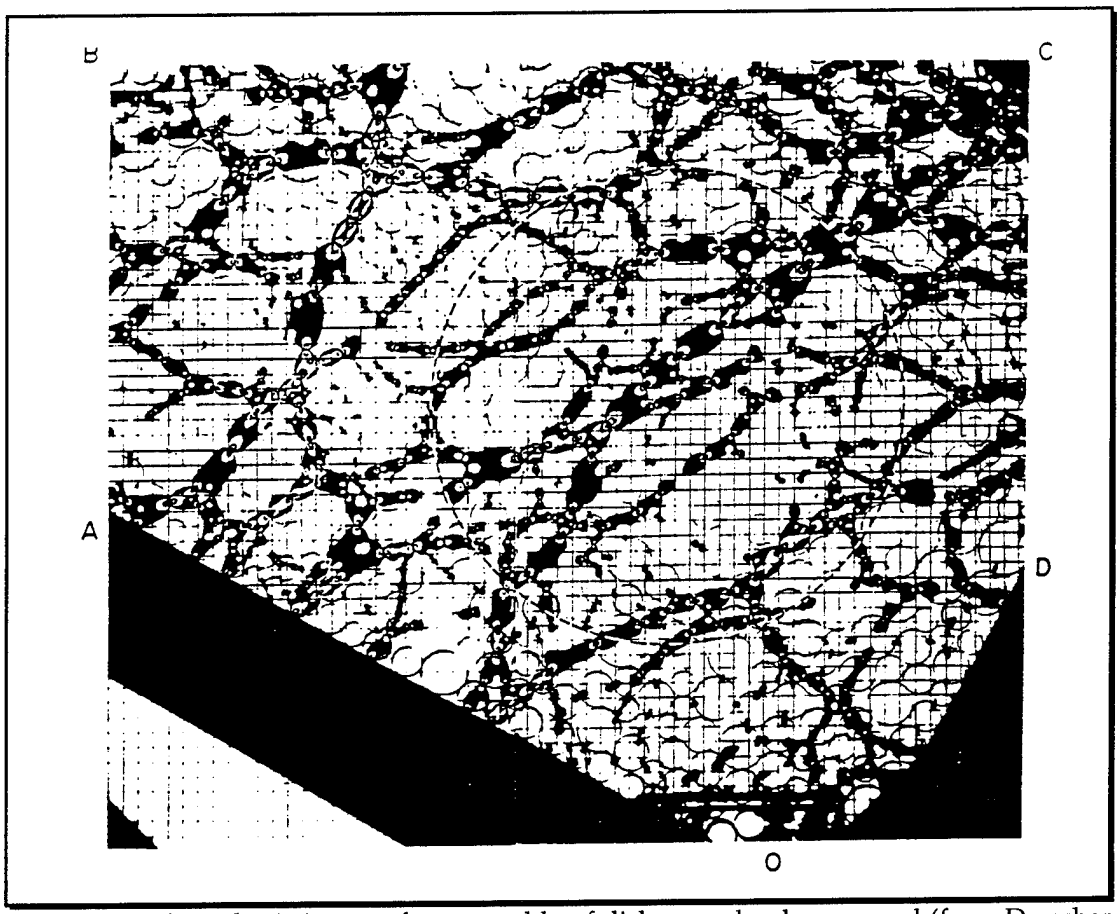

Figure 2.5. Photoelastic image of an assembly of disks, randomly arranged (from Drescher and de Josselin de Jong (1972). Disks with dark areas exhibit compression stresses and thus belong to the instantaneous structural skeleton of the assembly.

A similar problem exists for deformation. When just one contact yields to sliding, which occurs when the angle between the force between two disks and the normal to the contact exceeds the allowable friction angle, many contact points can be reoriented. This leads to a drastic, discrete redistribution of the contact forces. Thus the movements of the particles are discrete in character, which is again contrary to the approach taken for deformations in soil mechanics.

Of course, it is impractical to attempt a discrete stress and strain analysis when making soil mechanics computations. The authors introduce an

average stress and strain-rate tensor evaluation to interpret behavior in a granular assembly. Experimental results can then be compared with theoretically predicted behavior based on a mechanical model. The main observations of Drescher and de Josselin de Jong are that the division of the assembly into rigid, sliding blocks, and the free rotation of these blocks, are observed in practice.

2.3.2 Investigation of Granular Materials in Simple Shear

The deformation of a granular media was simulated by Oda and Konishi (1974) using an assembly of cylindrical rods made from photosensitive material packed at random into a simple shear apparatus. They concluded that the tendency of the concentration of the normal vectors to the contact planes was determined primarily by the mobilized stress ratio τ/σ_n, where τ is the shear stress and σ_n is the normal stress. By plotting frequency distributions of contact normals, they noticed that the preferred direction of these normals gradually rotates with the rotation of principal stress axes during shear deformation. They also concluded that sliding is confined to only a preferred set of contacts at any one time, implying, like Drescher and de Josselin de Jong, that particles group themselves into a system of rigid block that slide against one another.

2.4 Digital Image Processing

Digital imaging is a widely used computational technique for digitally representing an image by discretizing it and assigning numerical values to its components. Greyscale images, the type used in this project, are broken down into picture elements, or pixels, that have three dimensions: an x-coordinate, a y-coordinate, and a brightness value. The brightness value is a number between 0 (black) and 255 (white) that represents a relative luminosity of the pixel on an eight bit (2^8) scale. Once an image has been digitized, the three-dimensional array that represents it can be readily manipulated by imaging software. Imaging techniques such as smoothing, sharpening, and finding edges, which are valuable for extracting necessary information from the image, are based upon manipulation of the brightness values exhibited by each pixel in the image.

2.4.1 Image Processing in Photoelastic Analysis

A large body of literature has been produced in the past fifteen years on the subject of automating photoelastic data collection using digital image processing. These include Müller and Saackel (1979), Hu et al (1983), Umezaki et al (1988), Patterson (1988), Gillies (1988), Chen and Taylor (1989), Ramesh et al (1991) and many others. However, most of these works explain complex processing algorithms for such techniques as fringe separation, fringe thinning, etc. Since pre-packaged imaging software (which includes these and

other processing algorithms) is used in this study, it is unnecessary to detail these works.

Paikowsky and DiRocco (1993) have also developed an image analysis system exclusively for analyzing photoelastic images of two-dimensional modeling of interparticle contacts. They cite, as advantages to using image processing to analyze these images, (1) high resolution of enlarged portions of images and (2) the possibility of high frequency image capturing for motion analysis. Disadvantages include high capital cost and time consuming analysis.

They have also concluded that two of de Josselin de Jong and Verruijt's most critical assumptions lead to incorrect measurement of contact force magnitudes from photoelastic images. These assumptions are as follows: (1) the contact area of the particles is negligible and that (2) the fringes that result from contact forces are circles that pass through the contact point . They have thus developed their own technique for force magnitude and orientation determination, which is mentioned but not detailed in Paikowsky et al (1993). It will be shown (Chapter 4) that the method of force determination developed by de Josselin de Jong and Verruijt can be slightly modified to give satisfactory measurements of both force magnitudes and directions using digital image processing technology.

CHAPTER 3

SYSTEM SETUP

3.0 Introduction

Photoelastic analyses require the following: a polariscope, a load application mechanism, a photosensitive model, and system for acquiring and processing photoelastic images (Fig. 3.1).

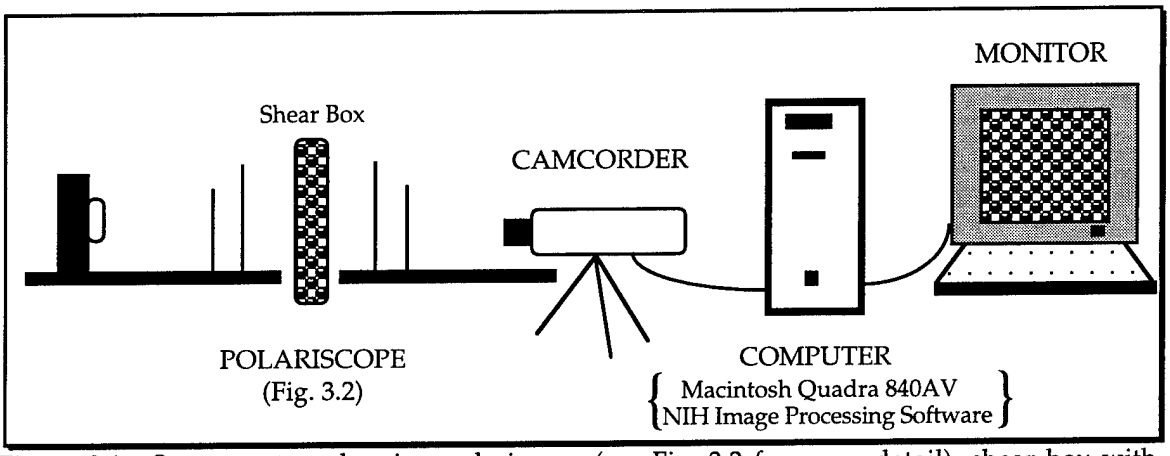

Figure 3.1. System setup showing polariscope (see Fig. 3.2 for more detail), shear box with photosensitive disks, camcorder for image capture, computer for image processing, and monitor for image analysis and display.

3.1 The Polariscope

The polariscope (Fig. 3.2) is a system of lenses and plates aligned to produce a field of circularly polarized light. It generally consists of a light source, a polarizer, two quarter-wave plates, and an analyzer. The light source produces white light, which is often immediately broken down into monochromatic light with a filter.

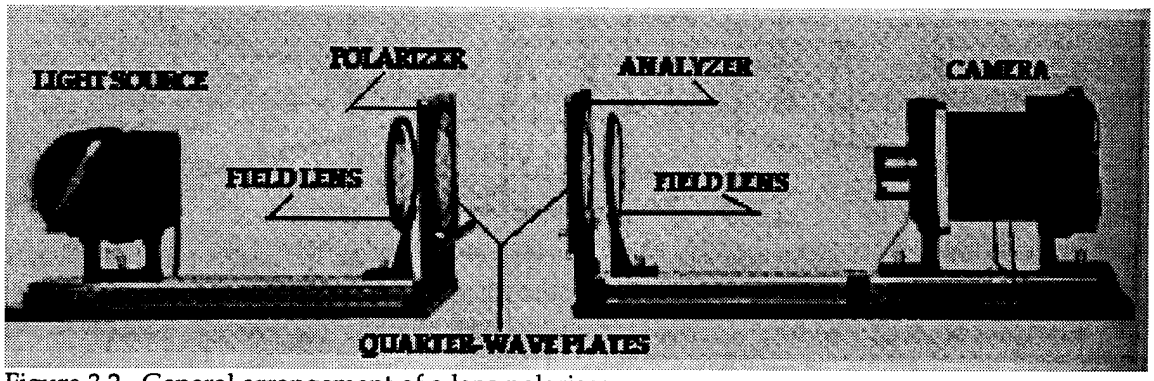

Figure 3.2. General arrangement of a lens polariscope.

The polarizer polarizes the light by restricting the light vector to single plane vibration. The light then passes through the first quarter-wave plate which circularly polarizes the light. A light field is circularly polarized when the tip of the light vector describes a circular helix as the light propagates. When this circularly polarized beam passed through the photosensitive model (set between the quarter-wave plates), which behaves as a doubly refracting crystal, it is resolved into two equally plane-polarized components in mutually perpendicular planes determined by the state of stress in the model. The second quarter-wave plate de-circularizes the light, giving it plane polarization once again.

The light finally reaches the analyzer, where it is either fully extinguished (dark field) or passed on (light field), depending on the desired effect. All photoelastic tests for the present study were conducted in light fields.

Additional optical devices are sometimes employed depending on the light source and desired final image. For example, partial optical mirrors can be used in such techniques as fringe sharpening or fringe thinning if additional stress information is required from a specimen.

Two polariscopes were used for this work: a *lens polariscope* with a small viewing area and a *diffused-light polariscope* with a large viewing area. The lens polariscope (the type shown in Fig. 3.2), manufactured by Polarizing Instrument Company, is used for the capture of images where sharp detail is required. This polariscope generally requires more exact lens alignment, plate rotation position, and camera focal length, which can make experiments relatively time consuming.

The light from the source of a lens polariscope, emitted through a small aperture, is subsequently diffused by a field lens before entering the polarizer, and is re-collected by another field lens before entering the camera. The viewing area of this polariscope was not large enough to capture full-field images of some of the models required, so a second polariscope was needed.

The diffused-light polariscope (Fig. 3.3), constructed in 1975 by undergraduate students of photoelasticity at the University of Arizona, has sufficient viewing area for all models used, and adjustments generally do not require the same degree of precision as the lens polariscope. Because this polariscope uses a diffused light source, it tends to reduce the sharpness and contrast of photoelastic images. Dark fringes appear gray, rather than black as in images from the lens polariscope (Fig. 3.4). Images from the diffused-light polariscope, because of their inferior contrast, are not sufficient for the high-resolution analysis required to collect quantitative data. The increased viewing area of the diffused-light polariscope is, however, taken advantage of for qualitative analysis.

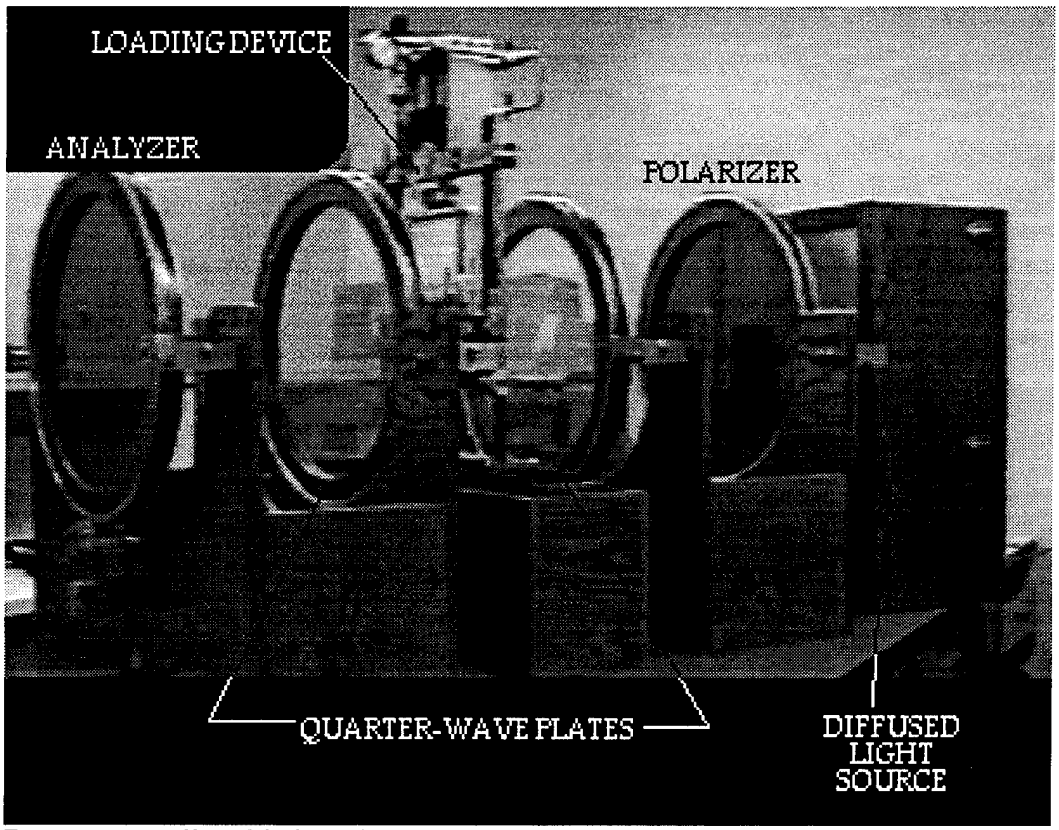

Figure 3.3. Diffused-light polariscope.

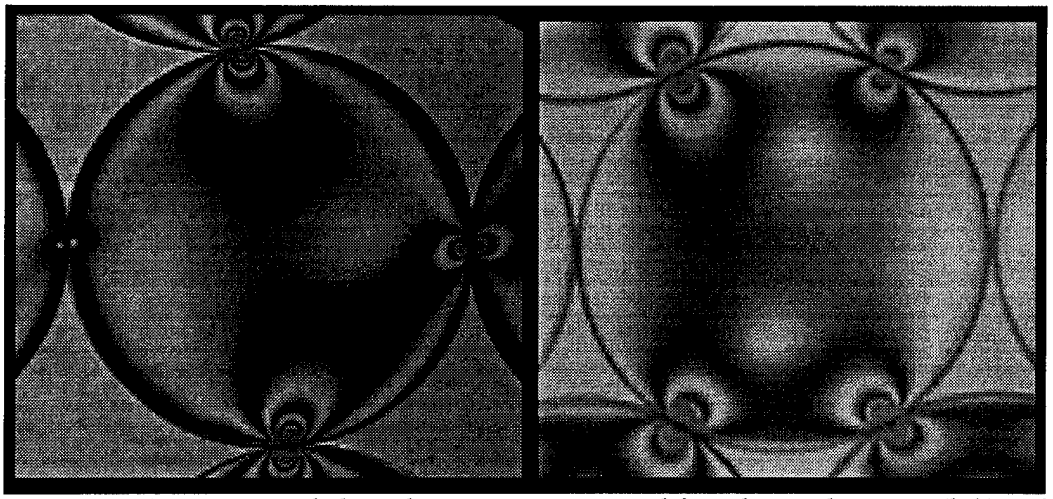

Figure 3.4. Comparison of photoelastic images captured from lens polariscope (left) and diffused light polariscope. Higher quality fringe contrast is available from the lens polariscope, which is used to capture images with better resolution for qualitative analysis.

3.2 Photosensitive Material

The models used to simulate grains in a particulate assembly were 0.75-in. diameter disks machined from PSM-1, a photosensitive polycarbonate material manufactured by Vishay Measurements Group. Vishay advertises PSM-1 as a material that is excellent for two-dimensional model work, is free of creep and edge effects, has excellent photosensitivity, is easy to machine, is non-brittle, and shows excellent transparency. It exhibits the following material properties:

Table 1. PSM-1 Material Properties

Elastic Modulus E, psi †	3.60×10^5
Poisson's Ratio ν †	0.38
Material Fringe Constant f_σ, psi-in ‡	92.0
P/Nd Constant, lb/in-fringe ‡	148.0
Thickness h, in.	0.25

† Property given by manufacturer
‡ Property calibrated in laboratory

Models were machined with an end mill at high rpm to avoid overheating of model boundaries, which could produce unwanted residual stress effects.

3.2.1 Calibration of Material Fringe Constant

To calibrate the material fringe constant f_σ of the PSM-1 photosensitive material used in these tests, the method suggested by Dally (1965) was employed.

It is known from the mechanics of materials that the principal stress difference along the horizontal diameter of a disk loaded in diametrical compression (Fig. 3.5) is given by the following equation:

$$\sigma_1 - \sigma_2 = \frac{8P}{\pi h D} \frac{D^4 - 4D^2x^2}{\left(D^2 + 4x^2\right)^2} \tag{3.1}$$

where D is the disk diameter, x is the distance along the horizontal diameter measured from the center of the disk, and h is the disk thickness.

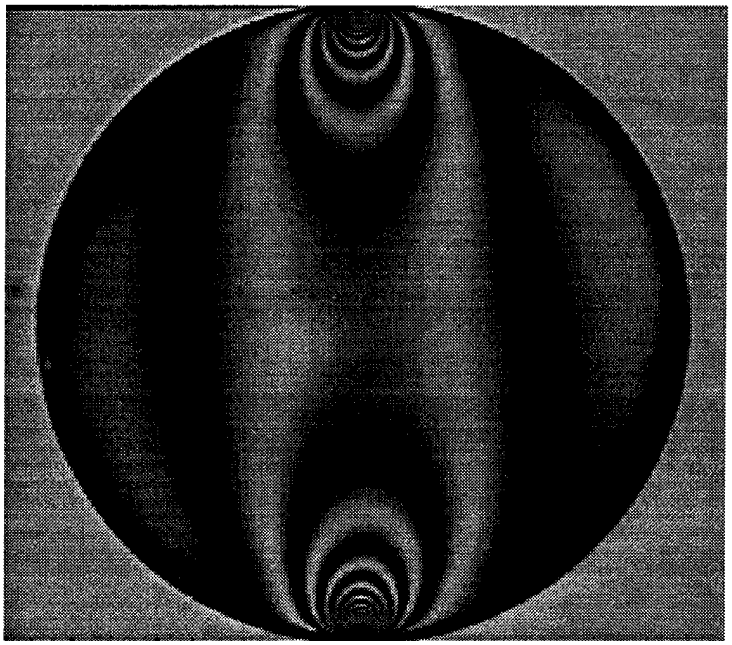

Figure 3.5. Photoelastic disk in diametrical compression.

It is also known from the stress-optic law that

$$\sigma_1 - \sigma_2 = \frac{Nf_\sigma}{h} \tag{3.2}$$

where N is the fringe order. Setting these equations equal and solving for the material fringe constant f_σ yields

$$f_\sigma = \frac{8P}{\pi DN}\frac{D^4 - 4D^2x^2}{\left(D^2 + 4x^2\right)^2} \tag{3.3}$$

If only the center of the disk is considered, $x = 0$, and Eq. 3.3 reduces to

$$f_\sigma = \frac{8P}{\pi DN} \tag{3.4}$$

Note that the value of f_σ is independent of the thickness of the disk. A test was arranged where the load on the disk in diametrical compression was applied in increasing increments while the fringe order at the center of the disk was read for each load. A plot of P versus N was made, and an average P/N value was found and substituted into Eq. 3.4 to find a value of f_σ.

The results of the above procedure are shown in Figure 3.6. The material fringe constant f_σ for PSM-1 was found to be 92.0 psi-in. To find the principal stress difference (and thus the maximum shear stress) in psi at any point in any model made from this material, this value of f_σ is simply multiplied by the fringe order N represented at that point and divided by the thickness of the model in inches (Eq. 3.2).

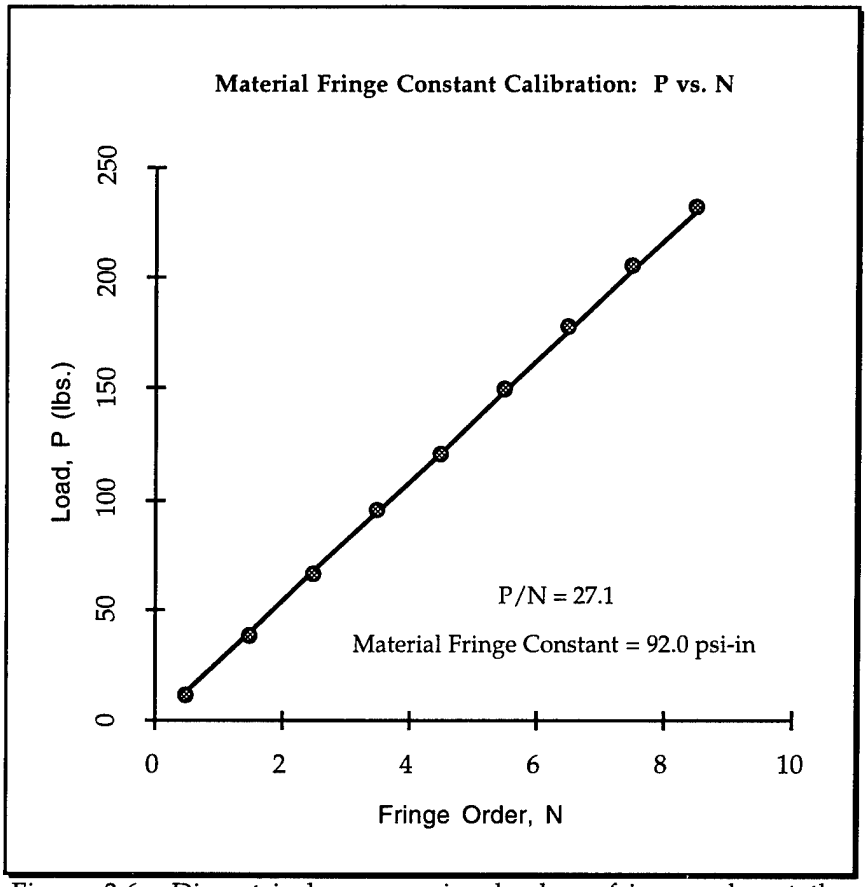

Figure 3.6. Diametrical compression load vs. fringe order at the center of the disk for the calibration of the material fringe constant f_σ. Calibration readings were taken on half-integer fringe intervals.

3.2.2 Calibration of P/Nd Constant

De Josselin de Jong and Verruijt (1969) determined that a concentrated load P acting on a semi-infinite plane produces circular fringes of constant maximum shear stress such that P/Nd is a constant for any given material (where N is the order of a circular fringe of diameter d). This constant can be easily calibrated for the PSM-1 material by capturing an image of a concentrated load on a semi-infinite plane (Fig 3.7) and measuring the diameter of fringes of known order.

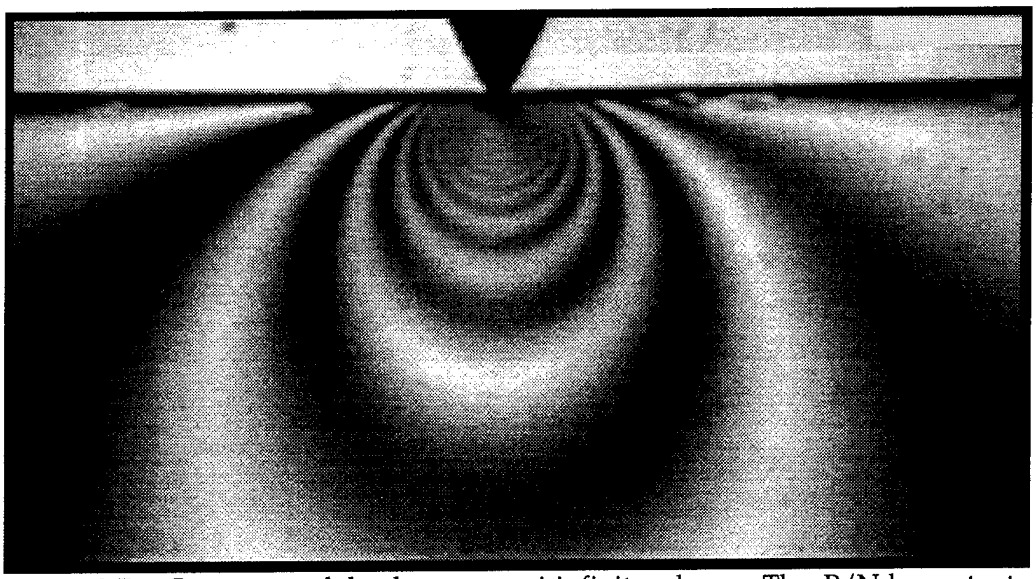

Figure 3.7. Concentrated load on a semi-infinite plane. The P/Nd constant, calibrated from this image, is 148 lb/in-fringe for the PSM-1 material.

Once this constant is known for the material, the magnitude of a force through a contact point can be found by measuring the diameter of a fringe of known order, and by solving for P from the constant. A detailed explanation of this procedure and its underlying theory is given in Chapter 4.

3.3 Disks Arrangements and Loading System

The 0.75-in. disks were arranged in two assemblies: a simple cubic packing to simulate a loose media and a simple stagger to simulate a dense media (Fig. 3.8). These packings illustrate the extremes of granular packings; that is, the disks cannot be packed any looser than the simple cubic packing nor any denser than the simple stagger.

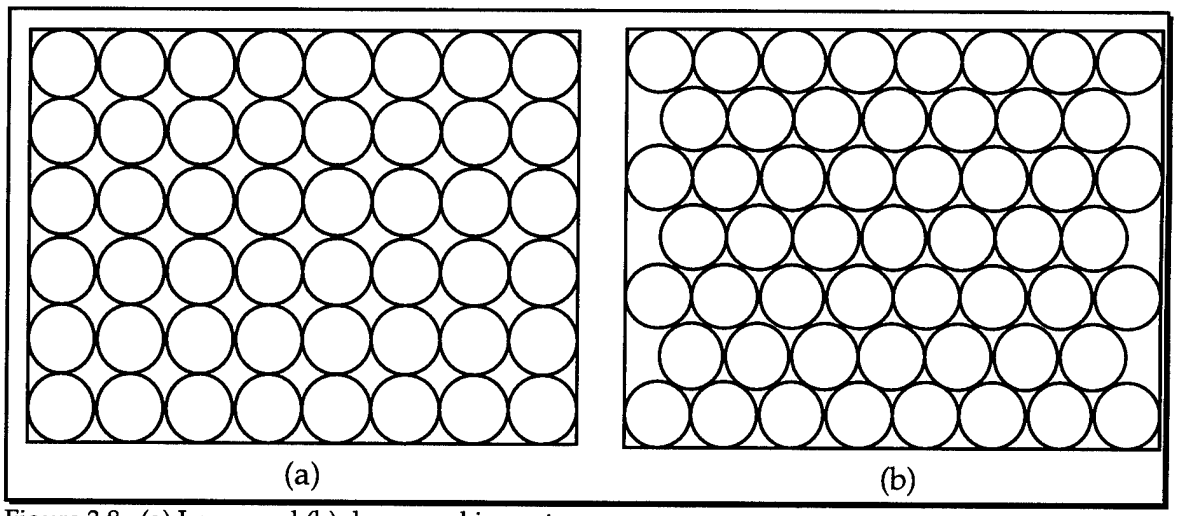

Figure 3.8. (a) Loose and (b) dense packing extremes.

The assemblies were placed into the simple shear box (Fig. 3.9) which consists of a base that moves horizontally by turning a screw; a top platen allowed to move only vertically, and two side walls allowed to pivot at the top (by pin connection) and bottom (by knife edge) to retain the parallelogram shape of the assembly (Fig. 3.10). The assembly was loaded vertically with a 100-psi pneumatic ram capable of applying 491 lb to the top platen, which contacted the top row of disks. The assembly was subject to simple shear by moving the base horizontally. The top platen was allowed to move vertically

as the assembly dilated or compressed while keeping the normal load constant.

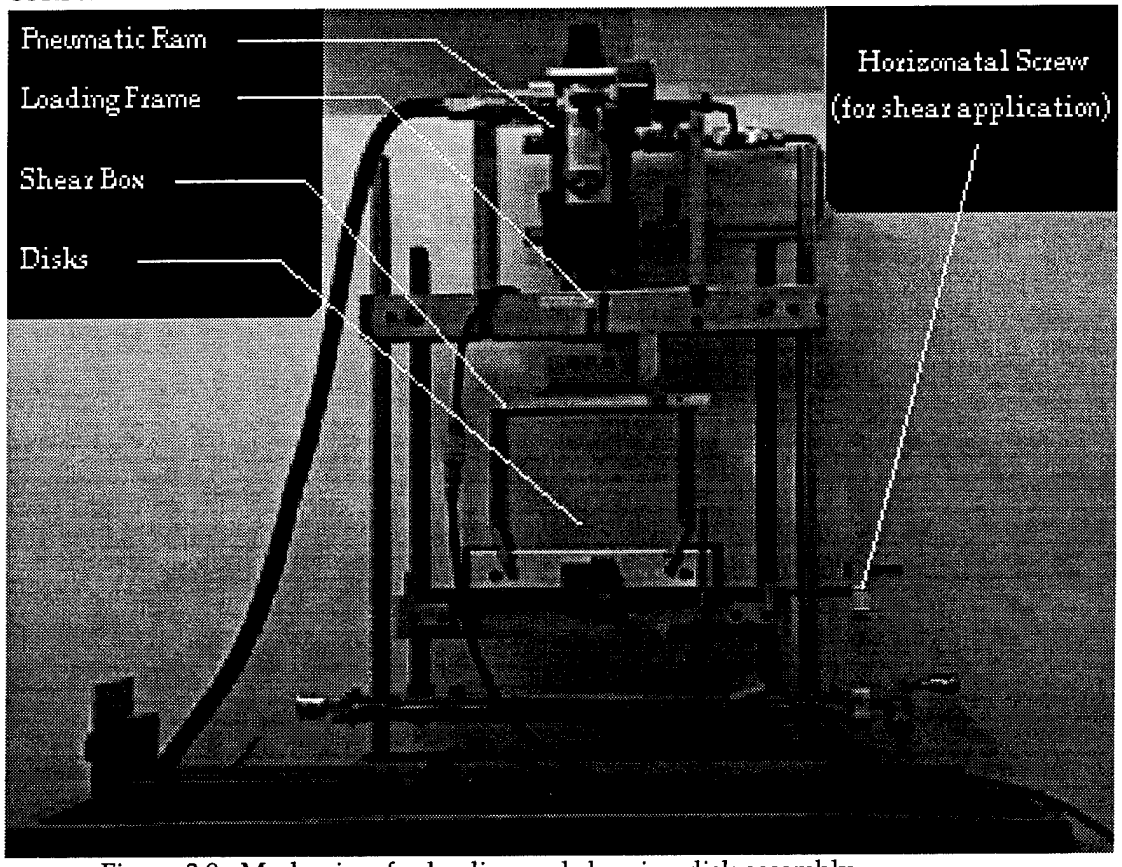

Figure 3.9. Mechanism for loading and shearing disk assembly.

Shear strains were calculated by measuring horizontal displacements of the base with a dial gauge, and volumetric strains were calculated from dial gauge readings of vertical displacements. Normal loads were measured by both a load cell and an air pressure gauge on the ram. Normal load was compared to the sum of the forces through the upper contacts in the top row of disks found by de Josselin de Jong and Verruijt's photoelastic force measurement technique.

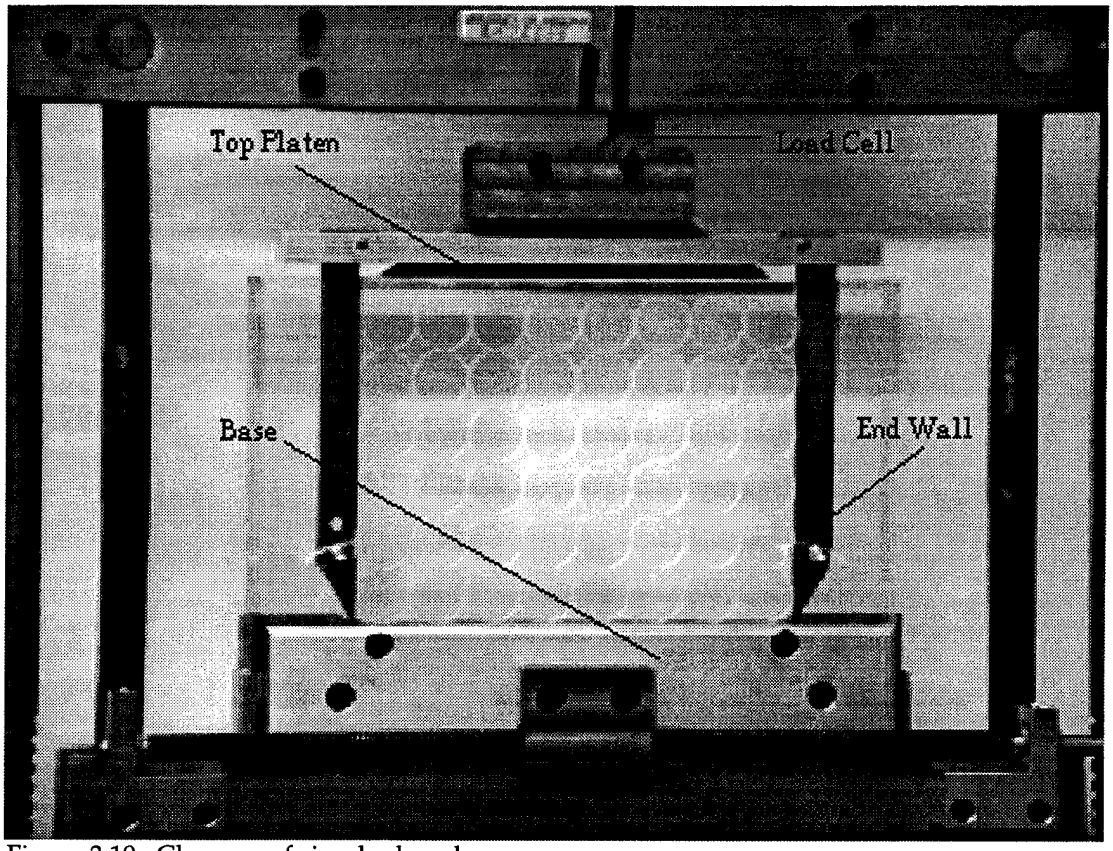

Figure 3.10. Close-up of simple shear box.

3.4 Image Processing System

Both still and moving photoelastic images were captured and processed by a digital image processing and analysis system consisting of the following components: (1) a Canon L1 camcorder with a 410,000 pixel, 0.5-in. CCD image sensor and a 15 times magnification zoom lens; (2) a Macintosh Quadra 840AV desktop computer with 32MB RAM, 1MB VRAM (video), and a Motorola MC68040, 40 MHz processor; (3) a Data Translation DT2255 frame grabber card; and (4) *NIH-Image*[1] image processing and analysis software.

Both qualitative and quantitative analyses were performed on photoelastic images. Full-field images of the entire assembly in the diffused-light polariscope were qualitatively analyzed for general stress transmission patterns under varying degrees of simple shear. Individual disk contact force magnitudes and directions were quantified by applying the modified version of de Josselin de Jong and Verruijt's technique to high-resolution images from the lens polariscope. This quantitative analysis was used to produce force vector plots for comparison with results from simple shear experiments and numerical algorithms.

---

[1] NIH Image is a public domain program and was written by Wayne Rasband at the U.S. National Institute of Health. It is available from the Internet by anonymous ftp from zippy.nimh.nih.gov or on floppy disk from NTIS, 5285 Port Royal Rd., Springfield, VA 22161, part number PB93-504868.

CHAPTER 4

DEVELOPMENT OF CONTACT FORCE ANALYSIS METHOD

4.0 Introduction

Paikowsky and DiRocco (1993) raised some concerns regarding the validity of the photoelastic method of contact force determination proposed by de Josselin de Jong and Verruijt (1969). In the present study it is shown that de Josselin de Jong and Verruijt (1969) method is valid provided that several adjustments are made to the analysis procedure to account for their assumptions. In this chapter the assumptions made by de Josselin de Jong and Verruijt (1969) are discussed and a modified version of their analysis technique is presented.

4.1 De Josselin de Jong and Verruijt Method of Force Analysis

De Josselin de Jong and Verruijt (1969) developed a relatively simple technique for using photoelastic fringe patterns to determine the magnitudes and directions of contact forces between cylinders. They made use of the linear relationship between the contact force P and the fringe order N to determine that

$$\frac{P}{Nd} = \text{constant} \tag{4.1}$$

where d is the diameter of the circular fringe of order N. This constant can be calibrated by measuring the diameter in inches of a circular fringe of known

order N near a contact point where a known force P acts. This value is constant for any model made from the same photosensitive material. Once the constant is known, any contact force can be determined by again simply measuring the diameter in inches of a circular fringe whose order is known, and solving for the magnitude of P from Eq. 4.1.

To arrive at this simple constant relationship, however, de Josselin de Jong and Verruijt had to make some assumptions, not all of which hold true all of the time. They first assumed that the fringes that develop in a disk are circles which pass through the point of contact. This assumption stems from Frocht's (1948) work on photoelastic analysis of a concentrated load on a semi-infinite plane, that is, a plane which extends to infinity in all directions on one side of an infinite line segment. In this case, the fringes that develop are indeed exact circles that pass through the contact point (Fig. 4.1) regardless of the angle of inclination of the force.

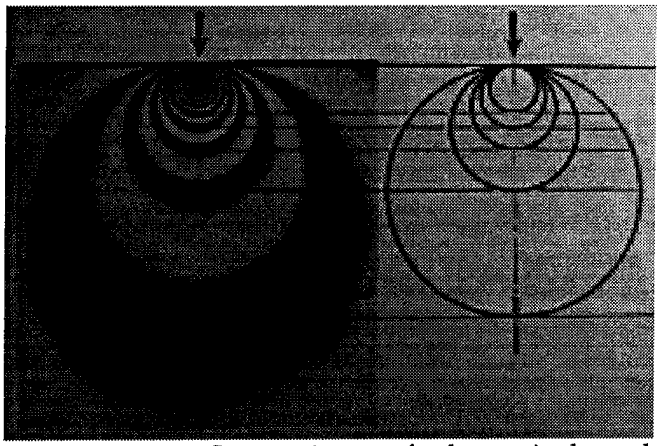

Figure 4.1. Comparison of theoretical and photoelastic stress patterns (from Frocht, 1948)

A contact force between two disks, however, is not exactly represented by a concentrated load on a semi-infinite plane, which can therefore be only

an approximation. There are three major factors that separate Frocht's work with a concentrated load on a semi-infinite plane and the case of contact between two disks: (1) the load characteristics (distributed vs. concentrated); (2) the plane boundaries; and (3) the potential superimposition of fringes from nearby forces (Table 4.1).

Table 4.1. Differences Between the Cases of (a) a Concentrated Load on a Semi-infinite Plane and (b) Contact Between Two Disks.

Category	(a) Concentrated Load on a Semi-Infinite Plane	(b) Contact Force Between Two Disks
Load Characteristics	Concentrated	Distributed
Plane Boundaries	Infinite Line Segment	Curved
Potential Superimposition of Fringes from Nearby Forces	No	Yes

As noted by Paikowsky and DiRocco (1993), these differences lead to quite different fringe geometries, making de Josselin de Jong and Verruijt's assumptions invalid. However, since each difference affects only certain fringe development areas, de Josselin de Jong and Verruijt's technique can still be used if these areas are avoided when choosing a fringe for analysis. Each of these categories are discussed below.

4.1.1 Distributed vs. Concentrated Loads

Fringes that develop as a result of concentrated loads have significant geometric differences, in the region near the point of contact, from those induced by distributed loads (Fig. 4.2).

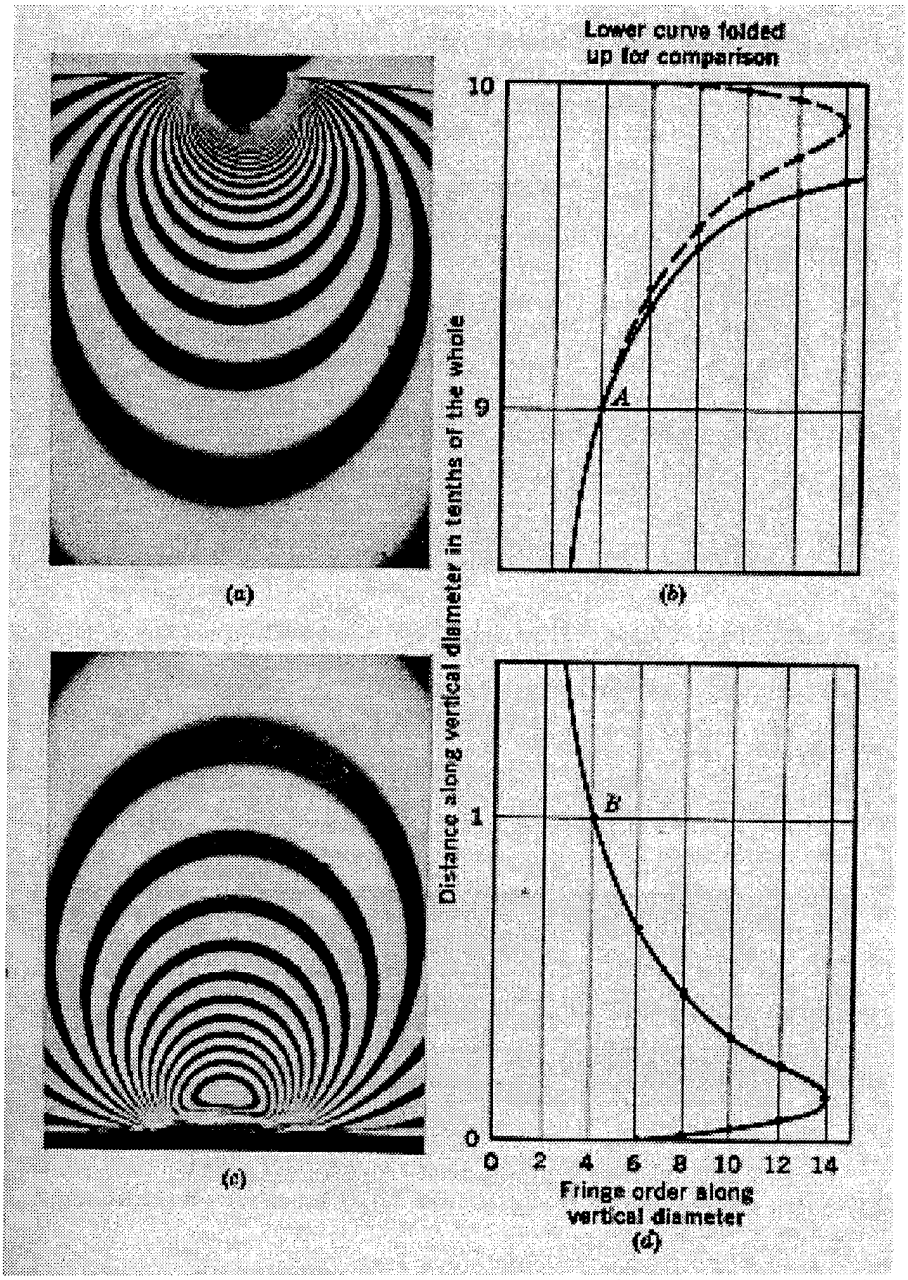

Figure 4.2. Close-up photoelastic images of disk contacts. (a) Concentrated Load (c) Distributed Load (b,d) Illustration of St. Venant's Principle (from Frocht, 1948)

Those very near the concentrated load are so close together that they begin to blend into one another until they are obscured by total light extinction. Those very near the distributed load, however, are quite clear, with a small,

ovalesque fringe surrounding a point of isotropy near the contact. The differences in fringe geometry that result from the two different loading cases imply that the choice of the fringe to be measured in de Josselin de Jong and Verruijt technique will affect the calculated magnitude of the contact force. To resolve this issue, St. Venant's principle can be invoked.

St. Venant's principle states that stresses produced in a body are identical when applied by any statically equivalent load system except over regions near the points of load application. Therefore, in regions sufficiently far away from the contact point, the stresses produced by the distributed contact load are identical to those produced by a concentrated load.

To quantify St. Venant's principle for the specific case of a disk in diametrical compression, Frocht tested the photoelastic disk in Figure 4.3 (the contacts of which are enlarged in Fig. 4.2) with both large (bottom) and small (top) contact areas which represent approximately distributed and concentrated loads, respectively. He found that stresses become identical at points further than 0.1 times the diameter of the disk from the contact point.

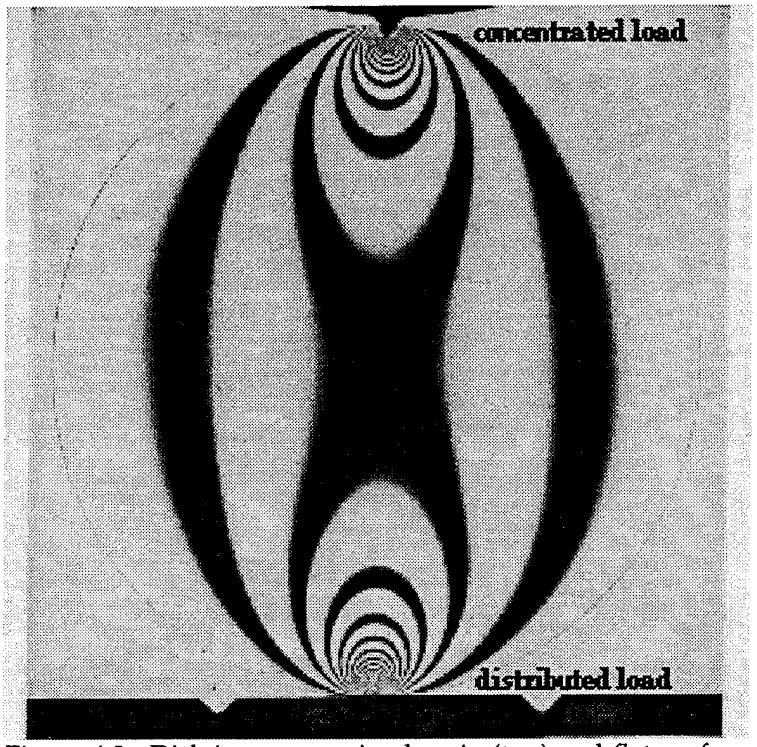

Figure 4.3. Disk in compression by pin (top) and flat surface (bottom) to approximate concentrated and distributed loads. (from Frocht)

De Josselin de Jong and Verruijt's technique assumes that all fringes are circles passing through the point of contact. From Frocht's tests it is clear that only a concentrated load produces exactly circular fringes in the region near the application of the load. But by St. Venant's principle it is clear that any fringe produced by a disk contact (distributed) force that is at least 0.1d from the contact point will be the same (circular) fringe that would have been developed by the application of a concentrated force. Hence, the fringe chosen for analysis must be at least 0.1d away from any contact to be free from loading-induced geometric distortions.

4.1.2 Semi-infinite Plane vs. Curving Plane

The fringes developed in a semi-infinite plane from a concentrated force will remain circular at any distance from the contact point (Fig. 4.1). In a disk, however, the fringes begin to be affected by the curving boundary of the disk (where the fringe order is forced to remain at zero) so that they become oblong rather than circular (Fig. 4.4). Again, because de Josselin de Jong and Verruijt's technique assumes that fringes are circular, a fringe so far from the contact that it loses its circularity cannot be used in analysis.

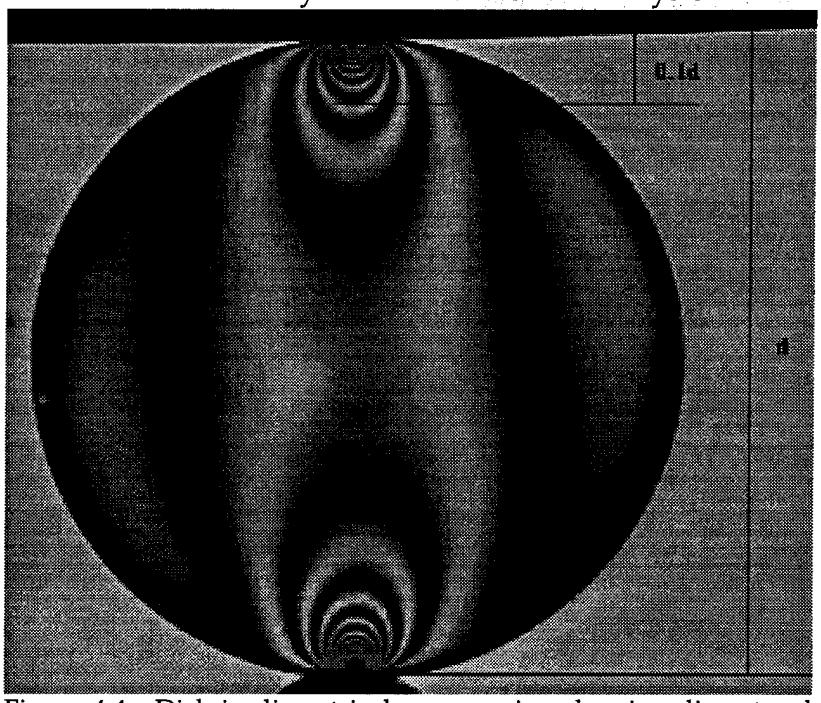

Figure 4.4. Disk in diametrical compression showing diameter d and 0.1d zone.

To compare fringes developed in a semi-infinite plane and a disk under similar loading conditions, a disk and semi-infinite plane were compressed together (Fig. 4.5). All fringes in the semi-infinite plane remain

circular regardless of the distance from the contact, while the disk's fringes with orders smaller than about 3.5 become distorted.

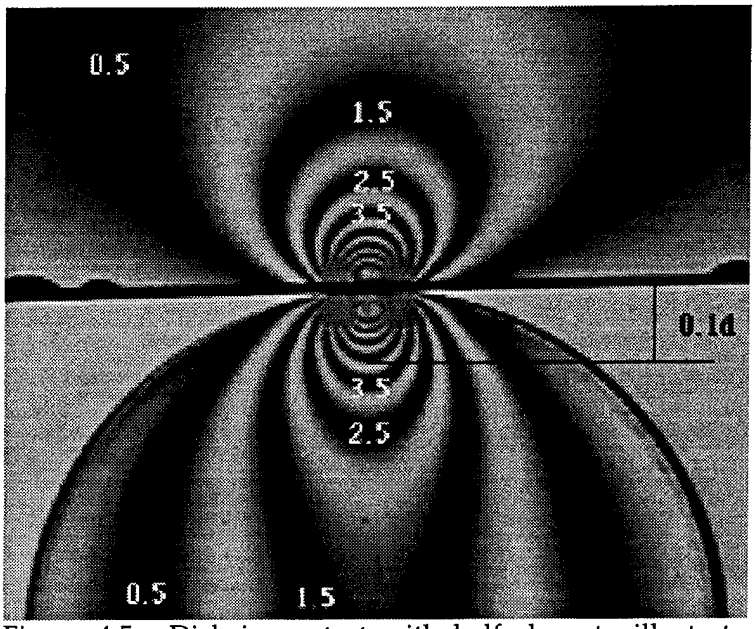

Figure 4.5. Disk in contact with half-plane to illustrate differences in fringe development between a disk and a semi-infinite plane. Note that the 3.5 order fringe in the disk is still a circle and is outside the 0.1d zone.

In summary, if a fringe developed by two disks in contact is too near the contact, the circular geometry that would have resulted from a concentrated load will be distorted by the distributed load. But if a fringe is too far from the contact, its circular geometry will be distorted by the disk boundaries so that it becomes an ellipsoid. The fringe chosen for analysis must then be between these two regions if it is to remain circular as presumed by the de Josselin de Jong and Verruijt technique.

4.1.3 Superimposition of Fringes

Paikowsky and DiRocco (1993) addressed, in considerable detail, the concern that since the fringe pattern is a result of the superimposition of stresses induced by *all* forces acting on the disk, the circular shape of a fringe induced by one force will be altered. This is true in regions further away from contact points, where multiple forces influence fringe shape, but the influence of a force in the region near its contact point dramatically overwhelms the influence of other relatively near forces.

Paikowsky and DiRocco performed tests to illustrate fringe superimposition. They loaded a 1.2" disk with two different loading schemes (Fig. 4.6a). The disk used was 1.2" in diameter, which means that the fringe chosen for analysis by de Josselin de Jong and Verruijt's technique, as superimposition becomes a factor further away from the contact, but does not affect fringes in the area of interest.

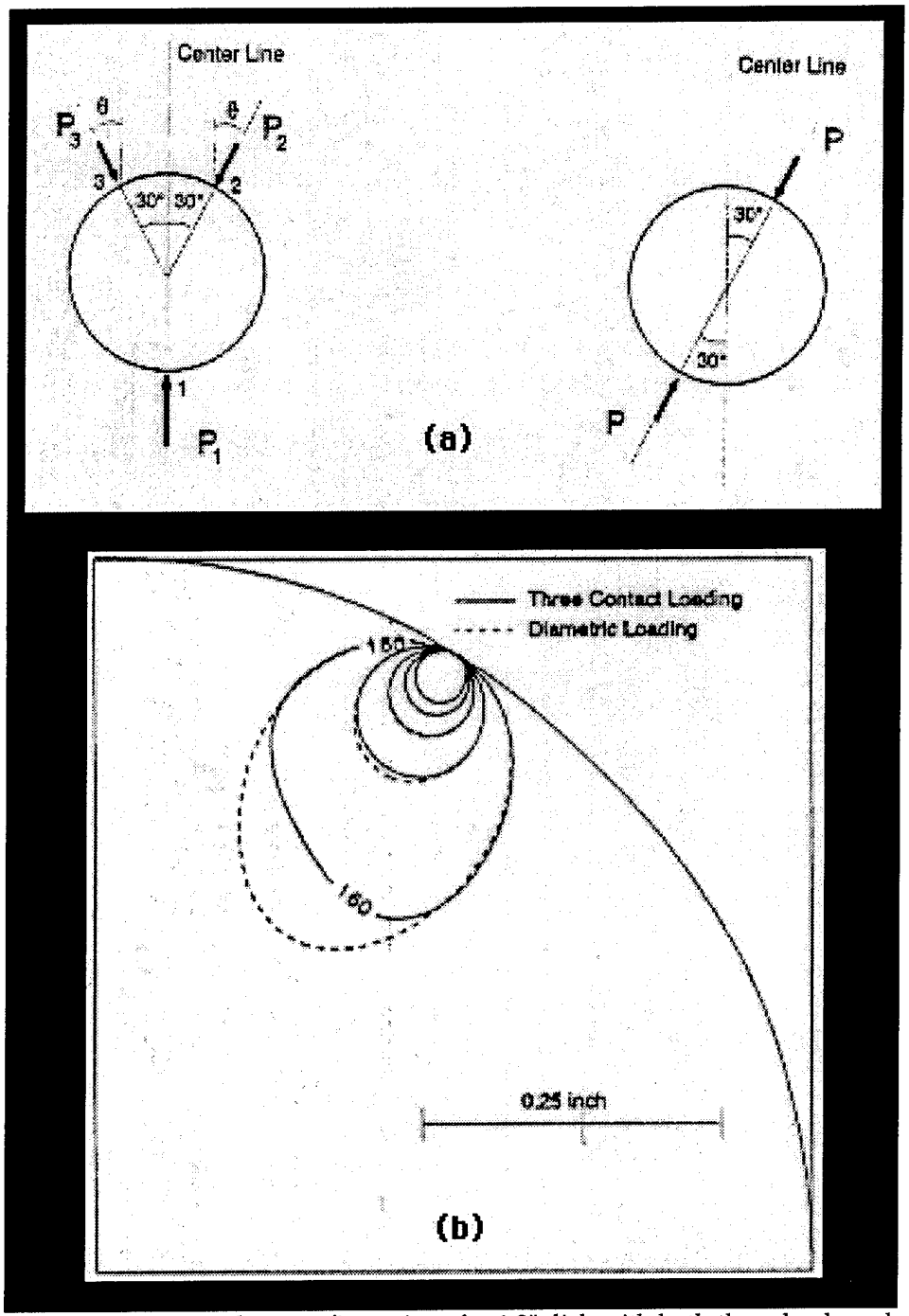

Figure 4.6. (a) Loading configurations for 1.2" disk with both three loads and diametrical loads. (b) Enlargement of fringes developed near upper right contact for both cases. Solid line represents three contact loading, broken line represents diametrical loading. Fringes are almost identical in the region 0.1d (.12") from contact. (from Paikowsky and DiRocco, 1993)

The loading situations that are investigated for the current work contain small enough loads that neighboring forces are not expected to have significant influence upon the fringes in the regions used for analysis.

It is concluded that de Josselin de Jong and Verruijt technique for determining contact forces simply by geometric measurement of fringes is indeed valid, provided that only fringes within a certain region are considered in analysis. Fringes measured for contact force determination must have a diameter of approximately 0.1 times the diameter of the disk and must pass through the contact point under analysis.

4.2 Application of Force Analysis Method

From a photoelastic image of two right circular cylinders (disks) in contact, it is possible to determine both the magnitude and direction of the contact force between them, provided that model material has been calibrated. By slightly modifying the method proposed by de Josselin de Jong and Verruijt (1971) for force determination through a single contact, and using an image processing system to automate several time-consuming steps, the load transmission pattern through a photoelastic model of a granular media can be determined.

Using a camcorder to capture digital images and a framegrabber card to store them on a computer eliminates the former need to shoot and develop careful photographs for later hand analysis. The image processing software allows geometric measurements such as distances and angles to be made quickly and accurately.

After the disks are packed into the loading device and subjected to load and shear, the assembly is placed in line with the polariscope. The camera is positioned to capture high-resolution close-ups of each disk. All images, including a full-field shot and close-ups, are captured at one sitting and stored for later analysis. After all images have been captured, the force magnitude and direction at each contact within the assembly is obtained by the following procedure.

4.2.1 Contact Force Magnitude

The full-field image (Fig. 4.7) is captured while the assembly is in the diffused-light polariscope for its greater viewing area. This image gives the general, qualitative stress transmission pattern and is used for later comparison with a force vector plot made from the quantification of forces at individual contacts.

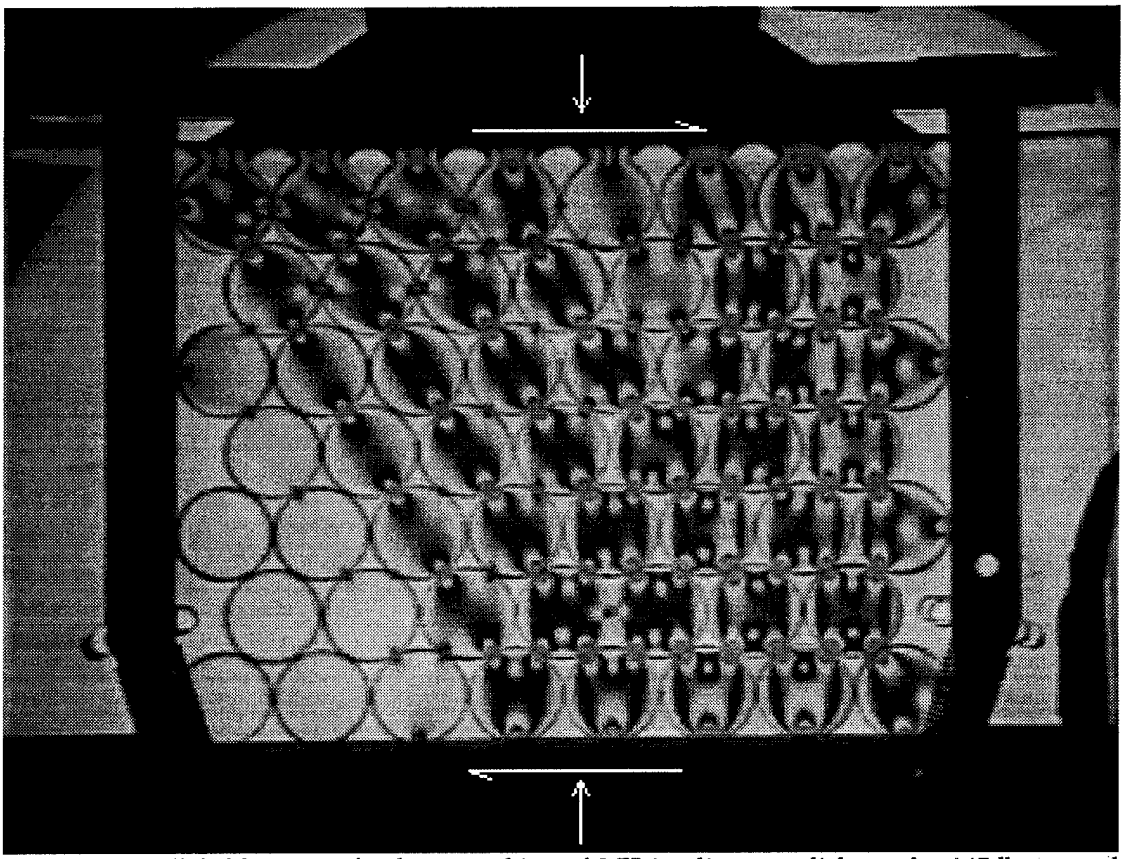

Figure 4.7. Full-field image of a dense packing of 0.75-in. diameter disks under 145 lb. normal load and a shear strain of 0.0186. Captured from a diffused-light polariscope.

Individual disk images are then taken from the *lens* polariscope for its sharper, more detailed images (Fig. 4.8). NIH Image 1.57 (Image), the image

processing software used for the current work, is then used to manipulate the image for all necessary measurements. The diameter of the disk, known in this case to be 0.75 in., is measured in pixels, and the scale of the image is calculated and recorded.

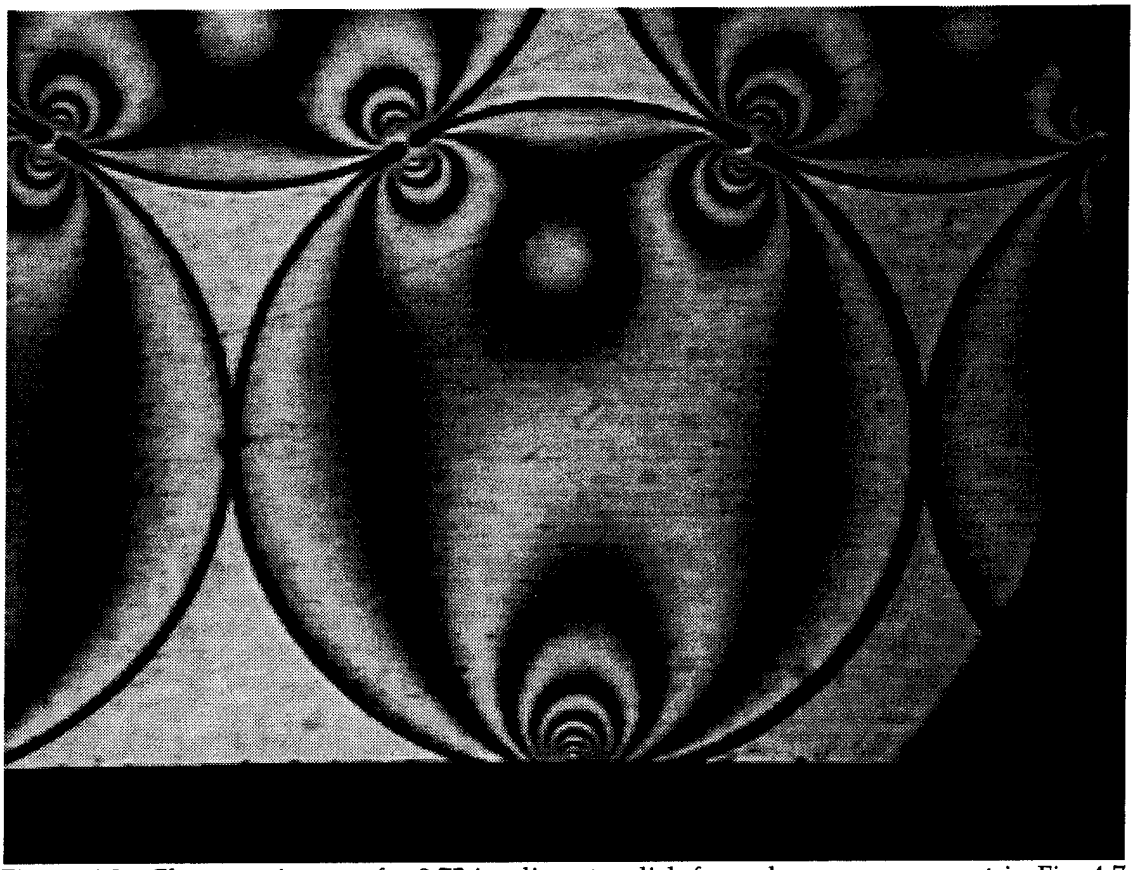

Figure 4.8. Close-up image of a 0.75-in. diameter disk from dense arrangement in Fig. 4.7 (bottom row, fifth from left). Note the improved contrast (darker fringes) in this image captured from a lens polariscope.

The contact to be measured is magnified for better manipulation. A circular region of interest (ROI) equal to 0.1 times the diameter of the disk is created and placed so that it approximates a contact force-induced fringe (Fig. 4.9). (It was shown above that a fringe produced by a distributed force on a disk boundary will have the same circular geometry as a fringe produced by a

concentrated force on a semi-infinite plane provided that the fringe diameter is approximately 0.1 times the diameter of the disk, and passes through the contact in question.) If a fringe does not fall exactly on the ROI, either (a) the fringe order at the ROI can be interpolated from the two bordering fringes, or (b) the ROI can be slightly reduced or enlarged to meet the nearest fringe.

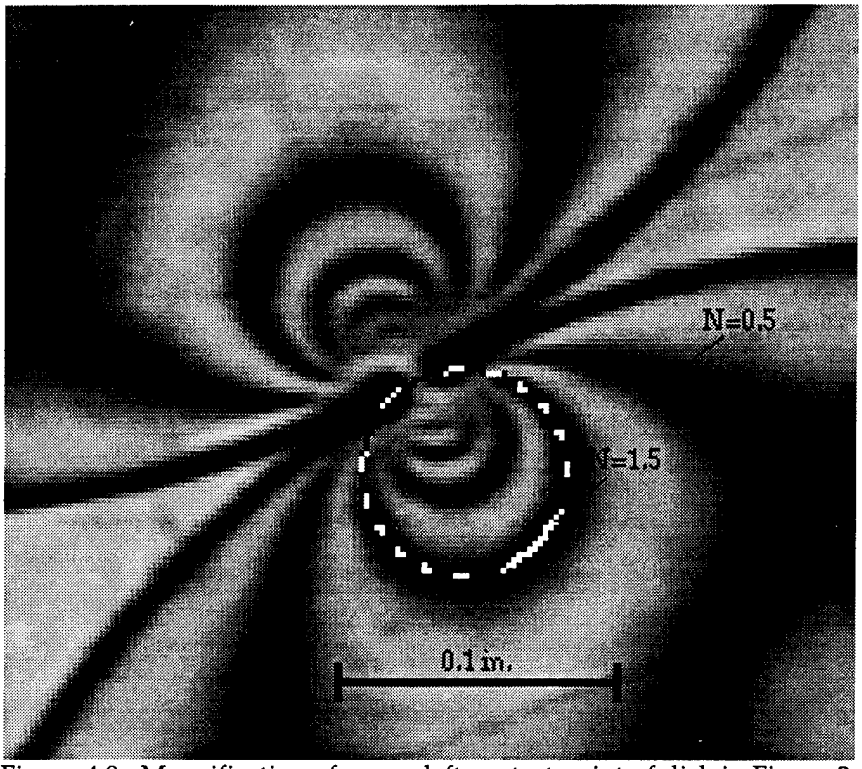

Figure 4.9. Magnification of upper left contact point of disk in Figure 2. ROI with diameter of 0.075, or 0.1d, is shown to coincide with fringe of order 1.5. Force can be calculated from the equation: P/Nd = constant.

It was shown that P/Nd is a constant for any given material (Eq. 4.1), where P is the force through the contact, N is the fringe order, and d is the diameter of the circle that best approximates the fringe. After this constant has been calibrated for the model material, the force through the fringe is easily calculated from the constant.

4.2.2 Contact Force Direction

It is also known that a contact force passes through the centroid of any contact-induced fringe whose diameter is greater than one-tenth that of the disk. Within the 0.1d region, fringes are often distorted by non-uniform boundary conditions that are intensified by distributed loading, and should be avoided. The centroid of a circular fringe that is approximated by an ROI is easily calculated by Image. The line segment that connects the contact point and the centroid of the measured fringe coincides with the line of action of the force (Fig. 4.10).

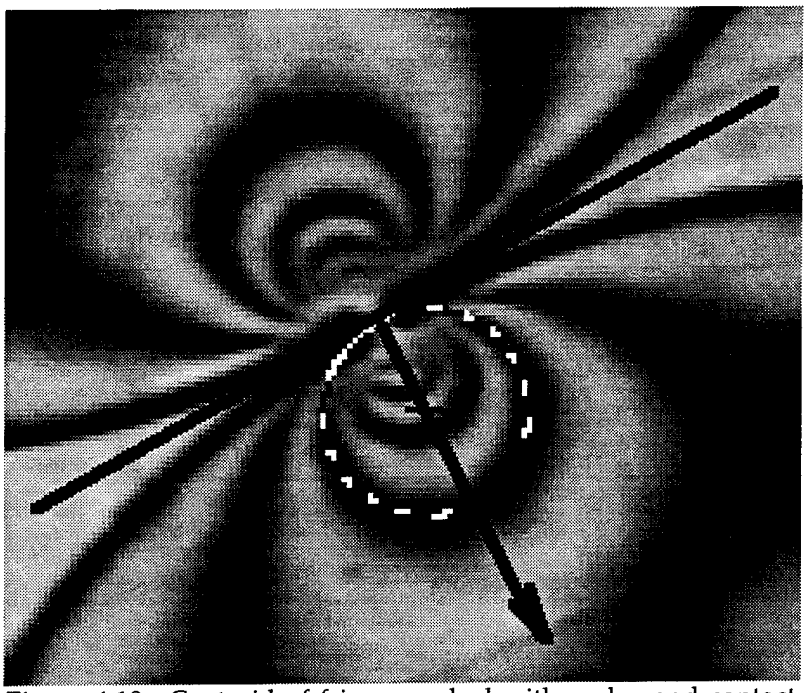

Figure 4.10. Centroid of fringe marked with a plus and contact force vector plotted with origin at the contact and passing through fringe centroid. Angle with contact plane can easily be calculated with Image.

4.3 Semi-automation

The above procedure has been semi-automated by programs written to take advantage of several of Image's built-in measurement features. Routines were written that allow incremental manipulation of the size and position of the ROI, that automatically calculate the force with manual input of only the fringe order, and that find and mark the center of the ROI for determination of contact force direction. If large assemblies with many contacts are to be analyzed, it may be worthwhile to attempt the automation of fringe order determination based on coordinates of the disk boundary and contacts, and fringe/background brightness contrast. The assemblies analyzed for this work were small enough that manual analysis was less time-consuming than attempting to program detailed automation. The semi-automation, however, allowed more rapid measurement and recording than would have been achieved by hand-measuring photographic prints.

The force magnitude and direction for each fringe is then recorded in a file, and used to plot the force vector diagram (Chapter 5) for the assembly. Creation of a force vector diagram is also a procedure that could potentially be automated within Image if desired, but was not done for this work for the reasons mentioned above.

CHAPTER 5

RESULTS AND DISCUSSION

5.0 Introduction

Several qualitative observations have been made regarding the behavior of the disk assemblies in simple shear. These include the frictional behavior between disks, disks rotations, volumetric strains, boundary stress uniformity, and load distribution. Force vector plots have been obtained for different stages of simple shear deformation of the disk assemblies.

5.1 Behavioral Observations

5.1.1 Interdisk Frictional Behavior

Motion pictures reveal that a slipping and locking mechanism exists at disk contacts. As the disks are forced to move relative to one another, their surfaces either slide past or lock together, the latter occurring when the interface friction between the disk surfaces is sufficient to resist the force driving the relative movement.

Throughout the range of the shear deformation, the disks continuously engage and disengage one another. Interdisk forces lock the disks together, then overcome the friction between them by either growing too large for the friction to resist, or by acting at an angle larger than the maximum angle of friction resistance. In a large granular assembly such as sand, this mechanism is quantified by assigning the material an angle of

internal friction, an average value that is affected by grain shape, size, distribution and constituent minerals.

5.1.2 Volumetric Strain

Granular materials have been observed to undergo volume change when sheared in triaxial, direct shear, and simple shear tests. Densely packed materials tend to dilate (increase in volume), while loosely packed materials tend to compress (decrease in volume). Dense packings exhibit significant particle interlocking which must be overcome when sheared, forcing the particles to roll up and over one another, increasing the volume of the specimen. Loose packings show less particle interlocking, so the grains can slide into void spaces, resulting in compression.

In the present study, extremes of both conditions are examined. The loose assembly of disks, described as a simple cubic packing, represents the loosest way in which the disks can be arranged, one stacked directly upon another. The dense assembly, described as a simple stagger, is the densest possible arrangement of disks (Fig. 5.1).

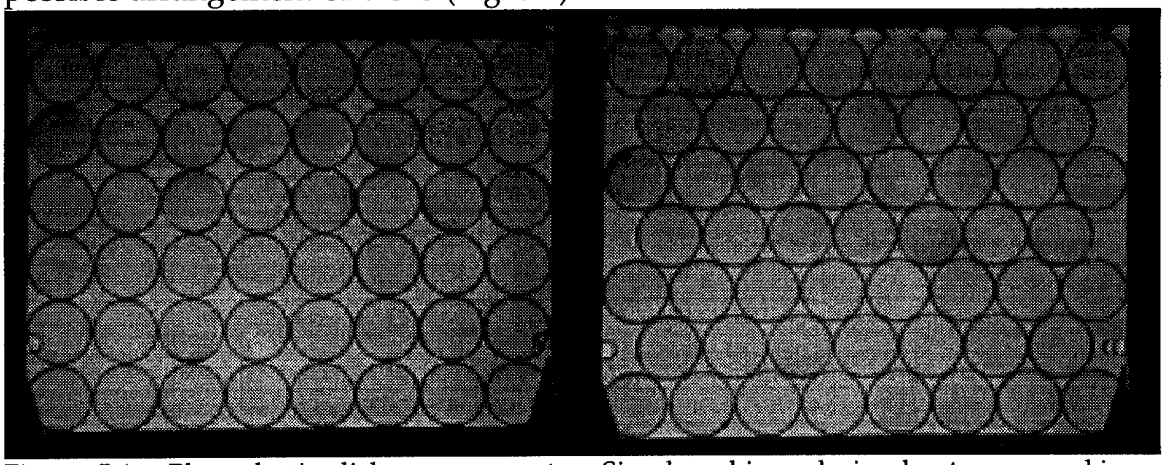

Figure 5.1. Photoelastic disk arrangements. Simple cubic and simple stagger packings representing loose (e_o = 0.27) and dense (e_o = 0.15) granular assemblies, respectively.

Volumetric strain is often plotted against axial strain in triaxial and direct shear tests or against shear strain in simple shear tests. Volumetric strain, ε_v, is defined as

$$\varepsilon_v = \frac{\Delta V}{V_o} \tag{5.1}$$

where ΔV is the change in volume of the specimen and V_o is its initial volume. Since only vertical movement of assembly boundaries is allowed, $\Delta V = \Delta y$ where Δy is the vertical movement of the top platen, and $V_o = h_o$ where h_o is the initial height of the assembly. Volumetric strain versus shear strain plots for both the dense and loose arrangements of disks follows similar patterns to those of sands (Fig. 5.2).

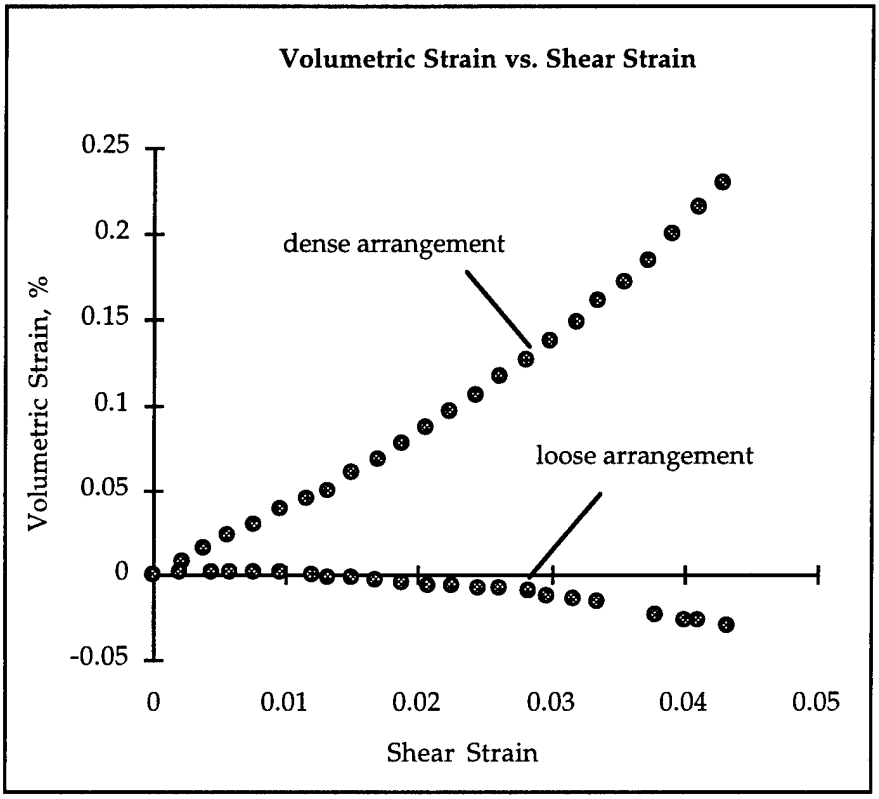

Figure 5.2. Volumetric strain vs. shear strain. Comparison of volumetric changes with shear strain for dense and loose disk arrangements.

Normally, a dense sand will exhibit some compression during the initial stages of shearing, and will strongly dilate thereafter. Since the dense disk assembly is in its densest possible state, it shows no initial compression and exhibits immediate dilatation. Likewise, a loose sand, after some shearing, will become denser by compression and, because of its increased density, will begin to show a lower rate of compression. The loose disk assembly is in its loosest state, however, and therefore requires significant shearing to reach a dense enough state to begin to exhibit the reduced compression rate.

5.1.3 Disks Rotations

Disks rotations in a particulate medium, depending on the degree of particle angularity, can significantly affect the path by which a load is transferred through the medium. Understanding why and how individual disk rotates during simple shear is an integral part of an attempt to model its behavior.

To measure the rotation of individual disks during simple shear, a reference line (appearing as a dark line in the photoelastic images) was etched across the diameter of a representative disk in the assembly, and its position was measured before and after a desired simple shear strain was applied (Figs. 5.3, 5.4, 5.5).

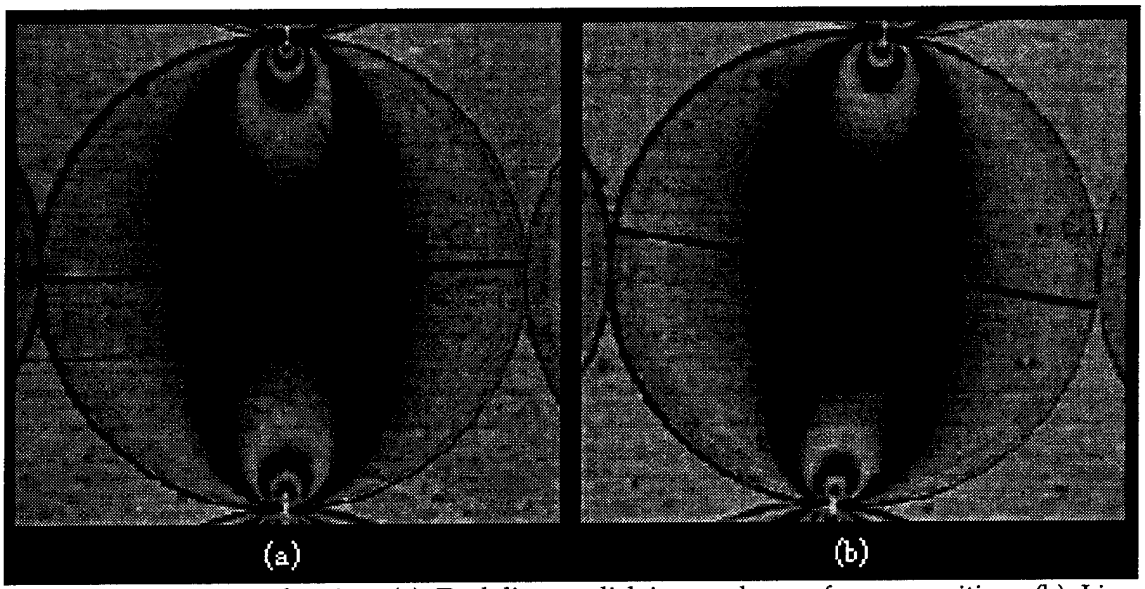

Figure 5.3. Rotation of grains. (a) Dark line on disk in pre-shear reference position. (b) Line in post-shear position indicates 11° clockwise rotation during shear. Photoelastic image shows no stress band development on the vertical planes indicating that no locking with neighboring disks is occurring on these planes.

In the loose packing, which tends to deform as rigid columns of particles sliding relative to one another, individual disk rotation was observed in some cases. In general, if the vertical contacts of a disk in this arrangement was sliding relative to neighboring disks, the individual particle rotated relative to the loading frame (Fig. 5.3). If the vertical contacts are exhibiting friction locking, the disk will exhibit much less rotation relative to the frame (Fig. 5.4).

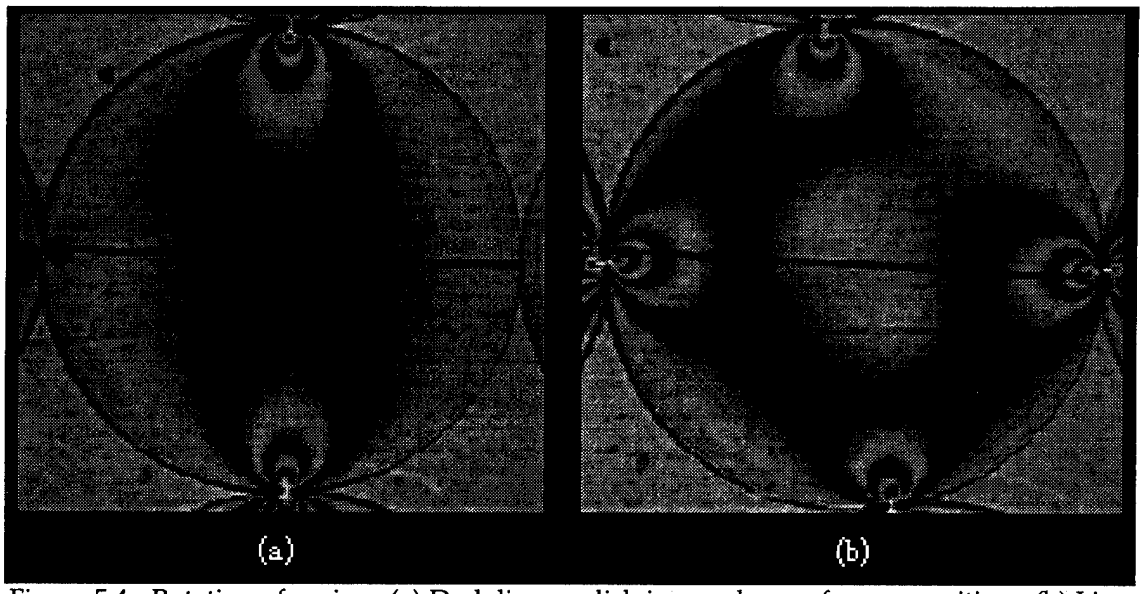

Figure 5.4. Rotation of grains. (a) Dark line on disk in pre-shear reference position. (b) Line in post-shear position indicates negligible rotation. The stress band development on the vertical contacts indicates locking with these neighboring disks. This mechanism is hypothesized to be responsible for the difference in rotation behavior from the disk in Fig. 5.3.

A disk in the densest possible arrangement has been observed to remain without rotating relative to the frame regardless of whether it is sliding or locking with neighboring disks (Fig. 5.5).

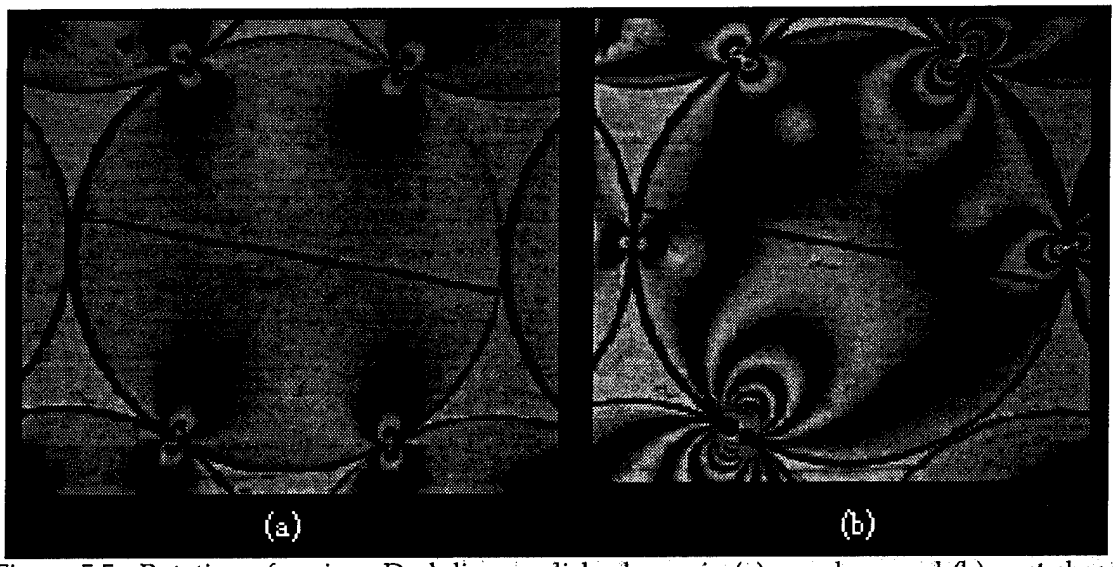

Figure 5.5. Rotation of grains. Dark line on disk, shown in (a) pre-shear and (b) post-shear positions, undergoes no rotation during shear.

5.1.4 Load Distribution

The observed pattern of stress transmission in the loose disk arrangement under simple shear is somewhat random. Before shearing, the disks are arranged in eight columns of six disks each, and the vertical load applied by the top platen is transmitted vertically through each column (Fig. 5.6).

As shear is applied, the disks begin to slide relative to one another at those contacts where the interdisk friction is overcome, and lock together at those where the friction provided between disks is enough to resist the driving contact force. The selection of these contacts appears, from resulting photoelastic images, to be quite arbitrary. Three tests ran under the identical vertical loads and shear strains exhibited significantly different stress transmission patterns (Figs. 5.7a-c).

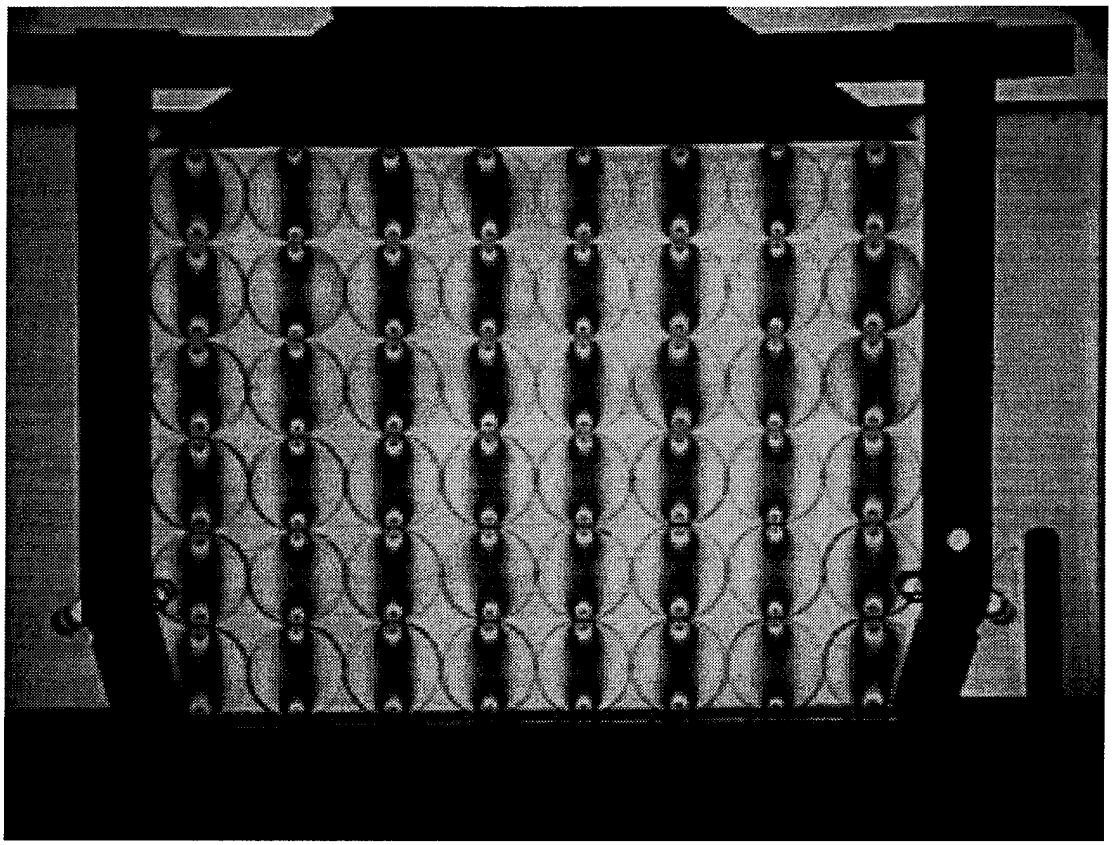

Figure 5.6. Loose packing before shear strain application. Notice that load is transferred vertically through each column of disks.

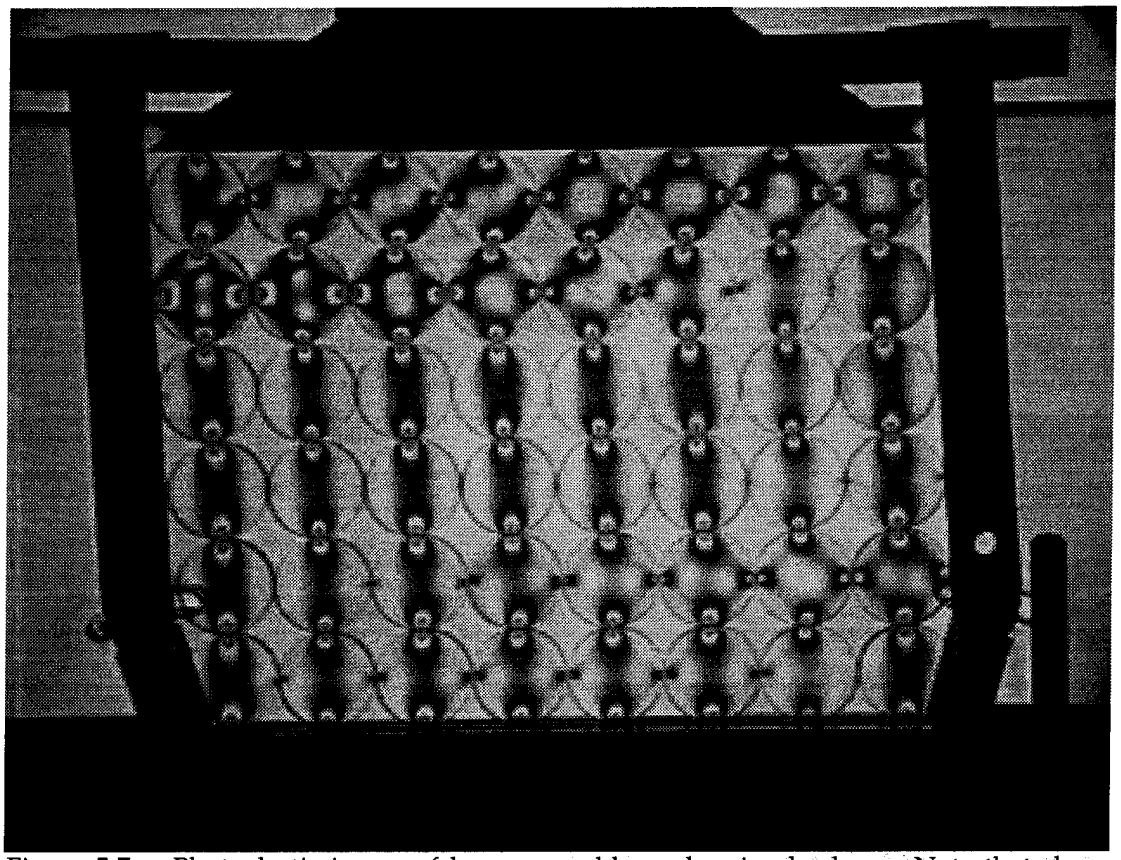

Figure 5.7a. Photoelastic image of loose assembly under simple shear. Note that shear changes the stress transmission pattern nonuniformly such that some vertically oriented disk contacts show load transfer while others do not.

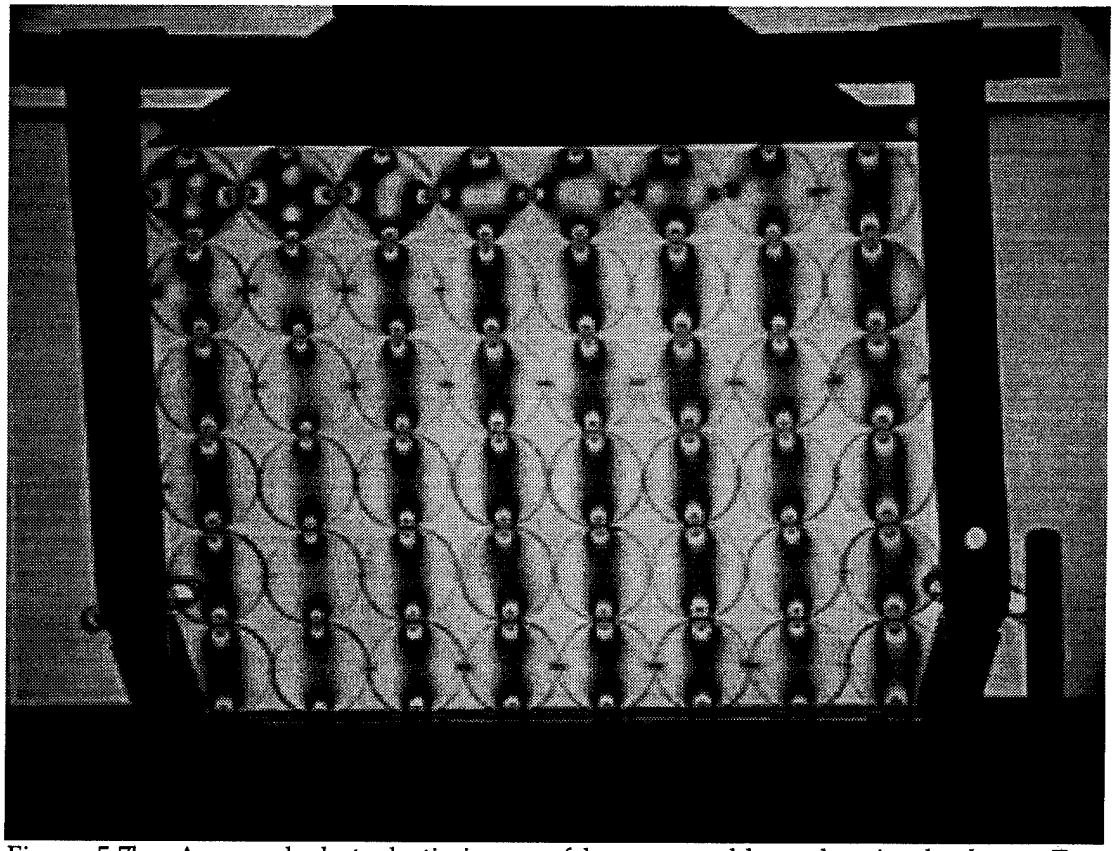

Figure 5.7b. A second photoelastic image of loose assembly under simple shear. Test procedure was exactly the same as in Fig. 5.7a, applying identical vertical loads and shear strains. Note that the stress is transferred across different vertical contacts in the two figures.

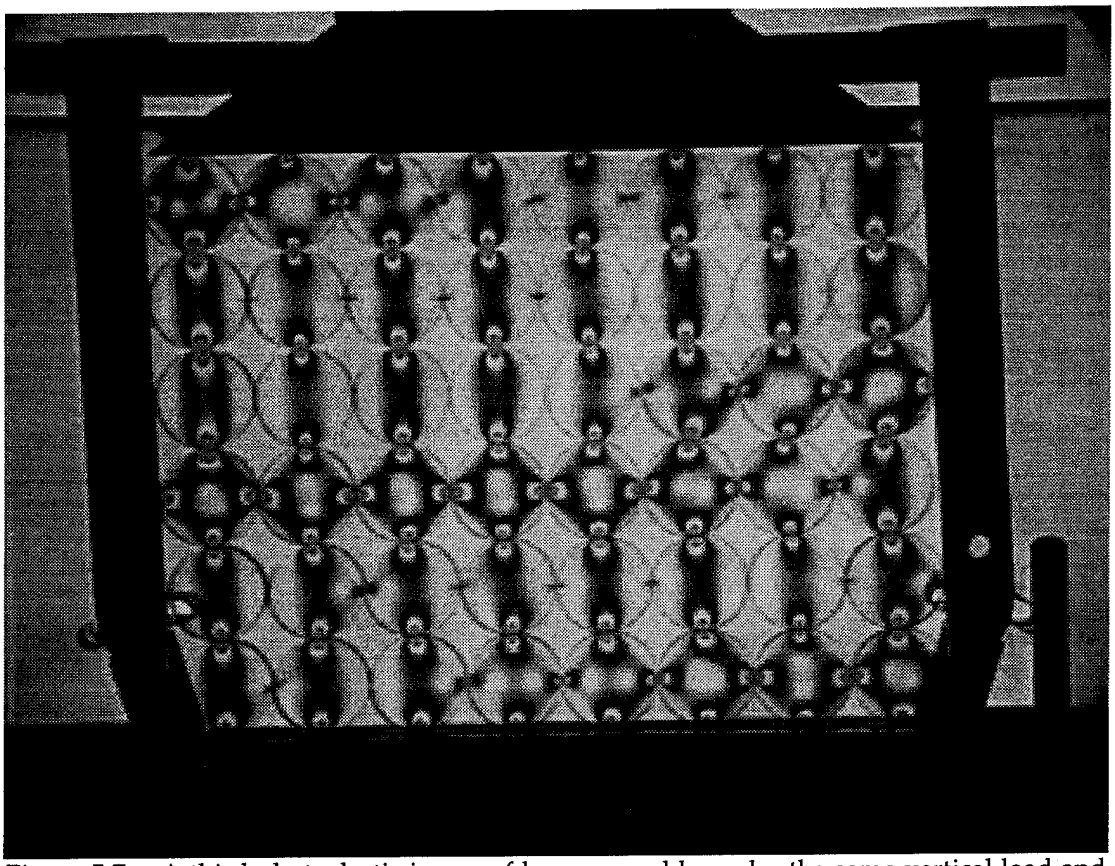

Figure 5.7c. A third photoelastic image of loose assembly under the same vertical load and shear strain as in Figs. 5.7a and 5.7b. Stress transmission pattern is again transferred across different vertical contacts.

This is partially attributable to the nature of the loose packing. In simple shear, the vertical load that initially caused stress to flow vertically is redirected to flow across the box's shorter diagonal. In the idealized loose packing, the disks are arranged such that the contacts are 90° from one another, making flow impossible between two diagonal (i.e., non-contacting) disks. The expected diagonal flow pattern is, however, exhibited by the dense packing. Load distribution in the dense assembly is discussed in detail in Section 5.2.1.

Drescher and de Josselin de Jong (1972) explained this phenomenon with a "double-sliding free-rotating model", in which the two mechanisms of rigid-block sliding and rotation are separate but simultaneous. This model was derived from Horne's (1965) observation that the deformation of a granular material results from the relative movement of instantaneously rigid groups of particles, that constantly redistribute themselves in division and coalescence.

There are infinite combinations in which the assembly of disks can form rigid, sliding blocks (Fig 5.8a,b), then rotate, if necessary, to retain the geometric boundary constraints of the assembly. From all combinations, the one that provides the least resistance is chosen.

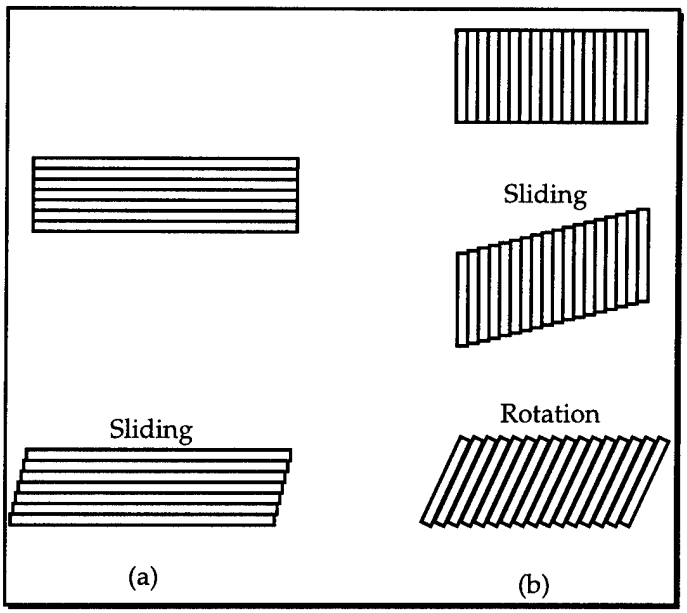

Figure 5.8. Bookstack analogy of simple shear deformation (from de Josselin de Jong (1972).

Microscopic variations on the surface of the disks, left behind from machining, produce a non-uniform roughness over the surface of one disk,

and a non-constant roughness from disk to disk. These variations provide the frictional variation throughout the assembly required to produce inconsistent deformation combinations from test to test in an apparently homogeneous assembly. Such microscopic inconsistencies are not accounted for in continuum mechanics but which can significantly affect load distribution calculations.

5.1.5 Uniformity of Boundary Stress

Theoretical approaches based on elasticity (Roscoe, 1953) and elastoplasticity (Budhu and Britto, 1987), and experimental approaches (Stroud, 1971; Budhu, 1979) have shown that nonuniformities develop along boundaries of specimens undergoing simple shear deformation. Nonuniform distribution of both shear and normal stresses along the top and bottom boundaries of sand specimens was measured in the Cambridge University simple shear device which was equipped with contact stress transducers, (Budhu, 1983).

Photoelastic analysis can detect nonuniform stress development. Images of the dense assembly of photoelastic disks showed that the normal stress nonuniformity is similar to that observed in tests on sand (Fig. 5.9).

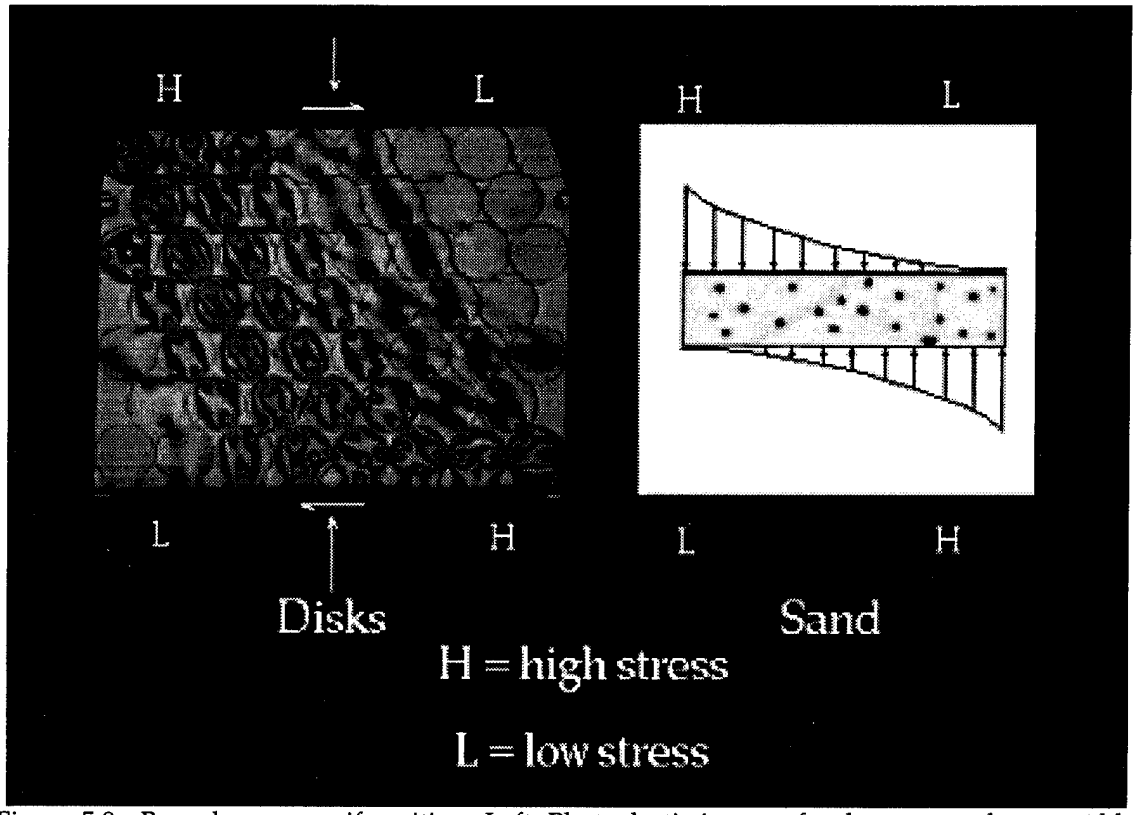

Figure 5.9. Boundary nonuniformities. Left: Photoelastic image of a dense granular assembly under simple shear. Note that disks at top right and bottom left show no stress, while the opposite corners exhibit high stresses. Right: Diagram showing normal stress nonuniformities of a simple shear test on sand (from Budhu, 1980). Experiments on disks and on sand qualitatively agree.

As the specimen is sheared, the stress flow, which was initially vertically oriented, gradually shifts to one that flows along the shortest diagonal of the shear box. This is reflected in stress distributions on the top and bottom boundaries wherein higher stresses developed on the top left and bottom right corners.

5.2 Comparison With the Lattice Model

On application of the vertical load with no applied shear strain, the internal distribution of stresses in the dense disk assembly, as revealed by the photoelastic image (Fig. 5.10), was not uniform. Under a relatively small shear strain (but large enough to exhibit visible directional stress flow) the disks formed rigid diagonal columns that transmit the applied normal force across the shorter box diagonal (Fig. 5.11).

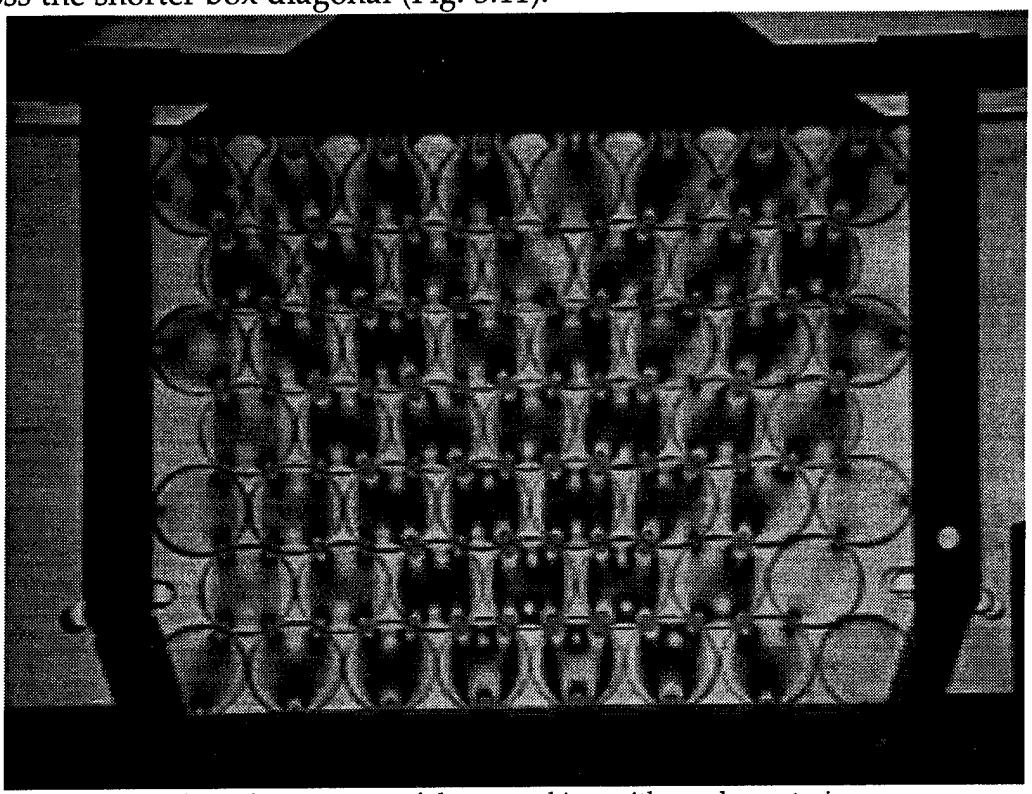

Figure 5.10. Photoelastic image of dense packing with no shear strain.

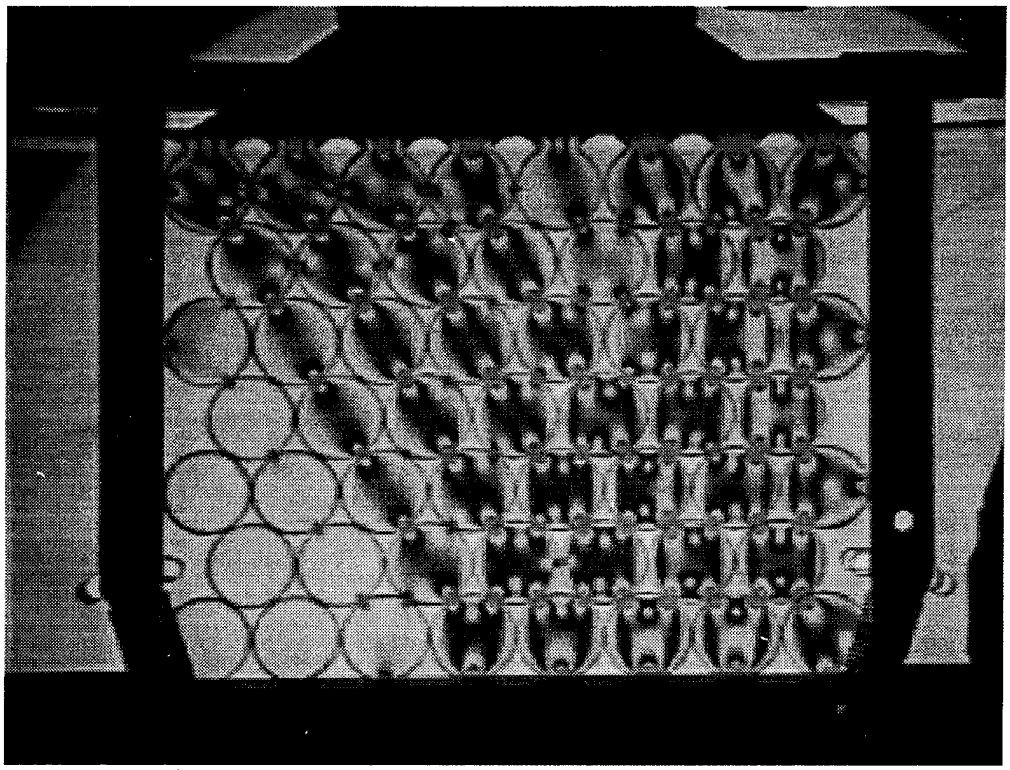

Figure 5.11. Photoelastic image of dense packing with shear strain (0.1%).

Force vector plots (Fig. 5.12a) from the photoelastic image (Fig. 5.10) showed that the vertical applied force is mainly transmitted by two pairs of inclined columns of disks originating from the two extreme pair of disks at the top right and left corners and meeting at the middle pair of disks at the bottom boundary. The lattice model predicted a similar force distribution (Fig. 5.12b) except that rather than two pairs of columns there are two distinct columns originating from the disks at the extreme corners of the top boundary meeting at the middle pair of disks at the bottom boundary. These results are intuitively correct since the disks at the extreme corners of the top boundary have only two neighboring disks each to transmit the vertical load compared to four disks for the other disks on the top boundary.

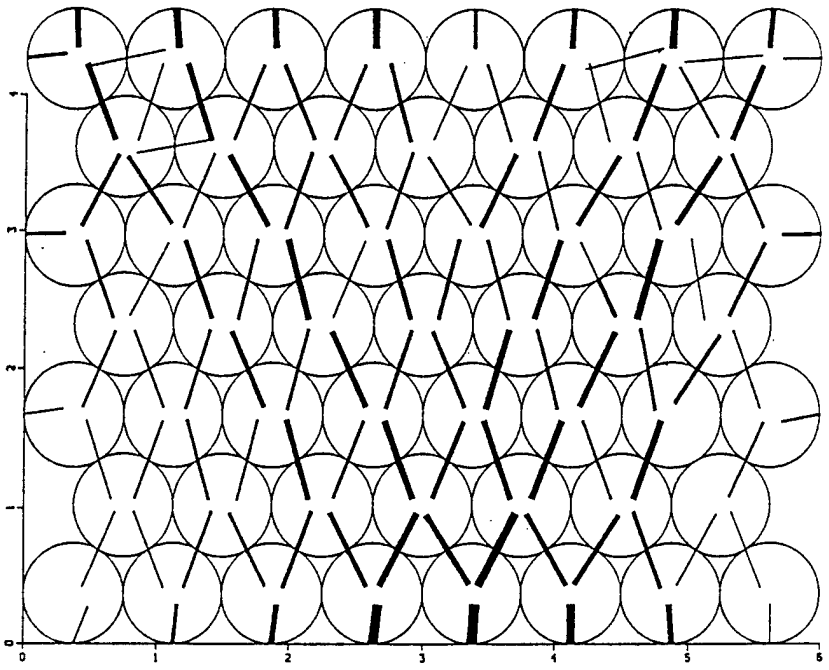

Figure 5.12a. Contact force vector plot of dense assembly at zero shear strain (Fig 5.10) created by using the modified version of de Josselin de Jong and Verruijt's method of finding contact force vectors.

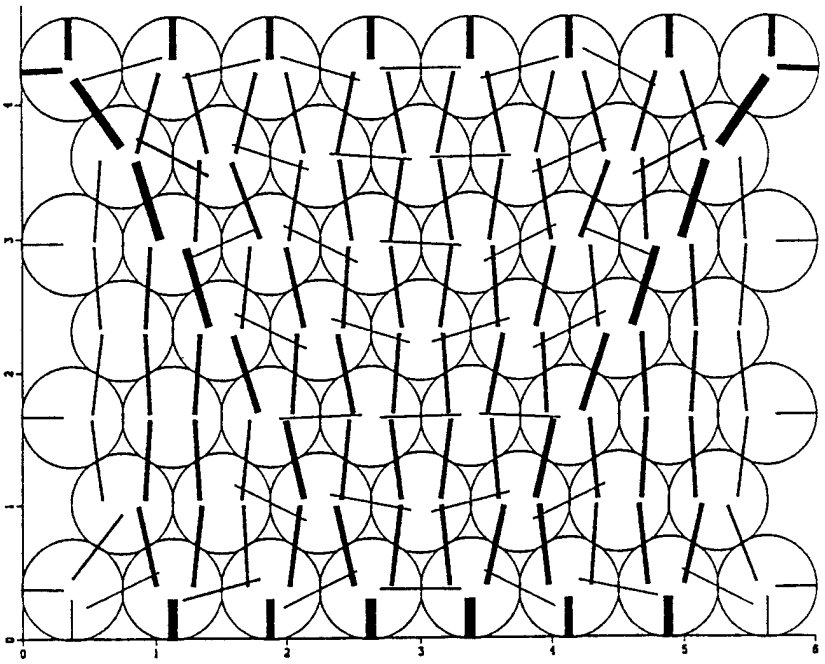

Figure 5.12b. Contact force vector plot at zero applied shear strain (Fig 5.10) predicted by the lattice type model.

The nonuniform distribution of load is bound to occur from the structural arrangement of the media and the conditions at the boundaries. One cannot expect to obtain exact replica of the force distribution from the simple shear tests and the lattice model. Although the disks used in the tests were machined with close tolerances, even small surface variations can significantly alter the force distribution from an ideal array of disks as assumed in the LTM. As the shear strain is applied to the assembly, load redistribution occurs and again LTM predicts load paths that are similar to the experiments (Figs. 5.13a,b).

For the loose assembly, the disks are aligned one on top of the other so that the load paths are vertical (Fig. 5.6) under the vertical load only. The LTM results show a similar load path (Fig. 4.9b, PART I). These initially vertical paths (columns) become inclined as shear strains are applied (compare Fig. 5.7b with Fig. 4.9b, PART I). Because of the slight discrepancies in the size and contact roughness of the disks in the experiments, it is not possible to conduct a realistic comparison between the experimental results and the results of the LTM. However, the predictions from the LTM and the experiments are qualitatively similar.

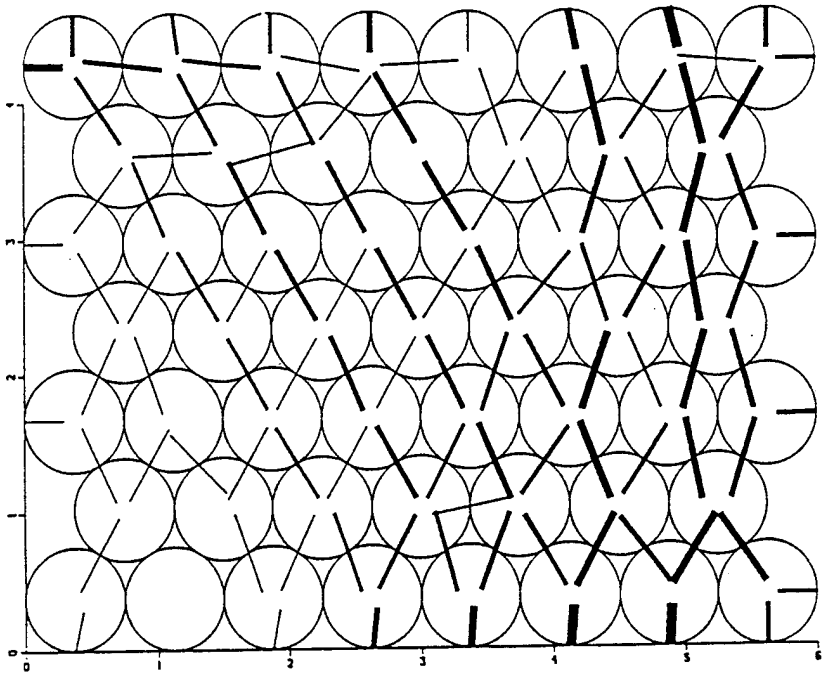

Figure 5.13a. Contact force vector plot dense assembly at a small shear strain (0.1%) (Fig 5.11) created by using the modified version of de Josselin de Jong and Verruijt's method of finding contact force vectors.

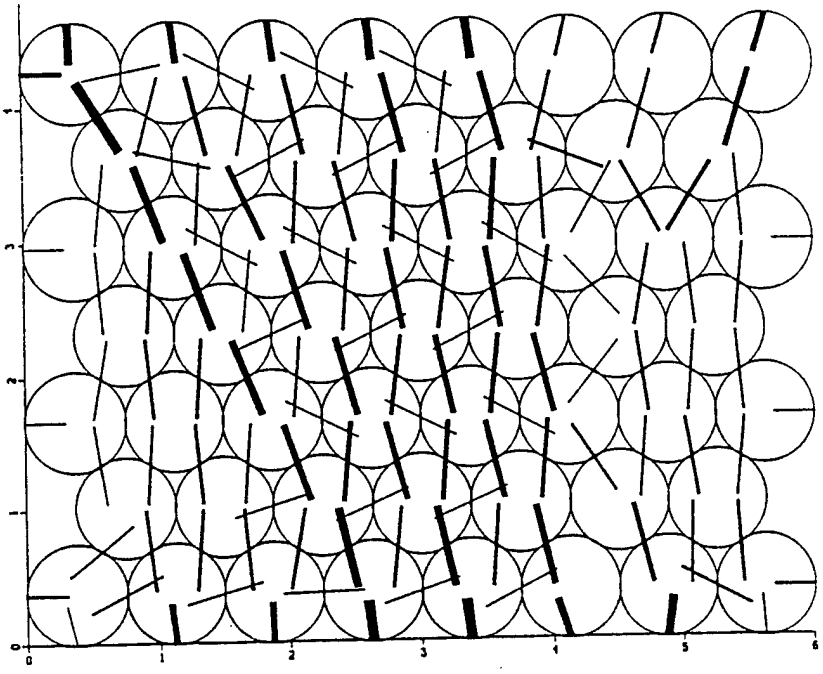

Figure 5.13b. Contact force vector plot: dense assembly at a small shear strain (Fig 5.11) predicted by the lattice type model.

CHAPTER 6

CONCLUSIONS AND RECOMMENDATIONS

6.1 Conclusions

An experimental system consisting of a shear box, photoelastic equipment and digital image processing technology was developed to investigate load distribution and preferred deformation mechanisms involved in the deformation of a particulate media under simple shear. The system was very effective. Micro-features that affect the behavior of particulate media can be individually addressed and analyzed in great detail.

A method of contact force analysis based on photoelastic data has been developed and implemented to determine contact force vector distribution networks for an assembly of photoelastic disks. Comparison of the load distribution networks with similar networks predicted by the lattice type model reveal concordance. The lattice type model appears to be a viable model to provide insights into the micromechanical behavior of granular assemblies.

Photoelastic motion pictures reveal that a slipping and locking mechanism exists at disk contacts. Throughout the range of the shear deformation, the disks continuously engage and disengage one another. Clusters or rigid groups of particles are formed during deformation. This is consistent with Horne's (1965) observation that the deformation of a granular material results from the relative movement of instantaneously rigid groups of particles, constantly redistributing themselves in division and coalescence.

It is also consistent with Drescher and de Josselin de Jong's (1972) double-sliding, free-rotating model.

Rotation of individual disk during simple shear has been observed to be dependent upon whether the disk in question is sliding relative to neighboring particles. In general, if the vertical contacts of a disk in the loose arrangement was slipping relative to neighboring disks, the individual disk rotated relative to the loading frame. If the vertical contacts exhibited friction locking, the disk showed almost no rotation relative to the frame. A disk in the densest possible arrangement has been observed to remain without rotating relative to the frame, probably because it has more contact points with neighboring disks, increasing the likelihood that it is locked against one or more of those disks.

The pattern of stress transmission in the loose disk arrangement under simple shear has been observed to be somewhat random. This is partially attributable to the nature of the loose packing. In simple shear, the vertical load that initially caused stress to flow vertically is redirected to flow across the box's shorter diagonal. In the idealized loose packing, the disks are arranged such that the contacts are 90° from one another, making load transfer impossible between two diagonal (i.e., non-contacting) disks. Load redistribution during simple shear is sensitive to frictional micro-variations in the surface profile of the particles.

6.2 Recommendations

1. The photoelastic experiments coupled with the image processing software is a powerful experimental method to determine load paths and deformation mechanisms. This arrangement can be used to make more direct comparisons with results from the lattice type model and discrete element methods provided that the disks are precisely the same size and roughness. This is possible by molding the disks rather than cutting them out from photoelastic sheets.

2. A better simulation can be accomplished using photoelastic spheres in a modified version of the simple shear device described here. The modification involves the redesign of the shear box to accommodate the spheres.

REFERENCES

Budhu, M., (1979) "Simple Shear Deformation of Sands," Ph.D. thesis, Cambridge University, Cambridge, United Kingdom.

Budhu, M., (1983) "Nonuniformities imposed by simple shear apparatus," *Canadian Geotechnical Journal*, **21**, 125-137.

Budhu, M., (1988) "Failure State of a Sand in Simple Shear," *Canadian Geotechnical Journal*, **25**, 395-400.

Budhu, M., and Britto, A.M., (1987) "Numerical analysis of soils in simple shear devices," *Soils and Foundations*, **27**(2), 33-46.

Chen, T.Y., and Taylor, C.E., (1989) "Computerized Fringe Analysis in Photomechanics," *Experimental Mechanics*, **29**, 1-15.

Dally, J.W., and Riley, W.F., (1965)*Experimental Stress Analysis*, McGraw-Hill, New York.

De Josselin de Jong, G., and Verruijt, A., (1969) "Étude Photo-élastique d'un Empilement de Disques," *Cahiers du Groupe Français de Rhéology*, **2**, 73-86. (in French)

Drescher, A., and De Josselin de Jong, G., (1972) "Photoelastic Verification of a Mechanical Model for the Flow of a Granular Material," *Journal of the Mechanics and Physics of Solids*, **20**, 337-351.

Feda, J., (1982) *Mechanics of Particulate Materials: The Principles*, Elsevier, New York.

Frocht, M.M., (1941) *Photoelasticity*, John Wiley and Sons, New York, Vol I.

Frocht, M.M., (1948) *Photoelasticity*, John Wiley and Sons, New York, Vol II.

Gillies, A.C., (1988) "Image Processing Approach to Fringe Patterns," *Optical Engineering*, **27**(10), 861-866.

Hu, F., Yu, Y.S., Hua, Z.Y., Gung, W.S., (1983) "Automatic Acquisition and Processing of Photoelasticity Data," *Proceedings of the Third Scandinavian Conference on Image Analysis*, 210-215.

REFERENCES (cont.)

Müller, R.K., and Saackel, L.R. (1979), "Complete Automatic Analysis of Photoelastic Fringes," *Experimental Mechanics*, **19**, 245-252.

Müller, R.K., and Saackel, L.R., (1979) "Complete Automatic Analysis of Photoelastic Fringes," *Experimental Mechanics*, **29**, 245-251.

Oda, M., (1972a) "The Mechanism of Fabric Changes During Compressional Deformation of Sand," *Soils and Foundations*, **12**, No. 2, 1-18.

Oda, M., (1972b) "Deformation Mechanism of Sand in Triaxial Compression Tests," *Soils and Foundations*, **12**, No. 4, 45-63.

Oda, M., (1974a) "A Mechanical and Statistical Model of Granular Material," *Soils and Foundations*, **14**, No. 1, 13-27.

Oda, M., and Konishi, J., (1974b) "Microscopic Deformation Mechanism of Granular Material in Simple Shear," *Soils and Foundations*, **14**, No. 1, 25-38.

Paikowsky, S.G., DiRocco, K.J., (1993) "Image analysis of Interparticle Contact Modeling," *Digital Image Processing: Techniques and Applications in Civil Engineering: Proceedings of a Conference*, Kona, Hawaii, February 28-March 5.

Paikowsky, S.G., DiRocco, K.J., and Xi, F., (1993) "Interparticle Contact Force Analysis and Measurements Using Photoelastic Techniques,"*Second International Conference on Discrete Element Methods*, March 18-19, MIT, Cambridge, Massachusetts.

Patterson, E.A., (1988) "Automated Photoelastic Analysis," *Strain*, **24**(1) 15-20.

Poritsky, H., (1950) "Stresses and Deflections of Cylindrical Bodies in Contact With Application to Contact of Gears and of Locomotive Wheels," *Journal of Applied Mechanics*, **72**, 191-201.

Ramesh, K., Ganesan, V.R., and Mullick, S.K., (1991) "Digital Image Processing of Photoelastic Fringes - a New Approach," *Experimental Techniques*, **15**(5), 41-46.

REFERENCES (cont.)

Roscoe, K.H., (1953) "An apparatus for the application of simple shear to soil samples," *Proceedings of the Third International Conference on Soil Mechanics and Foundation Engineering,* Zurich, **1**, 186-191.

Shukla, A., and Damania, C., (1987) "Experimental Investigation of Wave Velocity and Dynamic Contact Stresses in an Assembly of Disks," *Experimental Mechanics*, **30**, 80-87.

Shukla, A., and Nigam, H., (1985) "A Numerical-Experimental Analysis of the Contact Stress Problem," *Journal of Strain Analysis*, **20**, 241-245.

Stroud, M. A., (1971) "The behavior of sand at low stress levels in the simple shear apparatus," Ph.D. thesis, Cambridge University, Cambridge, United Kingdom.

Umezaki, E., Tamaki, T., Takahashi, S., (1988) "Image Analysis of Photoelastic Fringes,"*Japanese Society of Mechanical Engineers International Journal*, **31**(1), 70-75.